

Figure 0-1. (Cover illustration). The innovation of this project, compared to current medical imaging devices, lies in its elimination of two bottlenecks and two “brick walls” in the electronics, allowing a much lower radiation dose to the patient and the extension of the field of view of the detector from about 20 cm to over 150 cm. The result is that the radiation exposure of the patient, as well as the scanning time and the cost per examination are greatly reduced, while the quality of the image is greatly improved. An excerpt of the project can be found in the PREFACE; the scope of the book is described in Section 1.2; the advantages are described in Section 14, Section 1.3, and shown in Figure 14-1 and Figure 1-3. The elimination of the bottleneck on input is described in Section 14.7.1.3; the elimination of the bottleneck on output is described in Section 14.7.2.4. The elimination of the brick wall on the detector boundaries is described in Section 13.3.8, and its implementation is shown in Figure 15-7; and the elimination of the brick wall on the coincidence detection is described in Section 14.7.2, and in Section 13.3.14.

**400⁺ times improved PET efficiency for
lower-dose radiation, lower-cost**

cancer screening

Dario B. Crosetto

3D-Computing

Copyright © 2000 by Dario Crosetto

All rights reserved. No part of this book may be reproduced or transmitted in any form or by any means, electronic or mechanical, including photocopying, recording, or by any information storage and retrieval system, without permission in writing from the Publisher.

First published in the United States of America in 2000 by 3D-Computing, Inc.

Library of Congress Catalog-in-Publication Data

Crosetto, Dario

400+ times improved PET efficiency for lower-dose radiation, lower-cost cancer screening

Dario Crosetto.

Includes bibliographical references.

ISBN 0-9702897-0-7

©2000 by Dario Crosetto

All rights reserved.

Printed in the United States of America

To my mother, my family and my friends

Trademarks

The following trademarks are the property of the following organizations:

.

UNIX is a trademark of AT&T Bell Laboratories.

IBM PC is a trademark of International Business Machines Corporation.

G10, G11, and G12 are trademarks of LSO Logic.

ECAT, EXACT HR, and PETLINK are trademark of CTI/Siemens.

GE Advance is a trademark of General Electric Corporation.

Posicam is a trademark of Positron Corporation.

CYDAS is a trademark of CyberResearch Corporation.

Windows NT is a trademark of Microsoft Corporation.

.

PREFACE

The invention described in this book makes it possible to build a medical imaging device that detects cancers and other diseases at an early, curable stage; delivers a safe dose of radiation, permitting annual usage; results in improved image quality; and reduces cost to patients and their insurance companies.

It is not merely an improvement of the order of two or three times the efficiency of the current detector as a consequence of advances in technology, but a qualitative breakthrough of the order of over 400 times the efficiency of the current device. These benefits are provided by a set of inventions that makes possible a change in the role of Positron Emission Tomography (PET) from that of monitoring the progress of a disease and its treatment to a screening device for early detection of cancer and other common diseases.

This innovation represents a major advancement in preventive health care and treatment that will substantially reduce deaths from cancer (the leading cause of death for people 45 to 64 years of age in the US) with an annual check-up which can detect cancer at a very early and curable stage. It can also benefit the diagnosis of other common diseases such as brain disorders (Parkinson's and Alzheimer's diseases) and coronary artery disease. PET can detect presence or absence of blood flow and/or metabolism in an area of the heart, indicating how it should be treated, whether surgically, by transplant or bypass, or if surgery is not necessary, by another technique. For instance, absence of metabolism in a large area of the heart would indicate that the tissue is dead and a cardiac transplant is necessary.

PET shows functional imaging at the molecular level as opposed to the anatomical imaging of other devices. Thus, it can indicate if a primary cancer has metastasized to other parts of the body. It replaces multiple medical testing procedures with a single examination, and in many cases it diagnoses disease before it shows up in other tests or with other medical imaging devices (see reference [40]).

During treatment, PET immediately shows the progress of the disease and the way in which the body responds to treatment by monitoring at the molecular level instead of needing to wait for weeks or months for an anatomical change.

The principle of operation of PET is simple:

- Compounds that are normal components of the metabolic process of the body such as sugar (glucose), are labeled with photon-emitting tracers and are injected into the body.
- The tracers emit signals (a pair of photons) from their hosting molecule (or imaging agent) during their journey through the human body, and end their trip in the various organs targeted for examination. (See a more thorough explanation at Section 3).
- A detector senses the signal that was emitted and transmits the information to the electronic circuit, which calculates the location where the signal was emitted (the source) and records its path during the entire journey, detecting also the concentration of the imaging agent molecules carrying this transmitter in the different organs at the end of their trip.

A computer uses the information of the recorded signals to build a dynamic image that shows the normal biological process of healthy organs and the abnormal biological process in organs with disease.

Desirability of utilizing PET as a screening device

PET technology would seem to lend itself to diagnosing the early stages of cancer and other diseases. However, in spite of all the improvements made by extensive research and investment in the past 25 years, this technology has failed to advance beyond its role of targeting higher risk patients and people with an advanced stage of cancer. Present machine designs are not sensitive enough to allow the delivery of an acceptable radiation dose. Instead, the dose to the patient required by PET machines currently in use is equivalent to that which a person receives from all other sources of radiation combined (Radon from the ground, cosmic rays from the sky, radiation from other medical examinations and from consumer products) in about 3 to 8 years. (The average dose per year is 360 mrem in the U.S. In Seattle or Dallas the average radiation is 240 mrem per year, and in the general coastal population it averages less than 360 mrem per year.) To use PET technology yearly as a virtually harmless screening device, the dose required must be kept to about 25 mrem (or commensurate to the total from the other sources of radiation received). A machine designed to that specification, which is out of reach of current PETs, would be greatly beneficial.

The need to reduced the radiation delivered to the patient

PET medical imaging devices have been available now for more than 25 years, but they have not been widely used for two main reasons: One is the high cost of a PET examination (from \$2,000 to \$3,000).

The far more important reason, however, is the high radiation dose that must be delivered to the patient because of the limited sensitivity of the PET device. Current PETs detect, at most, only 2.5 photons out of every 10,000 photons emitted by the radioactive source in the patient's body.

Today's PET requires delivery to the patient an effective radiation dose equivalent of 1,100 mrem for the most common examination with 10 mCi of ^{18}F -FDG tracer, or higher with other examinations. This is equivalent to what a person in the U.S. receives on average from all other sources during three years.

During a visit to a PET center in a hospital in June 2000, the author and another former employee of the SSCL found the following conditions:

The whole-body PET device with a FOV of 16.2 cm was purchased by the hospital in 1998 for \$2 million.

A radiation dose from 12 mCi to 15 mCi of ^{18}F -FDG was delivered to the patient. Scanning usually started 30 minutes after injection and consisted of 50 minutes scanning in 2D mode.

The scanning was performed in five bed positions, each covering a field of view of 14 cm for a total of 70 cm, each position with a scanning time duration of 10 minutes. For each bed position a four-minute transmission scan, with three ^{68}Ge rod sources for a total of about 10 mCi was performed for the acquisition of the attenuation coefficients, followed by six minutes of emission acquisition.

The picture from the four minute scan for attenuation coefficients did not provide useful information but only black and white picture with no grey level that would allow identification of the details of the organs. The reason for the poor image was that the energy resolution of the device was not sufficient to plot the grey levels corresponding to different attenuation. The data could only be used for attenuation correction.

During the acquisition in emission mode, the count rate was about 20,000 coincidences per second for a radiation activity in the patient 30

minutes after injection of 12 mCi of ^{18}F -FDG of 322 million coincidences per second (calculated as $8/11$ of $12 \times 37 \times 10^6 = 322.9 \times 10^6$). This is equivalent to an efficiency of 0.0062%.

The novel approach of the electronics for PET described herein will actually show an efficiency improvement of about 1,600 times compared to the performance of this particular PET and not merely 400 times as is conservatively claimed in the title of this book.

The radiation dose required by the novel approach will be $1/40$ of the one currently delivered. While the effective dose equivalent of radiation delivered to the patient during the examination described above is about 1,620 mrem, an examination with the PET of this proposal will require a dose of only about 40 mrem or even less for the same amount of accumulated photons. (The dose equivalent of radiation during the examination performed during the recent visit to the hospital was calculated as follows: 12 mCi \times 110 = 1,320 mrem [11] for the ^{18}F -FDG radiotracer and about 300 mrem for the three ^{68}Ge rod sources (for a total of 10 mCi) used for 5×4 minutes = 20 minutes).

The duration of the scanning time using the proposed PET for the same field of view will be $1/18$ of the time required by examination with the current PET. The current PET examination required 50 minutes for a 70 cm field of view. (A 157.4 cm FOV of the PET design proposed herein would require 112 minutes). The examination with the proposed PET with 157.4 cm FOV will acquire 524 million coincidences in 6 minutes. The shorter examination time would make it possible to examine more patients each day, perhaps ten times as many as the seven examined with today's PET., thus lowering the cost of the examination.

The quality of the image acquired with the proposed device expressed as the total number of coincidences accumulated will be 14 times better than that acquired by the current PET. The current examination acquired 20,000 coincidences per second for 30 minutes, for a total of 36 million coincidences (6 minutes each bed position times 20,000/sec). The proposal described herein (see Table 1-2) accumulates 524 million coincidences in only 6 minutes.

The areas in which this invention provides benefits

The proposed PET design provides a thousand fold improvement in efficiency, a breakthrough which would allow this technology to be used for screening the entire population for cancer and other diseases, thus saving lives through early detection and treatment. The advantages and

benefits provided by the proposed invention impact three areas: a) the radiation dose delivered to the patient, b) the image quality, and c) the examination time (or cost).

This solution requires only a negligible radiation dose to the patient compared to the amount we receive every day from other sources. The design allows the capture of more information, which results in greater clarity of the image. The efficiency of the design also allows considerably shorter examination times (4 minutes instead of an hour) and lower cost per examination, both features very desirable to the patient and provider alike.

The benefits may be quantified as follows:

- requiring 1/30 the radiation to the patient;
- improved image quality (the number of photons in coincidence acquired during one examination) to a factor of 14 to 40 times.

While the above two parameters combine to result in efficiency improvement to a factor of 420 (14 x 30) and of 1,200 (40 x 30), (or 1,600 as described above for the visit to the PET center in June 2000), an additional benefit is the ensuing reduction in the cost of the examination: since the examination takes from 4 minutes instead of the current 60 (or longer for an equivalent FOV of 157.4 cm. See Section 18) minutes, many more patients can be examined in one day.

Two main targeted uses of the PET devices

In order to obtain the best benefits from this device and save lives from cancer, two main clinical uses should be kept in mind and targeted.

One use is for screening the entire population on an annual basis (and more often than once a year for people 45 years old and up). In these annual examinations radiation delivered to the patient should be limited to about 25 mrem of radiation (which is equivalent to the radiation dose received from three panoramic dental x-rays, or from the cosmic gamma ray radiation received during two flights between the U.S. and Europe). Also, the image quality should be optimized by an acquisition rate of about 200 million photons in coincidence per examination (representing the quality of the image) in a 4-minute examination time.

The second use is for more in-depth clinical examinations for cases of suspected cancer or other diseases. With these types of examinations, the most appropriate imaging agent (or tracer, e.g., ^{18}F -FDG, ^{13}N -ammonia) will be adopted to visualize the disease in the affected organ. The total dose delivered to the patient during one examination should be less than 50 mrem, and the duration of the examination should be commensurate to the findings and the need of acquiring more data. It should be considered, however, that current one hour examination with 10 mCi (1,100 mrem) ^{18}F -FDG provides at most 250 million coincidences per second [23, 22] during one hour of scanning, while the higher efficiency of the PET design proposed herein at the radiation dose 0.4 mCi (44 mrem) provides about 87 million coincidences every minute of examination.

Greater potentials of the PET compared to other functional imaging devices

Two other functional imaging devices have been investigated: the Single Photon Emission Computed Tomography (SPECT) and the dual-head camera.

SPECT uses tracers emitting a single photon, and thus requires a collimator placed in front of the crystals that acts like a lens in an optical imaging system. A way to implement a collimator is to have multiple parallel holes in lead material where the photons travelling with the desired acceptance angle pass through the holes to interact with the crystals. A dual-head camera (which can have SPECT and PET capabilities) instead of a full ring of detectors has only two modules of detectors (or heads) on the two sides of the subject (or body of the patient). Thus, the dual-head camera has a limited detector area capable of capturing the emitted photons.

The PET functional device has clear advantages over both the SPECT and dual-head imaging. The advantages result from the PET technique of the electronic collimator detecting two photons emitted in opposite directions at the same instant, as opposed to the SPECT technique of the hardware lead collimator.

In principle, a perfect detector and perfect electronics of a PET system should be able to capture and identify all photons in coincidence which hit the detector, while SPECT and the dual-head camera are intrinsically incapable of doing so because of their designs: many photons are prevented from hitting the detector, by the lead collimator, which absorbs

them, in the case of the SPECT, or by the reduced solid angle of the dual-head camera.

Even though the currently available PET devices can potentially identify all photons hitting the detector, they are far from efficient. Consequently, their low efficiency of detecting photons with the electronic collimator does not show a marked improvement over the photon detection capabilities of the SPECT and the dual-head camera (reference [159] reports the difference in performance between PET, SPECT and dual-head camera).

The construction of an efficient, low-cost PET imaging system such as the one described herein will sharply increase the difference in efficiency between the PET and the other two functional imaging devices (SPECT and dual-head camera), and therefore make it more advantageous to purchase and use PET instead of the other two devices. No less important is the fact that the relatively low dosage allowed is less harmful to the patient.

The only justification for using a SPECT at that point would be the types of examination that require the use of a tracer (such as Technetium Tc 99m Mebrofenin for hepatobiliary, Sestamibi, a myocardial perfusion for detecting coronary artery disease, Mertiatide renal imaging agent, or Albumin aggregated lung imaging agent) different from the ones emitting photons at 511 keV (such as ^{18}F -FDG, ^{13}N , ^{11}C , ^{15}O , and ^{82}Rb). The latter tracer agents do not allow the physician to perform the kind of specialized examination he formerly performed with SPECT tracers. In that case, the choice of SPECT would be dictated not by the lower cost, as is the case today, but by the need for specialized examinations which can only be performed with some tracer used by SPECT.

A multimodality approach

A further improvement in medical imaging to help the physician in clinical examinations is to combine different technologies in one device. The combination of the PET device with an x-ray computed tomograph (CT) scan is one example. This design provides the anatomical information by means of the CT, which helps to identify the organs in the body, and it provides the functional information by means of the PET, which provides real-time information of the biological process at the molecular level.

It is possible to combine PET and SPECT in a single multimodal device which has several parts in common (detector, mechanics, electronics) while the complexity of the electronics increases only slightly. However, the use of a lead septa as collimator between the patient and the detector will require the construction of a PET system which is larger in diameter. This will result in a longer path for the photons before they reach a detecting element. The longer path will require a longer coincidence time window. This in turn increases the possibility of acquiring multiples (see Section 13.4.5.2), and thus lowers the device efficiency. The need to build a PET/SPECT detector with a larger diameter to accommodate the septa will also increase the cost because it requires larger numbers of crystals and photomultipliers (PMT), or avalanche photodiodes (APD) and electronic channels.

Furthermore, the detector should have an elliptical shape as proposed herein for the section along the body of the patient (instead of the current circular shape) in order to minimize the distance from the radiation source to the detector, and it should have a circular, smaller diameter for the section of the head.

For the above reasons, the PET with CT capabilities should be the first choice and should be targeted to hospitals that will use the device for cancer screening. Smaller hospitals which cannot afford both SPECT/CT and PET/CT devices, could derive great savings from having a single device performing both SPECT and PET, combined with a CT scan to provide the precise information of the anatomy of the organs.

This document provides the design of a multimodal PET/SPECT/CT device. For the reasons mentioned above, however, especially that of achieving better efficiency with a PET device without needing to accommodate the septa for operating in SPECT mode, it is to be expected that many other, highly efficient PET/CT devices will be built. The same electronics described herein for PET/SPECT/CT could be used for the PET/CT device. The 3D-Flow electronics system can detect all three photons during the same examination and separate them (60 keV from X-ray, 140 keV for SPECT and 511 keV for PET).

Furthermore, the innovation described herein can also provide an advantage by increasing the efficiency in current and older PET devices by replacing the electronics of the old PET devices currently operating. The interface to the old or current PET devices can be done at the PMT

level, by taking the analog signals from the photomultipliers of the old or current PET devices and sending them to the 3D-Flow system.

Measurements of the limited efficiency of current PET devices and proof of the advantages claimed by this invention

The measurements of the efficiency of the current PET devices have been reported in articles and can be checked at any time during a PET examination. The proof and verification of the advantages claimed in this document are done by means of measurements and simulation and by comparing the concepts of the approaches used in the past 25 years and the concepts presented herein with this invention.

The efficiency of the current device can be easily computed by a patient by ascertaining two values, the size of the computer file built during the PET scan and the amount of activity of the tracer during the scanning period. Finding the ratio between them will give a measurement of the efficiency of the device.

For example, the radiation activity during the PET scanning time of 60 seconds after injection of 66 mCi of ^{15}O -water tracer (120 seconds half life time) with the scanning starting 20 seconds after injection, is calculated as 7/12 of $66 \times 37 \times 60 = 85.47$ billion pairs of photons generated during the scanning time period. Assuming that the file on the computer is 96 Mbytes and that 8 bytes defines a coincidence, the overall efficiency of the device is $(96 \times 10^6)/8 = 12$ million coincidences found. This is divided by the activity of 85.47 billion coincidences generated during the scanning period, which results in an overall efficiency of 1.4 photons detected out of every 10,000 photons activity in the patient's body.

Without having to go through the experience of a PET examination, one could find out the results of the above measurements reported in publications made by the manufacturers of the PET devices.

Michael Phelps and coworkers built the first PET more than 25 years ago [100]. The same author in an article [1] written in 1998 gives an overview of PET devices and describes the technical evolution and improvements of the PET devices since the first PET was built.

Most of the PET devices used in hospitals today, are manufactured by Siemens (ECAT, EXACT HR, and HR PLUS) [22, 19] and General

Electric (Advance) [23], still provide an overall efficiency of only 0.025%. (See also Sections 11.2.2.6.3, 11.2.2.6.4, 11.2.2.6.2).

Limited advances in PET efficiency in the past 25 years in spite of the excellent detectors for PET that have been available for more than a decade

Newer PET devices do not show great improvements in efficiency, although for more than a decade the detector technology has made available excellent detector blocks using fast crystals with remarkable performance. They are capable of decoding over 256 crystals by a single phototube (see Section 11.2.3.3) and measuring the depth of interaction using several techniques (see Section 11.2.3.2).

The limited improvement made during the past 25 years is reported by the manufacturers of the new PET devices, along with the areas to which the limitation factors apply (see Sections 3.1 and 14).

In summary the improvements in the past 25 years as well the plans for the new designs of PET under construction for the coming years as stated by the designers in several articles have shown two- to fourfold efficiency improvements every five years.

With this low rate of improvement in efficiency, the PET device will never change from the role of a device to be used for patients having higher risks justifying the delivery of a radiation dose which is not negligible (equivalent to what a person in US receives on average from all other sources in three to eight years), to the role of a cancer screening device requiring delivery of a minimal amount of radiation to the patient (equivalent to the cosmic radiation received during two flights between the U.S. and Europe or Japan).

Reasons for the limited advances in PET efficiency in the last 25 years

Reasons the efficiency has not increased are also reported in several articles written by the designers and manufacturers of PET, and again sources are given (see Sections 3.1, 11.2.2, and 14).

For the construction of a PET device with a field of view (FOV) increased from about 20 cm to 150 cm (as is proposed here in order to capture more photons for the implementation of the new role of the device for screening for cancer, the complexity of the electronics increases exponentially. Alternatively, one must drop many photons from being checked thoroughly (as is already partly done in the current PET devices).

In that case, however, no significant advantage accrues to the patient, because the radiation and cost have not been lowered.

Current electronics has the following limitations: a) not all information relative to the incident photon is extracted from the detectors because the digital signal processing on each channel is not present; b) the electronics that should perform a thorough signal processing cannot sustain the high rate of signals produced by the detector, c) the detector block boundary limitation loses information and there is no correlation with neighboring signals behind the 2x2 block,; and d) the approach is inefficient in detecting coincidences which requires many circuits, many comparisons and becomes impractical when the array increases in dimension (such as the increased FOV), requiring an astronomical number of comparisons being made in a very short time.

Assessment of potential for improvement of the 0.025% efficiency of the current PET devices.

Before looking into the construction of new electronics, one has to verify that increasing the efficiency of the PET is technically possible.

Several measures indicate that PET scanner efficiency can be much improved. For instance, when a detector block is used as a stand-alone, the efficiency is much higher. Thus, the problem arises when the electronic system has to handle many signals from several blocks or when “singles” are generated from different locations of the body instead of from just one source.

The current approach used by General Electric and CTI/Siemens, of accepting within a time window of 250 ns the first candidate based on the simple check of high-low energy thresholds and preventing all other candidates from being accepted, produces dead time. Likewise, each module which detects a “single” is dead in one to two microseconds.

Every time a new, higher performance electronics is built, the coincidence detection efficiency increases. This means that more photons in coincidence were there, and only needed to be detected. This occurred also when CTI/Siemens changed their electronics from ACS I to ACS II and from ACS II to ACS III. Only when a higher performance electronics fails to detect additional photons will it be proven that the maximum efficiency has been reached, because that outcome will mean that there are no more photons to be detected.

By analyzing the plot of the sensitivity or count rate capability as a function of radioactivity concentration shown in all articles with performance measurements on different PET devices, one can realize the limitation of the electronics in detecting a high rate of radioactivity. Such analysis shows that improving the electronics will improve the efficiency of the system. The plots will change and will not show saturation when radioactivity is increased if efficient electronics and fast crystals are used.

The simple observation reported in several articles (see Section 3.1) that the reduction of the coincidence time window will reduce the “randoms” (see Section 13.4.5.1), first, should make one realize that the definition of randoms as the detection of two photons in time coincidence belonging to two different positron annihilations has not been correctly used and displayed in the above mentioned plots. Second, if the reduction of the coincidence time window will improve efficiency in reducing randoms and detecting more coincidences, then those statements indicate that efficiency can still be improved with the improvement of the electronics (by using digital signal processing to improve signal-to-noise ratio and time resolution).

The need to improve the electronics is also shown by other simulations reported in the literature [17, 20] where the number of singles that hit the detector is much higher than the number detected by the electronics as coincidences.

Another factor affecting efficiency is the thickness of the crystals used. While 10 years ago most of the designers were using 30 mm crystals in order to have good stopping power, close to 100% interaction efficiency (see Table 1 of [1], and on reference [57]), the more recent PET devices are built with thinner crystals, which reduce the efficiency of the system CTI/Siemens used 15 mm in the ECAT EXACT HRRT, and 10 mm in the MicroPET, the GSO PENN-PET uses 10 mm.

There is also a possibility of improving the current 0.025% efficiency by increasing the field of view of the PET device.

How the present invention increases efficiency by a factor of one thousand and reduces the PET examination cost

The invention described herein provides advantages in efficiency and cost by way of its overall architecture: hardware, software, cabling, system architecture, component architecture, detector elements layout,

interfacing of the electronics to the detector elements, data acquisition, processing, and finding coincidences.

Improvements include:

Better identification of the position, energy, and timing of the photons hitting fast or slow detectors.

Overcoming the limit of handling a large number of channels with a simple electronics.

Sustainability of a high data rate which allows for acquisition of a larger number of coincident photons in a shorter time. This reduces the examination time. A reduced examination time is desirable from the standpoint of cost, allowing more patients to be examined in a day, and from the standpoint of the patient's well-being, reducing the discomfort and the hazard inherent in the procedure.

Scalability in requiring only one additional component to perform comparisons for coincidence detection in the event the average rate increases from 40 million coincidences per second to 80 million per second.

One example of improvement among several provided by this architectural design is the capability of finding coincidences among over a half billion crystal detectors at a rate of up to 40 million coincidences per second making use of very few components and requiring very few comparisons.

The merit of this architecture lies in its simplicity. The main outcome is that the construction of a PET with a field of view over five times the size of that of the current PET will not create the problem of increasing astronomically the number of comparisons required.

The novelty of the new approach with its hardware simplification is that only hits (or single photons) found within the sampling time period need to be compared and not all possible combinations of the pair of detector modules having a line of response passing through the body's patient, as is done now. The check of coincidences in a large array is accomplished by using a single 3D-Flow component which makes only 30 comparisons every 250 ns. This result should be compared with the result from current PET devices which find coincidences from fewer than 20,000 crystals at a rate of up to only 4 million coincidences per second,

using 7 ASICs which must make 700 comparisons every 250 ns regardless of the presence of a hit or coincidences.

All details, specifications, measurements, and simulation are presented and discussed in Sections 14, and 13.

Acknowledgements

The author wishes to acknowledge the many people who encouraged the writing of this book in the hope that it will shorten the wait for an efficient, affordable and safe cancer screening device.

First and foremost, I am indebted to Ms. Harriet Little, who provided invaluable help in correcting the English of this document and for being available to discuss the form of the presentation. I would like to acknowledge also the constant and continuing help of Ms. Maria de Vries in going through the English in both this and past documents. A special thanks also to my cousin Massimo Caprioli from Italy, who provided suggestions and comments after the first reading.

About the author

Dario Crosetto lives and works at the cutting edge of the technology and science of particle physics. He has collaborated for the past 20 years in experiments at the European Laboratory for particle physics at CERN Geneva, and designed the electronics for particles identification at 40 MHz and 60 MHz rate from thousands of channels for major experiments. His designs are included in the Letter of Intent, Technical Proposals and Technical Design Report of experiments of collaborations of hundreds and thousands of physicists (DELPHI-CERN, GEM-SSCL, and LHCb-CERN), and published in several articles in refereed scientific journals.

In 1988 he was appointed for 18 months as “Scientific Associate” at CERN to work full time on a parallel-processing front-end electronic project [2, 3] and on a project for the Q-measurement [4] of the beam at the SPS-CERN synchrotron (he designed and built the project based on the AT&T DSP with the help of the student Stefano Buono [5, 6]).

In 1991 he was invited to work at the Superconducting Super Collider Laboratory (SSCL) project in Texas. Later, when the SSC project was cancelled, he joined the Large Hadron Collider Beauty (LHCb) experiment at CERN.

Among the many other projects and experiments he has worked on is the design and construction of a parallel-processing system based on Texas Instruments DSP for electron identification at the second level trigger for the DELPHI experiment at CERN [7] (a VME board version [8] was marketed by the company Struck in Germany for quality control in the lamination industry).

He also designed the complete electronics system for identifying electrons, hadrons and jet clusters at 60 MHz from multi-channels for the half-billion dollar Gamma, Electrons, and Muons (GEM) experiment [9], and he collaborated in the design and construction of the ASIC for cluster finding in the Time Projection Chambers (TPC) detector of the Solenoid Tracker at RHIC (STAR) experiment of the Relativistic Heavy Ion Collider (RHIC) at Brookhaven National Laboratory.

He designed the electronics for the identification (at 40 MHz from multi-channels) of photons, electron, hadron, and muons for the LHCb experiment as reported in the LHCb Letter of Intent in 1995 and in the Technical Proposal 1998 [10]. He has been the single author of several articles in refereed scientific journals, among which is the article on photons, electron and hadron identifications published in *Nuclear Instruments and Methods in Physics Research, Section A*, vol. 436, Nov. 1999, pp. 341-385.

Table of Contents

PREFACE	i
Acknowledgements	xiv
About the author.....	xiv
1 Introduction.....	1
1.1 A breakthrough in the current evolution of medical imaging devices	1
1.2 Scope of the book	2
1.3 Over 400 times efficiency improvement.	4
1.4 Benefits in cancer prevention affordable in cost and radiation dose	6
1.5 Current and developmental PET scanners and comparison of their characteristics.	
11	
PART 1 CONCEPTS.....	13
2 Breaking the barrier of the high number of coincidences generated by larger system	13
3 Analysis of the nature of the physics experiment occurring in PET devices	13
3.1 Analysis of the performance of the current PET devices.....	17
3.2 Solution for overcoming the efficiency limitation imposed by the architectural approach used in current PET systems.....	22
4 Specifications of the most cost-effective PET.....	23
PART 2 CLINICAL USEFULNESS.....	24
5 Clinical and research applications	24
6 Impact of this improved design for the population	24
7 Radionuclides for PET and SPECT	25
8 Tracers kinetic, radiation activity to the PET and uptake dose by the patient	26

PART 3 BACKGROUND IN RADIATION 27

9 The nature of the radiation delivered to the patient 27

- 9.1 Radon in the home.....28
- 9.2 Terrestrial and cosmic gamma rays.....29

10 The electromagnetic spectrum 30

PART 4 IMPLEMENTATION 31

11 Different detector types..... 31

11.1 Detector requirements for high-efficiency low-cost photon detection31

11.2 Comparison of the characteristics of different detector modules.....32

11.2.1 Components of PET detector modules.....32

11.2.1.1 Gamma converter for 60 keV to 511 keV photons32

11.2.1.2 Transducers that generate an electrical signal proportional to an incident photon when the transducer is coupled to a gamma converter35

11.2.1.2.1 Photomultipliers (PMT)36

11.2.1.2.2 Avalanche Photodiodes (APD)37

11.2.1.2.3 Silicon Photodiode (PD)37

11.2.1.2.4 Multiwire Proportional Chamber (MWPC)39

11.2.1.2.5 Other transducers39

11.2.2 Assemblies of PET detector modules in blocks.....40

11.2.2.1 LSO/GSO crystals coupled to PMTs41

11.2.2.1.1 CTI/Siemens ECAT HRRT PET41

11.2.2.1.1.1 Performance measurements on CTI/Siemens ECAT HRRT PET42

11.2.2.2 LSO coupled to PMT43

11.2.2.2.1 CTI/Siemens MicroPET43

11.2.2.3 LSO coupled to APD44

11.2.2.4 LSO coupled at one end with photodiodes and at the other end with PMT.....45

11.2.2.5 GSO coupled to PMT.....45

11.2.2.5.1 GSO HEAD PENN-PET.....45

11.2.2.5.2 Assembly of an array of 36 GSO(Ce) crystals coupled to 4 phototubes.....46

11.2.2.6 BGO coupled to PMT47

11.2.2.6.1 CTI/Siemens PET966/EXACT3D47

11.2.2.6.1.1 Performance measurements on CTI Siemens PET966/EXACT3D47

11.2.2.6.2 CTI/Siemens ECAT EXACT HR PLUS.....48

11.2.2.6.3 General Electric Advance49

11.2.2.6.3.1 Details on the General Electric Advance PET hardware system and electronics ...49

11.2.2.6.3.2 Performance measurements on General Electric Advance PET51

11.2.2.6.4 CTI/Siemens ECAT EXACT HR52

11.2.2.6.4.1	Details on the CTI/Siemens ECAT EXACT HR PET hardware system and electronics	52
11.2.2.6.4.2	Performance measurements on CTI/Siemens ECAT EXACT HR PET	54
11.2.2.6.5	CTI/Siemens ECAT EXACT	54
11.2.2.6.6	Positron Posicam 6.5 PET	55
11.2.2.7	Multi-crystals with different physical properties coupled to PMT (Phoswich)	56
11.2.2.7.1	YSO/LSO coupled to PMT (for PET/SPECT scanners with DOI measurements)	56
11.2.2.8	Multi-crystals with different physical properties coupled to APD (Phoswich)	57
11.2.2.8.1	GSO/LSO/YSO coupled to ReAPD	57
11.2.2.8.2	YSO/BGO/LSO/CsI(Tl) coupled to APD	57
11.2.2.8.3	CsI(Tl)/LSO/GSO coupled to APD (for PET/SPECT/CT scanners with DOI measurements)	57
11.2.3	<i>Design of PET detector modules targeted to improve some characteristics</i>	59
11.2.3.1	Time of flight (TOF)	59
11.2.3.1.1	Super PET 3000-E Time-of-flight (CsI crystals)	59
11.2.3.1.2	Considerations in using LSO crystals for Time-of-flight PET	60
11.2.3.2	Depth of interaction (DOI)	61
11.2.3.3	Spatial resolution	63
11.2.3.4	Sensitivity or count rate (hazard to the patient)	64
11.2.4	<i>PET detector assemblies using a continuous crystal</i>	64
11.2.4.1	NaI(Tl) coupled to PMT (HEAD PENN-PET)	64
11.2.4.1.1.1	Performance measurements on HEAD PENN-PET	64
11.2.4.2	Design of the LSO coupled to PMT (Animal PET-UCLA)	66
11.3	The need for flexible and performance electronics for extracting and improving the characteristics of low-cost detector modules	67
12	The 3D-Flow architectural approach	67
12.1	DSP functions with neighboring signal correlation capabilities	68
12.1.1	<i>Extending the execution time in one pipeline stage</i>	68
12.1.2	<i>The intrinsic bypass switch in each 3D-Flow processor</i>	69
12.2	A single type of circuit for several algorithms	71
12.3	A single type of component for several algorithms	73
12.4	Versatility and flexibility of the 3D-Flow systems to different types of PET/SPECT/CT detectors	74
13	Design of a multimodality PET/SPECT/CT 3D-Flow based system ...	75
13.1	Description and requirements of a multimodality PET/SPECT/CT device	75
13.2	Example of assembly of a PET/SPECT/CT device.	77
13.3	Mapping the 3D-Flow system into the PET/SPECT/CT imaging system.	80
13.4	Solutions provided by the 3D-Flow system to the PET/SPECT/CT requirements..	85
13.4.1	<i>Latency time through the entire system</i>	85
13.4.2	<i>Ascertaining that the 3D-Flow system provides sufficient input bandwidth</i>	87

13.4.3	<i>Two examples of detectors: crystals with fast and slow decay time</i>	88
13.4.3.1	Example 1: interfacing between detectors with fast crystals and the 3D-Flow	88
13.4.3.2	Example 2: interfacing between detectors with slow crystals and the 3D-Flow	91
13.4.4	<i>The front-end electronics</i>	92
13.4.4.1	Constant Fraction Discriminator	93
13.4.4.2	Front-end electronics for fast crystals	93
13.4.4.3	Front-end electronics for slow crystals	95
13.4.5	<i>Definition and how to deal with randoms and multiples</i>	97
13.4.5.1	Randoms	97
13.4.5.2	Multiples	97
13.4.5.3	How to identify Randoms and Multiples, correct, and/or reject them	98
13.4.5.4	Compton scatter: how to detect these events, and/or correct and/or reject them.	98
13.4.6	<i>Attenuation correction</i>	100
13.4.7	<i>Difference between true event efficiency and coincidence efficiency</i>	102
13.4.8	<i>No detector boundaries for the centroid calculation with the 3D-Flow</i>	103
13.4.9	<i>Flexibility in measuring the depth of interaction with the 3D-Flow system</i>	106
13.4.10	<i>Time resolution of 500 ps for PET devices assisted by TOF information</i>	107
13.4.11	<i>Photon identification: The PET/SPECT/CT real-time zero dead-time algorithms for fast or slow detectors using the 3D-Flow system</i>	110
13.4.11.1	Format of the input word from the detector to the 3D-Flow system stack	110
13.4.11.2	Photon detection algorithm simulation with the 3D-Flow for PET/SPECT/CT	111
13.4.11.3	Simulation of the 5x5 clustering algorithm in 9 steps with the 3D-Flow	113
13.4.11.4	Format of the output word of the “singles” identified by the 3D-Flow “stack”	115
13.4.12	<i>Output of the identified photons: memory buffer and/or 3D-Flow pyramid</i>	115
13.4.12.1	Separating the single photons found by the 3D-Flow stack.....	116
13.4.12.2	Simulation of the channel reduction in the 3D-Flow pyramid.....	117
13.4.13	<i>Choice of an output bandwidth and design of the output stage to meet it</i>	120
13.4.14	<i>Coincidence identification functions implemented in the 3D-Flow pyramid</i>	121
13.4.14.1	Sorting events in the original sequence and regaining fixed delay between data at different stages.....	121
13.4.14.2	Example of a coincidence detection implementation with the 3D-Flow	124
13.4.14.3	General scheme for implementing a system with higher bandwidth and maximum coincidence detection efficiency	129
13.4.14.4	Format of the output word of the “coincidences” from the 3D-Flow pyramid to the buffer memory	130
13.4.15	<i>Device operation in PET, SPECT, and CT mode</i>	130
13.4.16	<i>Reading results from the event buffer memory and packing for transmission in the PETLINK digital interconnect standard</i>	131

14 Comparison of the 3D-Flow approach vs. current approach..... 131

14.1	Requiring 1/30 the radiation to the patient with the 3D-Flow system.	135
14.2	Identifying from 14 to 40 times more photons than the current PET	135

14.3	Photons scattered and absorbed in the body of the subject	136
14.4	Field-of-view (FOV)	136
14.5	Solid angle.....	137
14.6	Crystal stopping power, photofraction, and crystal scatter	138
14.6.1	<i>Crystal stopping power.....</i>	139
14.6.2	<i>Photofraction.....</i>	139
14.6.3	<i>Crystal scatter vs. scatter in the patient's body.....</i>	140
14.7	Electronics.....	140
14.7.1	<i>Identification of photons and extraction of their characteristics</i>	140
14.7.1.1	Front-end electronics of the 3D-Flow system vs. current PET FE electronics	142
14.7.1.2	Elimination of the detector blocks boundaries.....	143
14.7.1.3	Elimination of the incoming data bottleneck	144
14.7.2	<i>Coincidence detection logic.....</i>	145
14.7.2.1	The approach of coincidence detection used in the current PET	145
14.7.2.2	Elimination of need to compare an extremely large number of LOR when the FOV increases	149
14.7.2.3	3D-Flow coincidence detection circuits vs. GE Advance coincidence circuit.....	150
14.7.2.4	Elimination of the outgoing data bottleneck	152
15	Modular Hardware Implementation in IBM PC or VME platform for systems of any size	153
15.1	A single type of DAQ board	153
15.1.1	<i>IBM PC DAQ boards.....</i>	154
15.1.1.1	IBM PC board with 64 analog channels and 32 digital I/O	154
15.1.1.1.1	Timing and synchronization issues of control signals in the 3D-Flow system	156
15.1.1.2	IBM PC board with 256 analog channels and 32 digital I/O	157
15.1.2	<i>VME DAQ boards.....</i>	158
15.1.2.1	VME board with 64 analog channels and 32 digital I/O.....	159
15.1.3	<i>VME board with 256 analog channels and 32 I/O.....</i>	160
15.2	A single type of Pyramidal & buffer board.....	161
15.2.1	<i>IBM PC Pyramidal and buffer board.....</i>	161
15.2.2	<i>VME PC Pyramidal and buffer board.....</i>	162
15.3	3D-Flow neighboring connection on the edge of the IBM PC board, or on the backplane of the VME crate.....	164
16	Application: Replacing the electronics of the current and past PET for lowering the cost and the radiation to the patient.....	167
16.1	Logical layout for a 3D-Flow system replacing the electronics of the current and past PET for lowering the cost and the radiation to the patient	167

17 Application: Design for the construction of a PET with 400⁺ fold efficiency improvement	170
17.1 PET/SPECT/CT application using slow crystals	170
17.1.1 Logical layout of the electronics for a PET/SPECT/CT system requiring high performance for extracting photon characteristics from slow crystals	171
17.1.2 Logical and Physical layout for a PET/SPECT/CT requiring high performance for extracting photon characteristics from slow crystals.	173
17.1.3 Physical layout for a PET/SPECT/CT system requiring high performance for extracting photon characteristics from slow crystals.	176
17.2 Logical and physical layout for a PET/SPECT/CT system using fast crystals	178
18 Cost for a PET/SPECT/CT system of different sizes and using fast or slow crystals.....	181
19 Glossary	185
20 Bibliography	189

Figure 0-1. (Cover illustration). The innovation of this project, compared to current medical imaging devices, lies in its elimination of two bottlenecks and two “brick walls” in the electronics, allowing a much lower radiation dose to the patient and the extension of the field of view of the detector from about 20 cm to over 150 cm. The result is that the radiation exposure of the patient, as well as the scanning time and the cost per examination are greatly reduced, while the quality of the image is greatly improved. An excerpt of the project can be found in the PREFACE; the scope of the book is described in Section 1.2; the advantages are described in Section 14, Section 1.3, and shown in Figure 14-1 and Figure 1-3. The elimination of the bottleneck on input is described in Section 14.7.1.3; the elimination of the bottleneck on output is described in Section 14.7.2.4. The elimination of the brick wall on the detector boundaries is described in Section 13.3.8, and its implementation is shown in Figure 15-7; and the elimination of the brick wall on the coincidence detection is described in Section 14.7.2, and in Section 13.3.14.	i
Figure 1-1. The evolution of positron imaging systems (original source of the figure [1]). Section (a) shows the evolution of the PET using past and current approach, while Section (b) shows the improvements achievable with the novel 3D-Flow approach describe in this document.....	1
Figure 1-2. The breakthrough in efficiency achievable with the described invention.....	5
Figure 1-3. Only 1/30 the radiation dose delivered to the patient.....	7
Figure 1-4. Only 1/10 the duration for the long examination of 60 minutes with ¹⁸ F-FDG (@ 1/25 the radiation dose).....	9
Figure 1-5. Only 1/10 the examination cost to the patient.....	10
Figure 3-1. The annihilation of a positron and an electron in two 511 keV photons.	14
Figure 3-2. Graphic view of the ideal detection of “singles” photons by PET with a different field of view.	16
Figure 3-3. Graphic view of the detection of the coincidences by the current PET systems.....	18

Figure 3-4. Graphic view of the ideal vs actual coincidence detection of the current PET system and the solution to improve the efficiency.	23
Figure 4-1. Geometry of a cost-effective PET system derived from the analysis and specification definition	24
Figure 6-1. Deaths in the US in 1997 by cause and by age group.	25
Figure 9-1. Details of the background radiation in the US by subject.	27
Figure 9-2. Radon potential in US (source from reference []).	28
Figure 11-1. Layout of the detector block and assembly for the CTI/Siemens head PET ECAT HRRT.	42
Figure 11-2. Layout of the detector block and assembly for the CTI/Siemens MicroPET for small animals.	44
Figure 11-3. Layout of the detector block with 64 LSO coupled at one end with 64 photodiodes and at the other end with a single photomultiplier.	45
Figure 11-4. Layout of the detector block and assembly for the GSO HEAD PENN-PET.	46
Figure 11-5. Layout of the detector block and assembly for the CTI/Siemens PET966/EXACT3D.	47
Figure 11-6. Layout of the detector block and assembly for the CTI/Siemens ECAT EXACT HR PLUS.	48
Figure 11-7. Layout of the detector block and assembly for the General Electric Advance.	50
Figure 11-8. Layout of the detector block and assembly for the CTI/Siemens ECAT EXACT HR.	53
Figure 11-9. Layout of the detector block and assembly for the Positron Posicam 6.5 PET.	56
Figure 11-10. Layout of the detector block with BGO/LSO/YSO/CsI(Tl) coupled to an APD.	57
Figure 11-11. Layout of the detector block with a) CsI(Tl)/LSO/GSO coupled to APD, and b) YSO/LSO coupled to APD.	58
Figure 11-12. Layout of the detector block and assembly for the CsI Super PET 3000-E Time-of-flight.	60
Figure 11-13. Layout of the assembly of the continuous detector for the HEAD PENN-PET scanner.	65
Figure 11-14. Design of the layout of the assembly for the continuous detector for animal PET (UCLA)	67
Figure 12-1. One pipeline stage needs to have the processing time extended. The electronics of Stage 3 (St_3) consists of several layers of 3D-Flow processors called a “stack.” Each 3D-Flow processor executes the entire real-time algorithm. Programmability has been achieved, and ultra-fast cable logic implementation is not necessary. An intrinsic bypass switch in each 3D-Flow of the stack performs the function of routing the incoming data to the first idle processor.	69
Figure 12-2. The flow of the input data and output results in a 3D-Flow system. The example shows a 3D-Flow system executing an algorithm that requires three times the time interval between two consecutive input data where the input data rate is 1/8 the processor clock frequency. The left column of the table at the left shows how processors at each layer count the input data, bypass data, results, and bypass results in order to set the bypass switches appropriately at the processors at each layer. An example of the position of the bypass switches for clocks #34 and #35 is shown in the other columns of the table.	70
Figure 12-3. The 3D-Flow architecture based on a single type of circuit (PE). The left section of the figure shows a “stack” of 3D-Flow processors made of several layers, the right section of the figure shows the timing of a) the input data, b) the task executed by different layers and c) output results.	72
Figure 12-4. Technology independent 3D-Flow ASIC.	74
Figure 13-1. Example of an assembly of a PET/SPECT/CT multimodality device (lead septa that should be placed inside the detector between the crystals and the transmission bar, are not shown in the figure).	80
Figure 13-2. Mapping the 3D-Flow system into PET imaging system. Section a) shows the layout of the 3D-Flow electronics for current and old PET devices, b) shows the dimensions of the PET rings using current circular gantry, and c) shows the dimensions of the PET rings using the proposed elliptical gantry.	84
Figure 13-3. Time latency between data at different layers of the 3D-Flow system.	86
Figure 13-4. Examples of acquiring data by the 3D-Flow system, from the detector.	90

Figure 13-5. Constant fraction discriminator (CFD). Section (a) shows the relation between the output signal and the input signal and the intermediate steps of the delayed, inverted, and attenuated signals. Section (b) shows the zero crossing of signals with the same shape but with different amplitude occurring at the same time.	93
Figure 13-6. Block diagram of the front-end electronics for the fast crystals	95
Figure 13-7. Block diagram of the front-end electronics for the slow crystals.....	96
Figure 13-8. Randoms.	97
Figure 13-9. Multiples.	97
Figure 13-10. Compton scatter	99
Figure 13-11. Measurements of the attenuation correction for PET and determination of attenuation coefficients.	102
Figure 13-12. Comparison of the centroid calculation method using the 3D-Flow and the current PET systems.	105
Figure 13-13. Parallax error measured by the Depth of interaction.....	106
Figure 13-14. Flexibility of DOI measurements with the 3D-Flow vs. fix technique used by current PET systems.....	107
Figure 13-15. Time resolution of 500 ps for PET devices assisted by TOF information.	109
Figure 13-16. Calibration of the PET system.	109
Figure 13-17. Photon detection algorithm simulation with the 3D-Flow for PET/SPECT/CT.	112
Figure 13-18. 3D-Flow simulation of the 5x5 clustering algorithm in 9 steps.	114
Figure 13-19. Channel reduction scheme of the 3D-Flow pyramid.	119
Figure 13-20. Flow chart of the 3D-Flow program routing data in the pyramid.	119
Figure 13-21. Sequence of operations for the implementation of the circular buffer for sorting and regaining fixed latency of events.	123
Figure 13-22. Sorting the events in the original sequence and regaining a fixed delay of the data between stages.	124
Figure 13-23. Coincidence detection scheme with the 3D-Flow approach. Only the candidates found within a time of 50 ns are compared (no more than 4 are expected). The candidates from different detector blocks may require different numbers of clock cycles to reach the exit point; thus a sorting/resynchronizing circular buffer realigns the events in the original sequential order and within a fixed delay time from when they occurred. The left part of the figure shows how many types of 3D-Flow components are required to implement the different functions.	126
Figure 13-24. Definition of sectors for the detection of coincidences in PET mode.....	127
Figure 13-25. List of operations performed in the processors of component 158.	128
Figure 14-1. Comparison of the efficiency between the 3D-Flow PET system and the current systems.	134
Figure 14-2. Digital Signal Processing vs. Analog Signal Processing Front-End for PET with digital signal integration.	143
Figure 14-3. LOR checked for coincidence as implemented on the GE Advance. Data from 56 detector modules are sent to 7 ASICs according to the connection scheme reported in Table 14-1. Each ASIC performs 13 comparisons each time slot of 25 ns. The first row of the figure indicated with “Time 1” shows the detector modules that are compared (e.g. at top left of Time 1, module 0 is compared with module 16, then with 17, and so on). The figure shows only the comparisons along the line of response LOR during Time 1 and Time 5.....	148

Figure 14-4. Connection scheme of the 56 detector modules to the 7 ASICs for the GE Advance. See also Table 12-1. Each ASIC performs 130 comparisons every 250 ns. One coincidence can be found out of about 700 comparisons with data from modules every 250 ns.	149
Figure 14-5. The 3D-Flow PET coincidence detection approach vs. the current approaches to find coincidences in PET.	152
Figure 15-1. 64 channels IBM PC compatible 3D-Flow board. One analog channel to one 3D-Flow processor.	155
Figure 15-2. 256 channel IBM PC compatible board; four analog channels to one 3D-Flow processor	158
Figure 15-3. 64 channel VME board; one analog channel to one 3D-Flow processor	159
Figure 15-4. 256 channel VME board; four analog channels to one 3D-Flow processor	160
Figure 15-5. IBM PC 3D-Flow Pyramid board for channel reduction, event sorting, and coincidence detection.	162
Figure 15-6. VME 3D-Flow Pyramid board for channel reduction, event sorting, and coincidence detection..	163
Figure 15-7. Backplane carrying the information to/from the neighboring 3D-Flow processors.....	166
Figure 16-1. Logical layout for a 3D-Flow system replacing the electronics of the current and past PET for lowering the cost and the radiation to the patient.	169
Figure 17-1. Logical layout for a PET/SPECT/CT system requiring high performance for extracting photon characteristics from slow crystals.	173
Figure 17-2. Logical and physical layout for a PET/SPECT/CT system requiring high performance for extracting photon characteristics from slow crystals	175
Figure 17-3. Physical layout for a PET/SPECT/CT system using slow crystals	177
Figure 17-4. Logical and physical layout for a PET/SPECT/CT system using fast crystals	180
Table 1-1. Naming and relation among measuring units of radiation.....	6
Table 1-2. Effective dose equivalent of radiation delivered to the patient generated by different radiotracers vs. the quality of the image and system used.....	8
Table 1-3. Current and developmental PET scanners and some reported performance characteristics.....	11
Table 7-1. Most common radioisotope used in PET.....	26
Table 11-1. Characteristics of scintillation detectors for 60 keV to 511 keV photons.	33
Table 11-2. Characteristics of active detectors converting the 60 keV to 511 keV photon directly into an electrical signal.	34
Table 11-3. Transducers that generate an electrical signal proportional to the incident photon.....	35
Table 13-1. Mapping the 3D-Flow system to current PET devices and future PET devices of different sizes with circular and elliptical gantry.	83
Table 13-2. 3D-Flow instructions to move data in the 3D-Flow pyramid from several input ports of one processor to the designated output port of the same processor (depending on the location of the processor in the 3D-Flow array. The data received are sent to different output ports. Five programs contemplating the cases of the five ports of the processor are necessary. The following example contemplates the case of sending the input data to the output port East. Similar programs will send the received input data to North, West, South, and Bottom).....	120
Table 14-1. Connection of each of the 7 ASIC detecting coincidences to the 56 detector modules.	148
Table 15-1 . 3D-Flow IBM PC board component list and power dissipation estimate for 64 channels.....	156
Table 15-2. 3D-Flow IBM PC board component list and power dissipation estimate for 256 channels.....	157

Table 15-3 . 3D-Flow IBM PC pyramid board component list and power dissipation estimate.	163
Table 17-1 . 3D-Flow IBM PC base system for a whole-body PET with 157.4 cm FOV and 2,304 channels..	178
Table 17-2 . 3D-Flow IBM PC base system for a whole-body PET with 126 cm FOV and 1792 channels.....	181
Table 18-1. Cost of the main components of a current whole-body PET, 23.4 cm FOV, of recent development with slow crystals.....	182
Table 18-2. Estimated cost of the main components of a future whole-body PET, 157.4 cm FOV, with slow crystals based on the approach used in current PET.	182
Table 18-3. Estimated cost of the main components of a future whole-body PET , 157.4 cm FOV, with slow crystals based on the new approach of the 3D-Flow described herein.	183
Table 18-4. Estimated cost of the main components of a future whole-body PET, 126 cm FOV, with slow crystals based on the new approach of the 3D-Flow described herein.	184
Table 18-5. Estimated cost of the main components of a future whole-body PET, 126 cm FOV, with fast crystals based on the new approach of the 3D-Flow described herein.	184

1 Introduction

1.1 A breakthrough in the current evolution of medical imaging devices

The problem of improving PET efficiency was approached starting with a study of how many photons are created from the radioactive isotope delivered to the patient, how many of these photons are escaping from the patient's body and how many are detected by the PET/SPECT instrument.

The fact that most photons emitted escape detection (9,998 out of every 10,000 for PET and many more for SPECT) led me to inquire if an instrument could be designed which would detect more of them at a reasonable cost.

The result is a novel approach to the construction of the PET/SPECT electronics that introduces a major breakthrough in their performance.

A summary showing the evolution of the improvements is given in a figure taken from article [1] and reported here in Figure 1-1a.

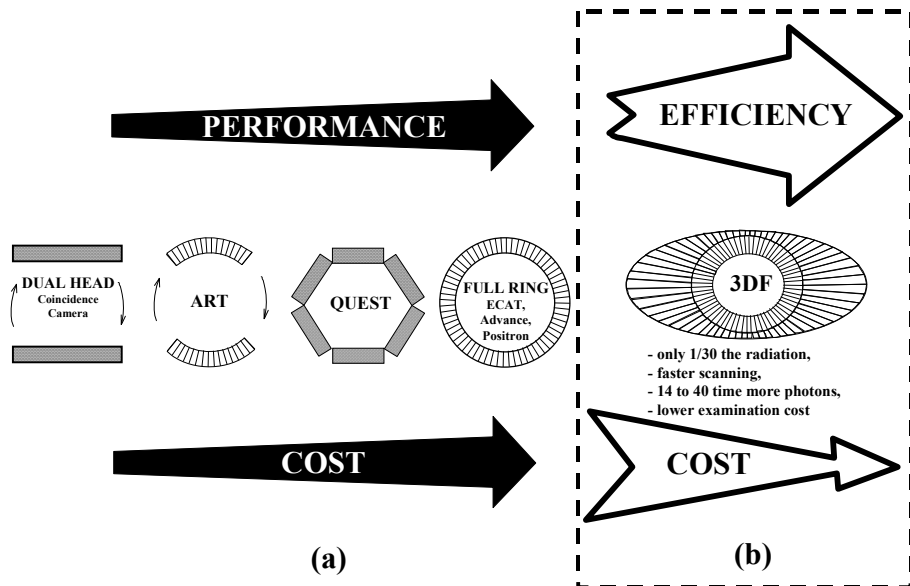


Figure 1-1. The evolution of positron imaging systems (original source of the figure [1]). Section (a) shows the evolution of the PET using past and current approach, while Section (b) shows the improvements achievable with the novel 3D-Flow approach describe in this document.

The original figure shows the evolution of PET instruments in the past several years and is updated here with the addition of a comparison to the approach described in this document.

The reduction in radiation dose required to be delivered to the patient, the lower examination cost, the faster scanning time, the better quality image obtained by accumulating more photons in coincidences shown in Figure 1-1b (3DF), are provided by the new gantry design and the new approach of the electronics as described in Section 14, Section 1.3, and shown in Figure 14-1 and Figure 1-3. The elimination of the bottleneck on input is described in Section 14.7.1.3; the elimination of the bottleneck on output is described in Section 14.7.2.4. The elimination of the brick wall on the detector boundaries is described in Section 13.3.8, and its implementation is shown in Figure 15-7; and the elimination of the brick wall on the coincidence detection is described in Section 14.7.2, and in Section 13.3.14.

1.2 Scope of the book

The purpose of this book is to present a Positron Emission Tomograph (PET) design with over 400 times greater efficiency than the current PET and allowing delivery of a lower radiation dose at a lower cost to the patient. It combines PET functional imaging at the molecular level with computer tomography (CT scan) imaging at the anatomical level to optimize the information needed by the physician.

The book begins with an analysis of the radiation dose of the PET device compared to other environmental and man-made radiation sources that the population receives annually.

Next, two targeted radiation doses are proposed: one for cancer screening of about 25 mrem (corresponding to 25 days of average radiation from all other sources) and the other of about 45 mrem for the case of a suspected cancer. (Today's PET requires the delivery to the patient of a radiation dose of 1100 mrem for the most common examination with 10 mCi of ^{18}F -FDG tracer, and other examinations require an even higher dose).

In the next step, the efficiency of most of the existing PET devices and those on the drawing boards are analyzed and compared and it is established that there is room for improvement of their efficiency.

Next, the shortcomings of current PET devices in achieving maximum efficiency are identified.

At this stage, a series of new approaches (inventions) are conceived to overcome the limitations of the current PET devices and to increase PET efficiency at a reduced cost per examination.

The detailed design is then described.

Next the two approaches, current and new, are compared and the differences evaluated.

I hope that by the end of the book the reader to whom radiation was an obscure subject before will have a greater understanding of it and will realize that while we must take care to limit our exposure to radiation as much as possible, we should still derive the benefits of it in preventive health care when it can be demonstrated to be unharmful.

A patient should be aware that he or she can and should monitor the doses of radiation received. With the conversion factor in disintegration per second, or coincidences per second given herein, **one can check the efficiency of the medical instrumentation** involved in a medical examination by first asking the physician how many millicurie (radiation (mCi or mSv, see conversion factor in Table 1-1) were delivered during the examination and then ascertaining from the PET operator how many coincidences were recorded in the file of the computer during the examination, and applying the ratio (see Section 3.1).

An approach to gauging one's exposure would be for the patient to ask the physician how much radiation (mCi or mSv) he received during an examination and then to compare it with the average received for a particular flight. The conversion factor from mCi (which measures the radiation dose delivered to the patient) to mrem (which measures the effective dose equivalent uptaken by the patient which is dependent of the half-life time of the radioisotope used and other factors) for the most common radioisotopes used in PET and SPECT are provided in Table 7-1. The radiation dose received during a flight instead can be found in various sources, and I have provided the web URL (see Section 9.2) of the Federal Aviation Administration (FAA), a U.S. government agency where a program can be accessed that allows the calculation of the cosmic gamma radiation received during specific flights.

Since air travel is common, it is convenient way of grasping the concept of average exposure to radiation and I have chosen to use it as a

means of comparison. The radiation received from the proposed PET design will be roughly equivalent to the radiation received during two round trips between the U.S. and Europe. At this comparatively low level, a screening examination with this new PET machine can be performed yearly to great advantage in detecting early-stage, curable cancers and other diseases.

Another important source of radiation to which we may be exposed is radon emitted from the soil under our homes (see Section 9.1). This book provides a map of the generalized geological Radon potential in U.S. and a source from which to purchase a kit for less than \$10 to check the level of radiation in the home. For new homes, a source is given for information on how to incorporate features which will reduce the Radon exposure.

For the most assiduous reader, all the details of the project, with comparisons between it and existing PET devices at the conceptual level as well as the detailed implementation, are provided.

Sometimes the advantages of this new scheme may seem to be described in overly abundant detail. This is attributable to my recent experience with the Superconducting Super Collider (SSC), which was cancelled by US Congress before it could be completed. It is generally agreed that part of the reason for the demise of the SSC was that the benefits to mankind of its great scientific potential were insufficiently explained to the decision makers in Washington, who then failed to appreciate the promise of the Collider. In attempting to avoid this same pitfall in regard to the present project, I may seem to overemphasize its benefits to the general health and well-being. While the reader may not expect such a in-depth and comprehensive study of the many facts simulations, measurements and statistics of the current state of medical technology, a cursory reading of this background information is illuminating and persuasive.

1.3 Over 400 times efficiency improvement.

The breakthrough in efficiency achievable with the proposed invention herein described is plotted in Figure 1-2. This figure clearly shows the

effect of the breakthrough approach described here in the sharp change of the slope of the improvements, the change of direction of the slope of the cost and radiation dose delivered to the patient.

$$\text{EFFICIENCY} = \frac{\text{radiation detected by the instrument}}{\text{radiation activity in the patient during the scanning time}}$$

Efficiency is defined as the ratio between the radiation detected by the instrumentation (that in the PET application is meant as the photons in time coincidences detected by the device. See Section 13.4.7 for further separation of trues, scatter and randoms all recorded by the instrumentation as “coincidences”) and the radiation activity in the body of the patient during the scanning time. The radiation detected by the PET (or other instrument) is considered useful when it helps to improve the quality of the image; in the case of the PET, the useful information consist of the true coincidences that originated by the annihilation of a positron β^+ and an electron β^- inside the body of the patient

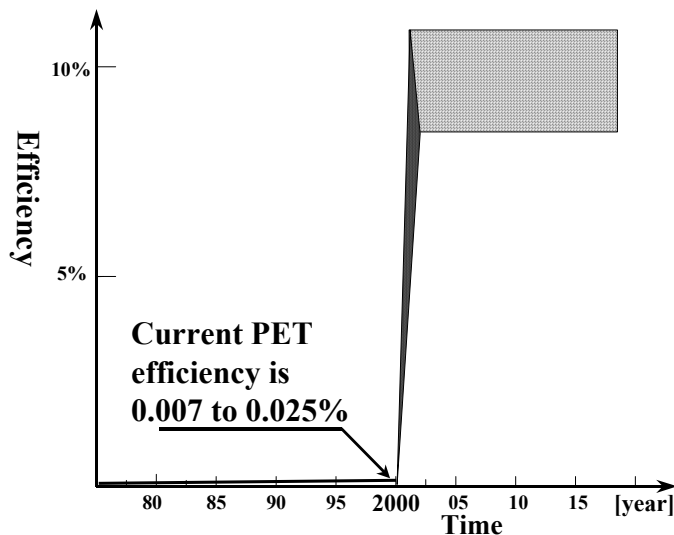


Figure 1-2. The breakthrough in efficiency achievable with the described invention.

1.4 Benefits in cancer prevention affordable in cost and radiation dose

The radiation delivered to the patient is measured in mCi (or Mbq – million Becquerel – or million of disintegration per second), the radiation detected by the PET detector is measured in coincidences per second.

Two sets of measuring units of radiation exist in the world today:

1. the common unit naming (Curie, Roentgen, Rad and Rem), and
2. the SI or International Units (Becquerel, coul/esu, Gray and Sievert).

The International Commission on Radiation Units and Measurements (ICRU) recommends the use of the SI units; in the United States the common units are mostly used.

One gram of radium undergoes 3.7×10^{10} nuclear transformations or disintegrations per second and is called 1 curie (Ci), named for Madame Marie Curie, a Polish born French chemist (1867-1934). In 1898, Marie and her husband Pierre Curie announced their discovery of polonium and radium; and in 1903 they shared the Nobel Prize in Physics with Becquerel for the discovery of radioactive elements.

The meaning and relation among the units used in this document are described in Table 1-1.

Table 1-1. Naming and relation among measuring units of radiation.

Function	Common unit naming	International unit naming (SI)	Relation	Description
Unit of activity	Curie (Ci)	Becquerel (Bq)	$1 \text{ Ci} = 3.7 \times 10^{10} \text{ Bq}$	Ci = number of disintegrations per second of 1 gram of uranium. Bq = one disintegration per second
Unit of equivalent dose	Rem	Sievert (Sv)	$100 \text{ Rem} = 1 \text{ Sv}$	Rem = Roentgen Equivalent for Man, a measure of radiation exposure that indicates the potential impact on human cells. Sv, same.

Example: The delivery by injection of 10 mCi to a patient generates 370 million pairs of photons per second inside the body of the patient. A PET device should detect 37 million coincidences per second for a 10% efficiency system. A common radiation dose delivered to the patients during today’s PET examinations is 10 mCi. The current PET devices

detect about 92,500 coincidences per second yielding an efficiency of approximately 0.025%.

Figure 1-3 shows the effective dose equivalent to the patient for a given amount of the most common radiotracers for PET. A small amount of ^{18}F -FDG has more hazard than others because its half-life time is 110 minutes. The correspondence of mrem to a given amount of mCi of radiotracer delivered to a person is available in ICRP publications or in reference [11].

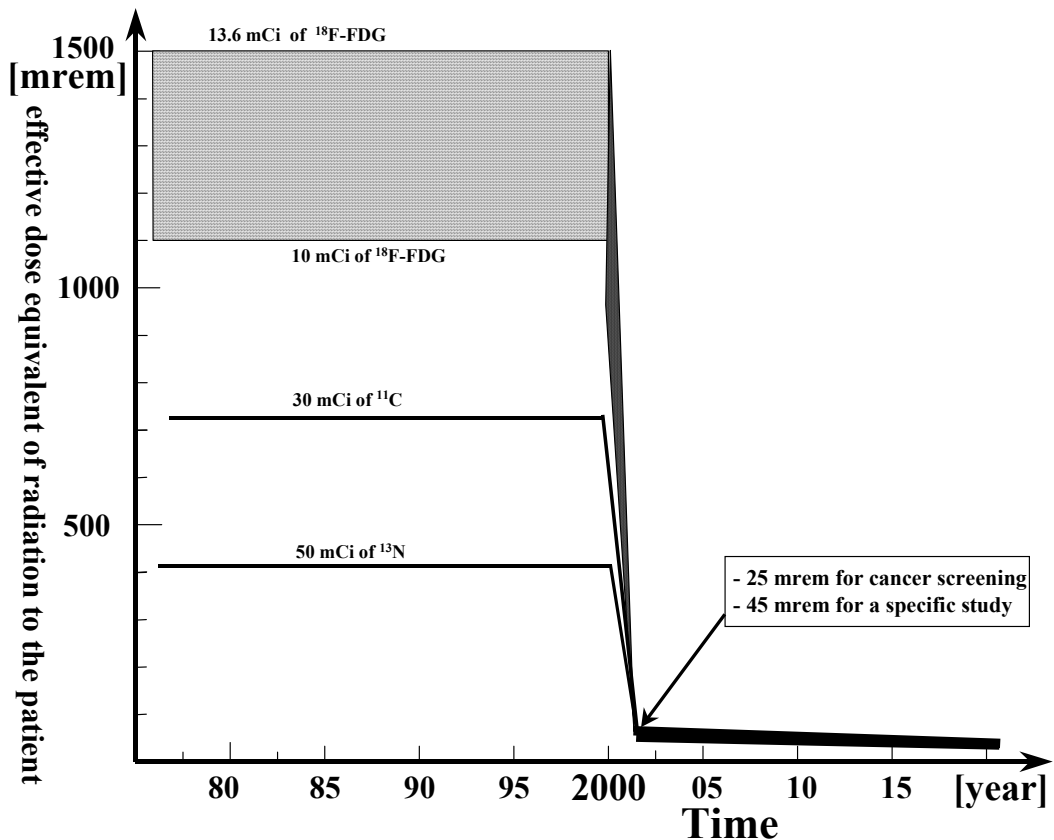


Figure 1-3. Only 1/30 the radiation dose delivered to the patient.

The radiotracers used during PET examinations have different half-life times and thus have a different impact on the human cells. At the same radiation activity per second, the ones that have longer activity in time

generate more damage to the cells, thus will have a higher equivalent dose than the ones that have a shorter lifetime.

Assuming that we would like to affect the patient with approximately the same radiation dose equivalent during different examinations, the amount of mCi of the different tracers injected to the patient should be different, such as the ones reported in the Table 1-2:

Table 1-2. Effective dose equivalent of radiation delivered to the patient generated by different radiotracers vs. the quality of the image and system used.

Current Systems				3D-Flow System			
Radiation dose delivered to patient. [mCi] – Radiotracer type	Duration of exam. [seconds]	Coincidences detected by the PET. (= quality of the image). [million counts]	Hazard to the patient. Radiation dose equivalent. [mrem]	Radiation dose delivered to patient. [mCi] - Radiotracer type	Duration of exam. [seconds]	Coincidences detected by the PET. (= quality of the image). [million counts]	Hazard to the patient. Radiation dose equivalent. [mrem]
10 (¹⁸ F)	3600	249.75^e	1100^a	0.4 (¹⁸ F)	360	524^m	44^a
30 (¹¹ C)	900	187.31^f	720^b	1.8 (¹¹ C)	240	1,548ⁿ	43.2^b
50 (¹³ N)	400	138.75^g	415^c	2.5 (¹³ N)	240	1,665^p	20.7^c
60 (¹⁵ O)	70	22.66^h	252^d	5 (¹⁵ O)	70	755^q	21^d

^asee [11] for 110 [rem/mCi] multiplying factor of effective dose equivalent for ¹⁸F (mCi x 110)

^bsee [11] for 24 [rem/mCi] multiplying factor of effective dose equivalent for ¹¹C (mCi x 24)

^csee [11] for 8.3 [rem/mCi] multiplying factor of effective dose equivalent for ¹³N (mCi x 8.3)

^dsee [11] for 4.2 [rem/mCi] multiplying factor of effective dose equivalent for ¹⁵O (mCi x 4.2)

^ecalculated as: $(3/4 \times (10 \times 3.7 \times 10^{10})) \times 0.00025 \times 3600 = 249.7 \times 10^6$ coincidences accumulated.

^fcalculated as: $(3/4 \times (30 \times 3.7 \times 10^{10})) \times 0.00025 \times 900 = 187.31 \times 10^6$ coincidences accumulated.

^gcalculated as: $(3/4 \times (50 \times 3.7 \times 10^{10})) \times 0.00025 \times 400 = 138.75 \times 10^6$ coincidences accumulated.

^hcalculated as: $(7/12 \times (60 \times 3.7 \times 10^{10})) \times 0.00025 \times 70 = 22.66 \times 10^6$ coincidences accumulated.

^mcalculated as: $(63/64 \times (0.4 \times 3.7 \times 10^{10})) \times 0.1 \times 360 = 524 \times 10^6$ coincidences accumulated.

ⁿcalculated as: $(31/32 \times (1.8 \times 3.7 \times 10^{10})) \times 0.1 \times 240 = 1,548 \times 10^6$ coincidences accumulated.

^pcalculated as: $(3/4 \times (2.5 \times 3.7 \times 10^{10})) \times 0.1 \times 240 = 1,665 \times 10^6$ coincidences accumulated.

^qcalculated as: $(7/12 \times (5 \times 3.7 \times 10^{10})) \times 0.1 \times 70 = 755 \times 10^6$ coincidences accumulated.

The nominal radiation activity of the radiotracer must be reduced because scanning usually does not start immediately after delivery of the radiotracer and the scanning duration is not the same for all radiotracers. The first fraction in the expression of the notes ^e, ^f, ^g, ^h, ^m, ⁿ, ^p, and ^q is the reduction factor used to calculate the total number of coincidences detected by the PET that are reported in Table 1-2. The value 0.00025 is the efficiency of the current systems (see Section 3.1), and the value 0.1

(See Section 3.2) is the efficiency of the system implemented with the novel idea described herein.

Figure 1-4 shows the number of photons in coincidence that were accumulated for a specific scanning time and the amount of radiation dose delivered to the patient. The projected parameters achievable after the year 2000 with a PET using the new approach are also indicated. We can note that the longest scanning time of 60 minutes with ^{18}F -FDG is reduced to 1/10 and in spite of that, the number of photons in coincidence accumulated are almost double.

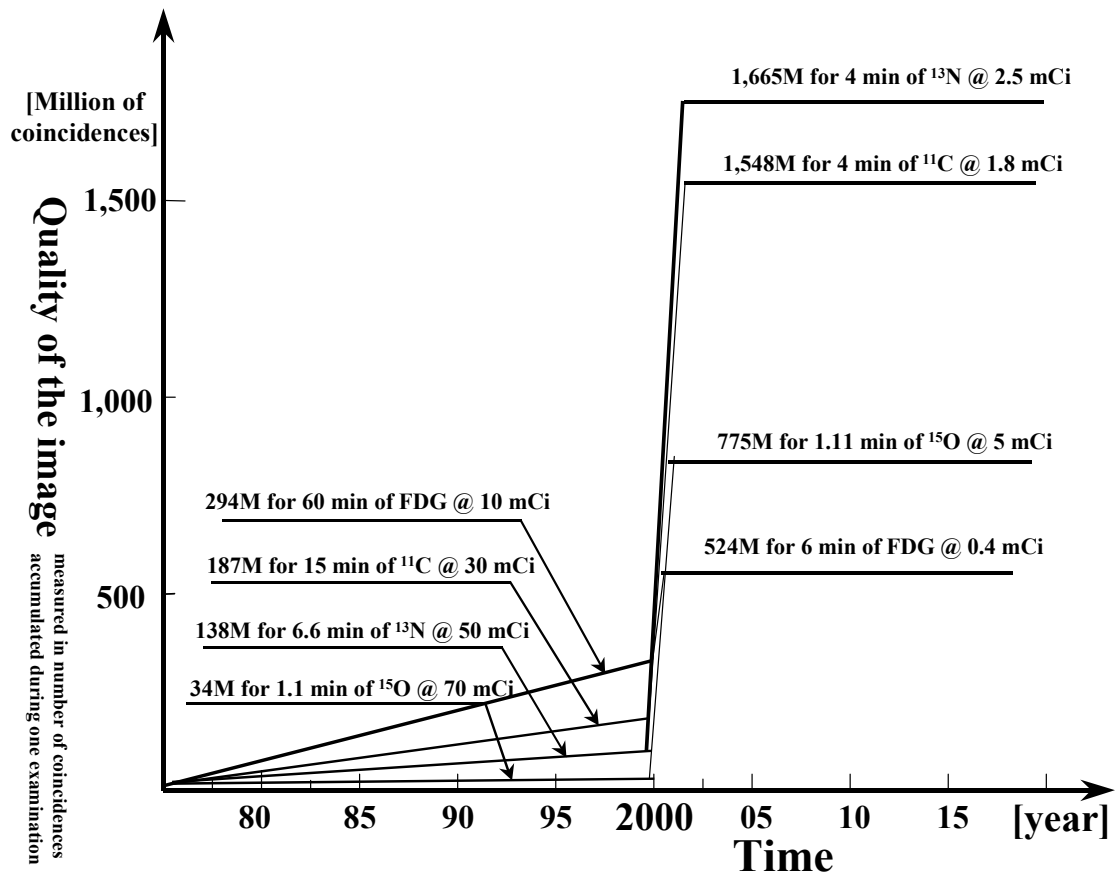


Figure 1-4. Only 1/10 the duration for the long examination of 60 minutes with ^{18}F -FDG (@ 1/25 the radiation dose).

The cost of the new PET device for an increase of about 7 times the Field-Of-View and over 400 times the efficiency will be only from two to three times the cost of the current PET as it is discussed in Section 18. The reason is that the volume of the crystals is decreased by the new elliptical gantry geometry compared to the current circular geometry. The cost of the phototubes is reduced by using larger phototubes. The simplification of the electronics based on the 3D-Flow architecture and the novel approach provides a powerful system with DSP at each channel and an efficient coincidence detection logic in only two IBM PC chassis.

The cost to operate the new PET will also be reduced because it requires to deliver to the patient only 0.4 mCi of radiotracer instead of 10 mCi (10 mCi of ^{18}F -FDG costs about \$600; 0.4 mCi will cost about \$24), and it requires only about 1/10 of the scanning time of the current PET.

Figure 1-5 shows the projected cost reduction per examination to the patient and insurance companies for the above reasons and because the duration of the PET examination with 3D-Flow systems will require only 4 minutes, instead of the 60 minutes of scanning time used by the current PETs. This will make it possible to examine many more patients each day, providing a cost reduction to the patient and amortizing the additional cost of the medical instrument in a very short time. .

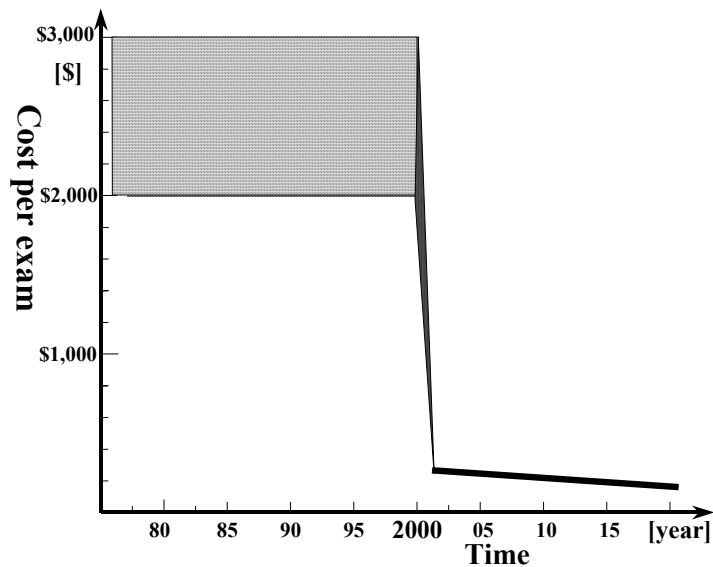


Figure 1-5. Only 1/10 the examination cost to the patient.

Furthermore the new PET device proposed herein extends the prospective market to include use of the device as a screening implement in addition to its current use as a diagnostic tool for patients at high risk for cancer. Thus, investors can expect a return of their investment in a shorter time and the possibility of realizing greater returns in an extended market.

1.5 Current and developmental PET scanners and comparison of their characteristics.

Table 1-3 show some characteristics of PET scanners on the drawing board and the one built during the last decade.

Table 1-3. Current and developmental PET scanners and some reported performance characteristics

PET Model	Ref.	Detector diameter Ring/Port [cm]	Length (FOV) [cm]	Solid angle/ # of signals	Resolution Transaxial/ Axial [mm] FWHM (for comparison, autoradiograph is ~100 μm)	Examina tion duration tiem [sec]	Quality of the image (number of coincidences accumulated) [million]	Radiati on dose deliver ed to the subject [mCi]	Hazard to the subject [mrem]
2000 (Design) 3D-Flow PET/SPECT/ CT	this docu ment	Max/min. 100-70/ 50-40 head 40/32	157.4	~92%/ 2,304	<1.3/<1.3	70	~755	5 [¹⁵ O]	21
2000 (Design) GSO HEAD PET-PENN	[110, 111]	42/30	25	/288	3/3.5				
1998 CTI/Siemens Head ECAT HRRT	[38, 102, 103]	35	25.2	/936	~ 1.3/ ~ 1.3				
1996 CTI/Siemens EXACT3D		82/56	23.4	/1,728	4.7/5.2				
1995 CTI/Siemens ECAT EXACT HR PLUS		82/56	15.5	/1,152	5.1/4.2				

1995 NaI(Tl) HEAD PENN-PET	[37, 152, 153]	42/30	25.6	/180	3.5/3.5	1800	100	2 (FDG)	220
1994 CTI/Siemens ECAT EXACT HR	[22]	82/56	15	18.8/ 1,344	3.6/4				
1994 General Electric Advance	[23]	92.7/59	15.2	/1,344	3.8/4	60	12.5	66 [¹⁵ O]	277
1994 Super PET 3000-E		90.5/52		/768	8.5/8.5				
1991 CTI/Siemens ECAT EXACT 921		82.5/56.2	16.2	/576	5.8/5				
1991 CTI/Siemens ECAT EXACT 713		64/40	5.4	8.4/ 320	3.8/4.4				
1990 Positron Posicam 6.5 BGO		78/58	11.9	/720	5.8/11.9				
1997 microPET	[69, 12, 101]	17.2	11.2	/960	1.68				
1994 Sherbrooke APD system	[13]	31/	10.5	32.1/	2.1/3.1				
1992 Hammersmith RATPET	[14]	11.7/	5.4	41.9/	2.8/4.7				
1992 Hamamatsu SHR-2000	[15]	35/	4.6	13/	3.0/4.8				

Part 1 Concepts

2 Breaking the barrier of the high number of coincidences generated by larger system

The key elements of this innovative project which provide not merely an improvement of the order of two or three times the efficiency of the current detector as a consequence of advances in technology, but a qualitative breakthrough of the order of over 400 times the efficiency of the current devices is summarized on the cover page of this book (see figure caption on the inside of the cover).

3 Analysis of the nature of the physics experiment occurring in PET devices

The behavioral model of the physics experiment occurring in the PET devices has been based on results from simulation reported in articles that have been cited, or from measurements or results from examinations conducted on existing PET systems as reported in the literature.

The nature of the physics experiment occurring in PET devices is the annihilation of a positron β^+ and an electron β^- generating two photons γ travelling in almost opposite directions at 180° and at 511 keV (see Figure 3-1). The positron is the result of the decay of a radioisotope.

A biologically active compound (e.g. glucose) labeled with a positron emitting isotope, is injected into (or inhaled by) the patient. The compound carrying the radioisotope is called a tracer or imaging agent. The PET scanner records the signals emitted by the tracer (decay of the isotope, emission of positron, annihilation of positron with an electron into two 511 keV photons in opposite directions) on its journey through the human body and when it ends its trip in the various organs targeted for examination.

The PET identifies the location of the individual positron annihilation by detecting the two photons that have hit the detector simultaneously. The position of the annihilation lies along the line (LOR) connecting the two crystals which detected the two photons. A mathematical technique then uses these detected millions of chords (called coincidences) to reconstruct the spatial distribution of the path and concentration of the

immediately where the weaknesses of the present systems occur and what the limitations are to making improvements.

The distribution of the radiation after injection of two type of isotopes: one the ^{15}O -water with a very fast half-life time of 2 minutes and the other, the ^{18}F -FDG with a slow half-life time of 110 minutes. Even if the dynamic of the distribution is more important in the first type than in the second, in both cases one can count on more than 90% of the radioactivity remaining in the head, torso, and the upper part of the legs of the patient, which is within the field of view of the PET (FOV =about 157.4 cm), and less than 10% of the activity going to the feet and lower part of legs, or outside the FOV.

Furthermore, while an examination of 2 minutes with ^{15}O -water should detect all radiation delivered to the patient (minus the radiation scattered or absorbed by the patient's body), for an examination with ^{18}F -FDG which starts usually after 30 minutes, the patient might have already released part of the radioisotope before its radioactivity life was terminated.

The activity of the radiotracer can be changed in some section of the body in the following way. It has been reported in the literature [19, 16] that switched and cold bolus/switched (CBS) protocols for ^{15}O -water “enhance the signal-to-noise ratio (SNR) of subtracted activation images by manipulating tracer kinetics in order to maintain the difference between activation and baseline signals longer than standard protocols The cold bolus is formed by occulting blood circulation to the lower limbs prior to tracer injection using pressure cuffs placed on both legs at upper high level. The cuffs are inflated above arterial pressure a few seconds prior to bolus injection thereby isolating about 20%-40% of the blood volume in the lower extremities. When activity concentration in the brain reaches a maximum, typically 40-60 seconds after isotope injection, the cuffs are released and the subject switches task execution. The effect of using a cold-bolus is two fold. First, lower-limb circulation occlusion decreases tracer dispersion during the uptake phase of the input function therefore increases tracer uptake in the brain. Second, release of the cold-bolus increases tracer washout from baseline regions during the washout phase of the input function since it is combined with task-switching.”

Row (2) of Figure 14-1 shows how it can be understood intuitively that the PET system with a smaller field of view (see left section of row 2 of the same figure) will have fewer singles hitting the detector. However,

the ratio between the hits in coincidences and the total hits on the detector is high, while for a greater field of view (see right section of row (2) of the same figure), even if the total number of singles increases, the ratio among the hits with coincidences and the total hits decreases.

Figure 3-2 summarizes the phenomenon described above in a graph with the vertical ordinate representing the photon count involved in the experiment, and the horizontal bottom axis representing the gradual increase of the field of view of the detector. The top line indicates the activity of a 10 mCi source, yielding 370 MBq (or 740×10^6 photons/sec). It will never be possible to obtain close to 100% efficiency because part of the photons are Compton scattered or absorbed in the body of the patient and will not exit from it, or else they will exit with the wrong direction information which will not point to the emitting source.

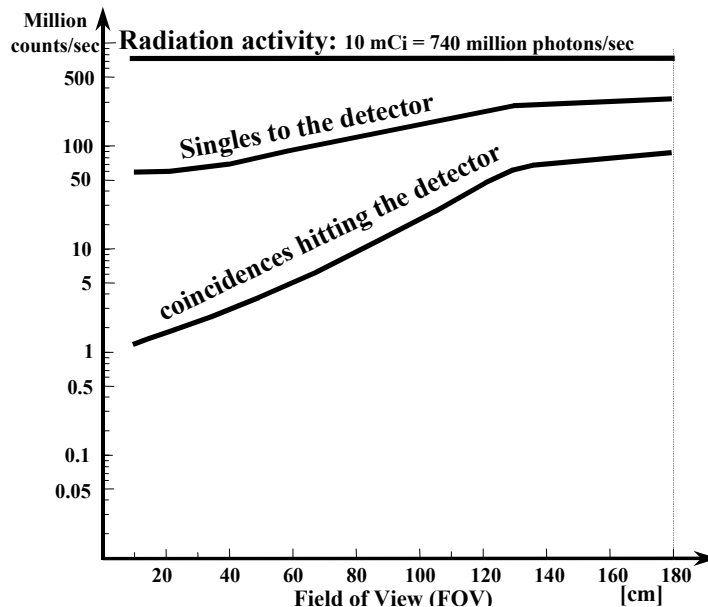


Figure 3-2. Graphic view of the ideal detection of “singles” photons by PET with a different field of view.

The second line from the top, indicates the “singles” which hit the detector. All hits on the detector, until they have been recognized as true coincidences, scatters, or randoms, are called singles. Depending on the weight of the body of the person being examined, we can account for a loss of singles of 50% to 73% at this stage. A simulations result of 100 million count per second of singles can be found in reference [17].

Section IV.B of this citation describes a simulation on an anthropomorphic phantom [18] using 10 mCi and a 60 cm axial field of view PET. (The Zubal phantom has been modified as described in [18] and the arms and legs have been included). Other simulations on a 20 cm phantom can be found in reference [19], and a PET design with 80 cm in diameter and 30 cm axial FOV in [20]. On the far right of Figure 3-2, where most of the radiation activity is captured by the detector with a long field of view, the main loss of singles is the one due to the scattering and absorption internal to the body, while on the top far left of Figure 3-2, many more singles are lost because the axial field of view is too short to cover all the area emitting radiation.

The third line from the top indicates the ideal number of coincidences that should hit the detector and that should be detected by the PET electronics. This includes True, Scatter, and Randoms. The count rate of the number of coincidences that should hit the detector in an ideal condition has been simulated and reported in several articles. The following is a citation of some of these: reference [17] in Section IV.B. shows that the total number of coincidences found in a PET with 60 cm axial FOV and 10 mCi radiation dose to the anthropomorphic phantom [18] modified as described in Section II.D of [18], is reported to be 8.5 coincidences per second ($= 17 \times 10^6$ singles per second). Other references [21] need the extrapolation of the ideal counts of the coincidences from a simulation performed on a 20 cm x 20 cm cylinder phantom. The counts difference indicated by the interval between the second line and third line on the right side of Figure 3-2 is due to the inefficiency of the detector (e.g., stopping power, dead areas in between the detectors). The counts difference indicated by the interval between the same lines on the left part of Figure 3-2 has an additional increase in singles rate due to the radiation that is next to the detector where only one of the two photons from the annihilation hits the detector while the other goes outside.

3.1 Analysis of the performance of the current PET devices

After having studied the behavior of the physics experiment in a PET detector we can plot the performance of PETs with different FOV in detecting coincidences vs. the activity of the γ -rays created inside the body, the ones that leaves the body and the ones that hit the detector aperture for different detector FOV.

Figure 3-3 shows the plot of the previous graph with the performance of the current PET systems added to it for graphical comparison. The curve at bottom has been calculated from the measurement of the performance of a few of the latest models of whole-body PET systems and/or simulations as reported in recent articles (see the following paragraphs in this section).

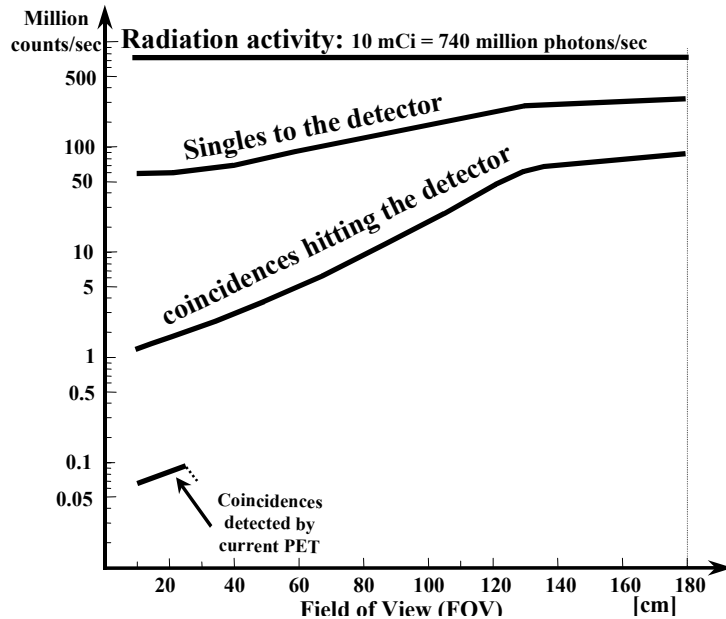


Figure 3-3. Graphic view of the detection of the coincidences by the current PET systems.

In particular one can find on page 115 of reference [22] the description of a PET examination using the model by Siemens ECAT EXACT HR providing an efficiency of only being 0.0193%. (See also description of the efficiency measurement performed in Section 11.2.2.6.4)

A second reference [23] (on page 1405, Figure 8) describes a PET examination using GE Advance with the injection of 8.5 mCi ^{18}F FDG in a human, yielding a total efficiency of 0.022% (See Section 11.2.2.6.3 for more details on the measurement performed).

The efficiency of the most advanced current PET devices is even lower when performance measurements are made using radiotracers such as ^{15}O -water, which generates a higher radiation activity for a shorter time.

The results of the PET brain examination performed with the GE Advance Positron Emission Tomograph on humans using 66 mCi of intravenous injection of the radiotracer ¹⁵O-water, yield a total efficiency of 0.0014%. (See Section 11.2.2.6.3 for more details on the measurement performed).

Another performance measurement result using a radiotracer generating high activity has been reported in reference [24] where a Siemens ECAT-831 Positron Emission Tomograph was used on a human subject into whom 50 mCi bolus of ¹⁵O-water was injected. As reported in Table 1 of the above-mentioned reference, the activity measured was only 1.08×10^5 true coincidences per second yielding an efficiency of only 0.0077% ($3/4$ of $(50\text{mCi} \times 37\text{Mbq}) = 1,387.5 \text{ MBq}$). This yields $1.08 \times 10^5 / 1.3875 \times 10^9 = 0.0000778$.

The whole-body scanner, model 966/EXACT3D delivered by CTI/Siemens in 1997, is reported by the designers in Section V of [114] to have an overall efficiency higher than any previous tomograph. The maximum total coincidence event rate on the EXACT3D is limited to about 3 million events/sec. The maximum true rate is about 850 kcps (for 90 MBq or 2.4 mCi in the FOV). The article reports that “the fall off after this point is not due to paralyzable deadtime behavior but to a limit in the sorter board of the current acquisition system (ACS).” The same article reports that the 966EXACT3D is 4 times more efficient than the model ECAT 953B brain tomograph with 10 cm FOV and about 2.5 times for a 15 cm FOV such as ECAT EXACT [29] (see Section 11.2.2.6.5) designed and manufactured by the same company in 1992.

With regard to the ECAT EXACT HR PLUS, Section II of [19] reports “... The one-session protocol employs 12 bolus injections/subject.” Other hospitals report using up to 70 mCi dose of ¹⁵O-water per injection. It is obvious that the efficiency of the PET system at 70 mCi will be very low. Section III of the article reports that “...Thus over 70% of all detected events were true when injecting 5 mCi, while only 50% of the events were true when the dose increased to 20 mCi Dead time grew linearly from just over 10% when 5 mCi injections were used to over 25% when 20mCi were injected.” to over 25%.”

Other current Positron Emission whole-body Tomographs available on the market today (see the following references for other PET instruments and for more performance measurements on the PET listed above [25, 26, 27, 28, 29, 30, 31, 32, 33, 34, 35] do not provide efficiency much

different from the ones reported above. The article by Lewellen et al., 1995, [36] reports results of measurements using different phantoms on a General Electric Advance PET, and the Lewellen et al., 1996, article reports the results on the same PET in 3D mode.

Among the more recent smaller PET cameras for brain or pediatric scanning which in general provide a slightly higher efficiency due mostly to the smaller radius of the scanner, we have several new developments.

One of them is the HEAD PENN-PET for brain or pediatric scan described in reference [37]. Performance measurement was the following: 1.9 mCi of the radiotracer ^{18}F -FDG was injected into the patient, who was scanned for 1 hour. During that time, 150 million counts were accumulated. The count rate is: $150 \text{ million counts} / 3600 \text{ sec} = 41,666 \text{ counts/sec}$. The activity of the radioactive source is: $(7/8 \text{ of } (1.9 \text{ mCi} \times 37)) = 61.5 \text{ MBq}$, yielding a total efficiency of 0.06%.

The designers of the new GSO-based HEAD PENN-PET under construction in the year 2000, project only a factor two improvement in coincidence sensitivity with respect to the previous model designed 6 years before by them [153], and explain the reason for the low efficiency in Section 3 of [110] where they state “The crystals were chosen to be relatively short (10 mm) to limit the cost and to minimize parallax in the system with a small diameter. Rather than using ‘extra’ crystal material for thicker crystals, we use extra crystals to extend the axial FOV to 25 cm While the interaction efficiency (about 57%) of 10-mm thick GSO...” Section 4 of the same article states “However, there is also a significant dead-time due to electronics...” Section 5. Discussion, reports “...the main cause of dead-time is due to pulse pile-up and is limited by the Anger-type detector design Although we also expect there to be significant losses due to electronic dead-time.” Article [37] reports the performance of the design of a previous HEAD PENN-PET in 1994; it states that with the current hardware it saturates at 500 kcps coincidences and that the final true event rate is 70 kcps for the large phantom at about 0.7 mCi activity.

Another small PET, model ECAT HRRT model manufactured by CTI/Siemens for scanning the brain with a small 35 cm patient port, was delivered to MPI Cologne (Germany) in February 1999, and was presented recently at the Nuclear Science Symposium and Medical Imaging in Seattle [38]. The article in Section III.A claims that it has only twofold gain in maximum NEC compared to the previous (1994) whole-

body PET ECAT EXACT HR [22]. More small PET devices were presented at the same conference in 1999; however, the efficiency improvement was not very different from the one described (see reference [39]).

The designers and manufacturers of the ECAT HRRT model, also state in [38] that it is difficult to have electronics sustaining the high rate of events and the authors indicate that a shorter coincidence time window is needed to reduce the randoms and that a better energy resolution is needed. In other articles it is recognized that the signal-to-noise ratio should be improved.

By analyzing the very common plot of the sensitivity or count rate capability as a function of radioactivity concentration shown in all articles performing measurements on different PET devices, one can immediately realize the limitation of the electronics in detecting a high rate of coincidences from higher radioactivity. The statement found in the literature by many authors, that by making the coincidence time window shorter, the randoms decrease and the efficiency increases (see the paragraph above and [38]), should make one realize that the definition of randoms as the detection of two photons in time coincidence belonging to two different positron electron annihilations has not been correctly used and displayed in all the plots showing the PET sensitivity or count rate capability.

Likewise, phantoms of different volumes have been used in performance measurements (e.g. in the same article [36] phantoms of three different volumes have been used); consequently, the comparison of the count rate of different PET with the same radioactivity per cc cannot be made.

Hopefully, if the detailed definition of the Zubal phantom (which is the most accurate representation of the human body) together with the definition of a standard kinetic behavior to characterize blood flow, is adopted in all measurements, it will be easier to have a meaningful measurement of PET sensitivity which will be more realistically linked to the radioactivity that a human body receives and it will also be more meaningful at that point to compare the sensitivity among the different PET devices.

When we hypothesize that the electronics is not the cause of the curve saturation of the true coincidences found and the cause of the rising of the rate of the randoms, a modification of the electronics in doing signal

processing to enhance time resolution, and in shortening the coincidence time window should not affect the curve response. In fact, the randoms are reduced and the trues are increased if the coincidence time window is shortened

CTI/Siemens and General Electric have not proposed increasing the field of view to 120 cm, which would capture most of the radiation delivered to the patient instead of capturing only about 0.022% of the coincidence photons generated, because the current approach that they are using of checking for coincidences on each Line-Of-Response (LOR) would require the number of LOR to increase as the formula $((n \times (n-1))/4)$. Using the current CTI/Siemens and GE approach, the complexity of the electronics would increase enormously, or, alternatively, one would have to drop many photons from being checked. In that case, however, no significant advantage is provided to the patient, because the radiation and the cost have not been lowered.

During these past 25 years, the problem of the electronics has always been considered greater than the benefit which would accrue from the availability of a more efficient PET device. However, a device capable of shortening the examination time would in effect lower the cost per examination, since more patients could be examined each hour. Even more important, lowering the radiation dose to the patient, would enable patients to take the examination more often.

Finally, simple method of calculating the efficiency of a PET device is that of asking the physician or the operator of the PET device at the hospital how many Mbytes of data were acquired during his/her PET examination. By checking the size of the file on the PET computer, and knowing the number of bytes used to define the coincidence of two photons (the standard PETLINK protocol considers 8 bytes to define a coincidence, while older protocols require only 4 bytes), the operator can easily calculate the number of coincidences acquired. When the amount of activity of the tracer during the scanning period is known, the efficiency can be easily calculated with the ratio of the two values.

3.2 Solution for overcoming the efficiency limitation imposed by the architectural approach used in current PET systems

Figure 3-4 shows the area of improvements of the current PET devices that are: increasing the Field-Of-View and improving the electronics.

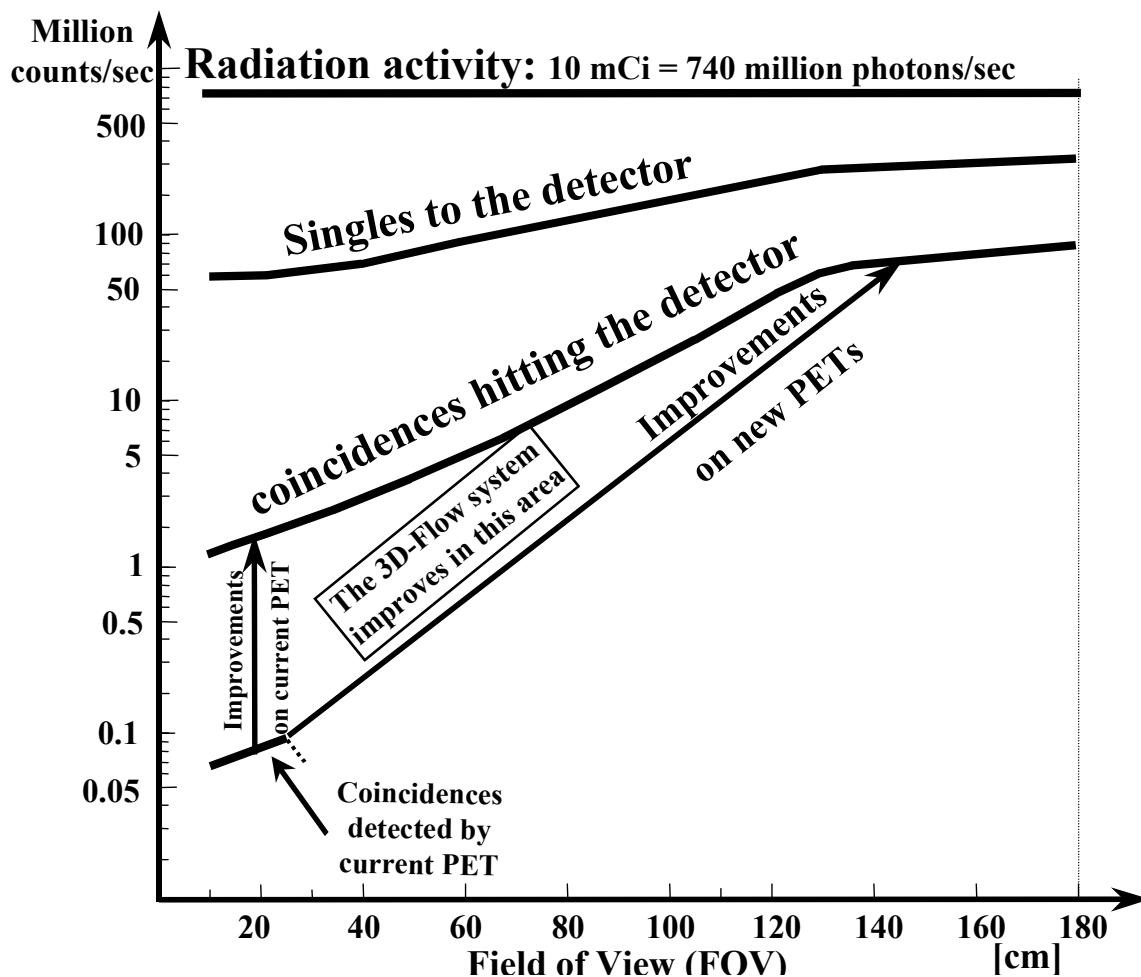


Figure 3-4. Graphic view of the ideal vs actual coincidence detection of the current PET system and the solution to improve the efficiency.

4 Specifications of the most cost-effective PET

A cost-effective PET should have the characteristics of improving energy, spatial, and timing resolution for being effective and having a geometry which will reduce the volume of crystals required.

Figure 4-1 shows the geometry of a PET detector with elliptical torso and circular head to minimize the volume of the crystals. This will also keep as short as possible the path of the photon from the patient's body to the crystal in order to improve the timing resolution. An electronic with high processing capabilities will solve the parallax error measurement required when crystals are very close to the patient.

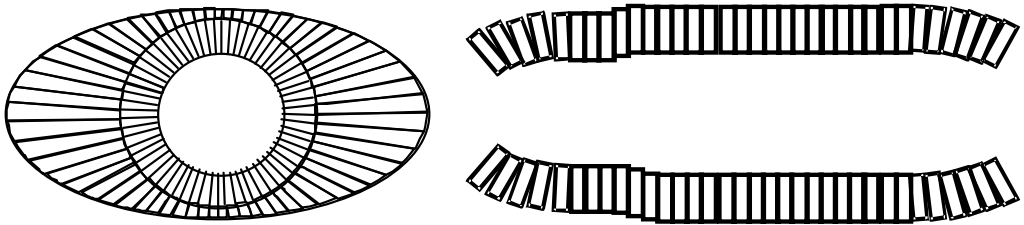


Figure 4-1. Geometry of a cost-effective PET system derived from the analysis and specification definition

Part 2 Clinical usefulness

5 Clinical and research applications

The PET functional imaging can detect a disease in many cases before it shows up on other tests or medical imaging devices. A tumor can be detected in PET at an earlier stage compared to CT which needs for the tumor to be large enough to be detected [40].

6 Impact of this improved design for the population

Figure 6-1 shows the deaths in the US in 1997 by cause and by age group. From a total number of 2,314,245 deaths in the US in 1997 the highest cause of deaths for the age group 45-64 years old is 131,743 people who die of cancer.

Only in the age group 65 years old and over, heart related diseases account for the most deaths, at 606,913, while 382,913 people over 65 died of cancer. One should make the observation that for the oldest population it is expected that one organ of the body is going to fail before another and will be the cause of death. However, for the group aged 45 to 64, many cancer patients can and should be saved, because in most cases the organs of the body are functioning properly.

The PET diagnostic imaging can also detect several diseases related to the heart, such as coronary artery disease.

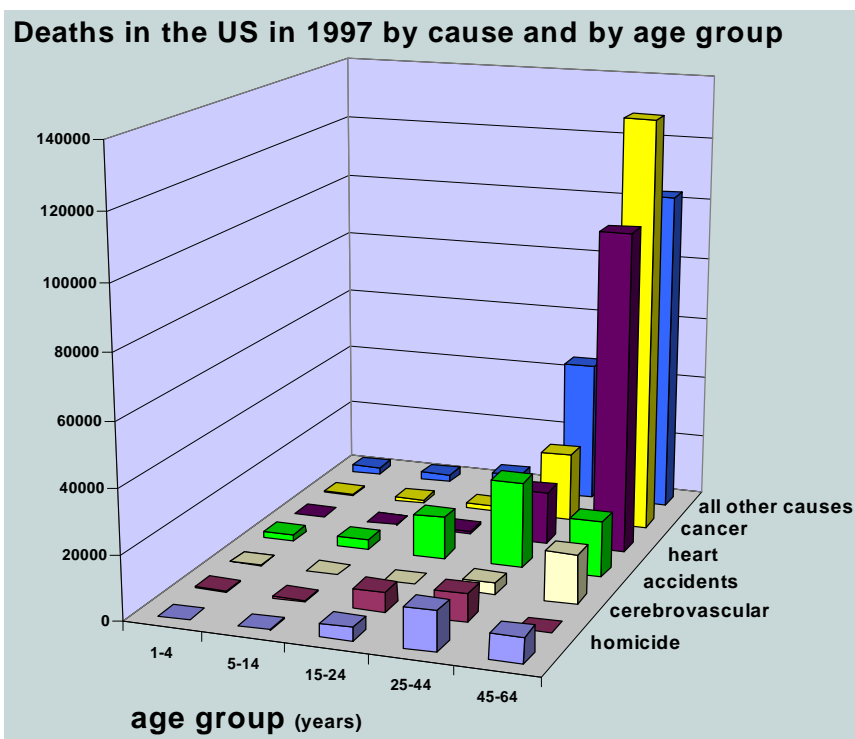


Figure 6-1. Deaths in the US in 1997 by cause and by age group.

7 Radionuclides for PET and SPECT

Table 7-1 shows the most common radioisotope used for PET examination. Several parameters are provided that will allow to calculate the best scanning time period, the effective dose equivalent and the spatial resolution. The spatial resolution of the current PET is better than the effective range of ^{15}O , and ^{82}Rb (See also references [11, 41]).

Table 7-1. Most common radioisotope used in PET.

Isotope	half-life [sec]	Positron end point [MeV]	Effective range (FWHM) [mm]	Effective dose equivalent [rem/mCi]
^{11}C	1218	0.96	2.06	24
^{13}N	600	1.20	3	8.3
^{15}O	124	1.7	4.5	4.2
^{18}F	6600	0.64	1.4	110
^{82}R	75	3.15	13.8	4.3

8 Tracers kinetic, radiation activity to the PET and uptake dose by the patient

A tracer is a compound that follows a biochemical process. Tracer can be a radionuclide or a compound labeled with radionuclide. A tracer labeled with an isotope (e.g., ^{18}F , ^{11}C) that is not originally present in the compound must behave similarly to the natural substance or in a way that differs in a known way.

Different tracers labeled with different isotopes are used to study different functions such as: glucose metabolism, blood flow, filtration, etc. ^{18}F FDG is a glucose analog used in the investigation of myocardial cerebral glucose metabolism. A mathematical model for the distribution of the Fluorodeoxyglucose (FDG) in human is reported in reference [42], The kinetics of ^{13}N -ammonia incorporated in human tumors is described in [43], the Myocardial blood flow using ^{13}N -ammonia is reported in [44] and the comparison of the use of oxygen-15-water bolus injection vs. an oxygen-15-carbon dioxide is reported in [45].

The construction of a whole body blood flow model for use in positron emission tomography imaging with ^{15}O -water is reported in [46]. Uptaken dose of radiation by the patient can be found in [11].

Part 3 Background in Radiation

9 The nature of the radiation delivered to the patient

The radiation dose to the patients from radiopharmaceuticals is reported in ICRP 53 publication, and the exposure of the U.S. population from diagnostic medical radiation with the recommendation of the National Council on radiation protection and measurements is reported in [47].

Figure 9-1 shows the source of radiation exposure in the U.S. annually. The average is 360 mrem per year or approximately one mrem per day. The highest source of radiation received annually is from radon (about 200 mrem). From nuclear medicine it is accounted only 4 mrem per year. The current PET examination delivering from 1,000 to 1,600 mrem is far to high from the average statistic. Other radiation dosage are reported on the top right of the figure for comparison.

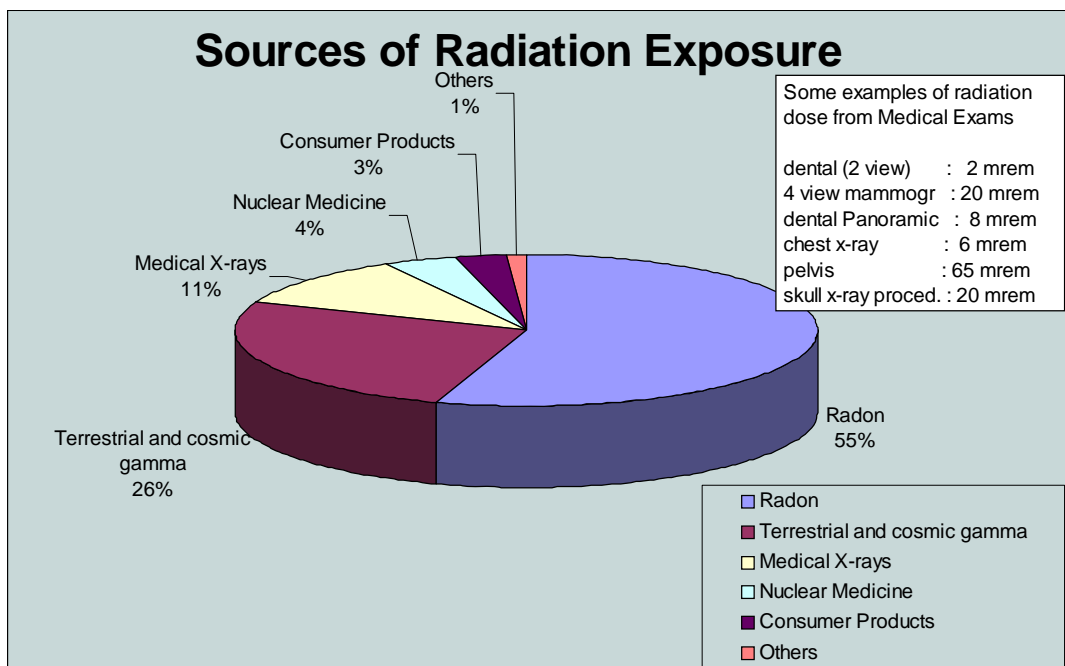


Figure 9-1. Details of the background radiation in the US by subject.

9.1 Radon in the home

Figure 9-2 shows the generalized geological radon potential of the United States. Radon is estimated to cause about 14,000 deaths per year in the U.S. In general, the population living close to the sea is less subject to radon while there are more probabilities to have an high level of radon on the mountains. However, the recommendation is to measure it by purchasing a kit which costs about \$10. The measurement is simple, it requires to leave the kit in a room for four days and then send it back to NSCR. The kit can be purchased at the National Safety Council Radon, P.O. Box 33435 Washington, DC 20033-0435, Tel. 1-800-557-2366.

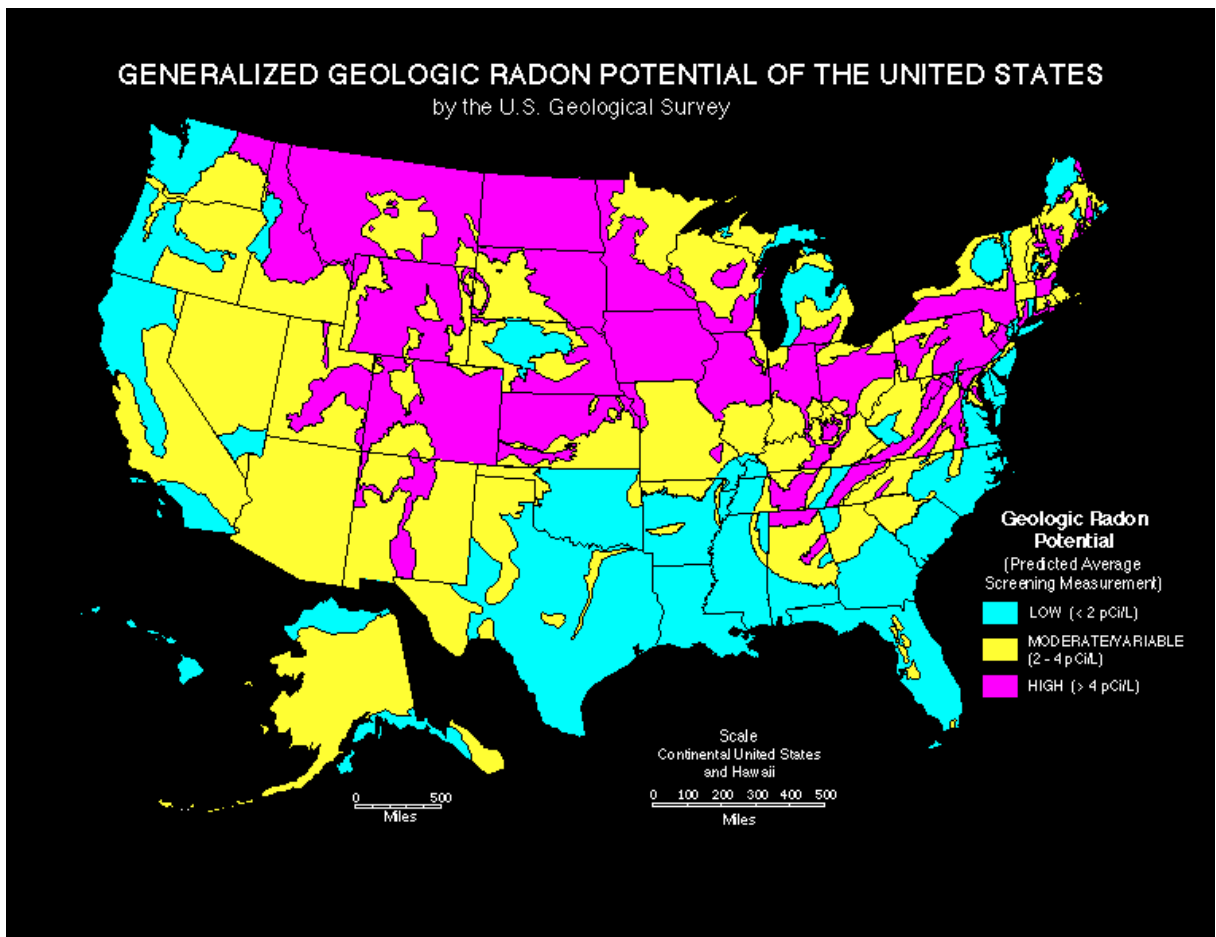


Figure 9-2. Radon potential in US (source from reference [48])

After having measured the radon in the house, if the level is high, it is possible to modify the construction (or best the measurement should be made before construction) in order to reduce its level. Information on how to reduce the level of radon in the house can be obtained from the agency: EPA, United States Environmental Protection Agency, Washington D.C. 20460.

9.2 Terrestrial and cosmic gamma rays

The radiation that can be accumulated in higher dose compared to other sources of terrestrial and cosmic gamma rays is during flights.

A reference is provided of a web site (see also reference [49]) where you can find a program that allows to calculate the galactic cosmic radiation during a specific flight. The program is provided by the Federal Aviation Administration (FAA), the URL is:

<http://www.cami.jccbi.gov/AAM-600/610/600Radio.html>

The program makes an accurate calculation based on the altitude and itinerary. A table of coefficients reflecting the solar activity can be downloaded and is updated monthly. The number of galactic radiation particles entering the atmosphere, and as a result the radiation dose rates, is related to the 11 years cycle of rise and decline in solar activity. This variation is particular evident where both latitude and altitude are high (Flying over the pole is subject to more radiation. The current year corresponds to the period of high solar activity of the 11 years cycle, thus the solar wind generated scatter the low-energy galactic particles, providing a lower radiation dose when we fly compared to 5 years from now).

As an example, the flight between London and Los Angeles (one way) is equivalent to a radiation dose of 8 mrem, or 8.2 between Tokyo and New York, or New York Athens.

The Federal Aviation Administration (FAA) has adopted as its recommendations, radiation limits recommended by the International Commission on Radiology Protection (ICRP) and the National Council on Radiation Protection and Measurements (NCRP). These limits are: for nonpregnant crewmembers, no more than 2,000 mrem per year and for pregnant crewmembers, starting when the pregnancy is reported to management, a maximum of 100 mrem to the conceptus during the remainder of the pregnancy, with no more than 50 mrem in any month.

The FAA has no recommendation for the general population; the ICRP recommends a limit of 1,000 mrem per year. (see reference [50]).

10 The electromagnetic spectrum

The electromagnetic spectrum covers a wide range of wavelengths and photon energies.

The spectrum of waves is divided into sections based on wavelength. The shortest waves are the gamma rays, the longest are the radio, which have a wavelength of many kilometers. The range of visible consist of a narrow portion of the spectrum, from 0.4 microns (bleu) to 0.7 microns (red).

All electromagnetic waves move at 300,000 km per second, the speed of light. The only difference among them is their wavelength, which is directly related to the amount of energy the wave carry. The shorter the wavelength of the radiation, the higher the energy. The photons for X-ray of our study has 60 keV, the photon for the SPECT has 140 keV, and the photons for PET have 511 keV.

Part 4 Implementation

11 Different detector types

11.1 Detector requirements for high-efficiency low-cost photon detection

An efficient detector block should have the following characteristics:

High detection efficiency. Most detectors are made of scintillating crystals. The efficiency of detecting a photon is different for different energies of the incident photon. The interaction efficiency of the crystal with the photon is also called stopping power of the crystal and depends on several characteristics, such as crystal density, cross section, etc. Table 11-1 reports the density of the most common crystals used in PET, Table 1 of reference [1] reports the efficiency of different common crystals with different thickness to detect single photons at 511 keV and 140 keV. Reference [57] reports the photon cross-sections in the range of 0.001 to 100 MeV for elements with $Z = 1$ to 100. (e.g. 25 mm BGO or LSO crystal thickness have about 90% efficiency to detect 511 keV photons and only about 60% for 10 mm thickness).

High spatial resolution. The high-resolution identification of the location where the scintillation light occurred in the crystal is very important for obtaining images with high spatial resolution. The number of photons acquired will determine the quality of the image.

Low cost. The most common detector blocks are made of a gamma converter (crystal) and a transducer (PMT or APD). Among the low-cost crystals there is the BGO, which has a large-volume cost of about \$10 per cm^3 . The APD cost should be lower in the future, as all other solid-state devices will be getting more economical. Currently, PMTs with a price in large quantities of \$260 for a 2" square tube, are still more cost effective and have better characteristics than APDs.

Short or zero dead time. When crystals are used in a detector block, a long crystal decay time will increase the number of pile-up events when the rate of the incident photons increases. Thus it will increase the dead time in cases when the pile-up cannot be avoided. The optimum solution is a detector which offers zero dead time at the desired rate of incident photons.

Good timing resolution. In the event the detector block is designed for a Time-of-flight (TOF) PET, the timing resolution should be of the order of tens of picoseconds (100 ps provide a spatial resolution of 7.5 mm). If, however, as in the case described herein, the detector block is used in PET devices using TOF information to reduce the accidental coincidence rate, a timing resolution of the order of hundreds of picoseconds is sufficient.

Good energy resolution. A good energy resolution is essential information to distinguish 60 keV (x-ray), 140 keV (SPECT), 511 keV (PET), and photopeak from Compton-scattered data.

11.2 Comparison of the characteristics of different detector modules

A PET detector module consists of a gamma converter read out by a transducer, which produces an electrical signal.

The most common gamma converters used in PET are scintillator crystals. The 511 keV photons interact in scintillator crystals by providing a scintillation light, which is detected by a transducer, such as a photomultiplier tube (PMT), an Avalanche Photo Diode (APD), or photodiode (PD). The transducer then converts it to an electrical signal. Other less common detector modules are built from gamma converters (heavy metal of foil of Pb or W, or BaF₂ scintillator /TMAE gas combination), read out by multi-wire proportional chambers (MWPC) [51, 52, 53], and still others are made of active gamma detectors which directly convert the incident gamma into an electrical signal.

11.2.1 Components of PET detector modules

11.2.1.1 Gamma converter for 60 keV to 511 keV photons

Table 11-1 shows the characteristics of the scintillation detector for 60 keV to 511 keV which are related to the requirements (in parenthesis in the first row) for the construction of a cost-effective multimodal device. The purpose of Table 11-1 is to provide general information regarding the detector characteristics and to identify the limits of less costly detectors that could be improved by higher-performance electronics.

Although not a single detector module now available offers the characteristics for building a multimodal device with the best efficiency at the lowest cost, the characteristics of the different detector modules can be compared with the performance of the 3D-Flow system, which can compensate for and improve upon the limitations of some low-cost

detector modules. It can be shown that the 3D-Flow system can provide the means of building an efficient and cost-effective multimodal PET/SPECT/CT system.

The 3D-Flow system can increase the performance of some detectors by means of digital signal processing. This improves S/N ratio, allows for correlation between neighboring detector signals for improving particle identification/resolution, and provides high efficiency in coincidence detection by routing the validated singles to the exit point and comparing their time and original location in a pipeline mode.

Table 11-1. Characteristics of scintillation detectors for 60 keV to 511 keV photons.

	Density [g/cm ³] (high, provides good stopping power = high sensitivity)	Index of refraction (low, provides good light coupling to PMT)	Attenuati on length [mm] 511keV	Decay time [ns] (low, for better coincidence detection, and avoiding pileup and dead-time)	Light yield (high, provides energy and time resolution useful to reject scatter and accidentals)	Cost
LSO	7.35	1.82	12	40	75	High
LPS:Ce [59]				30		
LGSO [54]				60		High
YSO	2.7	1.8		70	120	High
GSO	6.7	1.9	14	55	15	High
BGO	7.13	2.15	11	300	8	Low
CsI(Tl)	4.51	1.8		1000	210	
NaI(Tl)	3.67	1.8	30	230	100	Low
CsF	4.61	1.48	23	5	7	Low
BaF ₂	4.89	1.56	21	0.8/620	20	Low
PbF ₂	7.77	1.8				
Plastic (pilot U) ^a	1.03	1.58		1.4		
Plastic (10%) ^{ab}	1.17			2		
Plastic NE102 ^c				2.4		

^aSee reference [55].

^bPilot PS/Pb with 10% Pb by weight

^cNuclear Enterprises – Bicon. See reference [56].

The first crystal used in nuclear medicine, single photon and positron, was the NaI(Tl). Later, BGO were used and more recently LSO are used. For brevity, only some characteristics of the material of the crystals are reported in Table 11-1; however, more information can be found in the

references [57, 58]. The first row of Table 11-1 lists the characteristics of the crystal. LSO has among the best characteristics compared to the others, but it is expensive. BGO is less expensive, has good stopping power, but has poor light yield and long decay time. NaI(Tl) has excellent stopping power and photo fraction for 140 keV (SPECT), but is not as good for 511 keV (PET) and is hygroscopic, which presents some deterioration in crystal properties and performance over time.

CsI(Tl) has high light output and long emission wavelength. It is a better choice than YSO and NaI(Tl) for detecting low- and medium-energy gamma-rays (used in x-ray and SPECT imaging) due to the higher stopping power and higher photoelectric absorption capability (e.g. a 3-mm thick layer of CsI(Tl) provides about the same detection efficiency as 15 mm of YSO and 5 mm of NaI(Tl) for 140 keV photons (used in SPECT).

A novel inorganic scintillator: $\text{Lu}_2\text{Si}_2\text{O}_7:\text{Ce}^{3+}$ (LPS-Ce) [59] was presented at the Nuclear Science Symposium and Medical Imaging (NSS-MIC) conference in Seattle (WA) on October 24-30, 1999. The LPS-Ce crystal has an excellent short decay time without a long component or afterglow, and the process to grow the crystal is not difficult.

Measurements of the intrinsic rise times of 14 common inorganic scintillators with a list of their suppliers were reported at the 1999 NSS-MIC conference [60].

Table 11-2 lists the active gamma converters which directly convert the incident photon into an electrical signal [55].

In these detectors, the 511 keV photon is converted into a large number of electron-hole pairs. These electrons are collected at the end of the detector (generating a timing pulse which provides a means of identifying the position of the interaction) after drifting at a relatively slow speed. In order to have sufficient efficiency for detecting 511 keV photons, the detector must have a thickness of about 3 radiation lengths (equivalent to about 10 cm). The charge collection time of hundreds of nanoseconds makes the coincidence timing and the event pile-up very long, thereby making the system inefficient. These detectors are impractical because their production is expensive and the liquid xenon [61] proportional chambers require refrigeration to approximately -100°C .

Table 11-2. Characteristics of active detectors converting the 60 keV to 511 keV photon directly into an electrical signal.

	Density [g/cm ³] (high, provides good stopping power = high sensitivity)	Time resolution [ns]	Pulse height threshold [keV]	Detection efficiency (for 20 mm x 20 mm x 40 mm)
Ge	5.38	0.4	100	53%
^a HgI ₂	6.3	2	400	70%
^b CdTe	6.2	0.8	100	66%

^aSee reference [62].^bSee reference [63].

11.2.1.2 Transducers that generate an electrical signal proportional to an incident photon when the transducer is coupled to a gamma converter

Table 11-3 lists some transducers that, when coupled to the gamma converter, generate electrical signals. These transducers are used in the PET camera to generate an electrical signal, which is proportional to the incident 511 keV gamma.

Table 11-3. Transducers that generate an electrical signal proportional to the incident photon.

	Description	comments
PMT	Photomultipliers (PMT), Position-Sensitive PMT (PS-PMT), Multi-channel photomultipliers (M-PMT)	The most common transducers used in PET
APD	Avalanche Photodiode (APD)	Good characteristics, good quantum efficiencies (60%). There are several new developments for APD.
PD	Photodiode (PD).	Compact, inexpensive, stable, high quantum efficiency, no gain, relatively noisy, provide poor timing
VLPC	Visible Light Photon Counters (VLPC).	High quantum efficiencies (85%), gains greater than 10 ⁴ , but needs to be operated at cryogenic temperature (6-8 K).
MWPC	Multi-Wire Proportional Chamber. The 511 keV photon interacts with a heavy metal foil Pb or W. The gamma converter is read out by a MWPC	Low cost, but provides low detection efficiency and poor energy and time resolution.
SSPC	The Solid State Proportional Chamber (SSPC) [64] consists of a Barium Fluoride (BaF ₂) scintillator coupled with MWPC. The scintillation light is detected in the MWPC by adding a few torr of tetrakis (dimethylamine) ethylene (TMAE) vapor to the gas chamber	Medium cost, but the energy and time resolution remains low.

SDC	Silicon Drift Chambers. SDC [65] coupled with CsI(Tl) performs the measurement of the position of interaction by using the centroid method with better than 1 mm FWHM resolution.	Suitable for small scintillator cameras. The low electronics noise allows for 16% FWHM to be reached at 122 keV energy resolution.
-----	---	--

11.2.1.2.1 **Photomultipliers (PMT)**

The most common transducers used in commercial PET are photomultipliers. Among the companies producing photomultipliers are Burle [66], Hamamatsu [67], and Photonis [68]. Burle specializes in fast photomultiplier tubes for time-of-flight applications. Square and round photomultiplier tubes have been used in PET applications.

A common and widely used round phototube at a low price from Hamamatsu is the R1450 which is a 19 mm diameter, 10 stage, Bialkali photocathode.

Position Sensitive Photomultiplier (PS-PMT) tubes have crossed-wire design with multi-dynodes that provide the light position by the center-of-gravity method. To facilitate readout, each anode wire is connected with an adequate resistor chain which provides only 4 outputs.

The square R5900U-00-C8 phototube has been used in several detector modules for PET and its test performance has been reported in several articles. This tube has a 4 + 4 Cross Plate Anode (assume four strips covering an area of 22 mm x 22 mm providing four signals to one side, which may be called x, and four overlapping strips covering the same area and positioned at 90° with respect to the previous strips, providing four signals in the y direction). By means of ladder resistors between the dynodes, four analog signals carrying the position, energy and timing information are provided to the PET electronics. The dimensions of the phototube are 27 mm x 27 mm.

Other test results on phototubes reported in [69, 70, 71] are for multi-channel photomultiplier tubes (MC-PMT's) Philips-Photonis XP1722 (or XP4722), XP1702 (or XP4702) [72], XP1704 (or 4704), and XP1724 (or XP4724).

Among the square phototubes, the Hamamatsu R1548 is widely used in PET devices. It is a 10-stage device, with the dimensions of 24 mm x 24 mm with two sensitive rectangular areas of 8 x 18 mm each, providing a signal to an anode, and with a typical time resolution of 2.4 ns when coupled to the BGO crystal (FWHM).

A comparison of performance results of the square photomultiplier tubes used in the CTI/Siemens EXACT HR PET detector modules, as well as the round photomultiplier tubes used in the Siemens EXACT HR PLUS, is reported in [73], in which it is shown that in spite of the lower coupling area between the crystal and the phototube, the HR PLUS compares favorably with the HR block.

The above-mentioned companies (Burle, Hamamatsu, and Photonis) are now making larger photomultipliers with better timing characteristics specifically for PET applications. One example is the square 51-mm x 51-mm photomultiplier from Photonis XP5292, which will reduce the cost of the PET detector because it requires a smaller number of tubes.

11.2.1.2.2 Avalanche Photodiodes (APD)

Recently, the development of the APD has received considerable attention, and substantial effort has been made to improve their characteristics and lower their cost. At the last Nuclear Science Symposium and Medical Imaging in Seattle (WA) in October 1999, four talks out of five in the section dedicated to “photodetectors” dealt with APD [74, 75, 76].

The Lecompte group [77] in 1990 presented the results of the first APD-based PET camera, in which the APD was coupled to BGO crystals. At that time, the APDs in APD/BGO detectors offered poor timing resolution [78] compared to the timing resolution of a typical PMT/BGO detector [79]; this was due to the relatively low light output of the BGO. The development of LSO crystals, which provide significantly more light than the BGOs, together with the improvements in the APD technology, increase the probability that APD-based PET scanners may become commercially available. To this end, the development of preamplifiers implemented as a monolithic integrated circuit has been pursued [80].

Tests on a newly developed reach-through avalanche photodiode array fabricated by EG&G Optoelectronics, which is coupled to four different types of scintillators with different decay times are reported in [81]. The tests described in [82] point out the operating constraints on “buried junction” or “reverse” APDs (EG&G ReAPDTM) [83] when coupled to phoswich detectors with multiple crystals. Other tests on ReAPD coupled to GSO, LSO and YSO scintillators are reported in [84].

11.2.1.2.3 Silicon Photodiode (PD)

Results of the use of photodiodes in a 64-channel PET detector module targeted to the measurement of the depth of interaction were presented by Huber at the Nuclear Science Symposium and Medical Imaging on October 24-30, 1999 in Seattle (WA) [85]. Preliminary results of the use of photodiodes by the same group in 1993 were reported in [86]. At one end, the 64 LSO crystals are coupled individually to each one of the 64 photodiodes, and at the other end they are all coupled to a single one-inch-square PMT. The scintillating light is detected by the PMT at one end and by the 64 photodiodes at the other end. Each of the 64 photodiodes is coupled to one side of one of the 64 LSO crystals and detects the scintillation light emitted by it. On the other side of the 64 LSO crystals, all are coupled with a single one-inch PMT. The PMT provides an accurate timing pulse with energy information for all crystals, while the photodiodes identify the crystal of interaction (4 adjacent crystals also receive a signal). The timing resolution for a single LSO measured is 750 ps fwh, while the depth of interaction measurement resolution is 8 ± 1 mm fwhm. Similar measurements for timing, energy and crystal identification were performed by the same group on a BGO detector module [87] coupled to a photomultiplier on one side and to photodiodes on the other.

Pin silicon photodiodes have been also tested on other scintillator crystals such as CsI(Tl) for breast cancer imaging for the 140 keV gamma in [88]. The 16 photodiode output signals are amplified and sent to a “Winner Take All” (WTA) [89] custom IC which identifies the crystal of interaction based on relative signal amplitudes. The six-bit digital address of the crystal with the highest signal is also computed by the WTA circuit and sent to the PET coincidence-processing electronics. The basic cell of the WTA circuit, has been used recently on the Winner-select-output (WSO) [90] circuit which compares 16 analog input voltages and then outputs the maximum signal the “second” maximum and their addresses. This circuit is intended to be used for the Depth of interaction (DOI) in PET modules.

Previous work in using position-sensitive photodiode/BGO for PET detectors is described in [91].

The solid-state photodiodes (PD) coupled to an individual crystal (or small group of crystals) are attractive because they are compact, inexpensive, and stable, have high quantum efficiency, and do not require high voltage, whereas ordinary photodiodes have no gain, are relatively noisy, and give poor timing.

11.2.1.2.4 Multiwire Proportional Chamber (MWPC)

Among the most important designs are the CERN high-density avalanche chamber (HIDAC) [92], and the Rutherford Appleton Laboratory (RAL) design [93]. The MWPC RAL design was used for clinical trials at the Royal Marsden Hospital [94]. The camera [52] consists of two MWPC detectors opposite each other mounted on a rotating gantry. Each detector consists of a stack of cathode/converter planes interleaved with anode wire planes. The stack is enclosed in a sealed vessel filled with isobutane and 0.1% freon at atmospheric pressure. Each converter plane has 60-mm thick lead-foil conversion/read-out strips on either side. Strips run in orthogonal directions on either side of the wire plane. The detection process involves the photoelectric or Compton interaction of a 511 keV annihilation photon with one of the lead converters, resulting in the production of a fast electron which may subsequently escape into gas and produce a trail of ionization. The ionization charge is detected by gas amplification at the nearest wire, the anode plane being held at a potential of +3.7 kV. The energy of the electron on leaving the lead converter is only weakly related to the energy of the incident photon, and its path length in the gas will also vary. The detector therefore has no energy resolution. The spatial energy of the detector is determined by the distance that the electron travels transversely along the gap parallel to the converter planes.

The efficiency of MWPC systems for detecting 511 keV photons is significantly lower than that of the BGO-based systems (10-30% compared to 90%), so these systems would require a high radiation dose to be delivered to the patient in order to obtain acceptable quality images. Given the low cost of this type of detector, the PET based on a MWPC detector could have an advantageous application in industry in the quality control of cavities in materials. In those applications, the radiation dose is not of much importance because no humans are involved and the lower cost of the detector might be the driving factor.

11.2.1.2.5 Other transducers

Reference [95] provides an overview of current developments in position-sensitive photon detectors and photomultipliers. References [96, 97] provide information regarding the Visible Light Photon Counters (VLPC), which have the drawback of having to be operated at cryogenic temperatures (6-8 K). The problem may be solved with light guides or

fiber optics, although they considerably reduce the amount of light to the photodetector.

11.2.2 Assemblies of PET detector modules in blocks

The coupling of the gamma converter to the transducers which generates an electrical signal proportional to the 511 keV photons described above is called a detector module for PET. The coupling between the gamma converter and the transducer is done either directly with some light conductive grease or via light guides up to a few meters long. In the latter case, the light reaching the transducer is attenuated and may introduce inefficiency if the electronics cannot discriminate the signal from the noise when signals are generated from a low level of scintillating light. In the past several years, many combinations of the two elements have been assembled and tested. Some of them have been used in small animal cameras, head cameras or whole-body cameras. The following gives the reference and a short description of some of these.

There have been two main approaches in assembling and coupling gamma cameras to transducers. One approach is that of coupling a “continuous detector” (with the dimension of the gamma converter of several centimeters or even a detector made of a single annular crystal block [37]) to an array of transducers. The other approach is based on building a detector block made of many small crystals (with dimensions as small as 2 mm x 2 mm or 1 mm x 4.5 mm) coupled to a PMT (or APD). The block is then replicated many times to cover the geometrical photon detecting surface of a PET scanner. During the last 15 years, the segmentation of the detector block has become smaller and smaller to increase the PET spatial resolution, and the number of crystals per detector block has become larger and larger to use a small number of PMTs (or APDs) in order to lower the cost of the entire PET.

The latter technique of identifying the single crystal within a detector block” has improved in the past several years. In 1993 it was demonstrated in [98] how to identify a crystal out of 256 crystals coupled to a single PMT (or APD) transducer.

Both continuous detectors and block detectors have been developed and constructed during the past 20 years and are now commercially available. A group from the University of Pennsylvania (see Karp et al. [37]) had a great deal of experience with the “continuous detector” type, and work on PET systems based on this approach has been reported in several articles. Recently, however, they have proposed the construction

during the year 2000 of a GSO HEAD PENN-PET [99] based on the other approach, the “block detector” approach.

On the other hand, the study and construction of PET systems based on the “block detector” approach have been carried out by many universities and companies. One group leading the study and development of this approach is M. Phelps (who, with coworkers developed the first PET scanner, see reference [100]).

Recently, in 1994, this group also performed a study using the continuous-detector approach [101] for the construction of a high-resolution animal PET system. However, later the proposed high-resolution PET for small animals called MicroPET [69, 12] was built using the “block detector” approach.

Following is a list and a description of some “block detector” devices developed during the past several years. A brief list of “continuous detectors” is given in Section 11.2.4.

11.2.2.1 LSO/GSO crystals coupled to PMTs

11.2.2.1.1 CTI/Siemens ECAT HRRT PET

The CTI/Siemens ECAT HRRT PET for brain cameras [102, 103] with a patient port 35 cm in diameter and a field of view (FOV) of 25.2 cm is built of 936 blocks (13 x 72), each made of 64 LSO and 64 GSO crystals. Individual crystals measure about 2.1 mm x 2.1 mm x 7.5 mm in each crystal layer (see Figure 11-1). The two crystal layers are coupled to a photomultiplier (19 mm in diameter) through light guides. There are 128 crystals for each analog signal from the photomultipliers for a total of 119,808 crystals in two layers and 936 photomultipliers. It is based on a phoswich detector block design (see also Section 11.2.2.7) with Depth of interaction (DOI) capabilities (see Section 11.2.3.2). The intrinsic spatial resolution is about 1.3 mm.

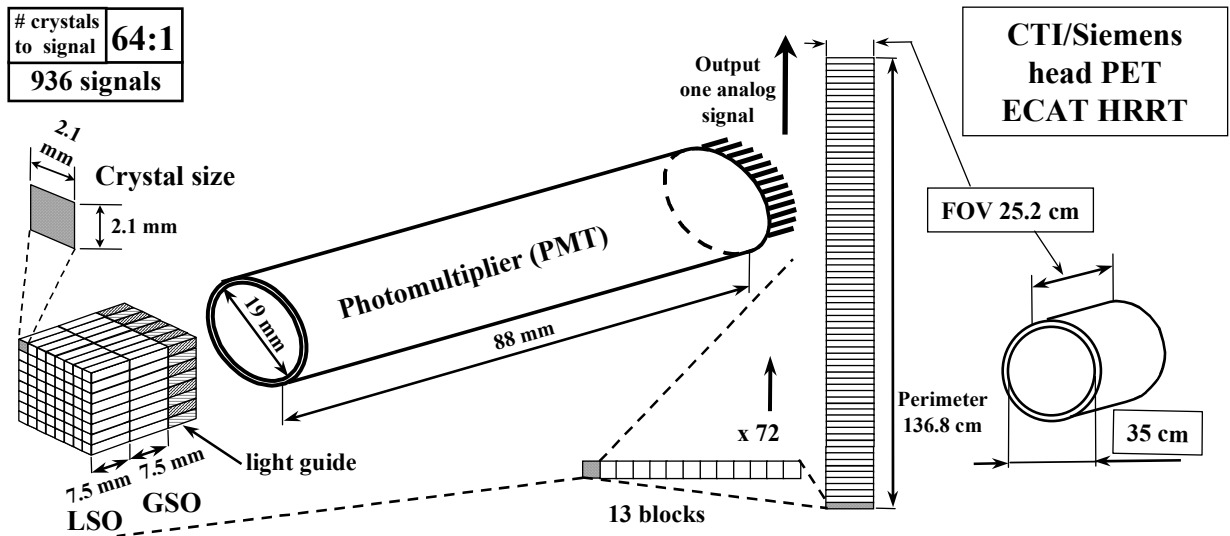


Figure 11-1. Layout of the detector block and assembly for the CTI/Siemens head PET ECAT HRRT.

11.2.2.1.1.1 Performance measurements on CTI/Siemens ECAT HRRT PET

Performance measurements comparing the new PET with the PET model from the same company delivered 5 years before are reported in [38], and Section II.A states “A comparison with the ECAT EXACT HR [22] shows that twofold gain in maximum NEC with the new tomograph in spite of the largely increased random rate is mainly due to improved dead time characteristics of the fast scintillator LSO.” The same article

indicates in the conclusions made in Section IV "...The high random rates and SF fraction measurements underline the necessity for a short coincidence time window and an improved energy resolution for such an open geometry....On the other hand the noise level in the images reveals a not yet optimized setup and reconstruction parameters...." It is clear that the design of the detector modules is more advanced than the electronics used and that there is a need to improve the latter; in particular, the statement in the article draws attention to the need to improve the signal-to-noise ratio. A higher-performance electronics with accurate event timing information will overcome the problems mentioned. A later article [38] mentions that both crystal layers in the HRRT are LSO (fast and slow instead of GSO/LSO) with a light decay difference greater than 7 ns. A shorter decay time offers the possibility of using shorter coincidence time windows thus reducing the random coincidences.

11.2.2.2 LSO coupled to PMT

11.2.2.2.1 CTI/Siemens MicroPET

The CTI/Siemens MicroPET for small animals [12] with a port 17.2 cm in diameter and a field of view (FOV) of 11.2 cm is made of 240 blocks (8 x 30), each made of 64 LSO crystals with an individual crystal size of 2 mm x 2 mm x 10 mm (see Figure 11-2). The 64-crystal block is coupled to a multichannel Philips-Photonis MC-PMT XP1722 photomultiplier tube through light guides 240 mm long. The intrinsic spatial resolution is 1.68 mm. The same detector configuration with optical fibers 25 cm in length connecting the crystal with the PMT, using BGO crystal instead of LSO, was investigated earlier and results are reported in [69, 104].

The XP1722 MC-PMT is a 64 channel PMT, 3" in diameter, with pixels arranged on an 8x8 grid. A charged division readout converts the 64 independent outputs into four position encoding signals. The X and Y positions of the incident photons were calculated using the Anger Logic (see right side of Figure 13-12). Section III reports in [12] that the MicroPET uses the 1994 electronics described in reference [105], which decodes the crystal receiving the incident photon by means of an analog signal-processing circuit [106].

The count rate has not improved significantly, and Section V of reference [12] states that "...Much work still remains to be done to optimize the detector and electronics..."

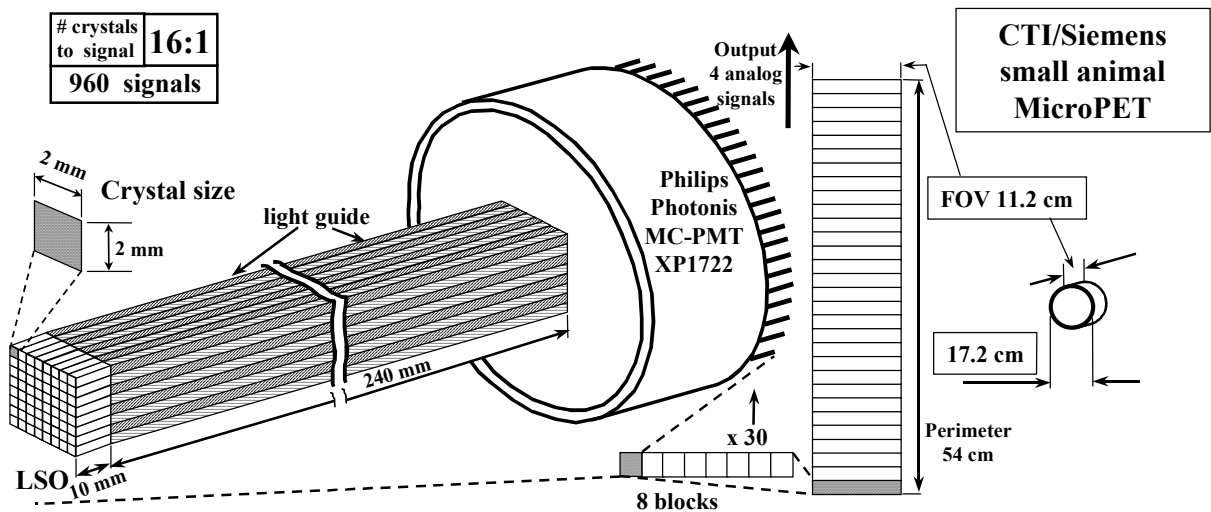


Figure 11-2. Layout of the detector block and assembly for the CTI/Siemens MicroPET for small animals.

The scintillation properties of 1880 LSO(Ce) crystals are investigated [107]. Measurements on modules made of LSO crystal were performed in [142] with two PMTs connected at the opposite ends of the crystal (see also Section 11.2.3.2). Detector modules made of LSO viewed from just one end were investigated for their feasibility in [108].

The investigation of the impact in replacing the BGO in the CTI/Siemens HR PLUS by LSO reported in [109].

11.2.2.3 LSO coupled to APD

A preamplifier [80] in conjunction with a Photonix, a 5-mm diameter beveled-edge APD coupled to LSO crystals showed a timing resolution of 1.57 ns FWHM.

The characteristics of a new planar process silicon avalanche photodiode (APD) for direct X-ray detection are described in [76]. The following statement was made in the summary of the measurements performed: “The device shows excellent energy and timing resolution and appears to be very promising for medical imaging applications such as PET and SPECT.”

11.2.2.4 LSO coupled at one end with photodiodes and at the other end with PMT

Detector modules made of 64 LSO crystals coupled at one end with photodiodes and at the other end with photomultipliers are described in [85, 86] and shown in Figure 11-3. The photomultiplier (PMT) provides an accurate timing pulse and energy threshold for all crystals, the photodiode (PD) identifies the crystal of interaction, the sum (PMT + PD) provides a total energy signal, and the PD/(PMT + PD) ratio determines the depth of interaction (DOI, see also Section 11.2.3.2). Previous work by the same group can be found in [148, 147] and the same technique on BGO in [87].

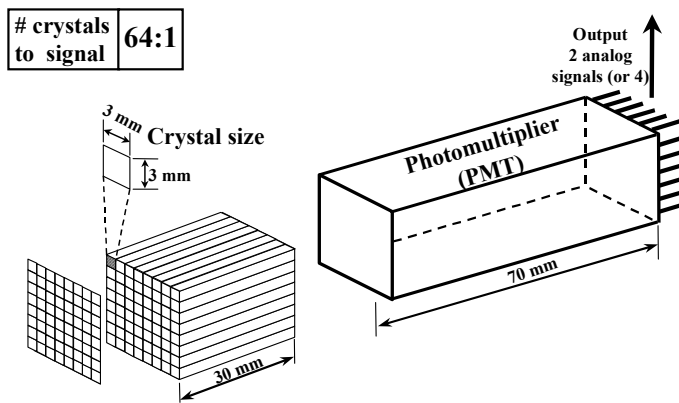


Figure 11-3. Layout of the detector block with 64 LSO coupled at one end with 64 photodiodes and at the other end with a single photomultiplier.

11.2.2.5 GSO coupled to PMT

11.2.2.5.1 GSO HEAD PENN-PET

The GSO HEAD PENN-PET [110, 111], with a patient port 30 cm in diameter and a field of view (FOV) of 25 cm, is designed to be made of 288 blocks (8 x 36), each made of about 64 GSO crystals with an individual size of 4 mm x 4 mm x 10 mm (see Figure 11-4). The 288 photomultipliers, 39 mm in diameter, are coupled through a continuous light-guide with 18,560 BGOs crystals (58 x 320). Crystal rings and photomultipliers ring are staggered (one-half crystal width, and one-half PMT width respectively) with respect to the adjacent rings.

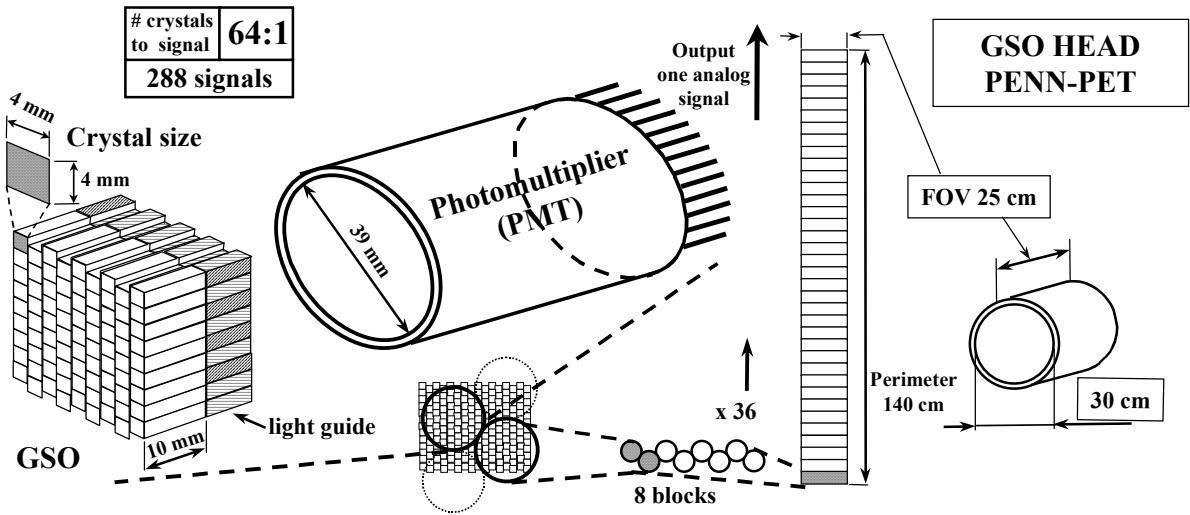


Figure 11-4. Layout of the detector block and assembly for the GSO HEAD PENN-PET.

The 'local centroid' method [112] used in this detector is the ideal algorithm to be used with the 3D-Flow architecture, since that architecture provides for communication with the neighbors. It allows the rapid exchanging of information to North, East, West and South after having normalized the ADC counts to energy, which it does via the look-up table memories available in each 3D-Flow processor (see Section 12).

11.2.2.5.2 Assembly of an array of 36 GSO(Ce) crystals coupled to 4 phototubes

The measurements of an assembly of 36 crystals (4.5 mm x 4.5 mm x 30 mm) coupled to 4 round photomultipliers, are reported in reference [113]. The measurements shows that the 56 ns decay time of the GSO(Ce)

should allow to increase one order magnitude the count rate compared to the BGO crystals.

11.2.2.6 BGO coupled to PMT

11.2.2.6.1 CTI/Siemens PET966/EXACT3D

The CTI/Siemens PET966 EXACT3D for whole-body scanning [114], with a patient port 56 cm in diameter and a field of view (FOV) of 23.4 cm, is built of 1728 blocks (12 x 144), each made of 16 BGOs with an individual BGO crystal size of 4 mm x 4.1 mm x 30 mm (see Figure 11-5). The block of 16 crystals is coupled to a photomultiplier measuring 19 mm in diameter.

There are 16 crystals for each analog signal for a total of 27,648 crystals and 1728 photomultipliers (analog signals).

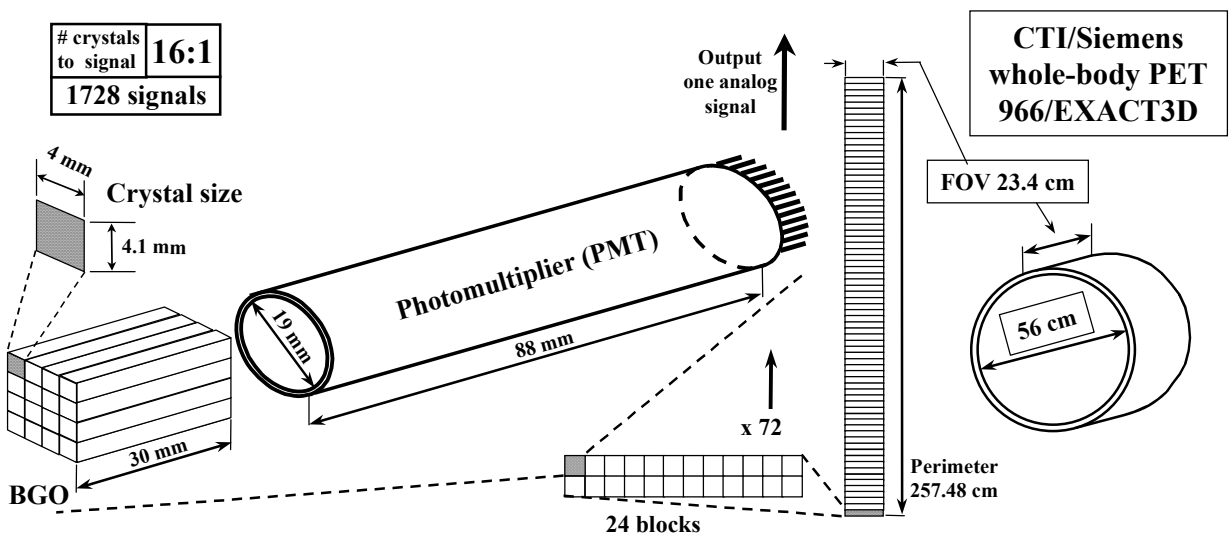


Figure 11-5. Layout of the detector block and assembly for the CTI/Siemens PET966/EXACT3D.

11.2.2.6.1.1 Performance measurements on CTI Siemens PET966/EXACT3D

The intrinsic spatial resolution is 4.7 mm. The maximum total coincidence event rate is limited to about 3 million events/second. The maximum true rate is about 850 kcps (for 90 MBq or 2.4 mCi in the

FOV). The article reports that “the fall off after this point is not due to paralyzable deadtime behavior but to a limit in the sorter board of the current acquisition system (ACS).” The same article reports that the 966EXACT3D is 4 times more efficient than the model ECAT 953B brain tomograph with 10 cm FOV and about 2.5 times more efficient than a 15 cm FOV such as ECAT EXACT.

11.2.2.6.2 CTI/Siemens ECAT EXACT HR PLUS

The CTI/Siemens ECAT EXACT HR PLUS for whole-body scanning [115, 19] with a patient port 56 cm in diameter and a field of view (FOV) of 15.5 cm is built of 1152 blocks (8 x 144), each made of 16 BGO with an individual BGOs crystal size of 4 mm x 4.39 mm x 30 mm (see Figure 11-6). The block of 16 crystals is coupled to a photomultiplier which is 19 mm in diameter.

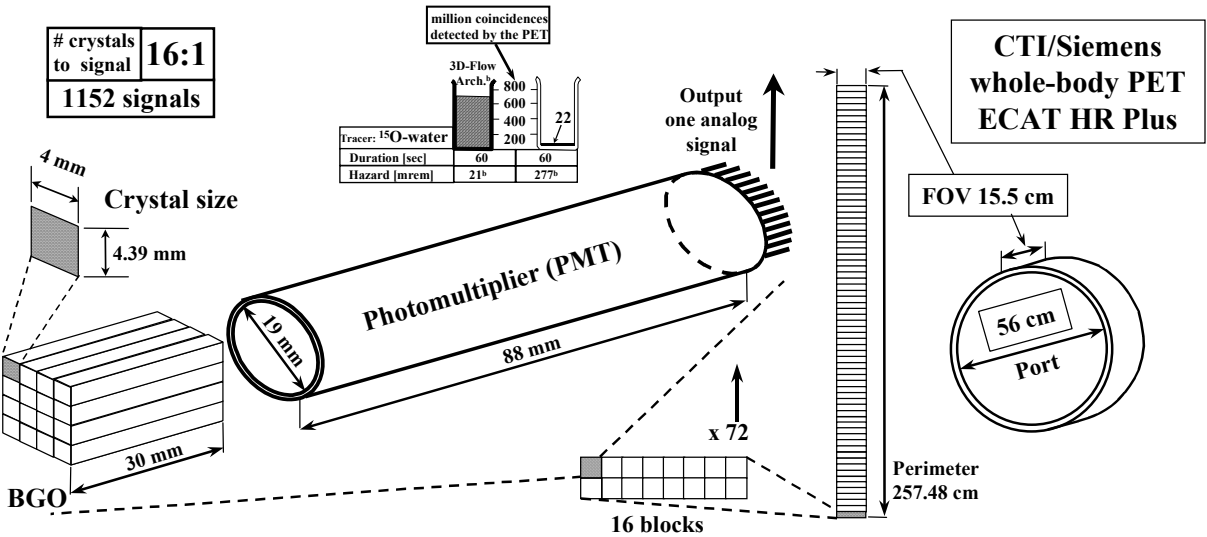


Figure 11-6. Layout of the detector block and assembly for the CTI/Siemens ECAT EXACT HR PLUS.

There are 16 crystals for each analog signal for a total of 18,432 crystals and 1152 photomultipliers (analog signals). The transaxial resolution is 5.1 mm FWHM at 1 cm and the axial resolution is 4.2 mm FWHM at 0.4 cm.

Section II of reference [19] reports “... According to these guidelines, volunteers for ¹⁵O-water studies can receive a total maximum of 240 mCi [which corresponds to 1008 mrem in dose equivalent] The one-session protocol employs 12 bolus injections/subject.” Section III of the article reports that “...Thus over 70% of all detected events were true when injecting 5 mCi, while only 50% of the events were true when the dose increased to 20 mCi Dead time grew linearly from just over 10% when 5 mCi injections were used to over 25% when 20mCi were injected.”

11.2.2.6.3 General Electric Advance

The General Electric Advance model whole-body PET scanner [23] and patent [116] with a patient port 59 cm in diameter and a field of view (FOV) of 15.2 cm is built of 672 blocks (6 x 112), each made of 18 BGO with an individual BGO crystal size of 4 mm x 8 mm x 30 mm (see Figure 11-7). The block of 18 crystals is coupled to a square photomultiplier (24 mm x 24 mm).

There are 9 crystals for each analog signal for a total of 12,096 crystals and 672 photomultipliers providing 1344 analog signals to the readout. The transaxial resolution is 3.8 mm FWHM, and the axial resolution is 4 mm.

11.2.2.6.3.1 Details on the General Electric Advance PET hardware system and electronics

The entire hardware system of the PET and the coincidence electronics are described in the patent [116] and in references [117]. The 1344 blocks are reduced in number and grouped in 56 modules (24 per module) because it would be costly to implement a circuit testing all possible combinations (LOR) of 1344 blocks.

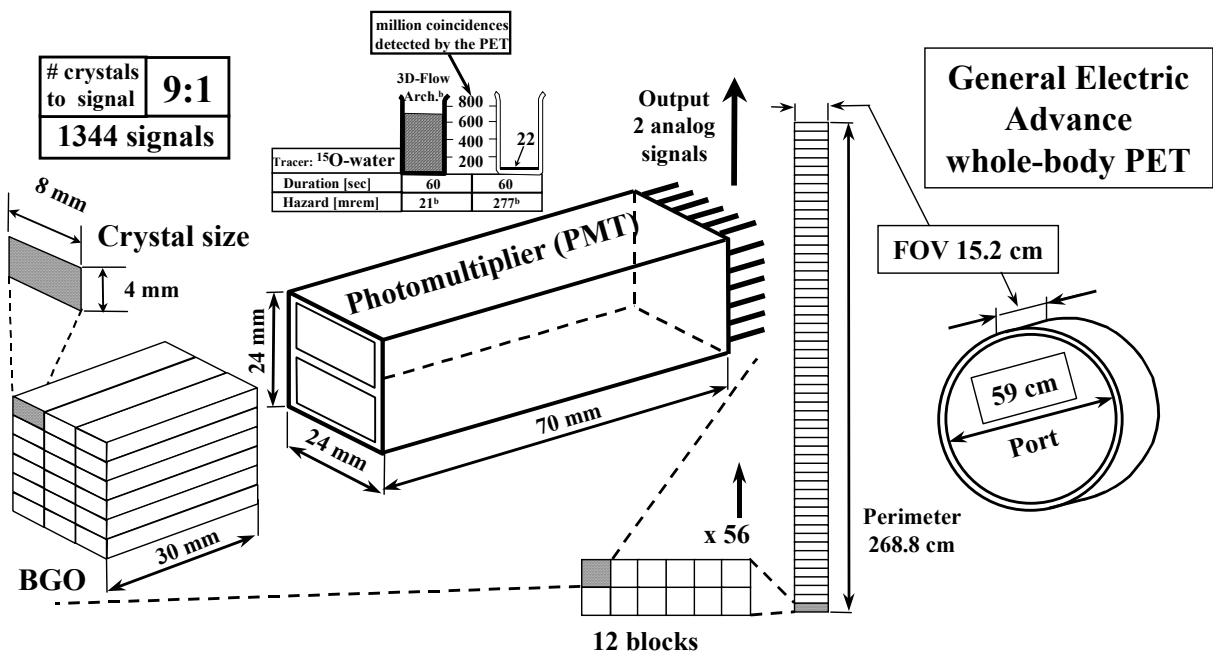


Figure 11-7. Layout of the detector block and assembly for the General Electric Advance.

Every 250 ns, all modules acquire information from a set of 24 crystal blocks. The first “single” satisfying the energy requirements received in one of the 24 blocks of a module prevents other “singles” received in the same module from becoming a coincidence candidate. This arbitrary selection of the first singles among all the possible candidates introduces dead time.

Coincidence detection circuits are connected to each of the detector modules in the ring, and they look for such coincident events in all of the approximately 700 possible detector pair combinations (see also Section 0). The coincidence detector circuit, therefore, has one complete channel for each possible detector pair to be examined. All of the approximately 700 examinations on a set of 56 elements are performed in parallel once during each 250-nanosecond sample period in the GE Advance.

On the other hand, it is interesting to note here that the novel 3D-Flow circuit of the new design presented here has, fewer coincidence circuits, which test all possible candidates that move from the detector to the circuit exit point.

During every sampling time of 50 ns, the novel 3D-Flow architecture performs only a few examinations on a set of 672 elements. The only ones examined are those that satisfied the criteria of a coincidence candidate, which average fewer than 4 every 50 ns. The efficiency in using the 3D-Flow approach is increased, because the set of 1344 elements is larger than 56 and because all possible candidates are considered and checked out thoroughly by means of digital signal processing, neighboring signal correlation, local maxima, and energy clustering calculation. In the GE Advance approach, *a priori* selection reduces the candidates to the first candidate satisfying the high/low energy window threshold. This results in the rejection of all the others, among which may be some with better characteristics.

11.2.2.6.3.2 Performance measurements on General Electric Advance PET

Measurements using different phantoms are reported at a later date in [36], and transaxial resolution, axial resolution, dead time, and slice sensitivity measurements are reported in [118].

Reference [23] (on page 1405, Figure 8) describes a PET examination using a GE Advance in which a total of 3 million counts per plane in the center plane were acquired for a duration of 20 minutes after the human patient had received an injection of 8.5 mCi ¹⁸F-FDG 30 minutes earlier. For the reason that center slices are more sensitive than those at the sides, as explained on page 2202 of [118], and on page 2346 of [119] if approximately 72×10^6 total coincidence counts were accumulated on 35 planes during the entire 20-minute period, the average rate would be 60,000 coincidence counts per second. This count rate at an approximate activity of the source of 275×10^6 disintegrations per second ($7/8$ of $(8.5 \text{ mCi} \times 37 \text{ MBq} = 275 \text{ MBq})$ yields a total efficiency of 0.022%. (60×10^3 coincidence counts/sec divided by $275 \times 10^6 \text{ Bq} = 0.022\%$).

The same reference [23] reports the results of the examination performed using 66 mCi of intravenous injection of the radiotracer ¹⁵O-water in a normal human brain. A total of half a million counts were accumulated in the center plane during the entire examination. For the same reasons described before, a lower coincidence count is accumulated on the lateral plane (see reference [119] on page 2346, Figure 6), giving a total of approximately 12×10^6 coincidence counts on all 35 planes during the entire examination period of 1 minute. The radiation dose activity of 60 second scanning that commenced 20 seconds after injection of the bolus ¹⁵O-water is approximately 85.47×10^9 disintegrations ($7/12$

of $(66 \text{ mCi} \times 37 \times 10^6 \text{ Bq} \times 60 \text{ sec}) = 85.47 \times 10^9$ disintegrations). Thus the total efficiency is $(12 \times 10^6) / (85.47 \times 10^9) = 0.014\%$.

11.2.2.6.4 CTI/Siemens ECAT EXACT HR

The CTI/Siemens ECAT EXACT HR for whole-body scanning [22] with a patient port 56 cm in diameter and a field of view (FOV) of 15 cm is built of 672 blocks (6 x 112), each made of 28 BGOs with an individual BGO crystal size of 2.9 mm x 5.9 mm x 30 mm (see Figure 11-8). The block of 28 crystals is coupled to a square photomultiplier, 24 mm x 24 mm.

There are 14 crystals for each analog signal for a total of 18,816 crystals and 672 photomultipliers providing 1344 analog signals to the readout. The transaxial resolution is 3.6 mm FWHM, and the axial resolution is 4 mm.

11.2.2.6.4.1 Details on the CTI/Siemens ECAT EXACT HR PET hardware system and electronics

The approach to detecting coincidences is similar to the one described before for the General Electric Advance model. The design approach of the front-end electronics is described in [105]; its ASIC implementation is described in [120]. The coincidence detection circuit based on the same approach as the one described before for the General Electric Advance [117,116], but detecting coincidences among 16 modules instead of 56 modules as was the case for the GE Advance, is described in [121], its ASIC implementation is reported in [122]. (In contrast, the 3D-Flow with the novel approach detects coincidences among 672 or more modules with six comparisons)

In 1993, a subsequent VLSI implementation [123] of the coincidence circuit by the same group presents the improvement of "...using the vacant clock cycles to transmit any extra events that occur during non-zero clock cycles" to reduce the number of gates by using a multiplexer and a logic based upon adding and subtracting two numbers if they are within a specific range of each other. "...To reduce the number of gates in the gate array, the input data is time multiplexed into fourteen copies of the MODULE PAIR saves thirty-five copies of the MODULE PAIR the simplest is to add and subtract the range from one and compare the two results to the other".

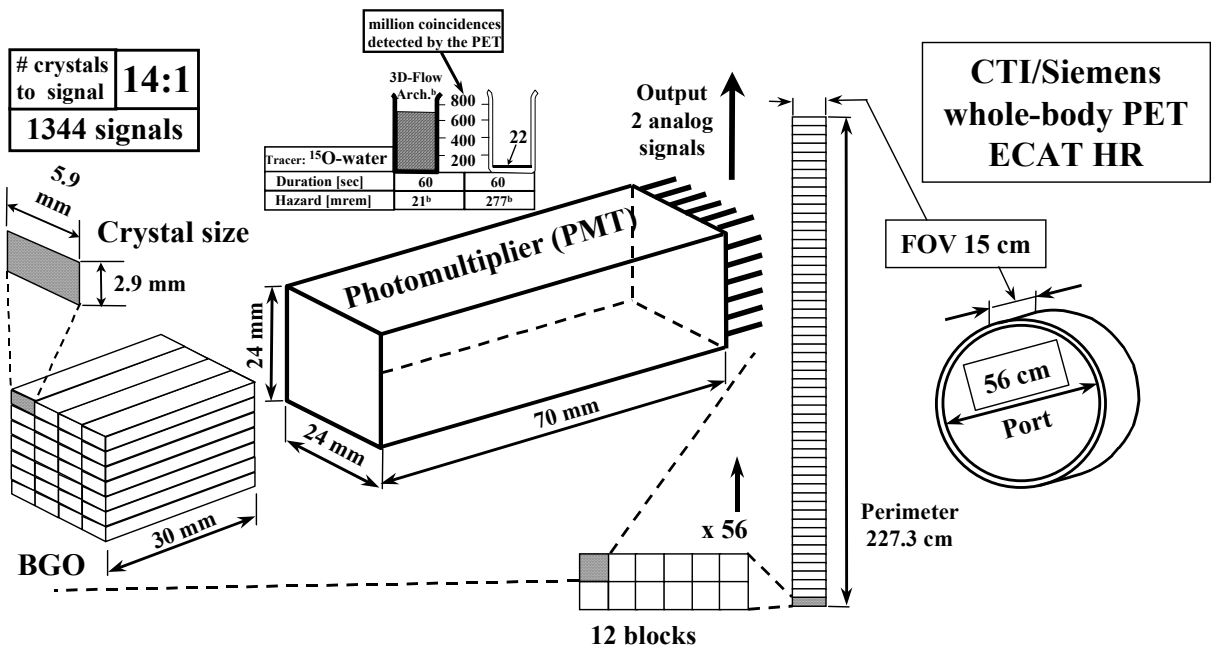


Figure 11-8. Layout of the detector block and assembly for the CTI/Siemens ECAT EXACT HR.

However, the 3D-Flow approach outperforms the current approaches in the number of gates and efficiency in detecting coincidences among a large number of modules. The current PET systems (CTI/Siemens, GE, etc.) require the number of modules to be reduced to several dozens; in larger PET systems with 120 cm FOV could not offer a high efficiency under those conditions. The 3D-Flow approach technique, on the other hand, by comparing a smaller number of "singles" that are routed through

the pyramidal coincidence detection circuit, can easily detect coincidences among a large number of modules using fewer circuits

The fact that the electronics of the ECAT EXACT HR needed some improvement is clear from the measurements reported in [124], where new hardware, referred to as ACSII, replaced the previous hardware, referred to as ACSI. Further investigation will show that additional improvement is still needed on the electronics. Besides the long decay time of the BGO, there are still other causes of inefficiency, including a) the arbitrary selection of one single per module at the front-end when channels are reduced from 1344 to 56, b) the dead time of the module, longer than one microsecond, when a “single” is detected. In this regard, measurements of the total efficiency reported on page 115 of reference [22] confirm the need to improve the efficiency in the different sections of the PET device.

11.2.2.6.4.2 Performance measurements on CTI/Siemens ECAT EXACT HR PET

The performance measurements reported in [22] on page 115 show that a total of 6×10^6 counts per center slice were acquired for 60 minutes, 30 minutes after injection of 10 mCi of ^{18}F FDG in a human. Given that there are 47 slices and that lateral slices accumulate fewer counts than the center slices (see reference [119] on page 2346, Figure 6), then the approximate total count of coincidences of 193×10^6 accumulated on 47 planes during the entire examination period of 60 minutes gives the average count rate of 53.6×10^3 coincidence counts per second. This count rate at an approximate activity of the source after 60 minutes of 277.5×10^6 disintegrations per second ($3/4$ of $(10 \text{ mCi} \times 37 \text{ MBq}) = 277.5 \text{ MBq}$) yields a total system efficiency of 0.0193%. (53.6×10^3 coincidence counts/sec divided by 277.5×10^6 disintegrations/sec = 0.0193%).

11.2.2.6.5 CTI/Siemens ECAT EXACT

The CTI/Siemens ECAT EXACT (model 921) for whole-body scanning [29] with a patient port 56.2 cm in diameter and a field of view (FOV) 16.2 cm in length is built of 576 blocks (6×96), each made of 16 BGO with an individual BGOs crystal size of 6.35 mm x 6.35 mm x 20 mm. The block of 16 crystals is coupled to a one-inch round photomultiplier.

There are 16 crystals for each analog signal for a total of 9,216 crystals and 576 photomultipliers (analog signals). The transaxial resolution is 5.8 mm FWHM, and the axial resolution is 5 mm FWHM.

Page 810 of reference [29] states that “the block detector performance gives major dead time contribution in the high count rate region The limited capacity of the ACS [hardware electronics] may, in its present design, cause serious limitations when operating in 3D mode The ACS limits then occur at ~0.25 mCi/ml.” Further measurements (see Section 11.2.2.6.4) assessed the limitation.

11.2.2.6.6 Positron Posicam 6.5 PET

The Positron Posicam 6.5 BGO PET whole-body scanner [33] with a patient port 58 cm in diameter and a field of view (FOV) 11.9 cm long is built of 720 blocks in a staggered geometry (6 x 120), each made of 2 BGOs with an individual BGO crystal size of 8.5 mm x 20 mm x 30 mm (see Figure 11-9). The block of 2 crystals is coupled to a round photomultiplier, 19 mm in diameter.

There are 2 crystals for each analog signal for a total of 1,320 crystals and 720 photomultipliers. (The number of the photomultipliers is the same as the number of analog signals. Due to the staggered geometry of the crystals, the total number of crystals in the PET system is lower than 720-PMT x 2). The transaxial resolution is 5.8 mm FWHM, and the axial resolution is 11.9 mm FWHM.

The staggered geometry of the crystals is described in the following patents [125, 126, 127, 128] and is now proposed in a new GSO HEAD PENN-PET (see Section 11.2.2.5.1).

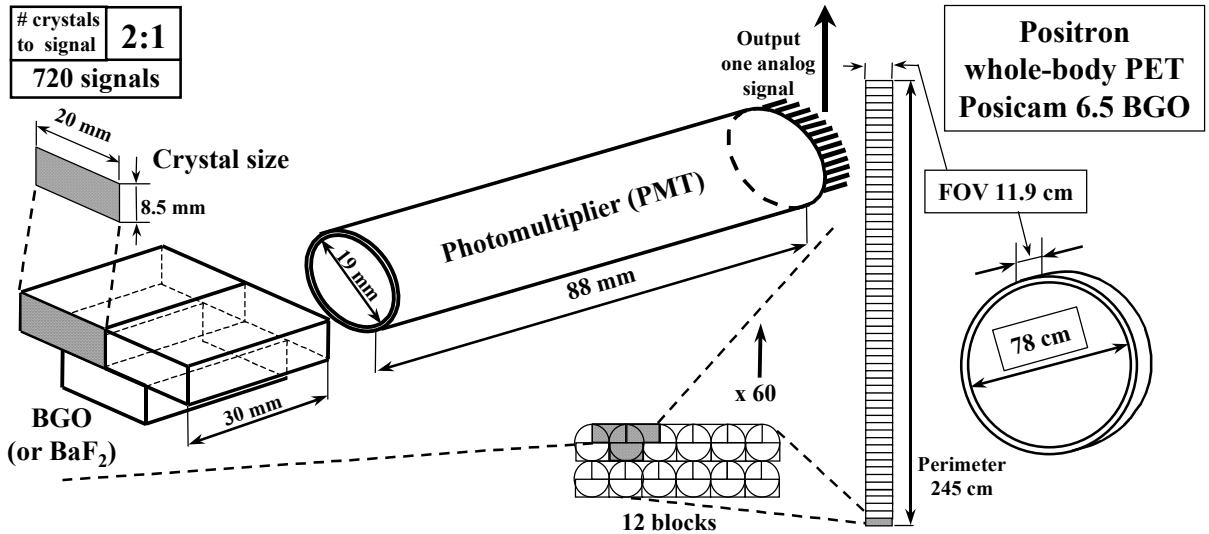


Figure 11-9. Layout of the detector block and assembly for the Positron Posicam 6.5 PET.

11.2.2.7 Multi-crystals with different physical properties coupled to PMT (Phoswich)

11.2.2.7.1 YSO/LSO coupled to PMT (for PET/SPECT scanners with DOI measurements)

The detector consists of a linear array of 4 mm x 4 mm x 15 mm YSO crystals, with a light decay time of 70 ns, coupled to a 10 mm thick combined detector array/light guide of LSO, with a light decay time of 40 ns. The study is for PET/SPECT applications. The events originating from the two different materials can be separated by pulse-shape discrimination (see Section 11.2.3.2 Depth of interaction (DOI)). The front layer of YSO is used for the detection of the low energy 140 keV single photons and the LSO layer is used for detecting the 511 keV from coincidence PET. The intrinsic radioactivity of LSO prevents the use of this scintillator in single-photon counting mode. It is reported in [129] that “The light collection of the PMTs coupled to the detector was found to be adequate to accurately identify each detector element in the array using the same positioning logic used in conventional BGO block detectors.” Previous study on this approach was reported in [130].

11.2.2.8 Multi-crystals with different physical properties coupled to APD (Phoswich)

11.2.2.8.1 GSO/LSO/YSO coupled to ReAPD

A reverse avalanche photodiode [83] coupled to BGO/LSO and YSO [84] provided the measurements which were compared to BGO. BGO and GSO are critically dependent on energy and timing resolution, while the LSO and YSO are not because of their high luminosity. The energy resolution of these crystals is demonstrated to be limited by the scintillator resolution. The signal-to-noise ratio of the lower-luminosity BGO and GSO is degraded by the dark and excessive noise of the ReAPD. These crystals coupled to the APD would reduce the cost and complexity in the implementation of PET detectors. In spite of these good features, the authors of the article state that the energy resolution of LSO and YSO scintillator is observed to be much worse than it should be.

11.2.2.8.2 YSO/BGO/LSO/CsI(Tl) coupled to APD

A detector module (see Figure 11-10) having the basic cell made of a 2x2 array of scintillators with different decay times can be identified by pulse shape discrimination. All four crystals in a BGO/LSO/YSO/CsI(Tl) [81] assembly can be clearly separated and individually gated for energy. The authors report that an energy resolution of better than 13% can be obtained in all pixels for 511 keV gamma rays.

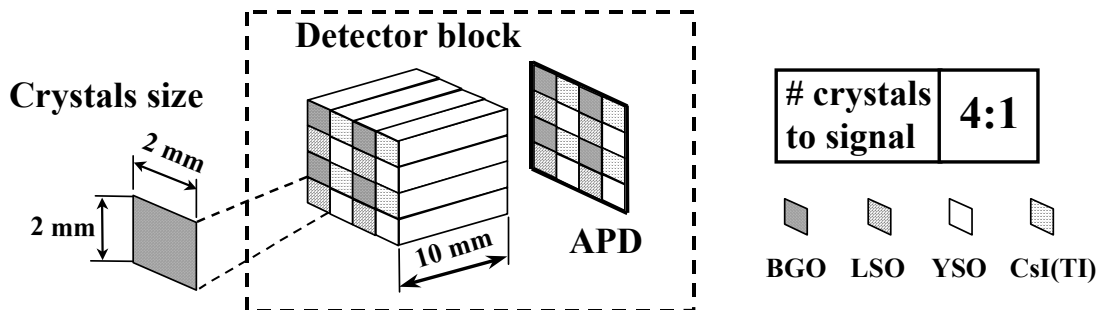


Figure 11-10. Layout of the detector block with BGO/LSO/YSO/CsI(Tl) coupled to an APD.

11.2.2.8.3 CsI(Tl)/LSO/GSO coupled to APD (for PET/SPECT/CT scanners with DOI measurements)

Reference [131] describes a detector module for multimodal PET/SPECT/CT scanners made of a multi-crystal detector CsI(Tl)/LSO/GSO coupled to APD, capable of discriminating low-energy

X-rays, medium-energy single γ -rays and 511 keV γ -rays (detecting X-rays).

In Figure 11-11a, the authors propose a thin (3 mm) CsI(Tl) scintillator sitting on top of a deep GSO/LSO pair read out by an avalanche photodiode.

The GSO/LSO pair provides depth of interaction (DOI) information for the 511 keV detection in PET. Measurements show that CsI(Tl) achieves the best energy resolution and largest time separation at all energies (60 keV, 140 keV, and 511 keV) and should have a thickness such that all X-rays will be absorbed in CT mode.

The medium γ -rays (140 keV) will interact in the two front layers of the detector (CsI(Tl) and LSO) and are not expected to reach the bottom GSO layer.

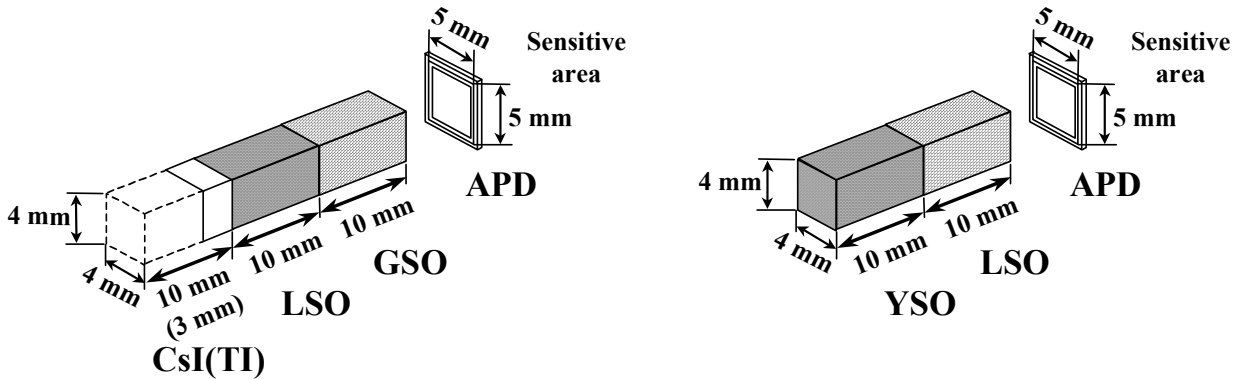


Figure 11-11. Layout of the detector block with a) CsI(Tl)/LSO/GSO coupled to APD, and b) YSO/LSO coupled to APD.

The authors of the article foresee some complexity in the electronics stating that “Although the implementation of the proposed CsI(Tl)/LSO/GSO detector raises special problems that increase complexity, it generally outperforms the LSO/YSO phoswich for simultaneous PET, SPECT and CT imaging....Possible improvements of the crystal identification with the GSO/LSO/CsI(Tl) detector include the use of distinct electronic channels for optimal, independent processing of the slow CsI(Tl) and fast GSO/LSO signals...”

The article also reports additional tests made on another phoswich detector that consists of YSO/LSO coupled to APD as shown in Figure 11-11b.

The 3D-Flow architecture can handle these problems and provide an elegant and simple solution to the problem of digital signal processing at each channel (see Section 12).

11.2.3 Design of PET detector modules targeted to improve some characteristics

11.2.3.1 Time of flight (TOF)

The position of annihilation can be determined from the difference between the times of flight of the γ -rays. The relationship between time difference ($t_1 - t_2$) and the source position between opposed detectors, x , can be expressed by $x = (t_2 - t_1) * c/2$, where c is the light velocity. (See Figure 13-15).

Applications of time-of-flight (TOF) measurements can be divided into two categories:

PET devices assisted by TOF information (The first TOF-PET was developed in 1982. The use of TOF information provides advantages such as the improved signal-to-noise ratio of images).

PET devices directly using TOF information in source positioning

Examples of TOF information used in PET devices can be found in the references [132, 133]. One example of the characteristics of a TOF-PET using CsI crystals is given in Section 11.2.3.1.1, while investigation using TOF information in PET based on LSO crystals is reported in Section 11.2.3.1.2.

11.2.3.1.1 Super PET 3000-E Time-of-flight (CsI crystals)

The Super PET 3000-E Time-of-flight for whole-body scanning [27] with a patient port 52 cm in diameter and a field of view (FOV) of 10.7 cm in length is built of 768 blocks (4 x 192), each made of one CsI (cesium fluoride) crystal measuring 12.5 mm x 23.5 mm x 43.7 mm (see Figure 11-12). The CsI crystal block is coupled to a photomultiplier, 19 mm in diameter.

There is one crystal for each analog signal for a total of 768 crystals and 768 photomultipliers (analog signals). The intrinsic resolution is 8.5 mm FWHM.

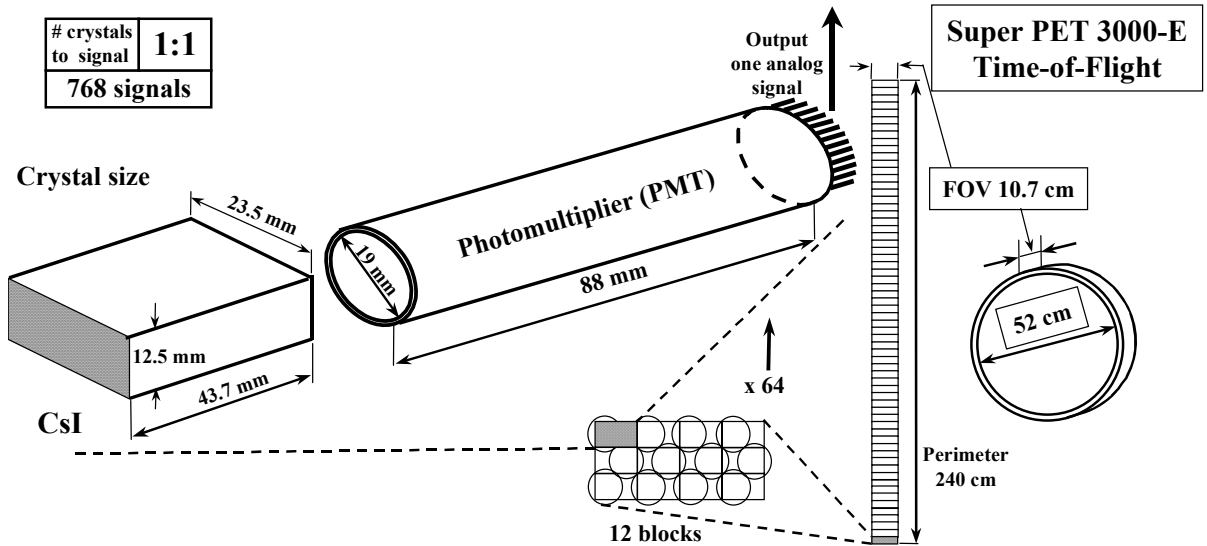


Figure 11-12. Layout of the detector block and assembly for the CsI Super PET 3000-E Time-of-flight

11.2.3.1.2 Considerations in using LSO crystals for Time-of-flight PET

Measurements were performed [134] on timing properties of incident photons at 511 keV on LSO crystals coupled to a photomultiplier. The LSO crystals had dimensions of 3 mm x 3 mm x 30 mm. Coincidence timing resolution of 475 ps FWHM was measured between two LSO crystals with the above dimensions.

The timing degradation of a fast crystal such as LSO is caused by the scintillation light which undergoes multiple reflections at quasi random angles within the scintillator crystal. The timing resolution of 500 ps provides a resolution of only 75 mm FWHM, which is not sufficient to be used for direct positioning of the source but can only be used to assist the tomographic reconstruction algorithm and improve the signal-to-noise ratio.

The timing resolution can be improved if the depth of interaction (DOI) within the crystal is known. Since the measurement of DOI is desirable in order to reduce spatial resolution artifact, it may be possible for the new PET design to acquire the measurements of both TOF and DOI.

11.2.3.2 Depth of interaction (DOI)

In order to increase the resolution of the PET camera, the size of the crystals has been made smaller and smaller. On the other hand, in order to achieve a good stopping power and capture all the incident photons, the thickness of the crystal should be about 30 mm (depending on the physical properties of different crystals). Although there are no problems in identifying the crystal when the incident photon is perpendicular to its face toward the emitting source, the resolution degrades toward the periphery of the field of view because of the oblique penetration of the incident photon into the crystal. This effect is commonly referred to as parallax. In order to eliminate the parallax error without reducing the sensitivity, detector modules have been developed that measure the depth of interaction (DOI) of the incident gamma rays.

Several techniques have been used to measure the DOI. One of them is the implementation of the detector with two or more layers of crystals (phoswich) with different physical properties such as light decay time or light yield. During the past 14 years, different techniques for extracting the DOI information have been discussed in several articles [81, 135, 136, 137, 138].

CTI/Siemens HRRT PET implements the DOI decoding reported in [102] by using a phoswich LSO/GSO. The separation of the LSO and GSO layer is done by pulse shape discrimination (PSD). The same article mentions that the use of an LSO/GSO with a difference of only 7 ns in light decay time (LSO/GSO has a difference of about 20 ns in light decay time) is sufficient to achieve DOI information by pulse shape discrimination. A shorter decay time offers the possibility of using a shorter coincidence time window thus reducing the random coincidences.

Beside the use of the pulse shape discrimination (PSD) technique in the time domain, investigations have been made also in the pulse height discrimination (PHD) technique in the energy domain. Both techniques aimed to qualify an event and assign it to a scintillation layer (DOI). The discrimination is based on time windows or energy windows which relate to the different physical characteristics of the crystals.

Comparisons of the two techniques have been made in several articles. In cases where PSD time or PHD energy discrimination alone is inadequate, more sophisticated PSD techniques using parametric time-energy histograms should be used to improve crystal identification.

The accuracy of the decoding of the depth of interaction in a detector module is also affected by the interdetector Compton scattering. Studies in this regard have been performed by several people. Miyaoka and Lewellen [139] have investigated the effect of detector Compton scatter on a detector that uses light sharing and ratio information in estimating the depth of interaction. The detector module and detector system were simulated.

The light sharing between crystals was done by placing an optical coupler in between two crystals at the top and an opaque reflector in between two crystals at the bottom, close to the coupling with the PMT. Investigation on PET block detectors, which optimize the way light is shared through the module for crystal identification, can be found in [140, 141].

Among the three methods investigated to locate the interaction, maximum energy, second maximum, and minimum DOI, “selecting the detector unit corresponding to the minimum DOI provided the best decoding accuracy for photons entering perpendicular to the detector. However, for photons entering at large angles of incidence (e.g., 30 degrees) the maximum energy selection criterion performed the best.” [139]. For practical implementation, the authors stated that “each of the three selection schemes investigated should yield very similar performance. Detector scatter had minimal affect on FWHM of the intrinsic image resolution throughout the FOV of the detector system.”

Shao and Cherry [142] have investigated the impact of the intercrystal scatter on BGO/LSO detector modules without DOI capabilities. They found that full-width half-maximum (FWHM) and full-width tenth maximum (FWTM) were not impacted by detector scatter. Comanor and Moses [143] also came to the same conclusion; however, if the initial interaction point can be determined, they stated “there is significant (10-20%) improvement in quantification in regions <1 cm in diameter.”

Pulse shape vs. pulse height discrimination and detector scatter identification in the time domain were investigated in [144] for LSO/LSO high resolution PET detectors, LSO/GSO and NaI(Tl)/LSO for a combined PET/SPECT detector. The investigation showed that the “pulse shape discrimination technique has significantly higher identification probability compared to pulse height discrimination and does make an interdetector scatter detection feasible.”

Measurements of DOI on a detector made of GSO/LSO/BGO/CsI(Tl) coupled to an APD using the PSD technique is reported in [82] and results confirm the feasibility of PSD DOI encoding with APD for PET.

Another simple technique for determining the depth of interaction is that of using a block of multistage crystals instead of a single one. This technique [145] “exploits the difference in the index of refraction between adjacent scintillator segments and the compound optically coupling them to induce discrete and resolved photopeak pulse heights depending on the segment of interaction of γ -rays.” This approach has the advantage of using only one type of crystal and results show that three segments connected with a clear glue can be resolved without any problem. Further tests on this depth of interaction encoding technique have been performed by Murayama et al., from Hitachi Chemicals Co. and Hamamatsu Photonics [146]. They designed and evaluated a detector unit consisting of four crystal blocks in a 2x2 array coupled to a position-sensitive photomultiplier tube (PS-PMT 4x4 multi-anodes). Each crystal block consists of three stages of 2x2 GSO arrays. Results from the tests showed a good positioning performance of incident photons.

Another, completely different approach aiming to identify the depth of interaction (DOI) is that implemented in a detector module that consists of an array of LSO crystals coupled on one end to a photomultiplier tube and on the opposite end to an array of silicon photodiodes [85, 86] (see also Section 11.2.2.4). Previous studies of this approach are reported in [147]. The investigation on the calibration of such detectors for the measurement of the DOI via an analog ratio is reported in [148]. Two methods were investigated and both are viable options for *in situ* calibration.

An approach similar to the previous one but using two photomultipliers at both ends of the crystals instead of a photodiode has been investigated by Shao et al. [149]. The detector module consists of a position-sensitive PMT (PS-PMT) at one end of an LSO multicrystal array for positioning and timing, and a PMT coupled at the other end through bent optical fibers (at 90°) with the ratio of the two signals to determine the DOI. Both PS-PMT and PMT can provide high signal-to-noise ratio outputs which improve DOI resolution. DOI measurements showed a resolution ranging from 4.2 to 6 mm, and the crystal identification and coincidence timing performance were excellent. The light loss due to fiber bending was less than 10%.

11.2.3.3 Spatial resolution

Detector blocks and PET devices with less than 1 mm resolution have been built and tested on small animals. Most recently, at the Nuclear Science Symposium and Medical Imaging, in October 24-30, 1999 the results of a small-animal PET with 1 mm resolution were presented [150]. Although the design is not optimized, because it used single ring of LSO crystals of 1 mm x 4.5 mm x 5 mm, it has demonstrated the feasibility of imaging at 1 mm. The crystal thickness of 5 mm and the small field of view cannot provide good count rate efficiency.

Another design of a PET with $\frac{3}{4}$ mm resolution was made by McIntyre [151] using plastic scintillators.

11.2.3.4 Sensitivity or count rate (hazard to the patient)

Unfortunately, when we look at the evolution of the new PET detectors with regard to this very important feature, we observe that increasing the sensitivity (which means lowering the hazard for the subject being tested) is not the first priority these days. The fact is that crystals of lesser stopping power are being phased into use. From a 30 mm crystal thickness of the PET manufactured 10 years ago by Positron, General Electric and CTI/Siemens, etc., which provided a stopping power close to 100%, we see that nowadays PETs, such as the ECAT HRRT and MicroPET by CTI/Siemens, have crystals with only 15 cm and 10 cm thickness respectively. The new GSO HEAD PENN-PET also has crystals only 10 mm thick.

11.2.4 PET detector assemblies using a continuous crystal

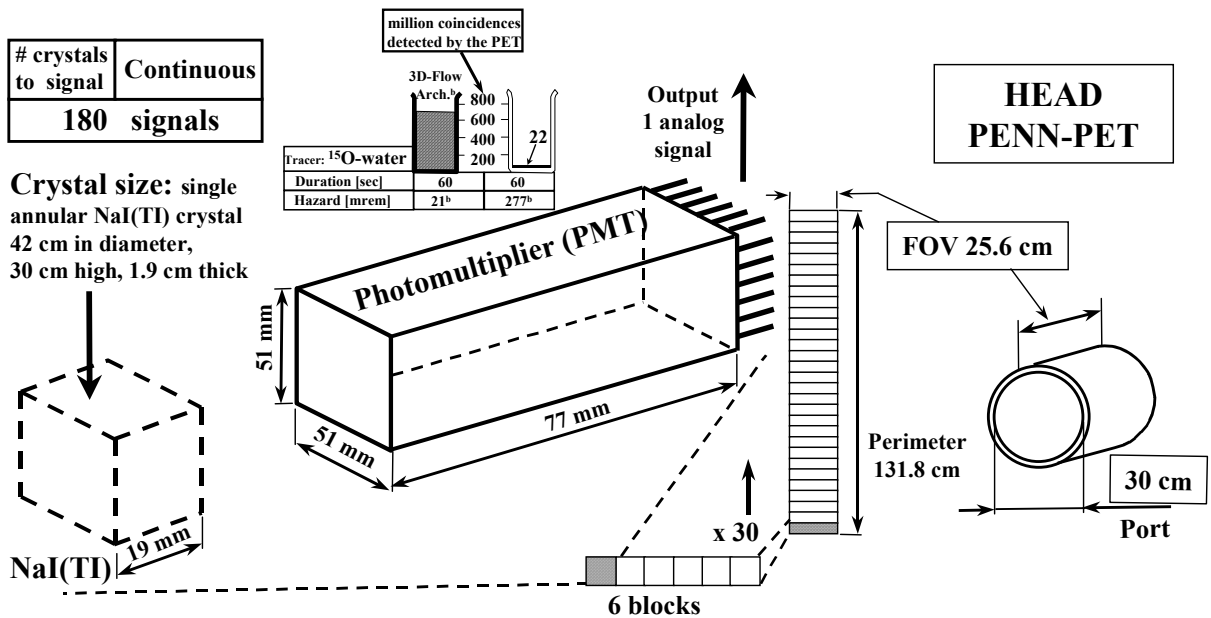
11.2.4.1 NaI(Tl) coupled to PMT (HEAD PENN-PET)

The HEAD PENN-PET scanner [37, 152, 153] with a patient port 30 cm in diameter and a field of view (FOV) of 25.6 cm is built of a single annular NaI(Tl) crystal 42 cm in diameter, 30 cm high, and 1.9 cm thick (see Figure 11-13). Using 2-inch photomultipliers coupled through light guides to the external side of the annular ring, only 180 PMTs convert the scintillating light in the annular crystal and send 180 signals to the readout electronics.

11.2.4.1.1.1 Performance measurements on HEAD PENN-PET

The system spatial resolution is 3.5 mm in both the transverse and axial directions, in the center of the FOV.

Figure 11-13. Layout of the assembly of the continuous detector for the HEAD PENN-PET scanner.



A performance count rate capability of the HEAD PENN-PET measurement is reported on page 640 of reference [37]. Using the NEMA protocol with 1.1-liter and 2.5-liter phantoms, at about 0.7 mCi ¹⁸F-FDG activity, the total detector singles counting rate is 7 Mcps. The coincident counting rate is about 600 kcps for the 1.1-liter phantom and 500 kcps for the 2.5-liter phantom, before energy gating. After energy gating, but without processing deadtime, the coincident counting rate of valid events drops to 240 kcps for the small phantom and to 200 kcps for the large phantom since the energy gate accepts only 40% of coincident events at this rate. With the current hardware of the HEAD PENN-PET, it is stated in the same article that the processing of coincident events saturates at 500 kcps. At 0.7 mCi, the processing deadtime, together with the energy gating requirements, results in a final event rate of 150 kcps for the 1.1-liter phantom and 135 kcps for the 2.5-liter phantom. After scatter and randoms subtraction, the true event rate is 100 kcps for the small phantom and 70 kcps for the large phantom. It is further stated that this activity of

100 keps corresponding to 0.7 mCi FDG in a 1.1-liter phantom represents a reasonable limit of the activity of the system.

Article [37] on page 637 points out the limits in sensitivity (count rate capability) of the HEAD PENN-PET scanner, stating, “A disadvantage of a small-diameter brain system such as ours, particularly a three-dimensional imaging system, is the lower counting rate performance compared to a large-diameter system, due to effect of dead time and randoms It will not offer optimal performance for ¹⁵O-water studies, which often require bolus injection with high initial activity.” The same article states, at page 641 that besides the detector dead-time, the inefficiency is also due to electronics which does not have digital signal processing [154] on each channel and fast signal correlation with neighboring channels. The coincidence triggering system also introduces dead-time [155].

Reference [153] Section 3 states “The count rate performance is a combination of the detector limitation as well as the electronic limitations.” The ‘local centroid’ method [112] for the calculation of the local energy and local position used in this detector is the ideal algorithm to be used with the 3D-Flow architecture, where the communication between neighboring crystals allows the rapid exchange of information with North, East, West and South (see Section 13.4.8).

Compared to the previous model PENN-PET 240H, this new model has the diameter of the ring reduced from 84 cm to 42 cm, the number of PMTs (2-inch photomultipliers) reduced from 240 to 180, the field of view increased from 14 cm to 25.6 cm, and the crystal thickness decreased from 2.5 cm to 1.9 cm (to improve the spatial resolution, even though this also reduced the detector sensitivity by about 30%). The total sensitivity increased by a factor of three, due to the larger FOV and smaller diameter.

11.2.4.2 Design of the LSO coupled to PMT (Animal PET-UCLA)

The UCLA group, as well, has designed a “continuous” detector for a high-resolution animal PET system [101] with the following characteristics: a patient port 16 cm in diameter and a field of view (FOV) of 15 cm is built of 7 blocks (150 mm x 76.2 mm). Each block is coupled to two square photomultipliers (76.2 mm x 76.2 mm).

Figure 11-14 shows the layout of the continuous detector for animal PET. The expected transaxial and axial resolution was less than 2 mm.

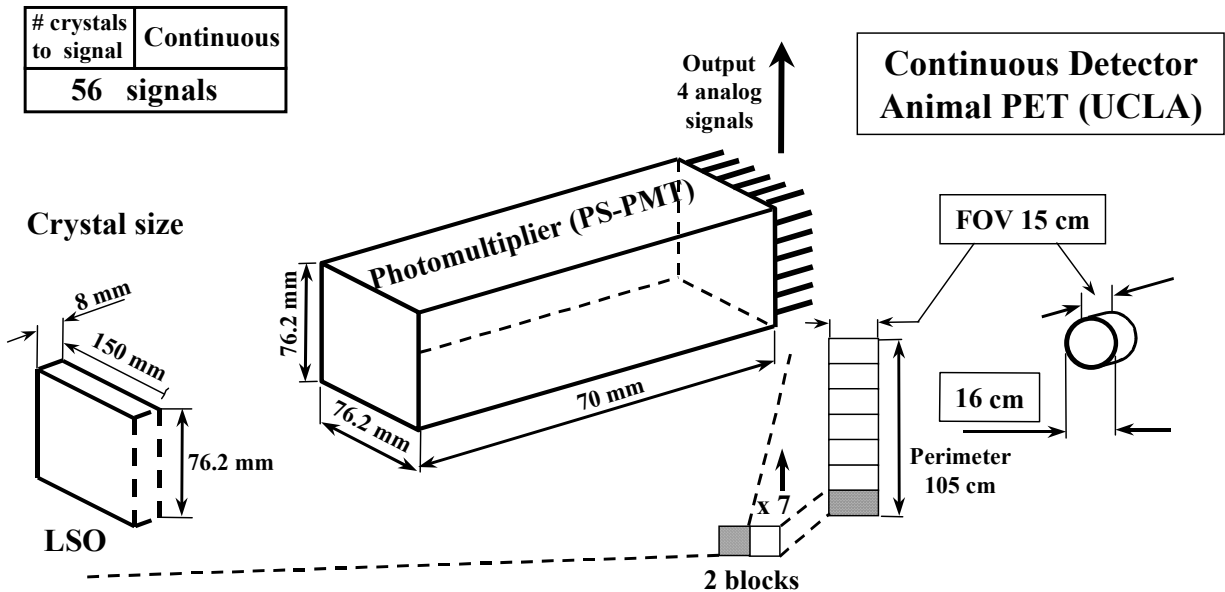


Figure 11-14. Design of the layout of the assembly for the continuous detector for animal PET (UCLA)

11.3 The need for flexible and performance electronics for extracting and improving the characteristics of low-cost detector modules

The previous Section shows that during the past number of years there has been an excellent development of detectors for PET.

What the facts do not show is the development or construction of digital multichannel systems at low cost which can extract and improve the characteristics of the detector. The 3D-Flow architecture is an architecture that provides these capabilities. It can provide at low cost digital signal processing on each channel with correlation with the neighboring signals. This will allow the characteristics of the detectors to be fully extracted and improved. Details of how this is accomplished is described in the following Sections.

12 The 3D-Flow architectural approach

12.1 DSP functions with neighboring signal correlation capabilities

12.1.1 Extending the execution time in one pipeline stage

The real-time algorithm in High Energy Physics (HEP) and in PET/SPECT/CT requires the performance of a sophisticated analysis on the input data produced at high rate to identify particles optimally.

The designers of electronics for the fast real-time algorithms in HEP or PET/SPECT have attempted to achieve the above goal by using cable logic circuits, fast GaAs technology, and fast memories. All these solutions have assumed that the processing time in one pipeline stage may not exceed the time interval between two consecutive input data.

In the above application as well as in others, however, it is desirable to extend the processing time in a pipeline stage.

The 3D-Flow system [156, 157] introduces a layered structure of processors and an intrinsic bypass switch in each processor that can extend this processing time in one pipeline stage. Each 3D-Flow processor in “Stage 3” (St_3 in Figure 12-1) executes the complete task of the real-time algorithm just as a computer in a large computer farm executes a complete task on a set of data. There is no division of the fast real-time algorithm into small steps, each executed by a different processor (or circuit) as would have been the case in a normal pipelined system.

If, for example, the time to execute the algorithm is four times the interval between two consecutive input data, the processor of the first layer fetches one set of data from the top port connected to the sensors and (without processing them) moves the following nine sets of data to the subsequent layers via a bypass switch intrinsic to each 3D-Flow processor (See Figure 12-3). The processor in the second layer will fetch one datum, move one result received from layer one and move eight input data received through layer one to the following layers through the internal bypass switches, and the process will continue in this way to parcel out the data.

Thus, the key element of the 3D-Flow system that serves to extend the processing time beyond the time interval between two consecutive input

data is the intrinsic bypass switch on each processor which allows a

parallel flow of layers.

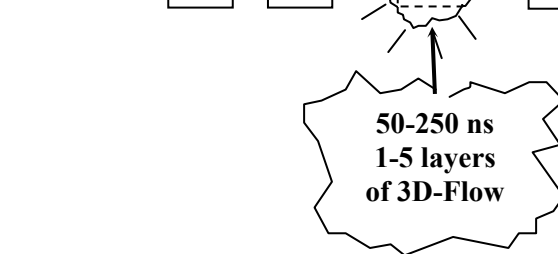


Figure 12-1. One pipeline stage needs to have the processing time extended. The electronics of Stage 3 (St_3) consists of several layers of 3D-Flow processors called a “stack.” Each 3D-Flow processor executes the entire real-time algorithm. Programmability has been achieved, and ultra-fast cable logic implementation is not necessary. An intrinsic bypass switch in each 3D-Flow of the stack performs the function of routing the incoming data to the first idle processor.

12.1.2 The intrinsic bypass switch in each 3D-Flow processor

Input data and output results flow from the top layer to the bottom layer of a stack of the 3D-Flow system as shown in Figure 12-3. The system is synchronous. The first layer has only input data at the top port which are received from the sensors, while the bottom layer has only results at the output port.

In the example of a 3D-Flow system shown in Figure 12-2, every eight clock cycles a new set of data (identified in Figure 12-2 as i1, i1; i2, i2, i3, i3, etc.) is received by layer 1 of the 3D-Flow processor stack. In the same example, each processor requires 24 cycles to execute the indivisible real-time algorithm.

The column of the table of Figure 12-2 labeled “switch status #34, #35” shows the position of the switches of the processors in layer 1, layer 2, and layer 3 respectively. The processors in layer 2 have the internal switches in the open position allowing input/output to the processor. This is called position ‘i’. The internal switches in layer 1 and layer 3 processors are in the closed position, blocking entry to the processor and moving data from the top port of the processor to the bottom port through a register ‘R’ and the bypass switch without processing them. This position of the switches is called position ‘b’.

In the example, the first set of data (i1, i1) is fetched from the processors in the first layer via the internal switches set in position ‘i’. Upon entry of the data into the processor, the internal switches are set in position ‘b’. The second set of data received at layer 1 at the clock cycle 9 and 10 is moved via the internal switches in position ‘b’ to the processors at layer 2, which are in position ‘i’ and free to start the execution of the algorithm. The data received at cycle 17 and 18 are moved to layer 3 via the internal switches in position ‘b’ of layer 1 and layer 2, these layers being occupied in processing the previous data. When the internal switches of the processors at layer 1 are set in position ‘i’ at clock cycles 25 and 26 as the new set of data are fetched by the processors at this layer, the results of the processing on the previous set of data on the same

layer are sent to layer 2 to be moved to the last layer of the 3D-Flow system.

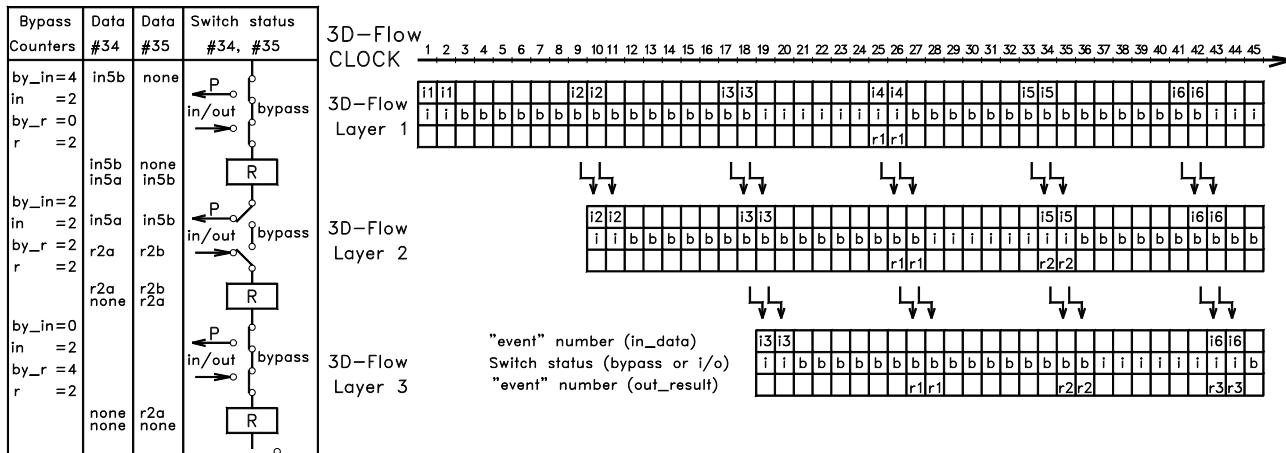


Figure 12-2. The flow of the input data and output results in a 3D-Flow system. The example shows a 3D-Flow system executing an algorithm that requires three times the time interval between two consecutive input data where the input data rate is 1/8 the processor clock frequency. The left column of the table at the left shows how processors at each layer count the input data, bypass data, results, and bypass results in order to set the bypass switches appropriately at the processors at each layer. An example of the position of the bypass switches for clocks #34 and #35 is shown in the other columns of the table.

At each clock cycle the data not processed by the processor, but only moved from the top port to the bottom port through the bypass switches are also buffered into a register 'R' as shown in Figure 12-2. Thus for each clock cycle a datum advances into the "flow" from the first layer of processors to the last layer, one layer at a time. This technique simplifies the hardware construction in allowing implementation of a 3D-Flow system made of a variable number of layers. The hardware simplification results from data at the bottom port being registered and the propagation delay of the signals (traces, register setup time, etc.) needing only to be satisfied between two adjacent layers. This is independent of the total number of layers of the system.

The table to the left of Figure 12-2 shows how the processors at each layer count the input data, results, bypass data, and bypass results

12.2 A single type of circuit for several algorithms

The overall architecture of the front-end electronics for the PET will be based on a single type of circuit, the 3D-Flow Processing Element [158] (PE), consisting of fewer than 100K gates. It is technology independent and is replicated several times in a chip, in a board, and in a crate. Implementation with the current technology of 0.25 μm which has a gate count of $\sim 30\text{K}$ gates per mm^2 requires about 3 mm^2 of silicon per PE. A chip accommodating 16 PEs requires a silicon area of about 25 mm^2 in 0.18 μm technology (leading to a chip @ 1.8 Volt, 672-pin FineLine BGA, 2.7 cm x 2.7 cm), dissipating only 23 nW per gate per MHz.

The 3D-Flow processor is essentially a Very Long Word Instruction (VLIW) processor. Its 128-bits-wide instruction word allows concurrent operation (up to 26 in one cycle) of the processor's internal units: Arithmetic Logic Units (ALUs), Look Up Table memories, I/O buses, Multiply Accumulate and Divide unit (MAC/DIV), comparator units, a register file, an interface to the RS-232 serial port used to preload programs and to debug and monitor them during their execution, and a program storage memory.

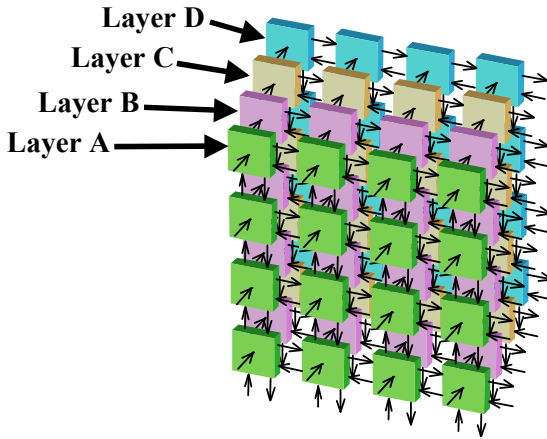
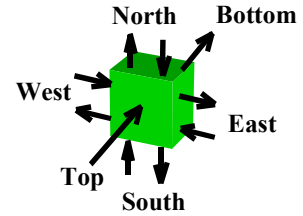
The high-performance I/O capability is built around four bi-directional ports (North, East, South and West) and two mono-directional ports (Top and Bottom). All of the ports can be accessed simultaneously (in data-driven or in polling mode) within the same clock cycle. N, E, W, and S ports are used to exchange data between processors associated with neighboring processing elements executing the same task. The Top port receives input data and the Bottom port transmits results of calculations along successive layers.

A built-in pipelining capability (which extends the pipeline capability to the system) is realized using a "bypass mode," in which a processor will ignore data at its Top port and automatically transmit it to the Top port of the processor in the next layer.

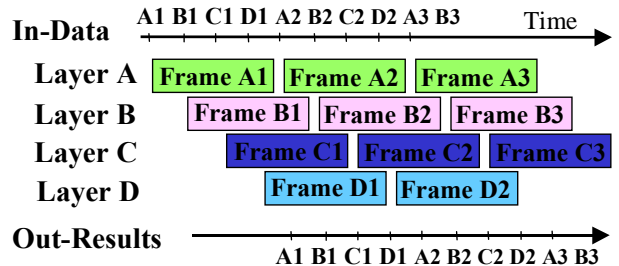
This feature thus provides an automatic procedure to route the incoming events to the correct layer.

Architecture (processor and system)

- **Modularity** (the same “logical unit,” the 3D-Flow PE, replicated several times -- in a chip, on a board, or on a system)
- **Powerful I/O**



No glue logic interface or MUX I/Os needed between SOC components



Pipelining of either partial or entire task (on a frame) if the algorithm cannot be partitioned (essential when the task needs to communicate with neighboring processors or due to the nature of the algorithm [e.g., presence of branches])

Figure 12-3. The 3D-Flow architecture based on a single type of circuit (PE). The left section of the figure shows a “stack” of 3D-Flow processors made of several layers, the right section of the figure shows the timing of a) the input data, b) the task executed by different layers and c) output results.

The goal of this parallel-processing architecture is to acquire multiple data in parallel (up to the clock speed of the technology implementation) and to process them rapidly, accomplishing digital filtering on the input data, pattern recognition, data moving, and data formatting.



The compactness of the 3D-Flow parallel-processing system in concert with the processor architecture allows processor interconnections to be mapped into the geometry of sensors (such as detectors in HEP or PET/SPECT in medical imaging) without the need of glue logic and without large interconnection signal delay, enabling real-time pattern recognition. To maintain scalability with regular connections in real time, a three-dimensional model was chosen, with one dimension essentially

reserved for the unidirectional time axis and the other two as bi-directional spatial axes (Figure 12-3 left).

The system architecture consists of several processors arranged in two-orthogonal axes (called layers; see Figure 12-3 left), assembled one adjacent to another to make a system called “stack.” The first layer is connected to the input sensors, while the last layer provides the results processed by all layers in the stack. Data and results flow through the stack from the sensors to the last layer

12.3 A single type of component for several algorithms

The basic 3D-Flow component shown in Figure 12-4 has been implemented in a technology-independent form and synthesized in 0.5 micron, 0.35 micron technology, and in FPGA’s Xilinx, Altera and ORCA (Lucent Technologies). The most cost-effective solution is to build the 3D-Flow in 0.18 μm CMOS technology @ 1.8 Volts, accommodating 16 3D-Flow processors with a die size of approximately 25 mm², and a power dissipation [gate/MHz] of 23 nW. Each 3D-Flow processor has approximately 100K gates, giving a total of approximately 1.7 million gates per chip. As the technological performance increases, so can the multiplexing of the I/O increase. For example, the (8+2):1 of the LVDS serial links can increase to 16:1 or (16+2):1 when the LVDS serial link speed reaches 1.2 Gbps or higher. (Please see the Web site of LSI-Logic as an example of technology currently available: <http://lsilogic.com/products/PRchart.html> and [../unit5_2.html](http://lsilogic.com/unit5_2.html)).

-  One 3D-Flow PE = 100K gates
 3D-Flow Chip = 16 PEs

Die Size:

0.35 μm has a gate count of ~ 14000 per mm^2
 0.25 μm has a gate count of ~ 30000 per mm^2
 0.18 μm has a gate count of ~ 65000 per mm^2

16 PEs in 0.25 μm technology can easily fit into the cavity of a 672 BGA FineLine package

Power Dissipation:

from 0.35 μm to 0.25 μm is three times less
 from 0.25 μm to 0.18 μm is ten times less
 (e.g., LSI-Logic Power Dissipation measured in Gate/MHz is: G10-0.35 μm = 700nW, G11-0.25 μm = 250nW, G12-0.18 μm = 23nW)

Basic Element: the 3D-Flow PE

- up to 26 operations per cycle
- Technology independent
- Scalable

The 3D-Flow approach allows the user to:

- **Select** the technology and the number of PEs per chip
- **Verify** quickly from system-level algorithm to gate-level by means of the **Design Real-Time** tools which **interface with third-party** Electronic Design Automation (**EDA**) tools.

See also: 3D-Flow System Monitoring
(for troubleshooting and software repairs during run-time)

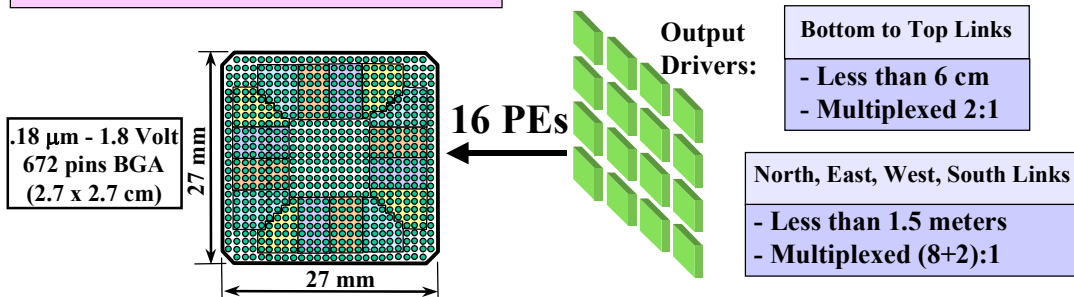


Figure 12-4. Technology independent 3D-Flow ASIC

12.4 Versatility and flexibility of the 3D-Flow systems to different types of PET/SPECT/CT detectors

The 3D-Flow system is versatile and will accommodate the interface to different types of “block” or “continuous” detectors and to different types of real time algorithms to identify the energy of different photons 60 keV (x-ray), 140 keV (SPECT) and 511 keV (PET), and to recognize photopeak from scattered events. The interface is also very simple because, after the assignment of a function to each of the 64-bits, it requires only that the information (digital or analog converted to digital) are sent every 50 ns to each 3D-Flow channel of the system. The bits in that word may carry the information from several different subdetectors (photomultipliers, photodiodes, avalanche photodiodes, etc.), and the program on the 3D-Flow system allows them to be manipulated and correlated with neighboring signals.

13 Design of a multimodality PET/SPECT/CT 3D-Flow based system

13.1 Description and requirements of a multimodality PET/SPECT/CT device

The combination of several medical imaging modalities in a single device is referred to as multimodality. It helps the physician in clinical examinations to see in a single image several pieces of information which before could only be acquired by having the patient go through several medical examinations.

The combination of the PET device with an x-ray-computed tomograph (CT) scan provides, by means of the CT, the anatomical information that helps to identify the organs in the body, and it provides, by means of the PET, the functional information that provides real-time imaging of the biological process at the molecular level. (In some area, such as the one showing increased brain activity caused by sensorimotor or cognitive stimuli, functional Magnetic Resonance Imaging (fMRI) , shows image contrast in regions where oxygen is highly extracted from blood by using the property that oxyhemoglobin is a strongly paramagnetic molecule. However, MRI is mainly anatomical, while PET is only functional and the best for oncology studies [40]).

The Single Photon Emission Computed Tomography (SPECT) medical imaging device uses tracers emitting a single photon, and thus requires a collimator placed in front of the crystals that acts like a lens in an optical imaging system. One way to implement a collimator is to have multiple parallel (or converging) holes in lead material allowing the photons travelling with the desired acceptance angle to pass through the holes to interact with the crystals. The dominant factor affecting image resolution in SPECT is the collimator [130] (section IV).

The PET functional device has clear advantages over the SPECT and the dual-head camera. A dual-head camera (which can have SPECT and PET capabilities), instead of a full ring of detectors, has only two modules of detectors (or heads) on the two sides of the subject (the body of the patient) who had received a radiotracer by injection or inhalation. Thus, the dual-head camera has a limited detector area capable of capturing the emitted photons. The comparison between PET, SPECT and dual-head cameras has been made in reference [159]). The advantages of the PET result from its technique of the electronic collimator detecting two photons emitted in opposite directions at the same instant, as opposed to the SPECT technique of the hardware lead collimator.

It is possible to combine PET and SPECT in a single multimodal device which has several parts in common (detector, mechanics, electronics) while the complexity of the electronics increases only slightly. However, the use of a lead septa as collimator between the patient and the detector will require the construction of a PET system which is larger in diameter. This will introduce a longer path to the photons before reaching a detecting element, which, in turn, will require a longer coincidence time window. This increases the possibility of acquiring multiples (see Section 13.4.5.2), and thus lowers the device efficiency. The need to build a PET/SPECT detector with a larger diameter to accommodate the septa will also increase the cost, because it requires a larger volume of crystals and a larger number of photomultipliers (PMT), or avalanche photodiodes (APD) and electronic channels.

For the reasons stated above, the PET with CT capabilities should be the first choice and should be targeted to hospitals that will use the device for cancer screening. The only justification for using a SPECT would be the types of examination that require the use of a tracer (such as Technetium Tc 99m Mebrofenin for hepatobiliary, Sestamibi, a myocardial perfusion for detecting coronary artery disease, Mertiatide renal imaging agent, or Albumin aggregated lung imaging agent) different from the ones emitting photons at 511 keV (such as ^{18}F -FDG, ^{13}N , ^{11}C , ^{15}O , and ^{82}Rb), because the latter ones do not allow the physician to perform the kind of specialized examination that might be required for specific conditions. In that case, the choice of SPECT would be dictated not by the lower cost as is the case today, but because of the overriding need for some specialized examinations, even though it may require a higher radiation dose and a higher cost.

The same electronics described herein for PET/SPECT/CT could be used for the PET/CT. The 3D-Flow electronics system can detect all three photons during the same examination and separate them (60 keV from x-ray, 140 keV for SPECT and 511 keV for PET).

The PET/SPECT/CT imaging devices use the following techniques:

1. PET detects emission¹ photons at 511 keV. There exist fast and slow crystals suitable to detect photons at this energy. The most commonly used crystal in past PET devices was BGO, while the

¹ “Emission photons” refers to the photons emitted from a radiotracer (e.g.: ^{18}F -FDG, ^{13}N , ^{11}C , ^{15}O , and ^{82}Rb for PET examinations, or $^{99\text{m}}\text{Tc}$ for SPECT exams) delivered to the patient.

most recent PET use, or plan to use faster crystals such as LSO and GSO. (Detection efficiency of 25 mm BGO and LSO is about 90%, while 10 mm GSO is about 57%.).

2. SPECT detects emission photons at 140 keV. Several crystals such as BGO, NaI(Tl), LSO provide a detection efficiency close to 100% with a smaller crystal thickness of only 10 mm, compared with the detection of 511 keV photons, which require 25-30 mm crystal thickness (5 mm of CdZnTe can detect 140 keV photons with an efficiency of at least 80%).
3. CT operates on transmission X-rays at 60 keV transmitted from a tube or a high-intensity radionuclide rod source which is placed on the gantry on the opposite side of the detecting element, across the patient's body. Several crystals are suitable to detect 60 keV photons. This document will refer to tests performed on 3 to 10 mm thickness CsI(Tl) crystal.

13.2 Example of assembly of a PET/SPECT/CT device.

The detector should have an elliptical shape as proposed herein for the section along the body of the patient (instead of the current circular shape) in order to minimize the distance from the radiation source to the detector, and it should have a circular, smaller diameter for the section of the head.

Three or more crystals can be assembled (such as reported in Section 11.2.2.8.3, and reference [131]) in a single detector which detects photons from the three modalities PET/SPECT/CT.

Figure 13-1 visualizes the example of an assembly for the two modalities, PET and CT, in a single device. The additional SPECT functionality requires a lead collimator to be placed between the horizontal bars (holding the X-ray transmission source) which rotate along the elliptical torso ring and along the circular head ring and the detector (crystals). By changing slightly the size of the crystals, the entire gantry can become smaller (increasing the resolution and efficiency of the entire device), or larger in order to accommodate thicker lead collimators; however, the ratio between the number of crystals and the number of electronic channels should be kept as is because of its optimal match between channels per board and board per detector ring. In the entire document the additional provision of SPECT functionality is described and anticipated in the hardware implementation, although some figures

may display only the PET/CT devices (e.g. not displaying the lead collimator). The most important outcome of using only PET/CT devices, besides the lower cost in requiring a smaller detector, is the lower radiation dose to the patient, permitted by the higher efficiency of smaller detectors.

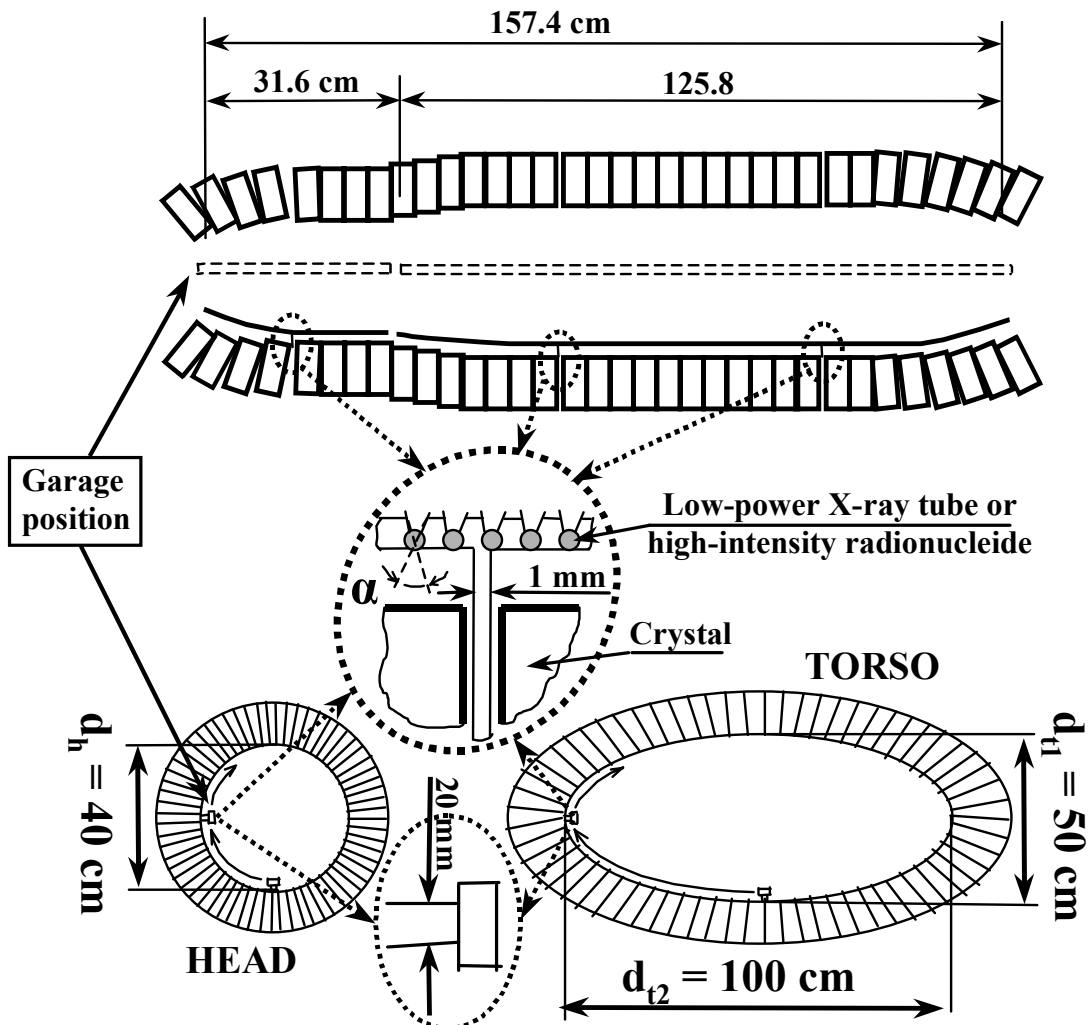
The top part of Figure 13-1 shows a longitudinal section (cut vertically) of the PET device. The inner crystals are 50 cm apart from top to bottom and 100 cm apart from left to right in the elliptical torso section (top right in the figure) and 40 cm apart in all directions in the circular head section (left in the figure). The longitudinal section of the brain and neck measures 31.6 cm accounting also for the sawcut of 2 mm in between the central rings of the head (as shown in the figure) to accommodate the movement of the X-ray transmission bar (128 rings times 2.45 mm of the crystal, which is the sum of 2.1 mm crystal plus 0.35 mm of material between crystals). The longitudinal section of the torso measures 157.4 cm, accounting also for the sawcut of two 2 mm in between the rings of the torso section (as shown in the figure) for the movement of the X-ray transmission bar (512 rings times 2.45 mm of the crystal, which is the sum of 2.1 mm crystal plus 0.35 mm of material between crystals).

The crystals at the extremities of the entire detector (which consist of a cylindrical barrel attached to an elliptical barrel) have an orientation of their longitudinal axis which minimizes their angle with the incident photons received from the patient's body. This is in order to facilitate the depth of interaction measurement. The two bars holding the X-ray transmission tube (or high-intensity radionuclide) shown on one side of the patient (the position called "garage") and on the bottom of the detector are attached to a support (similar to a metal blade of about 1.5 mm x 20 mm, see detail in the middle of the figure) and requires a cut of about 2 mm in between two rings of the gantry. The bar positioned along the length of the elliptical torso is attached in two places (as shown in the figure) by means of the metal blades described above to an apparatus at the external side of the gantry that provides the movement of the X-ray tube around the body of the patient of the elliptical torso and of the circular head detector ring.

Similarly, in the circular head detector ring, a metal blade, only one in this section, supports the X-ray transmission bar. In order to reduce the number of x-ray tubes required in the complete assembly, an angular movement (shown with the letter α in the details of the X-ray

transmission bar in the middle of Figure 13-1) of the tube allowing the transmission of X-rays to opposite detectors of the side rings can be provided. Alternatively, in the event a high-intensity radionuclide is used, the source is encapsulated in a source holder with a collimator and a shutter to control the transmission. The several rotations of the transmitting X-ray tubes (or high-intensity radionuclide) at several angles will cover the entire volume of the body.

Several solutions could accommodate the insertion and removal of a lead collimator for SPECT functionality. The solution of having a sector of lead collimator rotating inside the gantry, as it is proposed in some SPECT designs, is not advisable for two reasons: first, the elliptical gantry of the torso section will make rotation along the entire ring difficult and second, the efficiency in detecting photons is very low in the



at any
epend

nabled.
r of a
at one
e-like
e used

y in a
1 with
about
des a)
anics,
ne CT
e non-
ess of
age of
curate
on; f)
images
e PET

Figure 13-1. Example of an assembly of a PET/SPECT/CT multimodality device (lead septa that should be placed inside the detector between the crystals and the transmission bar, are not shown in the figure).

13.3 Mapping the 3D-Flow system into the PET/SPECT/CT imaging system.

Detectors of PET/SPECT/CT devices of different sizes and of different components (crystals coupled to PMT or APD, photodiodes coupled to crystals, solid state detectors, etc.) can be mapped to the 3D-Flow system.

The ratio of 256 crystals (or a single crystal of equivalent size in a “continuous” detector) coupled to a photomultiplier of 38 mm in diameter has been selected

1. based on the promising results by the tests performed by Andreaco and Rogers [98] in decoding 256 BGO crystals per block and not indicating that they had reached a limit in the number of crystals that could be decoded. The limit would be determined a) by the light emitted by the crystal, b) the S/N ratio, and the 3D-Flow capability to improve the S/N ratio with DSP processing.
2. based on the number of photomultipliers per detector area used in several PET built by Karp and co-workers on the “continuous” detectors (e.g., 180 PMTs were used in the HEAD PENN-PET with the ring of 42 cm in diameter and 25.6 cm FOV. See [37], Table 1-3, and Section 11.2.4.1). Each of the 2,304 PMT of the new PET proposal with 3D-Flow is coupled to an equivalent detector area.

In the event the light emitted by a certain type of crystal adopted in a particular PET design is not sufficient, or the S/N ration does not allow to decode 256 crystals, than the number of PMT and electronic channels can be multiplied by four and the 256 channels 3D-Flow DAQ-DSP board can be used at the place of the 64 channels. (The computation by the 3D-Flow DSP required for decoding 64 channels in place of 256 will be reduced, allowing each 3D-Flow to handle four electronic channels).

The Table 13-1 provides an example of the coupling of “block” detectors for PET/SPECT/CT with different FOV based on 64 crystals 4.55 mm x 4.55 mm coupled to a PMT of 38 mm in diameter, and 256 crystals 2.1 mm x 2.1 mm coupled to a 38-mm diameter PMT (about 0.35 mm is accounted for the space taken by the opaque reflector or the optical coupler placed in between the crystals). Slight increases or decreases in

the size of the entire PET/SPECT/CT device should preferably change the dimension of the crystals and the ratio between the number of crystals, while the number of electronic channels should be kept constant because of its optimal match between channels per board, and board per detector ring.

On Table 13-1, first the comparison is made between the current whole-body PET detectors [22, 23, 29, 19] made of about 12,000 to 18,500 crystals in a circular gantry to an elliptical gantry with the same field-of-view which shows a reduction in volume of crystals (thus reduction in cost) of about 12%. If the electronics proposed herein were to be installed in current PET with circular gantry, only 288 PMT 38 mm in diameter coupled to 288 electronic channels of five 3D-Flow DAQ-DSP and one 3D-Flow pyramid of IMB PC compatible boards would be necessary (see Figure 13-2). In the elliptical version of the same detector, only 256 PMTs would be required, coupled to four 3D-Flow DAQ-DSP boards and one 3D-Flow pyramid board.

Comparison has been made also between a PET detector with 157.4 cm FOV with a circular gantry of 96 cm in diameter versus one with the same FOV but with an elliptical gantry for the torso section 100 cm wide by 50 cm high. The elliptical shape of the torso section would save 20% in volume of the crystal.

The total number of crystals required for the elliptical version (each crystal having the dimensions of 2.1 mm x 2.1 mm) for a 157.4 cm FOV is 589,824; that for a crystal 25 mm thick is equivalent to a crystal volume of 65,028 cm³. Considering that crystals with slow decay time such as BGO have a cost of about \$10/cm³, the cost of the main components for the elliptical version of a PET (100 cm wide by 50 cm in height) is about \$650,280 for the crystals and about \$460,800 for the 2,304 PMTs 38 mm in diameter (assuming about \$200/PMT). Thus the elliptical version would require only 36 3D-Flow DAQ-DSP boards. This is to be compared with the cost for the circular version of the same PET, with a circular gantry (96 cm in diameter), which would cost about \$794,787 for the crystals and about \$563,200 for the PMTs, and would require 44 3D-Flow DAQ-DSP boards.

One implementation with a smaller FOV of 126 cm shown in Section 17.2 and Figure 17-4, using the elliptical implementation, requires only 458,752 crystals (2.1 mm x 2.1 mm) for a volume of 50,577 cm³ crystal (for 25 mm crystal thickness), and 1,792 PMTs. This implementation

would cost about \$505,770 for the crystals and about \$358,400 for the PMTs.

Another implementation that should demonstrate the significant advantages offered by the 3D-Flow architecture is the implementation of the PET/SPECT/CT device with a “continuous” detector with several layers of crystals arranged in annular rings of different types of crystals, one inside the other. Each layer would have a different decay time so that the 3D-Flow system could measure the depth of interaction. The “continuous” type of detector has proven [37] to be a viable solution. Moreover, the 3D-Flow architecture, because of its additional capability of detecting the head of a cluster corresponding to the location of the incident photon with great precision, allows reconstruction of the whole energy of the incident photon due to its elimination of the boundary limitation. This feature offers advantages compared to the electronics currently used and might greatly simplify the construction of PET/SPECT/CT detectors and save cost also in that area

Figure 13-2 shows the 3D-Flow system mapped to a PET detector, similar to those currently operating, with a ring of about 82 cm in diameter (or 56 cm in diameter of the patient’s port) and with a FOV of about 15 cm. Only five 3D-Flow DAQ-DSP boards and one 3D-Flow pyramid board would be required here. Section b) of the same figure refers to the column of the current circular gantry with 157.4 cm FOV of Table 13-1, and Section c) refers to the columns of the proposed new elliptical gantry with a FOV of 157.4 cm.

Table 13-1. Mapping the 3D-Flow system to current PET devices and future PET devices of different sizes with circular and elliptical gantry.

	Current Circular Gantry^a (PMT diameter = 38 mm)				Proposed New Elliptical Gantry Head Ring $d_h = 40$ cm (circular) Torso Ring $d_{t1} = 50$ cm; $d_{t2} = 100$ cm (ellipt.) (PMT diameter = 38 mm)			
- x and y dimensions of crystals are in [mm] (about 0.35 mm of opaque reflector or optical coupler is used between crystals)	15.6 cm FOV Ring $d = 82$ cm		157.4 cm FOV Head Ring $d_h = 40$ cm Torso Ring $d_t = 96$ cm		15.6 cm FOV		157.4 cm FOV	
	[number of crystals/PMT in a ring, PMT axial, crystals per PMT/ total PMT]	IBM PC boards [3D-Flow DAQ 64 ch./pyramid]	[number of crystals/PMT in a ring, PMT axial, crystals per PMT/ total PMT]	IBM PC boards [3D-Flow DAQ 64 ch./pyramid]	[number of crystals/PMT in a ring, PMT axial, crystals per PMT/ total PMT]	IBM PC boards [3D-Flow DAQ 64 ch./pyramid]	[number of crystals/PMT in a ring, PMT axial, crystals per PMT/ total PMT]	IBM PC boards [3D-Flow DAQ 64 ch./pyramid]
(4.55 x 4.55) head			16,348 cryst./ (32 x 8 x 64)/ 256 PMTs				16,384 cryst./ (32 x 8 x 64)/ 256 PMTs	
(4.55 x 4.55) torso	18,432 cryst./ (72 x 4 x 64)/ 288 PMTs	5 ^a /1	163,840 cryst./ (80 x 32 x 64)/ 2,560 PMTs	44/1	16,384 cryst./ (64 x 4 x 64)/ 256 PMT	4/1	131,072 cryst./ (64 x 32 x 64)/ 2,048 PMTs	36 ^b /1
(2.1 x 2.1) head			65,536 cryst./ (32 x 8 x 256)/ 256 PMTs				65,536/ (32 x 8 x 256)/ 256 PMTs	
(4.55 x 4.55) torso			163,840 cryst./ (80 x 32 x 64)/ 2,560 PMTs	44/1			131,072/ (64 x 32 x 64)/ 2,048 PMTs	36 ^b /1
(2.1 x 2.1) head			65,536 cryst./ (32 x 8 x 256)/ 256 PMTs				65,536/ (32 x 8 x 256)/ 256 PMTs	
(2.1 x 2.1) torso			655,360/ (80 x 32 x 256)/ 2,560 PMTs	44/1			524,288/ (64 x 32 x 256)/ 2,048 PMTs	36 ^b /1

^asee in Figure 13-2 the layout of 3D-Flow DAQ-DSP boards for current and old PET devices, the dimensions of the PET rings using current circular gantry, and the dimensions of the PET rings using the proposed elliptical gantry.

^bsee layout of 3D-Flow DAQ-DSP boards in Figure 17-2, and Figure 17-3.

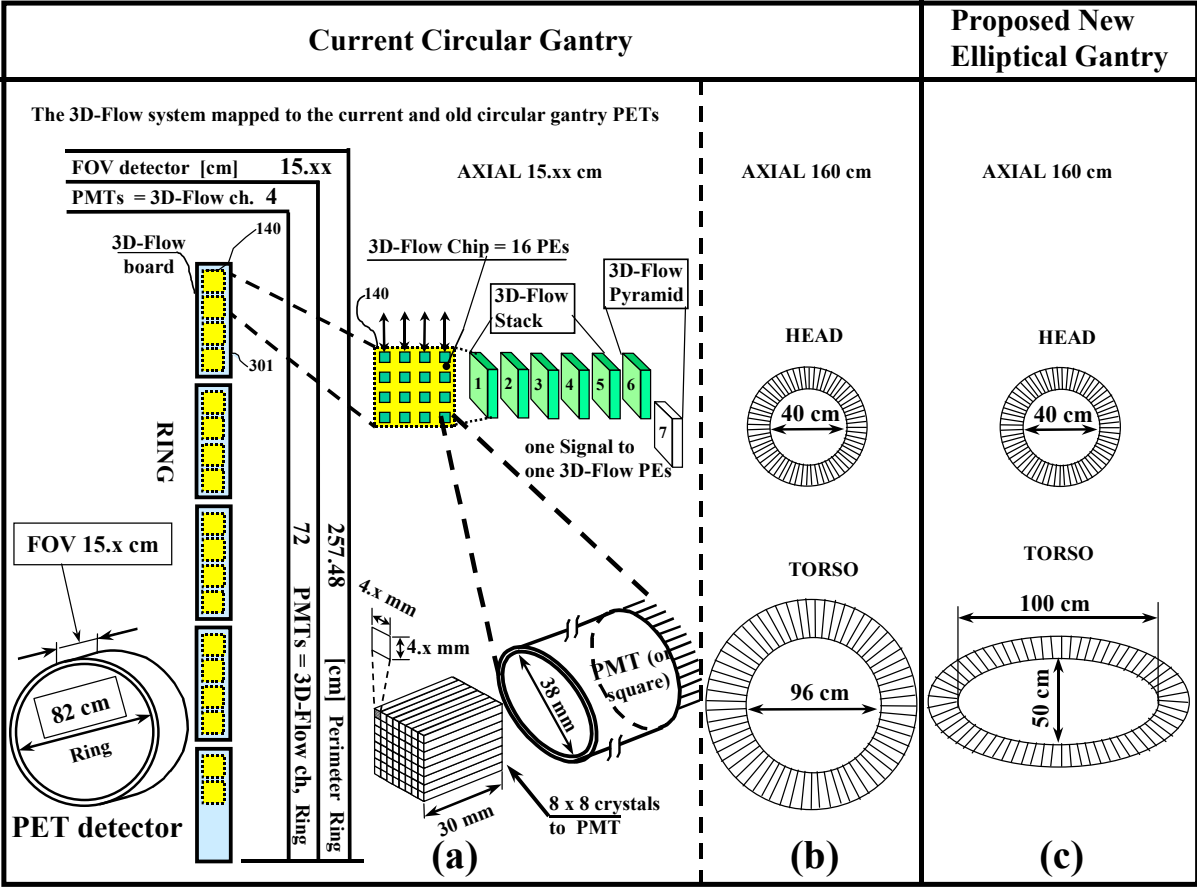


Figure 13-2. Mapping the 3D-Flow system into PET imaging system. Section a) shows the layout of the 3D-Flow electronics for current and old PET devices, b) shows the dimensions of the PET rings using current circular gantry, and c) shows the dimensions of the PET rings using the proposed elliptical gantry.

13.4 Solutions provided by the 3D-Flow system to the PET/SPECT/CT requirements

Electronics can be subdivided into two sections: one section, applicable to PET, SPECT, and X-ray instruments, identifies the particle and its characteristics (energy, position, timing, type, etc.) by means of a thorough analysis of the signal(s) produced by the incident photon. Another section, applicable to the PET device only, detects the coincidences.

13.4.1 Latency time through the entire system

An overview of the entire electronic system with the functionality of the different sections, the flow of the data through all of them from the input from the detector to the output for CT, SPECT and PET is shown in Figure 13-3.

The entire electronic system is synchronous and has a fixed time latency from the input data to the output results. While the time latency between data at different layers of the 3D-Flow system remains fixed during the photon identification operation (executed in the 3D-Flow DAQ-DSP boards, see Section 13.4.11) which is the only operation required by the CT and SPECT functionality, the additional coincidence detection function required by the PET functionality of the device, with the flow of the data through different paths of the pyramid (see in Figure 13-3 the second column from the left) introduces a variable time latency between data at different layers. The fixed time delay is regained before the data reach the coincidence circuit, as described in Section 13.4.14.1 and shown in the third column from the left in Figure 13-3.

The coincidence circuit stage is operating in synchronous mode on data sorted at a fixed latency time and in the same sequence as they were when received from the detector, just as it was operating the previous stage of the photon identification of Section 13.4.11. As before, at this stage also it is offered the provision to implement a second stack (with fewer channels) of 3D-Flow processors similar to the one implemented for the photon identification, in the case where the algorithm (comparisons and photons parameters checking) requires an execution time longer than the time interval between two consecutive input data at that stage.

The last column to the right of Figure 13-3 shows the operation performed for the coincidence detection required by the PET operation mode.

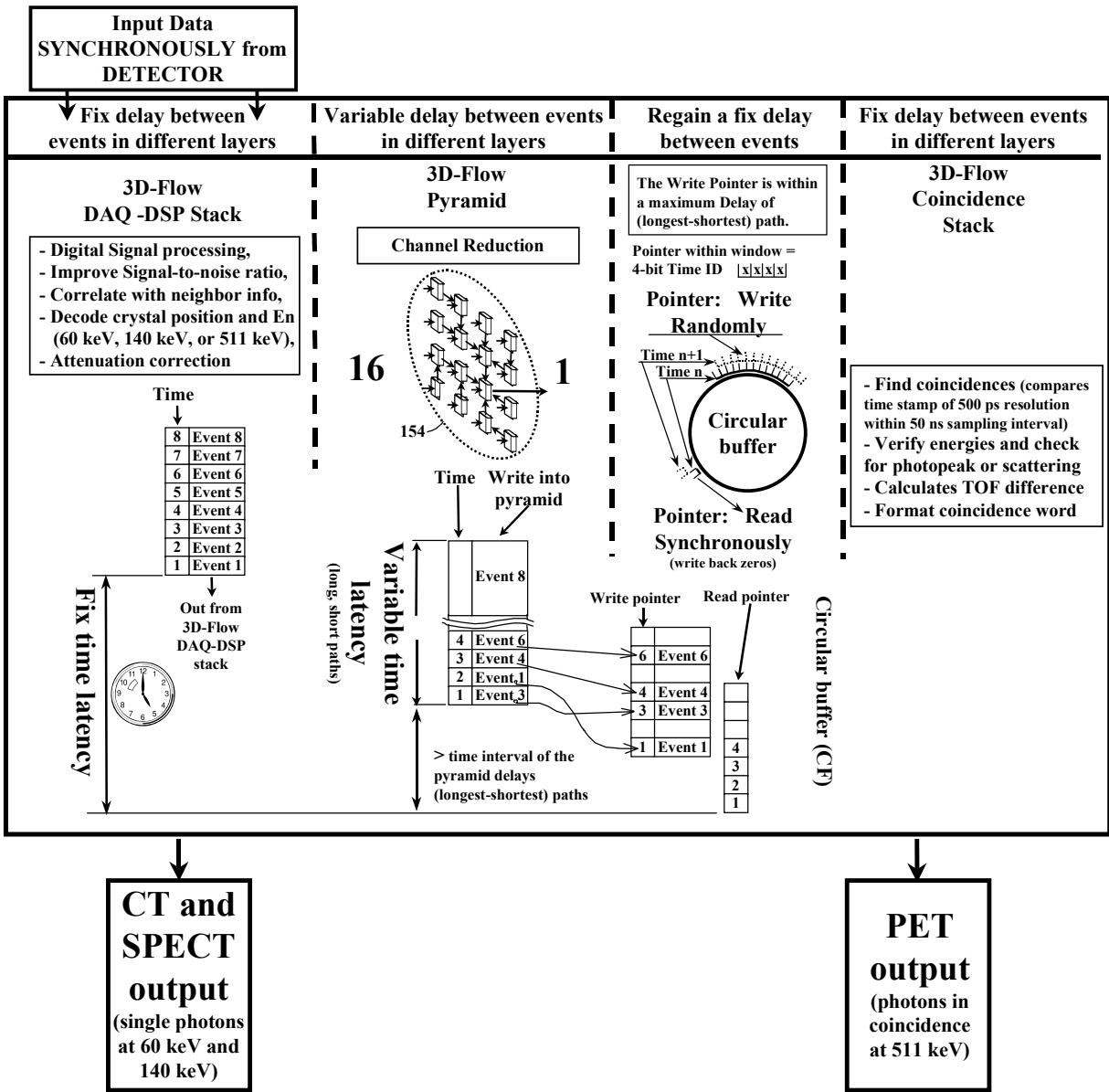


Figure 13-3. Time latency between data at different layers of the 3D-Flow system.

13.4.2 Ascertaining that the 3D-Flow system provides sufficient input bandwidth

The sampling rate of the detector signals every 50 ns seems reasonable for a maximum rate of about 105×10^6 single photons that can potentially hit the detector at start of scanning, 20 seconds after an injection of 5 mCi radioactive source dose is delivered to the patient (e.g., ^{15}O -water which is equivalent to 21 mrem effective dose equivalent to the patient. See Section 14.3 and Figure 14-1 for the calculation of the input data rate of photons to the detector for a specific delivered dose of radioactive source to the patient).

The calculation of the maximum rate of single photons hitting the detector for 5 mCi ^{15}O -water, 20 seconds after injection, is the following: The 10/12 of $(5 \times 37 \times 10^6 \times 2)$ single photons per second activity, 20 seconds after delivery of 5 mCi of ^{15}O -water, reduced to 39% single photons (equivalent to about 15% pairs of photons in coincidence as shown in Figure 14-1) leaving the patient's body, reduced to 95% FOV efficiency and 92% solid angle efficiency, provides $(10/12 \times 370 \times 10^6 \times 39/100 \times 95/100 \times 92/100) = \sim 105 \times 10^6$ single photons per second hitting the detector. A higher rate of photon emission by the radioactive source would require delivery to the patient more radiation. This is not recommended for even a short half-life radioisotope such as ^{82}Rb or ^{15}O -water, which have half-life times of 75 seconds and 124 seconds respectively.

At the above maximum rate, each crystal out of the total of 589,581 crystals of the detector would have a 0.00089% probability of being hit by an incident photon every sampling period of 50 ns. Each PMT out of the total 2,304 PMTs of the detector will have a 0.22% probability of receiving the signal of an incident photon to the detector every sampling period of 50 ns.

The architecture of the 3D-Flow (See Section 12) with the capability of extending the processing time beyond the time interval between two consecutive input data, allows each processor to execute the entire real-time algorithm (See Section 13.4.11) at each of the PMT channels thus providing zero dead-time with 100% capability to sustain one signal per channel every 50 ns.

This calculation should be persuasive evidence that the 3D-Flow system has been dimensioned with sufficient bandwidth at the input stage so that bottlenecks will not occur at the predicted radiation activity.

13.4.3 Two examples of detectors: crystals with fast and slow decay time

The following section describe all the functionality required by a PET/SPECT/CT system and the requirements are addressed one by one and a solution provided by the 3D-Flow system is described.

Two examples are presented for two different types of applications (see Figure 13-4):

1. one which makes use of more expensive, faster crystals with short decay time, for which analog integration would seem to be appropriate; and
2. one which makes use of more economical crystals with a longer decay time, for which a digital signal integration would be appropriate.

The analog integration of the signal for example 1 using fast crystals (with a decay time shorter than 40 ns) has been suggested in this application in the event it is intended to use the 3D-Flow processor at the relatively low speed of 80 MHz. This avoids exotic and more expensive electronics which would be required at higher speed.

However, if it is desired to solve all problems digitally, the speed of the 3D-Flow processor in example 1 can be increased by a factor of 2. In this way the 3D-Flow processor clock period of 6.25 ns will guarantee the execution of a few instructions and a few samplings during a 40 ns detector signal. By doing so, the same approach described for example 2 could be applied for example 1.

Along with the signals from the photomultipliers (or APD) coupled to the crystals (or, more generally, any gamma converter), the 3D-Flow system can acquire and process signals from any other sensors, such as photodiodes, VLPC, etc.).

Figure 13-4 shows two examples of the 64-bit word received by each 3D-Flow processor of one layer of the stack every 50 ns.

13.4.3.1 Example 1: interfacing between detectors with fast crystals and the 3D-Flow

Example 1 shows a 64-bit word carrying the information from four detector blocks made of fast crystals with short decay time (about 40 ns). Each detector provides three pieces of information: the time-stamp, the energy and the decay time.

The time-stamp (e.g., s_A in Figure 13-4) is the detection of a hit by the constant fraction discriminator CFD1 with short delay (see also Figure 13-5, Section 13.4.4.2, and Figure 13-6), which sends a logical signal to the time-to-digital (TDC) converter (see Section 13.4.10). The TDC produces a 7-bit time-stamp mapped in the 3D-Flow input word in bits 57-63.

The energy (e.g., E_A in Figure 13-4) is the peak of the analog signal from the shaper amplifier (see Figure 13-6), which is converted to digital and mapped into the 3D-Flow input word in bits 50-56.

The decay-time (e.g., d_A in Figure 13-4) is the difference between the time detected by the CDF2 after integration of the signal from the PMT (this time is proportional to the decay time of the crystal) and the previously detected time-stamp. The TDC produces the second time-mark, which is subtracted from the time-stamp of CFD1 and mapped into the 3D-Flow input word in bits 48-49 by the FPGA (see also Section 13.4.4.2, and Figure 13-6).

Similarly the information from the other three detector blocks are mapped into the remaining sections of the 3D-Flow input data word.

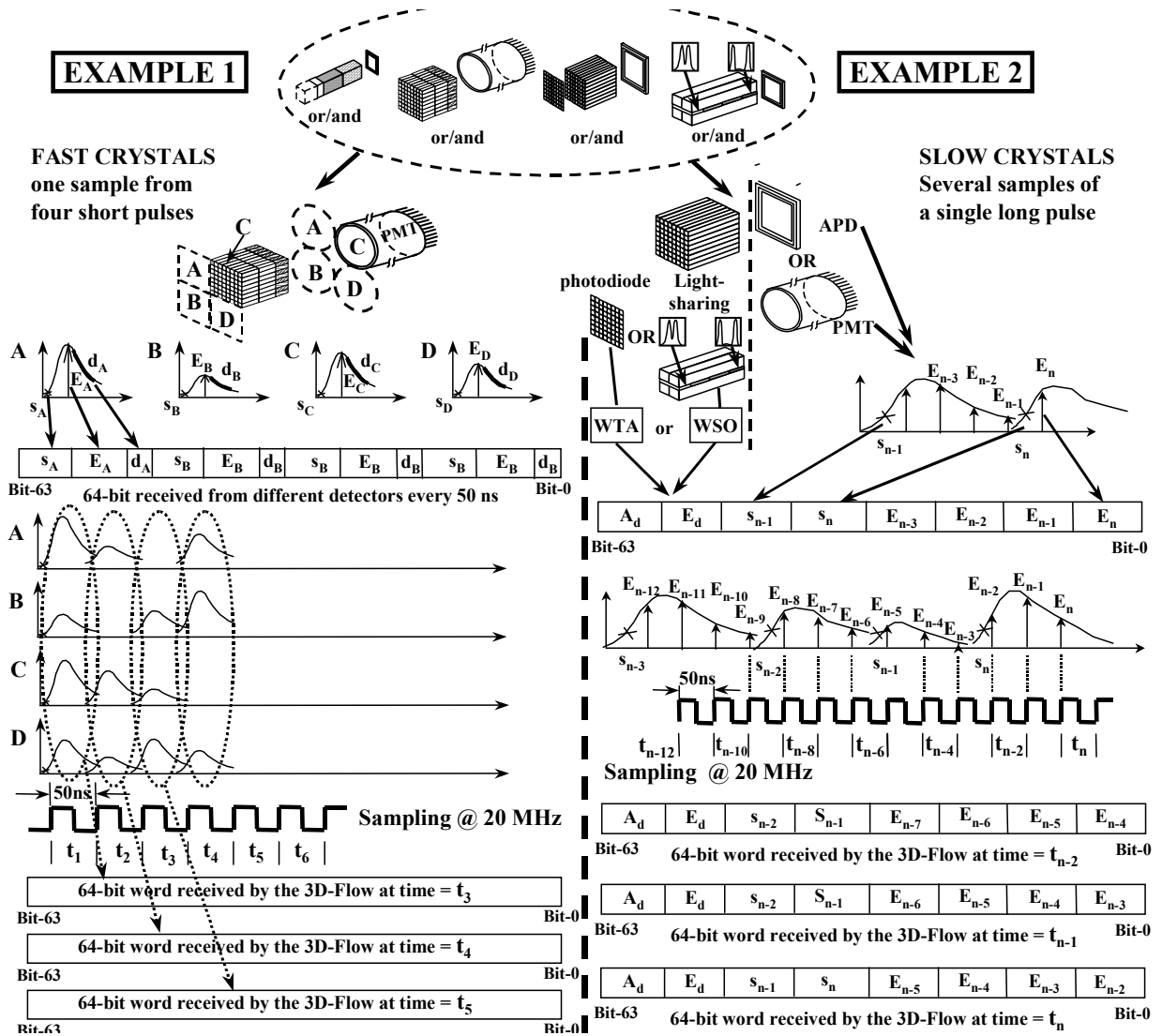


Figure 13-4. Examples of acquiring data by the 3D-Flow system, from the detector.

The data received by the front-end electronics during a given 50 ns sampling time period (e.g., t_3), are sent in a pipeline mode, e.g., two sampling periods later, in order to allow the analog and digital electronics to propagate and convert to digital the signals (e.g., at time t_5) to the 3D-Flow electronics (see bottom left of Figure 13-4).

13.4.3.2 Example 2: interfacing between detectors with slow crystals and the 3D-Flow

Example 2 shows a 64-bit word carrying the information from one or more transducers (PMTs, APDs, and/or photodiodes), coupled to a detector block made of slow crystals. Slow crystals have a long decay time of about 230 ns, which can be shortened to 200 ns. (Alternatively, the 3D-Flow CPU clock could be stretched). The detector provides the raw information of the ADC counts of the signals received every 50 ns, the time-stamp of the last two hits detected, and the position/DOI through photodiode and/or light sharing information.

All characteristics of the incident photon are extracted from the raw data received by means of the 3D-Flow digital signal processing capabilities (see Section 13.4.8, 13.4.9, 13.4.10, 13.4.6, 13.4.11).

Since the sampling time is 50 ns and the crystal decay time is expected to be on the order of 230 ns (shortened to 200 ns using the technique described in [160]), a buffer memorizes the last three samples. Each time a new sample of the input signal is acquired, the last value is grouped to the previous three samples and sent to one 3D-Flow DSP. The buffering function is implemented in the FPGA (see Section 13.4.4.3, and Figure 13-7).

The bottom right of Figure 13-4 shows that the amplitude of the signals E_{n-3} , E_{n-4} , E_{n-5} , and E_{n-6} , are sent at time t_{n-1} to the 3D-Flow and that the amplitudes of the signals E_{n-2} , E_{n-3} , E_{n-4} , and E_{n-5} , are sent at time t_n to the 3D-Flow. The above four 8-bit values of signal amplitude information (ADC counts) are mapped to the 3D-Flow input word in bits 0-31. Data are sent to the 3D-Flow system in a pipeline mode, e.g. two sampling periods later than the receiving time from the detector. This allows the analog and digital electronics to propagate, convert to digital, and align the time of signals belonging to the same event. Signals belonging to the same event are produced at different times because the transducers have different response times. (See reference [161] for the conceptual design down to the circuit description in graphic form and in VHDL form of the interface that aligns signals between different detector/transducer types with different response times.)

The rising edges of the signal from the PMT (or APD) above a certain threshold are detected by the CFD1 with short delay (see Section 13.4.4.3), and a logical signal is sent from the CDF1 output to the time-to-digital converter (see Section 13.4.10). This, produces a 9-bit time-stamp (e.g., s_n in Figure 13-4), which is mapped in the 3D-Flow input word in

bits 32-40. More bits for the time-stamp are needed in example 2 with respect to example 1, because, while the 500 ps resolution of the TDC is the same, the duration of the decay is longer (from 40 ns to 200 ns), and the longer time measurements require more bits. The previously recorded time-stamp (e.g., s_{n-1} in Figure 13-4) in the FPGA buffer is mapped in the 3D-Flow input word to bits 41-49.

Either technique -- ratio of signals from photodiode and PMT [87, 86] or the light sharing technique [141] -- can be used in the 3D-Flow system.

In the case of the use of a scintillator crystal coupled to the PMT at one end and at the other end to 64 photodiodes (PD), the following observations can be made:

- a) the crystal o interaction can be identified by the PD with highest signal;
- b) the sum (PD + PMT) contributes to calculate the total energy, and
- c) the ratio PD/(PD + PMT) determines the depth of interaction.

The 3D-Flow can perform the operations of addition and division to extract the photon's characteristics from the raw data that are provided by the "winner-take-all chips" (WTA) [89]. These are interfaced to the 64 PD and which produce one analog signal of the highest PD and its relative 6-bit address. The analog signal converted to 7-bit digital (e.g., E_d in Figure 13-4) can be mapped into the 3D-Flow input word at bits 50-56 and its relative address (e.g., A_d in Figure 13-4) at bits 57-62. Thus, one spare bit of the 64-bit 3D-Flow input data word remains.

In case the light-sharing technique is used, then the information can be mapped into the 3D-Flow input word at bit 50-56 for the maximum+partner and bits 57-63 for their address. This technique makes use of the "winner-select-output" (WSO) [90] chip, which provides the analog signal with the highest amplitude called "maximum," and second highest signal called "partner.")

13.4.4 The front-end electronics

The 3D-Flow system is **synchronous** with a proposed sampling time of 50 ns. The sampling time can be changed to best match the decay time of the crystal used.

Any rising edge detected within the 50 ns sampling time by the fast constant-fraction discriminator (CDF) causes a digital time-stamp with a

dynamic range of up to several microseconds and with the resolution of 500 ps to be generated and memorized by the time-to-digital (TDC) component. In this application only 9-bit will be used.

A preamplifier (called PRE on the figure of the printed circuit boards for IBM PC or VME), accommodates 32 analog channels as described in Sections 13.4.4.3, and 13.4.4.2.

13.4.4.1 Constant Fraction Discriminator

A constant fraction discriminator provides a logical output when the input amplitude reaches a certain fraction of its maximum amplitude, eliminating the time jitter caused by variable pulse heights.

Figure 13-5a and Figure 13-5b show how the technique is used by the CFD for a zero crossing time, which is independent of the amplitude of the signal. The technique is to send the input signal to two amplifiers. One amplifier delays the original signal by a fixed time (dashed line), the other one attenuates it by a fixed fraction and inverts it (dotted line). Then the two pulses from the two amplifiers are added together.

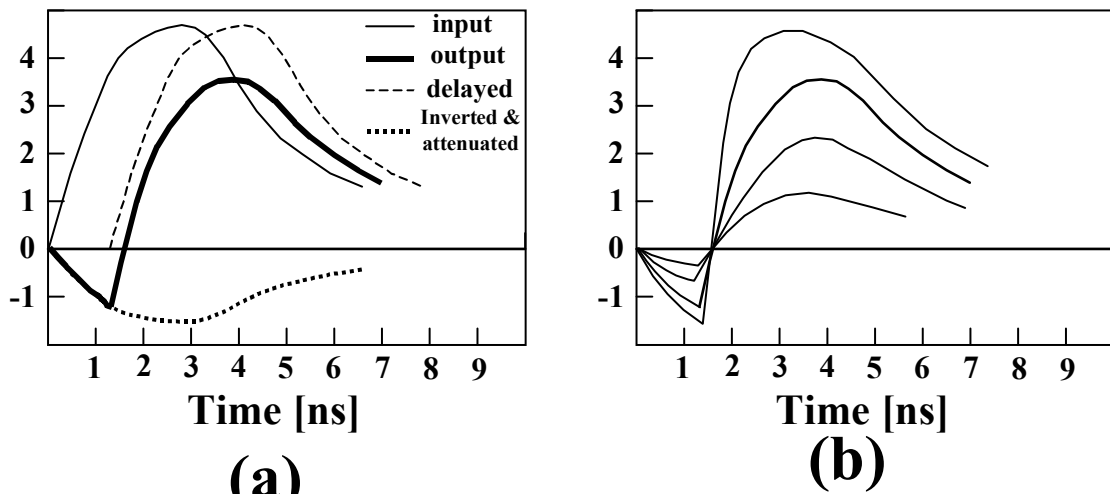


Figure 13-5. Constant fraction discriminator (CFD). Section (a) shows the relation between the output signal and the input signal and the intermediate steps of the delayed, inverted, and attenuated signals. Section (b) shows the zero crossing of signals with the same shape but with different amplitude occurring at the same time.

13.4.4.2 Front-end electronics for fast crystals

The front-end electronics for fast crystals, samples each channel of the detector at its peak amplitude every 50 ns using a delayed pulse generated by the CFD1 as described above.

The 7-bit amplitude of the sampling at time t_n , together with the converted amplitude of the samplings at time t_n from three adjacent PMTs (which form a 2x2 block), will be formatted in the FPGA with their timing and DOI information and will be sent to the 3D-Flow processor at time t_{n+2} .

Figure 13-6 shows the block diagram of the front-end electronics for fast crystals. The signal generated by the PMT and sent to the preamplifier is optimized by controlling the high voltage power supply to the photomultiplier.

The integrating amplifier generates an output pulse proportional to the decay time of the input pulse. The output of the integrating amplifier is sent to CFD2 and uses a delay₃, long enough to be able to integrate enough signals from the crystal with the slowest decay times and also sufficiently long to be able to measure the different decay time of the different crystals. On the other hand, the delay should be shorter than 50 ns, if possible to avoid system dead time. A pulse shortening technique [160] could be used if the crystal decay time is too long. However, sufficient light from the incident photon should be provided to be able to distinguish the signal from the noise.

The logical output generated by CFD2 is sent to the TDC, which generates a time-stamp of 7 bits. The FPGA reads from the TDC the information of the time-stamp generated by CFD1 and CFD2, and computes the difference, which is proportional to the decay time of the crystal that detected the incident photon.

This DOI information of 2 bits (allowing up to four crystals with different decay times to be used for DOI measurements) is formatted by the FPGA with the 7-bit time-stamp information (within the 50 ns sampling time period) and with the 7-bit photon energy converted by the ADC connected to the shaper amplifier. The information of four 16-bit channels is then sent to the 3D-Flow by the FPGA every 50 ns.

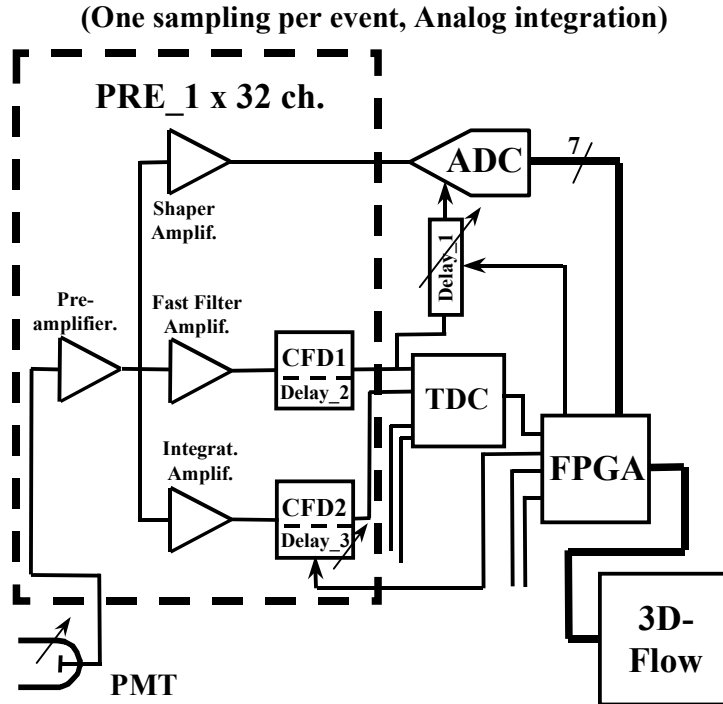


Figure 13-6. Block diagram of the front-end electronics for the fast crystals

13.4.4.3 Front-end electronics for slow crystals

The front-end electronics for slow crystals samples each channel of the detector every 50 ns using the system clock.

The 8-bit amplitude of the current sampling, together with the converted amplitude of the past three samplings as memorized in the FPGA, are sent to the 3D-Flow processor together with the last two time-stamps (9bits each) read from the TDC.

A different set of information for DOI measurements could be used for a total of 64 bits, which are then sent to the 3D-Flow processor every 50 ns. For instance, a 6-bit address from a WTA chip [89] and its analog amplitude pulse converted to digital for DOI technique with photodiode [87], could be used. Alternatively, the address bit from a WSO [90] chip and the analog amplitude pulse converted to digital for DOI technique with light sharing [139] can be used

The high-voltage control of the PMT, the preamplifier, and the fast filter amplifier are identical to the previous case in Section 13.4.4.2, and, therefore, are not described. In fact, a single chip of this type could be developed and used for both applications. This application will not use some of the pins and functions which have been developed for the other application.

Figure 13-7 shows the block diagram of the front-end electronics for slow crystals. Once the output of the preamplifier is sent to a shaper amplifier and then through the ADC, its digitalized amplitude is collected by the FPGA for packaging with other bits and is sent to the 3D-Flow.

The other output of the preamplifier is sent to a fast filter amplifier and then to CFD1, which uses a very short delay₂ and generates a prompt CFD logical output to the TDC.

The TDC generates a time-stamp of 9 bits which is read by the FPGA. The FPGA formats a 64-bit word of information at each clock cycle and sends it to the first 3D-Flow processor in the first layer of the stack.

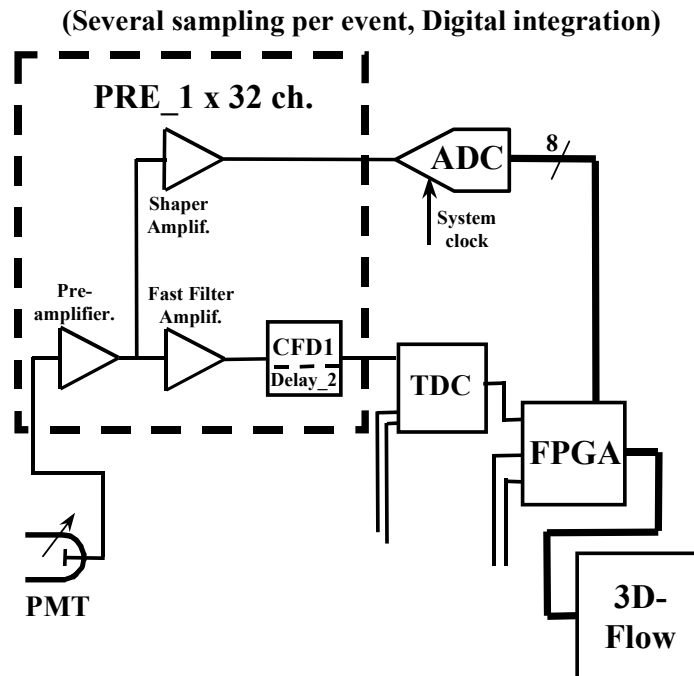


Figure 13-7. Block diagram of the front-end electronics for the slow crystals.

13.4.5 Definition and how to deal with randoms and multiples

Simultaneous annihilations (or pairs of photons generated by the source) can cause erroneous coincidence detection. This document makes a distinction between what are generally referred to in literature as Randoms and Multiple. Provisions are given on how to eliminate or account for them.

13.4.5.1 Randoms

Random coincidences occur when two unrelated photons hit two detectors (see Figure 13-8) within the time window used to detect true coincidences.

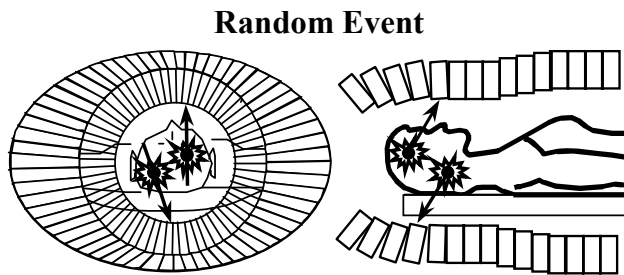


Figure 13-8. Randoms.

13.4.5.2 Multiples

Multiple coincidences occur when more than two photons hit more than two detectors (see Figure 13-9) within the time window used to detect true coincidences.

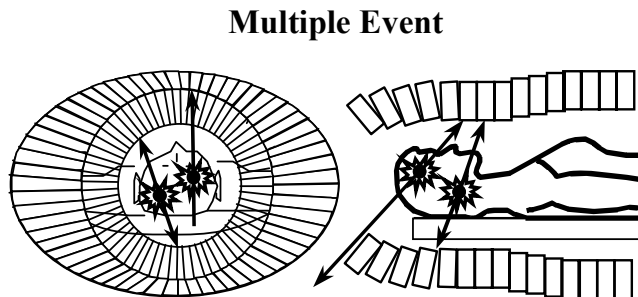


Figure 13-9. Multiples.

13.4.5.3 How to identify Randoms and Multiples, correct, and/or reject them

Random and Multiple rates are proportional to the rate of hits (or singles) to each detector and to the time coincidence window with the following relation:

$$(\text{Random} + \text{Multiple}) = \text{Rate}_1 \times \text{Rate}_2 \times 2\Delta t$$

Where Rate_1 is the rate of a single at detector 1, Rate_2 is the rate of singles at detector 2, and Δt is the time coincidence window. They are reduced by reducing the rate of the singles at the detector and the time window coincidence. Both parameters are reduced by the proposed design with the 3D-Flow because

- a) the increased FOV of the detector reduces the percentage of singles (see Section 3, and Figure 3-2) with respect to the total radiation activity (and an increased FOV requires also a lower radiation dose to be delivered to the patient); and
- b) the time window coincidence is reduced by the accurate time measurement, which is improved by the CFD, TDC, the front-end operations in the FPGA, and the DSP functionality of the 3D-Flow, which can improve accuracy of the time stamp assigned by the TDC with the digital signal analysis of the PMT pulse received from the shaper amplifier. This increased efficiency made merely with the improvement in the electronics. A further improvement in the time resolution can be effected by the use of faster crystals with shorter decay time; however, this strategy will entail additional cost.

13.4.5.4 Compton scatter: how to detect these events, and/or correct and/or reject them.

Compton scattering is the collision between a photons and a loosely bound outer shell orbital electron of an atom. Because the energy of the incident photon is much greater than the binding energy of the electron to the atom, the interaction looks like a collision between the photon and a free electron. The incident photon in a Compton scattering deflect through a scattering angle θ . Part of the energy of the incident photon is transferred to the electron and the energy loss is related to the scattering angle of the scattered photon at lower energy. It is a photon-electron interaction and the energy transferred does not depend on the density, atomic number or any property of the absorbing material.

Events of this type have one of the pair of photons at 511-keV that “Compton scatters” in the patient but still interacts in the detector ring. (Some others Compton scatter in the detector ring.) The result is a coincidence event because it satisfies the coincidence time window; however, the line connecting the detectors which sensed the hits is invalid.

Compton scattered Event

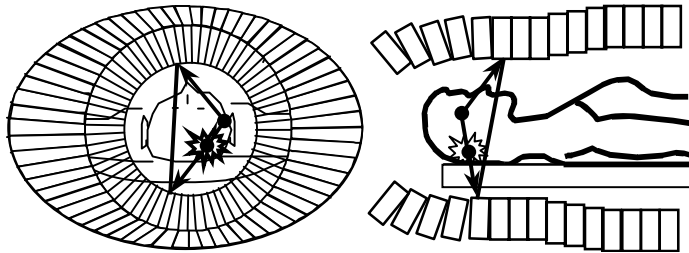


Figure 13-10. Compton scatter

Better energy resolution improves Compton scatter correction and rejection. The 3D-Flow system has the capability of improving the energy resolution by:

- a) handling the detector as a single large array of signals received from PMTs or other transducers or a combination of them, rather than by defining boundaries in the detector, as is the case in current detectors,
- b) having the capability of identifying, anywhere in the detector array, the head of the cluster (the sensor absorbing the highest scintillating light of the incident photon compared to its neighbors; see local maxima detection in Section 13.4.11.2) and then reconstructing the energy of the incident photon by adding the energy value of its neighbors (3x3, 4x4, or 5x5, etc., according to the size of the array). This calculation corrects for events which scatter in the detector
- c) applying the attenuation correction when the photon is identified in the stack of the 3D-Flow. This attenuation correction is for the SPECT operation mode, based on attenuation maps obtained with septa-in, and the calibrating parameters are obtained using the transmission source rotating around the patient's body. A more accurate attenuation correction can be obtained when the device is

operating in PET mode. When the coincidence is detected at the exit of the 3D-Flow pyramid, the x and y position of the crystals within the array are known, and the time-of-flight is known. The time-of-flight provides an accuracy of ± 7.5 cm because of 500-ps resolution, so it is possible to calculate more accurately the attenuation of the photons and, consequently, the energy of the pair of photons hitting the detector.

Further scatter correction and/or rejection can be calculated off-line during image processing, using the parameters of the incident photons provided by the 3D-Flow during their characterization.

13.4.6 Attenuation correction

The importance of the mass absorption effect of the body in PET and SPECT examination requires the use of an attenuation correction technique in order to improve quantification, quality image, and specificity.

In PET operation mode there is the advantage that the attenuation is less because the photons have higher energy (511 keV) compared to SPECT (140 keV), and accurate attenuation measurements on several lines through the patient's body can be performed. This provides a precise attenuation correction factor for different organs and sections of the patient's body.

In SPECT operation mode, attenuation maps are acquired with the transmission scan in order to correct for attenuation for the different organs.

Several techniques for attenuation correction have been developed with or without transmission scan and with or without septa. Many of them have the main goal of reducing the time required for calibration and of providing at the same time an accurate attenuation correction. The 3D-Flow architecture allows us to implement the methods providing highest accuracy while still requiring a very short overall time to run the attenuation correction because of its capability of sustaining continuously an input data rate of 20 MHz at each electronic channel (PMT, or APD, and/or photodiode, etc.).

Although only two examples are provided herein (one for SPECT and one for PET), several other techniques described in the literature can also be implemented with the 3D-Flow.

The attenuation coefficient for SPECT can be acquired from a rod source in transmission mode with septa-in at an acquisition rate of up to 20 million photons per second per PMT channel. It is then stored in the look-up table memories of each 3D-Flow processors in the stack.

A more precise attenuation coefficient for PET can be acquired from a rod source in transmission mode with septa-out and stored into a 512 MB (or greater) DIMM memory installed on the 3D-Flow pyramid-buffer board (see Section 15.2) This is accomplished in the following manner:

A blank scan is measured using rotating rod sources (e.g., ¹³⁷Cs emitting 662 keV γ rays) as shown in Figure 13-11a (see also Figure 13-1). The acquired coefficients are stored temporarily in the memory lookup tables of each front-end 3D-Flow processor in the stack.

A second transmission scan with the patient in place (see Figure 13-11b) measures the transmission attenuation coefficients with the same rotating rod source at different angles (e.g., about 10 rotations at 10 different angles requiring about one second for each complete rotation). The ratio of the coefficients from the “blank scan” with the acquired attenuation coefficients of the transmission scan (e.g., about 524,288, corresponding to 524,288 “roads” of attenuation coefficients) is sent to the PET attenuation coefficients look-up table memory on the 3D-Flow pyramid-buffer memory (see Section 15.2).

When a coincidence is found by the circuit described in Section 13.4.14 and implemented as described in Section 15.2, the position of the two crystals identifying the line on which the annihilation occurred allows the calculation of the address of the corresponding attenuation coefficient stored in the “PET attenuation coefficient look-up table memory.” The time-of-flight information of each photon with a resolution of 500 ps (corresponding to 7.5 cm spatial resolution of the annihilation occurring along the line connecting the crystals that detected the hit), which has been calculated by subtracting the time-stamp of the two photons in coincidence, allows the accurate calculation of the attenuation coefficient correction factor for the two photons in coincidence. Finally, the two calculated coefficients, which are related to the time-of-flight information for the photons and to the specific attenuation as a result of the mass encountered during their journey to the scintillation crystal detector, are used to correct the energy of the two photons in coincidence.

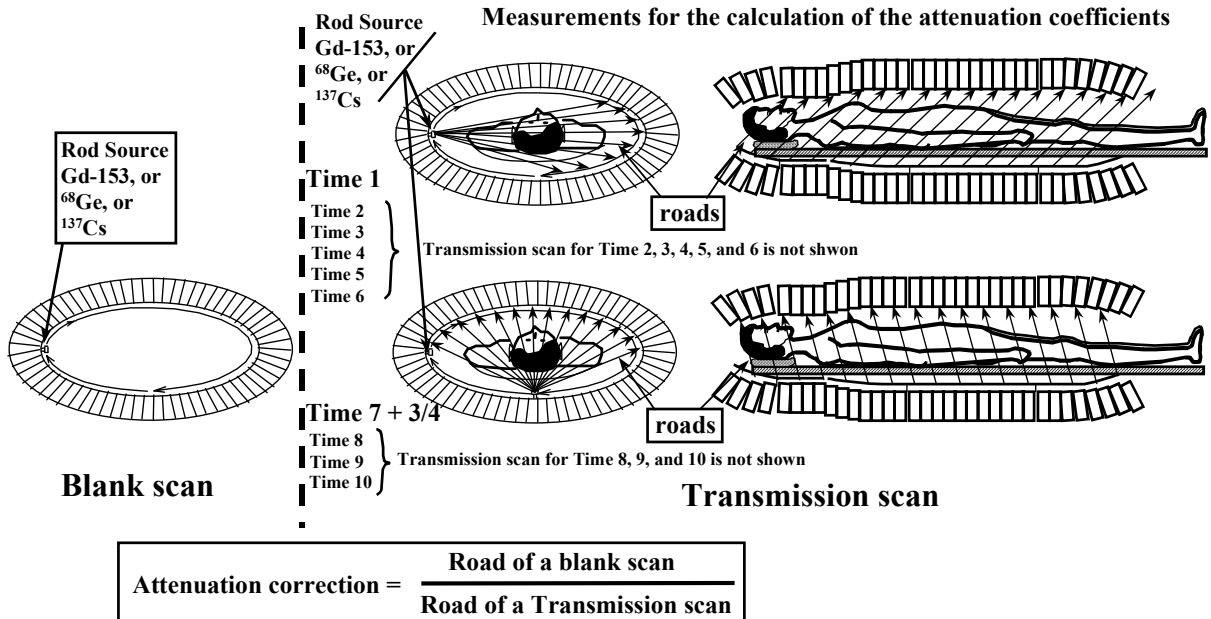


Figure 13-11. Measurements of the attenuation correction for PET and determination of attenuation coefficients.

13.4.7 Difference between true event efficiency and coincidence efficiency

The efficiency referred to in this document is the capability to detect photons in time coincidence (events) lying on a line connecting two detectors which passes through the patient's body. Included among these events are also all events that are not true events (such as Compton scatter and Randoms), which could not be rejected at this stage by the electronics.

The reason for using this type of measurement of efficiency based on the count rate of the coincidences and not based on the count rate of the true events is that:

1. it is not possible to separate out the non-true events until they are processed off-line during the phase of reconstruction of the image and their location in the patient's body is determined;
2. it is a parameter easy to calculate and for that reason the count rate of the coincidences is used by manufacturers and designers in the performance measurements.

The real efficiency of the device is then the ratio of the number of real events divided by the number of total events (or disintegrations) created by the radioisotope.

The total number of coincidences found should be reduced in some cases by up to 50% to obtain the count rate of the true events.

13.4.8 No detector boundaries for the centroid calculation with the 3D-Flow

In the PET implemented with the 3D-Flow system, the geometry of the PET sensors are mapped to the a 3D-Flow processor array in a manner that allows the exchange of information among the adjacent PET sensors through short signal delay.

The entire 3D-Flow system is a single array with no boundary limitation. The neighboring of sensors in the PET detector array is reflected with an identical neighboring scheme in the 3D-Flow processor array. Each channel (defined as all signals, from all subdetectors within a given view angle) in the 3D-Flow processor array, sends its information to, and receives their information from, its neighbors. This is equivalent to the exchange of information among adjacent channels (or sensors) in the PET detector array. The practical implementation of the data exchange between neighbors is shown in detail in Figure 15-7.

Once all data from each channel and its neighbors are moved into a single processing element, any pattern recognition-algorithm, and/or signal-to-noise filtering algorithm well known in the literature can be applied by using the DSP functions of the 3D-Flow processor. This is achieved with the instructions of arithmetic and logic operation including multiply-accumulate and divide.

These operations are accomplished in parallel on each channel. In the example of the application of Section 17, for instance, each of the 2,304 processors of one layer of the 3D-Flow stack executes in parallel the real-time algorithm, from beginning to end, on data received from the PET detector, while processors at different layers of the 3D-Flow stack operate from beginning to end on different sets of data—or events—received from the PET detector.

In the current PET system, on the contrary, if a photon hits the detector at the border of a 2x2 PMT block, releasing its energy partly in one block and partly in the neighboring block, then both might reject the photon as having failed to pass the energy threshold.

The centroid calculation with the 3D-Flow is straightforward after having gathered the information of 3, 8, 15, or 24 neighbors in a single processor, as is described in Section 13.4.11.2 for a 3x3 centroid calculation and in Section 13.4.11.3 for a 5x5 centroid calculation.

One example of a more accurate centroid calculation compared to the 2x2 example show on Figure 13-12b is for the calculation of Δ_x the ratio of the sum of the energies of all sensors at the west of the central element, divided by the sum of all sensors at the east of the central element ($\Delta_x = \Sigma E_W / \Sigma E_E$). Similarly for the calculation of Δ_y the ratio of the sum of the energies of all sensors at the north of the central element, divided by the sum of all sensors at the south of the central element ($\Delta_y = \Sigma E_N / \Sigma E_S$). Accuracy and algorithm execution speed will determine whether a ratio or a subtraction is needed (the subtraction algorithm is a faster hardware operation).

Another important advantage provided by the elimination of the boundaries within the detector array is the resulting increase in the accuracy of the energy resolution calculation of each incident photon.

The complete energy of the incident photon can be rebuilt by adding to the channel with the highest energy (head of a cluster), the energy values of the 3x3, or 4x4 surrounding the channels. Alternatively, when larger areas of 5x5 or 6x6 are added, the complete energy of photons which went through crystal scatter can be rebuilt.

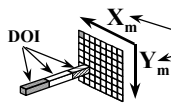
Increasing energy accuracy will improve spatial resolution, scatter rejection/acceptance, and attenuation correction.

Figure 13-12b shows the limitation introduced by the presence of 2x2 PMT block boundaries of the current PET systems. The bottom section of the figure shows one of the several figures available in several publications [73, 98, 105, 113]. Although on Section II.C of [105] it is stated that "...Detector boundaries may form any appropriate shape to account for nonlinearities in the positioning response....," the much lower thresholds (see Figure 3 of [105]) used for the corner and edge crystals of the 2x2 block compared to the thresholds of the center crystals (which are also corner crystals of PMTs) indicates that the energy of the incident photons detected by the corner/edge crystals is much lower than that detected by the center crystals. This is because part of the energy of the incident photon is detected by the adjacent 2x2 block and is lost when using the approach of the current PET, because there is no communication between 2x2 PMT blocks. The center crystals (which are also corner

crystals of the PMTs) have instead higher thresholds since the Anger logic [162] can account for the energy of the incident photon which was split among the four PMTs).

The proposed architecture of the 3D-Flow with no boundary between 2x2 PMTs provides a platform where all corner crystals will be like the ones currently located at the center of the 2x2 PMT block, or providing even higher accuracy by means of 3x3, or 5x5 neighbor clustering. Thus all measurements will be like the four crystals in the center of the 2x2 PMT block; no such difference of lower thresholds as the ones used in the current PET will be required, and the complete energy of the corner/edge crystals could be rebuilt as it is for the center crystals.

In the current PET, the fact of having blocks with 2x2 boundaries (the 2x2 boundary is provided by the grouping of the 2x2 PMTs) causes different signals in different positions of the 64-, 144-, or 256-crystal block (see the crystal-region boundary lines in Figure 3 of reference [98]) change the geometrical segmentation of the crystals into the layout of the crystal region boundary lines similar to the one shown in the bottom right of Figure 13-12b. The signal at the corner of the 2x2 PMT block (see Figure 13-12b1) has a high component of noise and only a fraction of the



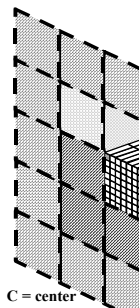
CENTROID CALCULATION

3D-Flow System

- NO Boundary limitation,
- NO duplication of events (local maxima)
- Suitable for "continuous" or "block" detectors.
- Flexible clustering/centroid 2x2, 3x3, 4x4, or 5x5,
- The energy of each PMT is checked if head of a cluster against its neighbors (3, 8, 15, or 24)
- Digital signal processing, high S/N ratio



sys

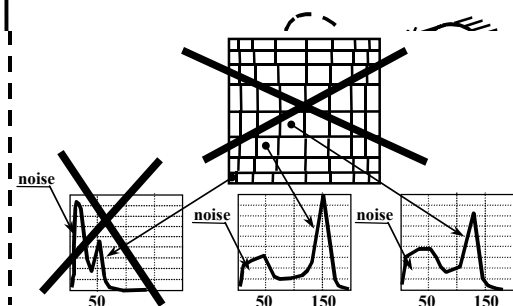


C = center
B = SW of center
A = W = West of cen
D = S = South of cen
E = East of center
N = North of center
NE = North East of

(a)

Current PET systems

- Boundary limitation at the block and module segmentation.
- Missing the detection of photons at the block boundaries, poor S/N ratio and lack of Signal Processing
- Fixed, hard-wired architecture for 2x2 centroid
- Analog signal processing



(b1)

(b2)

(b3)

the
in
no
ich
ital
73]
(as
x2

T

13.4.9 Flexibility in measuring the depth of interaction with the 3D-Flow system.

An oblique penetration of a incident photon into a crystal generates a parallax error if the depth of interaction (DOI) is not measured.

Figure 13-13 shows the effect of the parallax error and the technique of using different layers of crystals with different decay times in order to be able to identify at which depth the scintillation light occurred.

During the past 14 years, different techniques have been used to measure the DOI. The digital signal processing capabilities of the 3D-Flow system offer the possibility of implementing several of them. Figure 13-14 shows the block diagram of the logic to implement some of them. (See also the photon detection algorithm with the 3D-Flow in Section 13.4.11.2).

The different depth of interaction techniques described in Section 11.2.3.2 can be implemented with the 3D-Flow system because all necessary information from the detector needed for the calculation of the DOI are fetched from the detector as shown in Section 13.4.3. The operations among them can be executed by the DSP functionality of the 3D-Flow processor (arithmetic and logic operation typical of a DSP) during an execution time that can be extended as necessary, thanks to the bypass switches of the 3D-Flow (as described in 12 and in reference [163]).

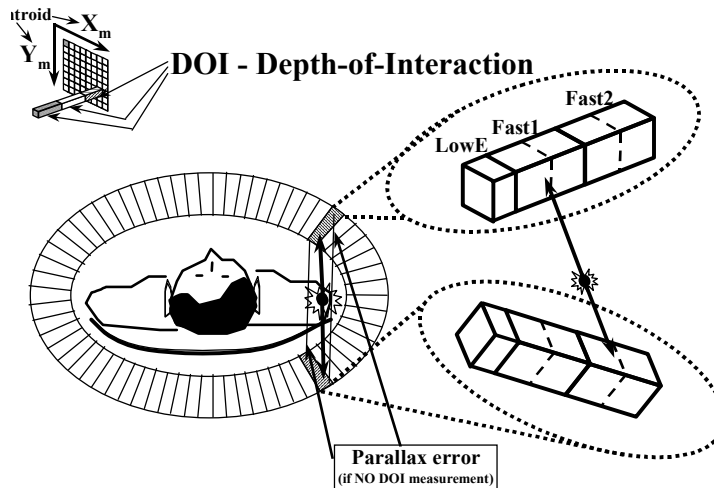
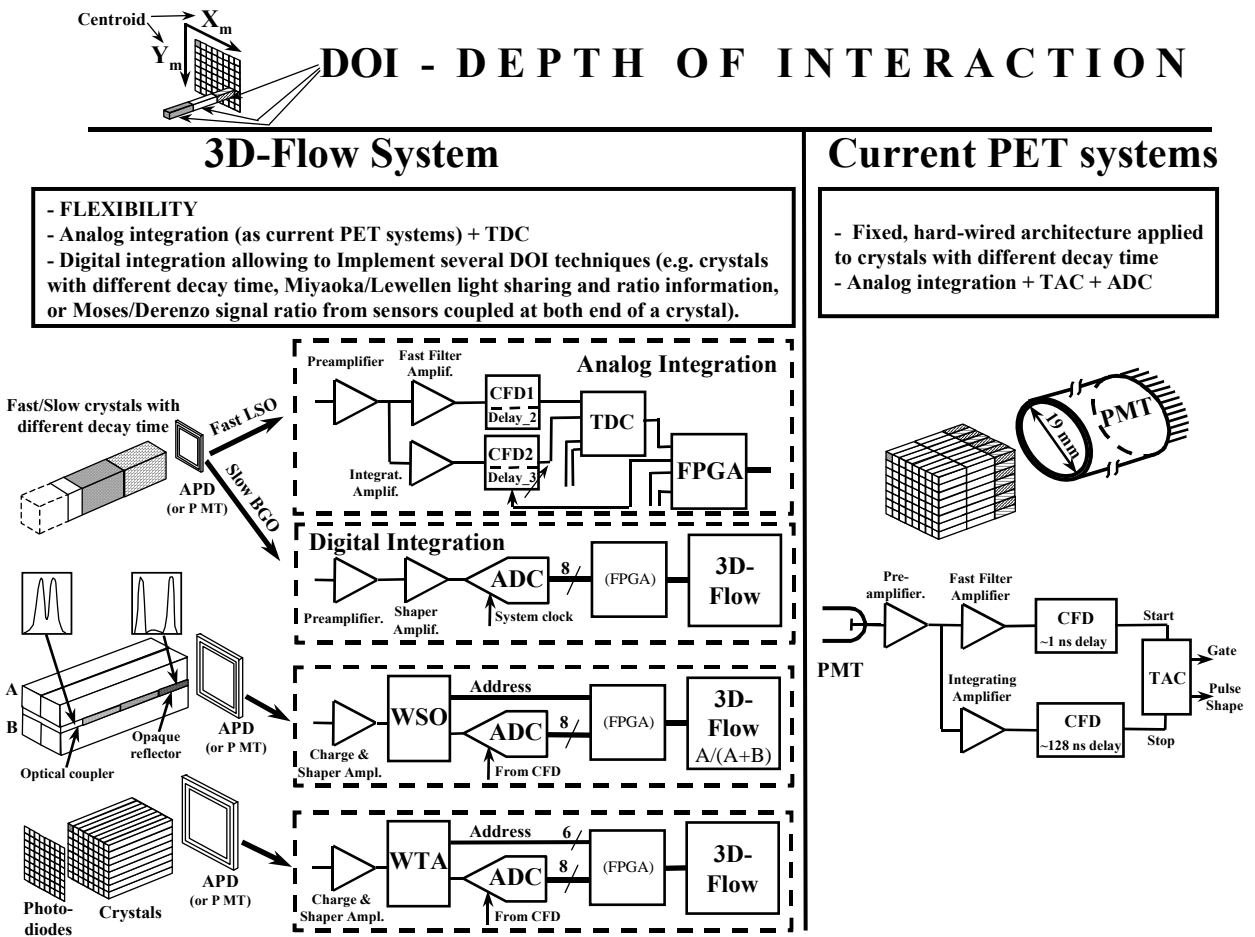


Figure 13-13. Parallax error measured by the Depth of interaction.



13.4.10 Time resolution of 500 ps for PET devices assisted by TOF information

The measurement of the time-of-flight in the proposed design is used for improving the signal-to-noise ratio of images, for the DOI measurement, and for narrowing the time window in order to eliminate multiples. It is not intended to directly use the TOF information in source positioning. The choice is dictated by economic consideration and the desirability of avoiding exotic and expensive electronics that need skew control at tens of ps.

The position of annihilation can be determined from the difference between the time-of-flight of the γ -rays. The relationship between time difference ($t_1 - t_2$) and the source position from the center of opposite detectors, x , can be expressed by $x = (t_2 - t_1) * c/2$, where c is the light velocity. (See Figure 13-15).

Before the digital TDCs were on the market, only analog TDCs which normally have a better accuracy (< 50 ps), were available. They have a very long dead time, however, and usually can record only one hit. These TDCs cannot be used in high-rate data acquisition. Most recently, however, digital TDCs have been developed that can record multi-hits with a resolution of 50ps. The cost of such digital TDC will be too high and will also increase the cost of the associated electronics. For the above reasons, a multi-hit digital TDC with a resolution of only 500ps and 24 or 32 channels per chip is the most appropriate for the proposed project. The TDC, costs about \$2 per channel.

At any time during the time interval of 50ns between the acquisition by the 3D-Flow system of two consecutive sets of digital input data, the TDC can memorize a signal received from the detector by the CFD on the analog interface with a time resolution of 500ps (see Section 13.4.4).

The simplified operation of the TDC can be described as a continuous running counter (a single counter for each group of 32-channels in a chip). When a signal is received from one of the 32-inputs, the current value of the counter is copied into a buffer. More hits could arrive within 50ns, thus more values are copied into the TDC buffer. Typically, the actual rate of hits at a single channel of the detector is much lower than 20MHz.

While there is no problem of relative time measurement between channels within the same chip (because there is only one counter), there might be a problem of counter alignment between different chips residing on the same board or on different boards. This problem can be overcome by making an accurate distribution of the signal of the reset of the counters of the TDC. The skew of the signal at the different locations of the components should be minimal as described in reference [163] Section 9, page 377.

A calibration of the system will correct all discrepancies from the different channels. A possible calibration of the system could be the following: a radioactive source is placed at the center of a collimator as shown in Figure 13-16 and moved longitudinally along the center of the detector barrel. The time measurement on one end of the detector (TDC counter value) should correspond to the time measurement of the sensor along the line passing through the radioactive source and located in the opposite side of the detector. Any count difference between the two counters should be memorized and used as a counter offset during subsequent measurements.

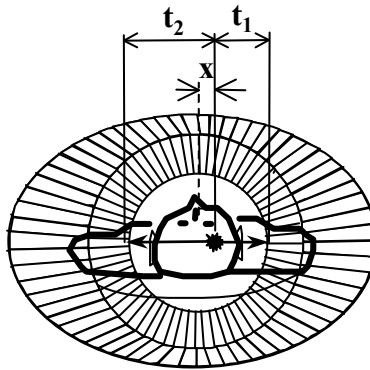


Figure 13-15. Time resolution of 500 ps for PET devices assisted by TOF information.

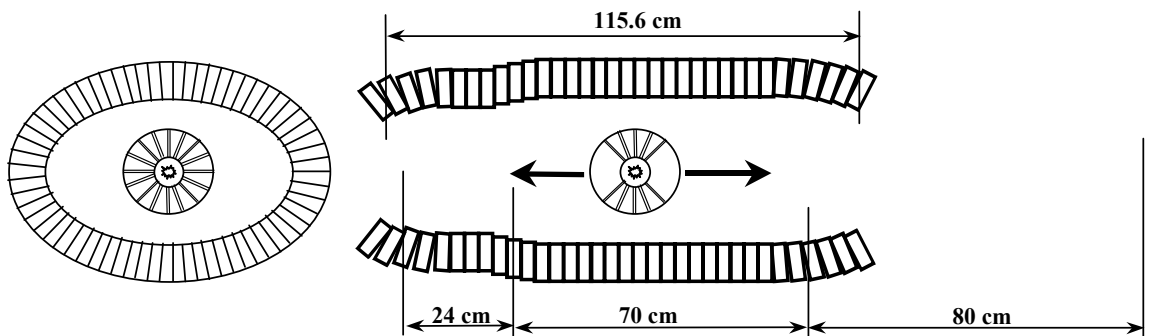


Figure 13-16. Calibration of the PET system.

13.4.11 Photon identification: The PET/SPECT/CT real-time zero dead-time algorithms for fast or slow detectors using the 3D-Flow system.

The detector should be made of at least three different crystals with different decay times and one with good stopping power for 60 keV, another of 140 keV and another for 511 keV (See Section 11.2.2.8.3, and reference [131]). The 3D-Flow real-time algorithm with digital signal processing and correlation with neighboring signals will decode the energy, time information, and spatial information and will identify the type of incident gamma ray.

The capability of the 3D-Flow system to apply any digital-signal-processing (DSP) filtering algorithm on the complete set of data relative to an incident photon (the head of the cluster of an incident photon with all its neighbors, including its timing information) can extract all relevant information of the incident photon (energy, position, timing and type of event, e.g. PET, SPECT, x-ray, scattered or photopeak) and enhance them.

13.4.11.1 Format of the input word from the detector to the 3D-Flow system stack

Two input words to the 3D-Flow processor are described, one for example 1 for slow crystals, and another for example 2 for fast crystals (see also Section 13.4.3):

input word to the 3D-Flow processors for example 1 (fast crystals):

bit 0-1 DOI of PMT_D, bits 2-8 amplitude of PMT_D, bits 9-15 time-stamp PMT_D;
 bit 16-17 DOI of PMT_C, bits 18-24 amplitude of PMT_C, bits 25-31 time-stamp PMT_C;
 bit 32-33 DOI of PMT_B, bits 34-40 amplitude of PMT_B, bits 41-47 time-stamp PMT_B;
 bit 48-49 DOI of PMT_D, bits 50-56 amplitude of PMT_D, bits 57-63 time-stamp PMT_D.

input word to the 3D-Flow processors for example 2 (slow crystals):

bit 0-7 amplitude (n) of PMT, bits 8-15 amplitude (n-1) of PMT,
 bit 16-23 amplitude (n-2) of PMT, bits 24-31 amplitude (n-3) of PMT;
 bit 32-40 time-stamp (n), bits 41-49 time-stamp (n-1)
 bit 50-56 amplitude highest PD, bits 57-62 PD address.

13.4.11.2 Photon detection algorithm simulation with the 3D-Flow for PET/SPECT/CT

The 3D-Flow system is synchronous.

Every 50 ns, upon reception of the 64-bit word from the FPGA, all processors of one layer of the 3D-Flow stack execute the following steps in parallel:

- Get data from detectors, convert ADC counts into energy value through look-up-table.
- Fetch four signals from fast crystals, TOF/decay time information, calculate DOI, or integrate signals from slow crystals, calculate DOI (signal decay time) and check for pileup.
- Calculate attenuation. Calculate time-stamp.
- Send data to North, East, West and South neighbors and save energy photon in R46. Increment time stamp.
- Save first 3x3 data into Sum1, route 3x3 corner values.
- Get energies from four NEWS neighbors, add them, and save into registers R0, R16, R32, and R48 for local maxima calculation.
- Get energies from four corner neighbors, add them, and save into registers R1, R17, R33, and R49 for local maxima calculation.
- Compare 9 energy values for “Local Maxima” tests to determine whether the energy of the central cell is larger than any of its neighbors. (This operation is executed in one CPU cycle). Compute the total energy sum of 3x3 array by adding the partial sums, Sum1 and Sum2. Check for “photopeak” and “scattered.” Calculate 3x3 “centroid” compute the energy asymmetries, for subsequent determination of the point of impact ($\Delta_x = \Sigma E_W - \Sigma E_E$ and $\Delta_y = \Sigma E_N - \Sigma E_S$.) Format output word, or reject event.

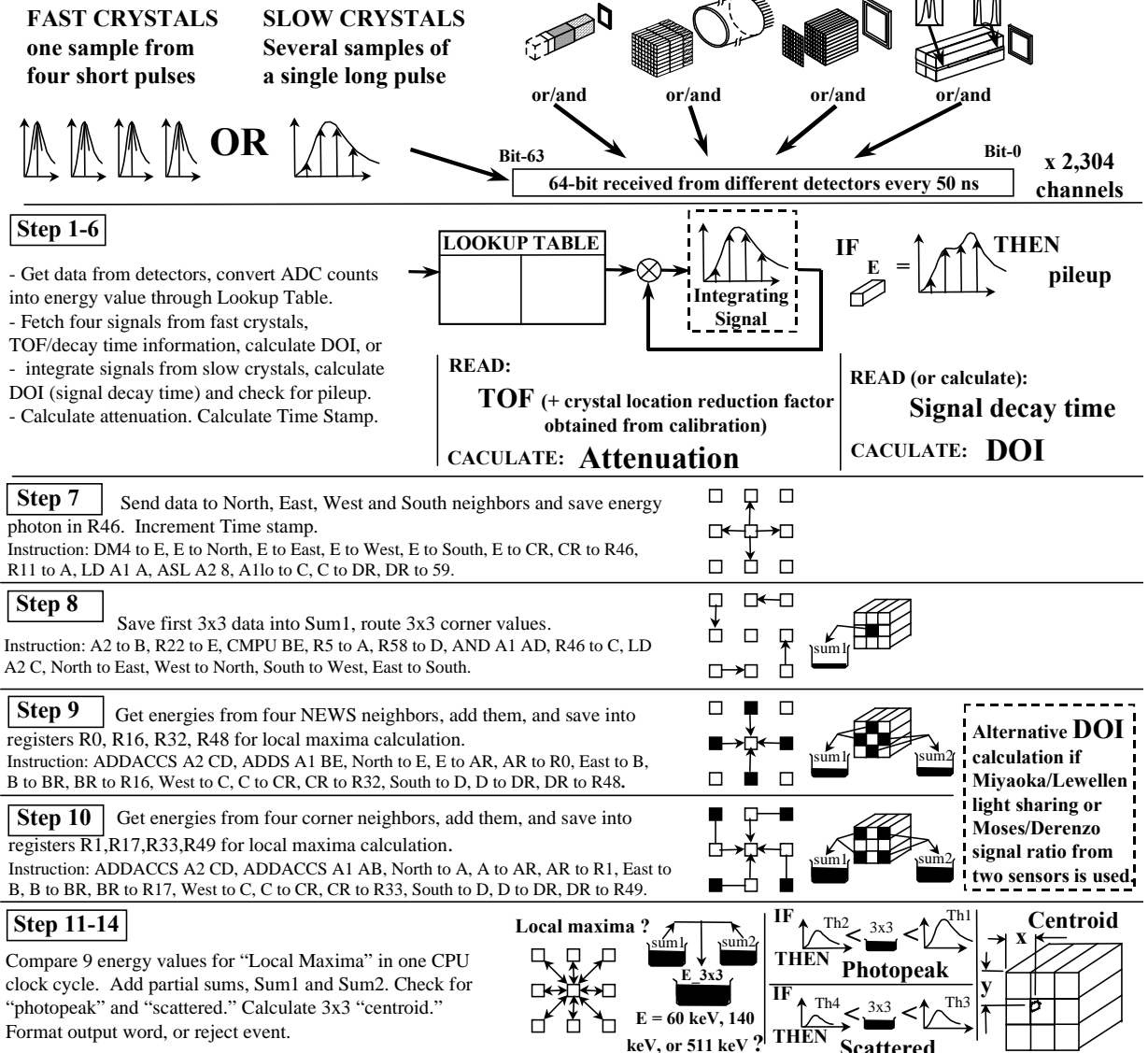


Figure 13-17. Photon detection algorithm simulation with the 3D-Flow for PET/SPECT/CT.

At this stage there is much information computed that allows conclusions to be drawn, whether the photon is a 60 keV (x-ray), 140 keV (SPECT), or 511 keV (PET), and if the attenuation, DOI, timing, spatial information are available. Any further operations can be executed upon the 9 data (the one received from the detector and its 8 neighbors) by the

CPU of the 3D-Flow processor, which can, in a single cycle, execute up to 26 operations, including all normal arithmetic and logic operations of a standard computer.

Each processor gathers the information from the neighbors and acts like the head of a cluster without boundary limitations. The calculation of the “local maxima” prevents duplication in the detection of photons because only one cluster can be larger than the neighbors.

Figure 13-17 shows the flow of the operation on each processor in a graphical form. In the event a 5x5 clustering calculation is desired in place of the 3x3 clustering, steps 7 through 10 must be replaced by the program of Section 13.4.11.3

13.4.11.3 Simulation of the 5x5 clustering algorithm in 9 steps with the 3D-Flow

Simulation of the 5x5 algorithm has been performed with the 3D-Flow real-time design and software tools [164].

Nine steps (each step corresponding to the 3D-Flow clock period of 12.5 ns) are required to send and receive the data to and from 24 neighbors while adding them.

Two 3D-Flow cycles are required to propagate signals from the internal bus of one processor to the internal bus of an adjacent processor.

During step 7, the data of one channel is sent to the North, East, West, and South ports. All processors are executing the same operation; thus the values from the neighbors, which were sent at the same time, are ready to be fetched two cycles later at step 9.

In order to move the data from the corner of a 3x3 and of a 5x5 and the value of the outer 5x5 ring to the inner ring during steps 8 to 12, the operation of moving data from one input to one output is performed.

The moving operations performed by each processor are identical (aside from the processors at the two sides of the array with no neighbors) and are performed in such a way that at each 3D-Flow clock cycle there are four new neighboring values at the North, East, West, and South ports to be fetched by each processor.

The move operations are performed according to the instructions listed in step 8 such as: North to East, West to North, South to West, East to South.

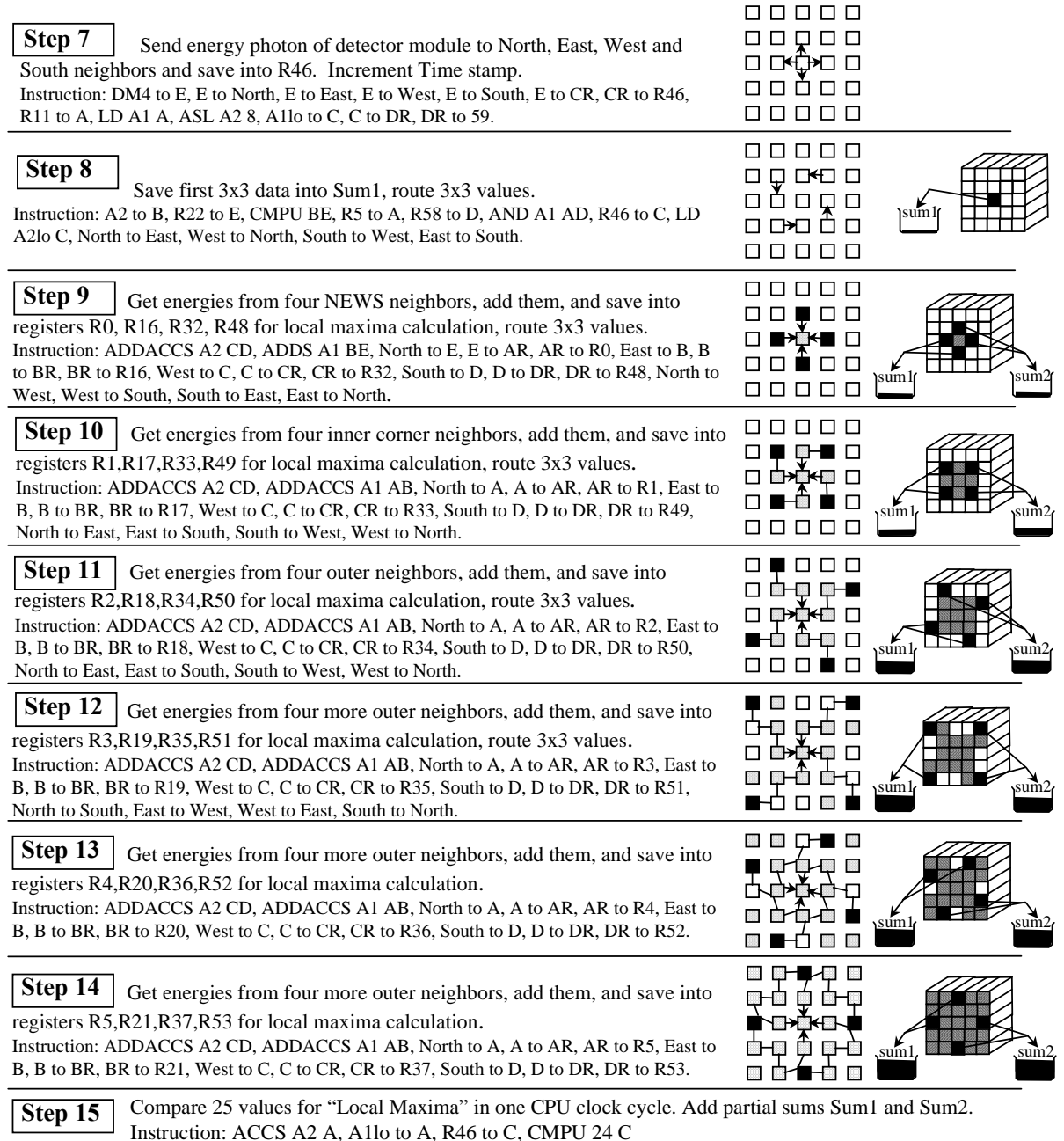


Figure 13-18. 3D-Flow simulation of the 5x5 clustering algorithm in 9 steps.

At step 9 through 12 the moving operations are different. The summaries of the path of each single datum going from an external position to the four North, East, West, and South processor neighbors of the central processor, are shown with thin lines in the graphic section of Figure 13-18. The starting processor is indicated with a black square, a line indicates the path from processor to processor at each 3D-Flow clock cycle, the four arrows indicate when the datum is fetched by the central processors.

This scheme can be applied to any processor of the 3D-Flow array; and at each step, the relative position of the central datum with respect to its neighbors in the process of being fetched is the same.

13.4.11.4 Format of the output word of the “singles” identified by the 3D-Flow “stack”

The format of the output word of the “singles” that passed the photon identification criteria of the real-time algorithm in the 3D-Flow stack, is the following:

bit 0-19 crystal spatial ID; bits 20-23 depth of interaction, bits 24-31 photon energy; bits 32-43 time-stamp; bits 44-50 for the type of photon, bits 51-63 not used.

The 20-bit field for spatial ID allows for coding up to 1,048,575 crystals. The 4-bit DOI field allows for a depth of interaction with up to 1.56 mm resolution when crystals 25 mm thick are used. The energy of the photon is coded in 256 intervals from the smallest to the highest energy value. The 12-bit field for the time-stamp allows a maximum latency of 4 μ s from when the photon hits the detector to when it reaches the coincidence circuit. Several types of photons could be coded such as: 60 keV for x-ray, < 60 keV for attenuated x-ray, 140 keV for SPECT, < 140 keV for attenuated SPECT, 511 keV for photopeak PET, and < 511 keV for scatter PET, and PET Randoms).

13.4.12 Output of the identified photons: memory buffer and/or 3D-Flow pyramid

The 3D-flow DAQ-DSP board provides the possibility of installing a memory buffer for accumulating the single photons found during scanning time (see the SO-DIMM buffer memory indicated with dashed lines on the physical layout of Figure 15-1, Figure 15-3, or Figure 15-4, and its dimensions, characteristics, and size in Table 15-1, and Table 15-2).

The 3D-Flow DAQ-DSP memory buffer can be used:

1. to store the single photons that passed the criteria of the real-time algorithm in the 3D-Flow stack and were recognized either as 60 keV x-ray of the CT scan, or 140 keV of the SPECT (including the ones attenuated) during the SPECT and CT operation mode. The buffer memory on each 3D-Flow DAQ-DSP board will provide a large buffering capability of several hours (or Gbyte) of data taking.
2. to store the single photons found during PET operation mode for the verification of the efficiency of the coincidence circuit operating in real-time. The circuit for real-time coincidence identification has the advantage of requiring less storage space and less computing power during successive processing phases of the data. The presence of the memory buffer on each 3D-Flow DAQ-DSP board will make possible a test on the efficiency of the real-time coincidence detection circuit when the PET is operating under different conditions. This test can be performed by spying and saving in the memory buffer the single photons acquired during a PET examination before they go through the circuit detecting the time coincidences among them in real-time. The photons in time coincidences could then be extracted from the raw data stored in the memory buffer by a slow algorithm running on the IBM PC CPU. The coincidences found using the circuit executing the algorithm in real-time and the slow off-line algorithm could be compared, and any discrepancies, could be investigated for the improvement of the real-time coincidence circuit.

In the event the output data rate never exceeds a few tens of MHz for the three modalities, PET, SPECT, and CT, then the memory buffer is not needed. All results found in the three modalities could be funnelled through the 3D-Flow pyramidal circuit and stored in the pyramid buffer memory located in the pyramid boards shown in Figure 15-5, and Figure 15-6.

13.4.12.1 Separating the single photons found by the 3D-Flow stack

Based on the reduction rate of photon activity at different stages of the PET acquisition detection system, as shown in Figure 14-1 and Section 13.4.2, only about 80×10^6 single photons per second are expected at the

start of scanning, 20 seconds after delivery of about 5 mCi of ¹⁵O-water tracer to the patient.

The processors at the first layer of the 3D-Flow pyramid will find no data from most of the 2,304 channels (see Example in Section 17) of the 3D-Flow stack. Only approximately four processors will find data during a sampling period of 50 ns.

Then,

1. in the event the memory buffer on the 3D-Flow DAQ-DSP board is installed, the data will be interpreted by checking the “type” bit-field of the output word received from the stack (see Section 13.4.11.4), and then routed to the DAQ-DSP memory buffer if 140 keV (and attenuated single photons) of SPECT modality are found or if 60 keV (and attenuated single photons) of CT modality are found;
2. in the event the memory buffer on the DAQ-DSP boards were not installed, the processors in the first layer of the pyramid will filter only the zero data and forward all single photon information found to the exit point of the 3D-Flow pyramid. The check of the content of the “type” bit-field will be performed only at the exit point of the pyramid. The single photons tagged as 140 keV (and attenuated single photons) of SPECT modality, or the 60 keV (and attenuated single photons) of CT modality, will be stored into the pyramid buffer memory (see Section 15.2, Figure 15-5, and Figure 15-6). Single photons tagged as 511 keV (or lower for Compton scattered events) PET events will be sent to the circuit that sorts the data in the same sequence as they were in the original sequence when they were created in the detector. The data flow will regain the fixed latency time with respect to when the event occurred in the detector, and the information will be sent to the time coincidence detection circuit.

13.4.12.2 Simulation of the channel reduction in the 3D-Flow pyramid

The pyramid is a series of 3D-Flow processor layers that has a reduced number of processors between the first layer of the pyramid adjacent to the last layer of the 3D-Flow processor stack and the next adjacent layer that carries out the information. Again between this layer, the number of processors is reduced, and so on, until the number of processors per layer reduces to one ASIC (equivalent to sixteen 3D-Flow processors).

The direct synchronization between instructions and I/O ports allows efficient routing of data in an array. It is possible to route data efficiently from n to m channels by a 3D-Flow layout arranged in set layers with a gradual reduction in the number of processors in each successive layer.

It is important to calculate the data rates and make sure that data reduction matches the reduction in the number of channels. Most of the data reduction by zero suppression is accomplished at the first layer of the pyramid, which is attached to the output of the stack of processors that execute the digital filter and pattern recognition algorithm. Each processor in the first layer of the pyramid checks to determine if there is a datum at the top port (from the last layer of the 3D-Flow stack that has executed the digital filter and pattern recognition algorithm) and forwards it toward the exit. Only valid information along with their ID and time stamp are forwarded. All zero values that are received are suppressed, thus reducing the amount of data.

In the event the buffer memories on the 3D-Flow DAQ-DSP are not installed, all photons of the three modalities, PET, SPECT, and CT, validated by the real-time algorithm in the 3D-Flow stack are moved through the 3D-Flow pyramid to the pyramid buffer memory. For the PET mode of operation, instead, the data of the photons candidate for coincidence will be moved to the circuit which regains the fixed time delay between data at different stages. and then finds coincidences.

The data are moved from many channels to fewer channels (reducing by a factor of 4 or 16) in the 3D-Flow pyramid in the way shown in Figure 13-19

The 3D-Flow processors in the pyramid, as in the stack, work in data-driven mode. A FIFO at the input of each 3D-Flow processor derandomizes data and buffers them when more than one neighbor is sending data to one processor during the same clock cycle.

Data in the example shown in Figure 13-19 flow from 16 processors of one layer to one processor of the next layer in the pyramid. The flow chart of the programs loaded into the processors of the channel reduction layers of the pyramid is shown in Figure 13-20

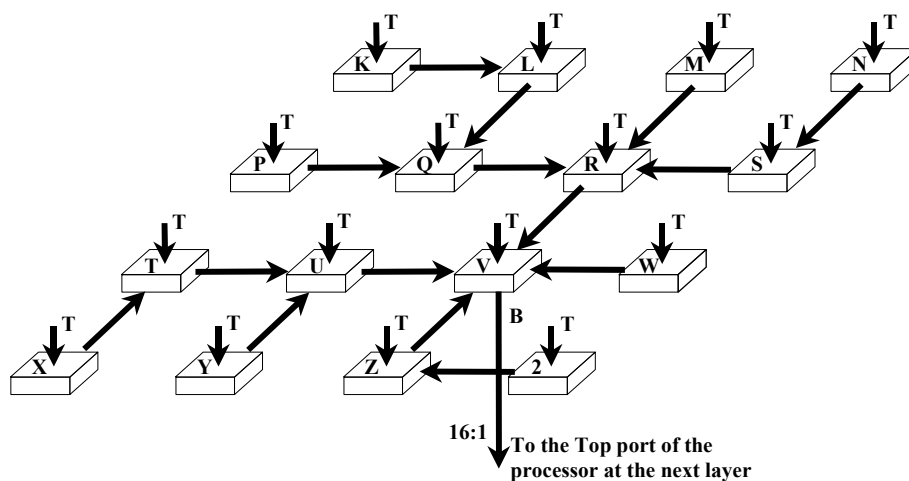


Figure 13-19. Channel reduction scheme of the 3D-Flow pyramid.

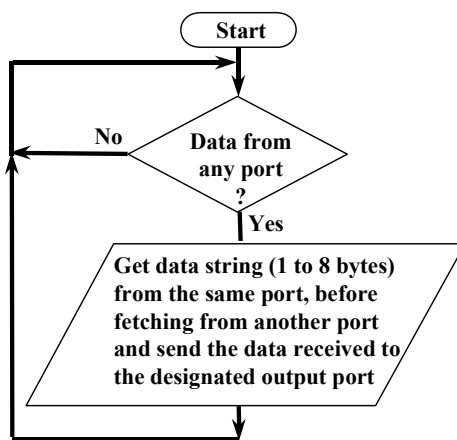


Figure 13-20. Flow chart of the 3D-Flow program routing data in the pyramid.

The 3D-Flow instruction of the program routing data into the pyramid without the buffer memory on the 3D-Flow DAQ-DSP board is shown in Table 13-2.

The same program should be modified for use with the buffer memory installed on the DAQ-DSP board. The 3D-Flow processor for this use, which has the bottom output port connected to the DAQ-DSP memory buffer, as shown in Figure 17-1, requires additional instructions to check

the field of the “event type” in the output word received (see Section 13.4.11.4) and send the received data either to the DAQ-DSP memory buffer through the bottom port in the event of a SPECT/CT datum, or to the designated output port in case of a PET datum.

Table 13-2. 3D-Flow instructions to move data in the 3D-Flow pyramid from several input ports of one processor to the designated output port of the same processor (depending on the location of the processor in the 3D-Flow array. The data received are sent to different output ports. Five programs contemplating the cases of the five ports of the processor are necessary. The following example contemplates the case of sending the input data to the output port East. Similar programs will send the received input data to North, West, South, and Bottom).

Next_event	ANYPORT TO C, C TO EAST	The 3D-Flow processor in data-driven mode operation executes the instruction when a datum at one port is present at its input FIFO. The received datum is sent to the East output port.
	SAMEPORT TO C, C TO EAST	Depending on the size of the word of the message, additional words are fetched from the same port until the message is complete. The received data are sent to the East output port.
	SAMEPORT TO C, C TO EAST	Same as above.
	SAMEPORT TO C, C TO EAST	Same as above.
	BRA Next_event	GOTO fetch another event

Besides routing the data from several input channels to fewer output channels, each processor in the pyramid has 1Kbyte of memory that can be used during the data flow through the pyramid to buffer high bursts of data for a short period of time or in case there is a concentration of input data in a restricted area.

13.4.13 Choice of an output bandwidth and design of the output stage to meet it.

Although the input bandwidth of the 3D-Flow system could sustain up to 40.08×10^9 single photons per second (calculated as 20 MHz x 2,304 PMTs), a radiation dose delivered to the patient of 5 mCi of ¹⁵O-water (equivalent to 21 mrem of effective dose equivalent to the patient) was selected. This provides a rate of about 105×10^6 single photons per second to a detector with a FOV of 157.4 cm as described in Section 17. (See Section 13.4.2, ascertaining that the 3D-Flow system provides sufficient input bandwidth).

The above consideration shows that the overall bandwidth of the system is determined by the design of the output stage of the pyramid and of the coincidence logic. The capability of the 3D-Flow system to sustain 40.08×10^9 single photons per second in input, will never impose a bandwidth limitation at the input stage for any reasonable level of radiation dose delivered to the patient, and will provide also the means to meet increased future requirements.

The above estimated 105×10^6 photons per second activity at the detector, corresponds to about 80×10^6 signals per second of single photons that are candidates for a coincidence and that produce a signal to the DAQ-DSP electronics. (The reduction from 105×10^6 to 80×10^6 is caused by the stopping power, photofraction, and crystal scattering, as described in Section 14.6). Statistically it is estimated that only 20×10^6 coincidences per second are expected out of 80×10^6 single photon per second generating a valid signal to the electronics.

Thus, from the above calculation and estimates, it is required to design the output stage of the pyramid and of the coincidence detector circuit with the capability of accepting in input about 80×10^6 single photons per second and the capability of finding 40×10^6 coincidences per second in the event that all photons at the input are good candidates for a coincidence.

The example of the design presented in Section 13.4.14.2, is a comprehensive way of describing a problem and a solution for it. However, for the actual implementation, a scheme that makes use of the same approach is introduced, with the difference that it accounts for the highest possible extraction of coincidences from the single photons and provides the flexibility to modify the design at a future time, in the event the user will desire to increase the output bandwidth (which in this case corresponds also to the overall system bandwidth. See Section 13.4.14.3).

13.4.14 Coincidence identification functions implemented in the 3D-Flow pyramid

13.4.14.1 Sorting events in the original sequence and regaining fixed delay between data at different stages

The original sequences of the events as they were acquired by the detector, as well as their latency time from a location in a layer of the pyramid with respect to the time when they were created, are lost at the

last stage of the pyramid. The reason is that events have followed different paths (short and long) when moved through the pyramid.

The task of this stage (or vertex of the pyramid) which is implemented with a layer of 3D-Flow processors (one component is sufficient for the applications described herein), is that of sorting the events in their original sequence and regaining the fixed latency time between data at different stages.

Figure 13-22 shows the flow of results (photons identified by the real-time algorithm in the 3D-Flow stack) from the 3D-Flow stack to the coincidence circuit.

The right side of the figure shows the flow of results from one stage of the 3D-Flow system to the next stage with the relation of the time delay of the data in different stages.

The real-time algorithm and its implementation with the 3D-Flow providing the results, shown on top left of Figure 13-22 as output from the 3D-Flow DAQ-DSP stack, is described in Section 13.4.11, Figure 13-17, and its implementation is shown in the left section of the logical layout of Figure 17-1, on the right section of the logical and physical layout of Figure 17-2, and on the physical board layout of Figure 15-1, Figure 15-2, Figure 15-3, and Figure 15-4.

The 3D-Flow program for the funnelling of the data through the pyramid, shown in the center left of Figure 13-22, is described in Section 13.4.12.2, Figure 13-19, Table 13-2; and its implementation is shown on the same figures mentioned in the previous paragraph.

The sequence of operations performed in the circular buffer shown in the center of Figure 13-22 are described in Figure 13-21, and their implementation is shown in the logical layout on the center section of Figure 17-1 (see processor 84 of chip 155, and processor 96 of chips 156 and 157), and on the IBM PC board layout of Figure 15-5, and Figure 15-6.

The circular buffer memory in the center of Figure 13-22 receives the data from the last layer of the pyramid. The program loaded into the 3D-Flow processor implementing the circular buffer, reads the field of the time-stamp of the event received from the pyramid and uses the value of its content to calculate the address (write pointer) of the circular buffer where the event just received should be stored.

This operation has the effect of sorting and regaining the fixed latency delay between data.

At the system speed of 20 MHz the circular buffer is read out when all photons with a given time stamp have been stored in the circular buffer. (The reading should allow the data of the photon from the channel that follows the longest path of the pyramid being stored in the circular buffer).

The reading of the circular buffer(s) at any given time (50 ns period) will provide all photons that occurred n time periods before in the detector. Not more than 4 are expected on average for each 50-ns period for a 5 mCi of ^{15}O -water radiation dose delivered to the patient for a PET with a FOV of 157.4 cm.

The task described in the next section will be that of executing all possible comparisons (6 comparisons) among the 4 photons found, in order to identify those in time coincidence that satisfy a certain set of criteria identifying the location of the radioactive source.

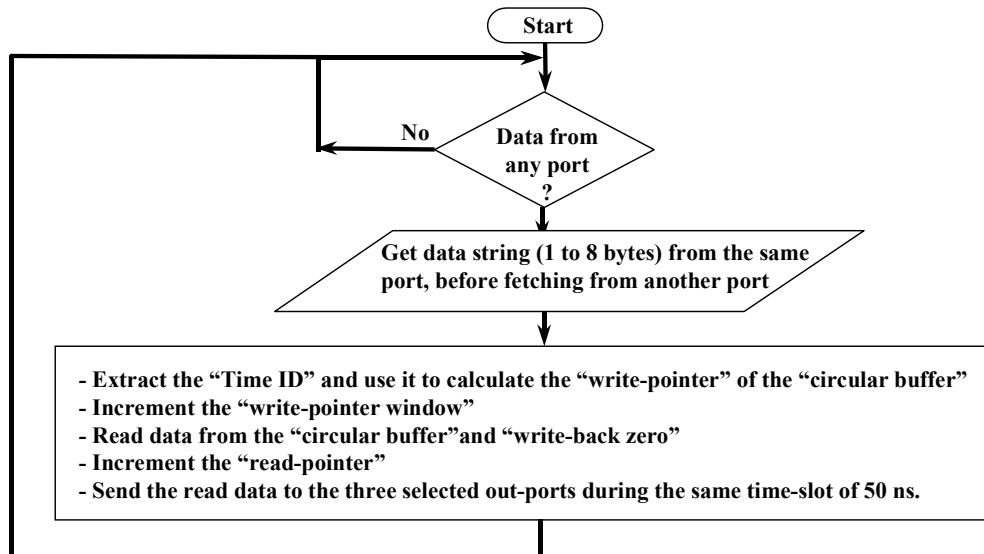


Figure 13-21. Sequence of operations for the implementation of the circular buffer for sorting and regaining fixed latency of events.

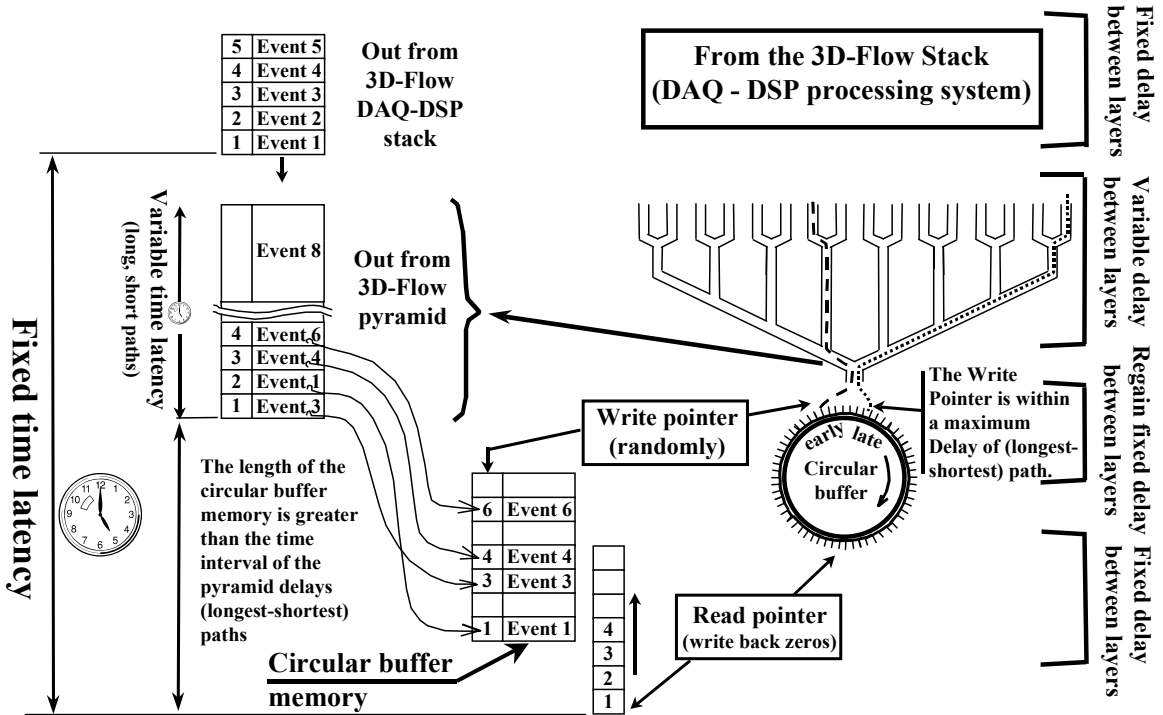


Figure 13-22. Sorting the events in the original sequence and regaining a fixed delay of the data between stages.

13.4.14.2 Example of a coincidence detection implementation with the 3D-Flow

There are several ways of using the scheme of the circular buffer described above for detecting all possible photons belonging to a specific time period n of 50 ns (or, any sampling time period of the system). One simple example is described in this section, while an example for a more general application requiring maximum photon detection with the possibility of increasing the output bandwidth of the system is described in Section 13.4.14.3.

In order to find a coincidence, a signal from a detector block needs to be compared with the signal from another detector block. For the sake of convenience, the detector blocks are grouped in sectors, and only 4 sectors are defined in this example. All detector elements connected by lines that do not pass through the body of the patient are grouped together in a sector (see top right part of Figure 13-23).

This scheme requires the implementation of 4 circuits of the type shown in Figure 13-22. An example of an implementation for 1,152 channels is shown in Figure 13-23 (see chips 155 and 156), and for 2,304 channels is shown in Figure 17-1 (processor 96 of chip 156 and 157, and processor 96 and 84 of chip 155).

For each sampling time period of 50 ns, the single photon detected in each of the sectors will be compared with the photon detected in the other sectors in the 3D-Flow processors of the chip indicated with the number 158 in Figure 13-23, and Figure 17-1. (In the very unlikely case that more than one photon is detected, the memory cell of that location is overwritten and the last value written is the one that will be compared). The operations performed on the data relative to the single photons received during a specific sampling time period in those processors are listed in Figure 13-25.

Figure 13-23 shows the coincidence detection scheme with the 3D-Flow requiring only one component instead of seven ASICs. Figure 13-24 shows the circuit, which requires only six comparisons amongst 4 photons (A-B, A-C, A-D, B-C, B-D, and C-D) every 50 ns, as opposed to approximately 700 comparisons every 250 ns, in current PET, and provides a rate of coincidences found up to 40 million coincidences per second instead of 4 million coincidences per second, as is the limitation of the current PET (see references [116, 121]).

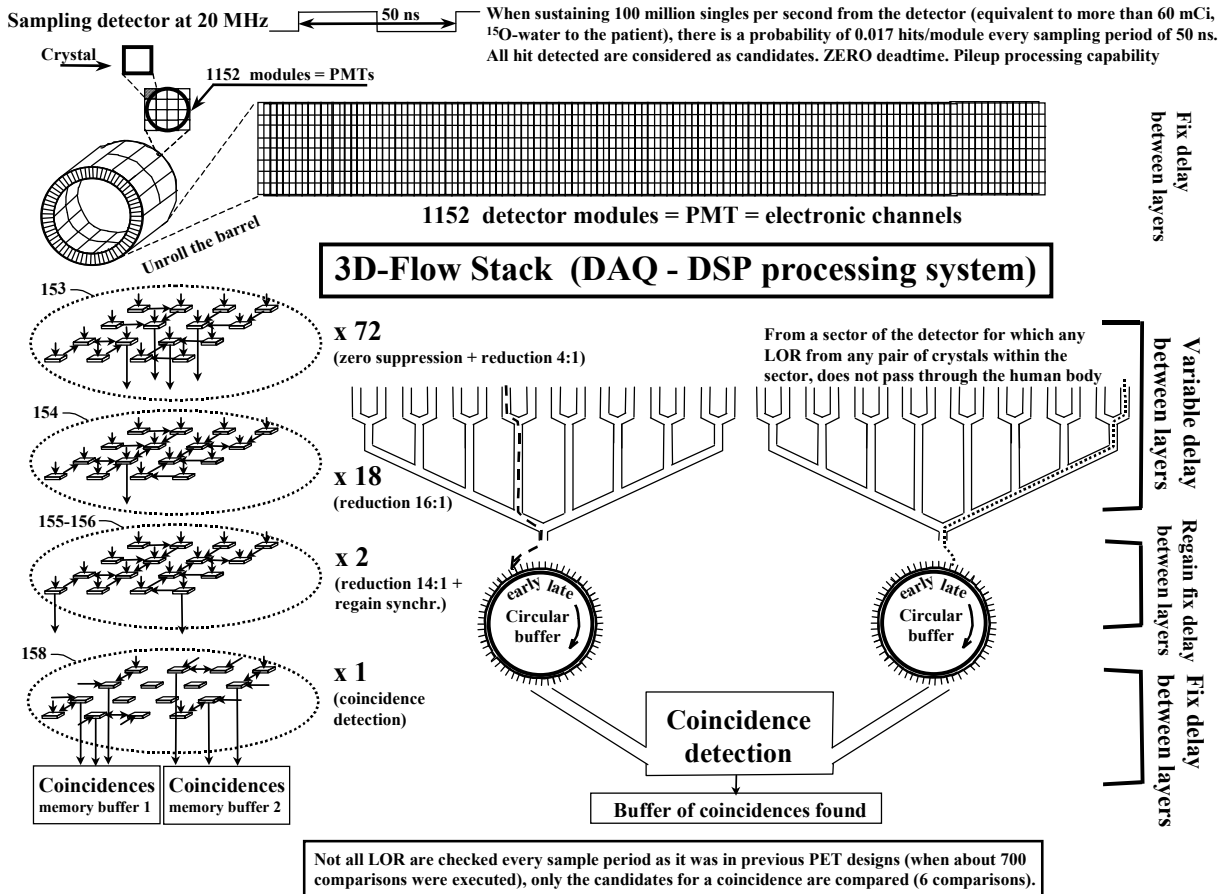


Figure 13-23. Coincidence detection scheme with the 3D-Flow approach. Only the candidates found within a time of 50 ns are compared (no more than 4 are expected). The candidates from different detector blocks may require different numbers of clock cycles to reach the exit point; thus a sorting/resynchronizing circular buffer realigns the events in the original sequential order and within a fixed delay time from when they occurred. The left part of the figure shows how many types of 3D-Flow components are required to implement the different functions.

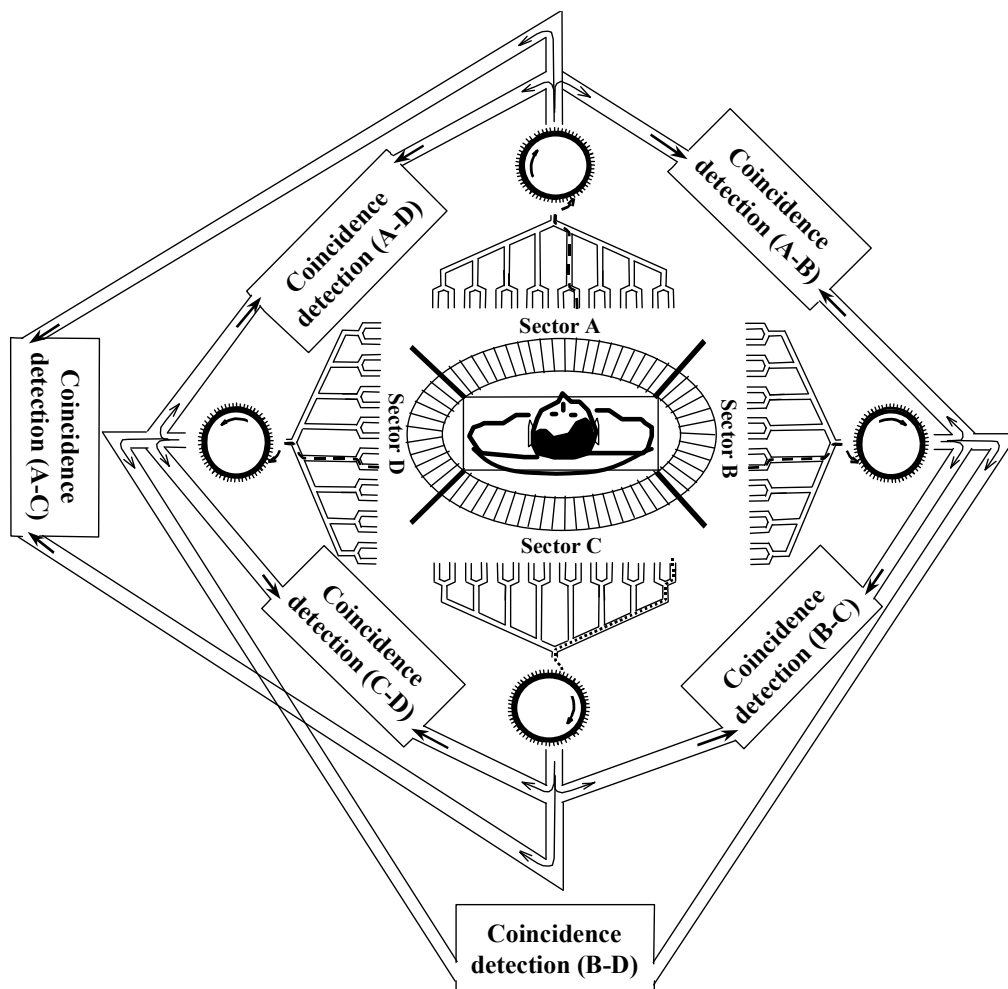


Figure 13-24. Definition of sectors for the detection of coincidences in PET mode.

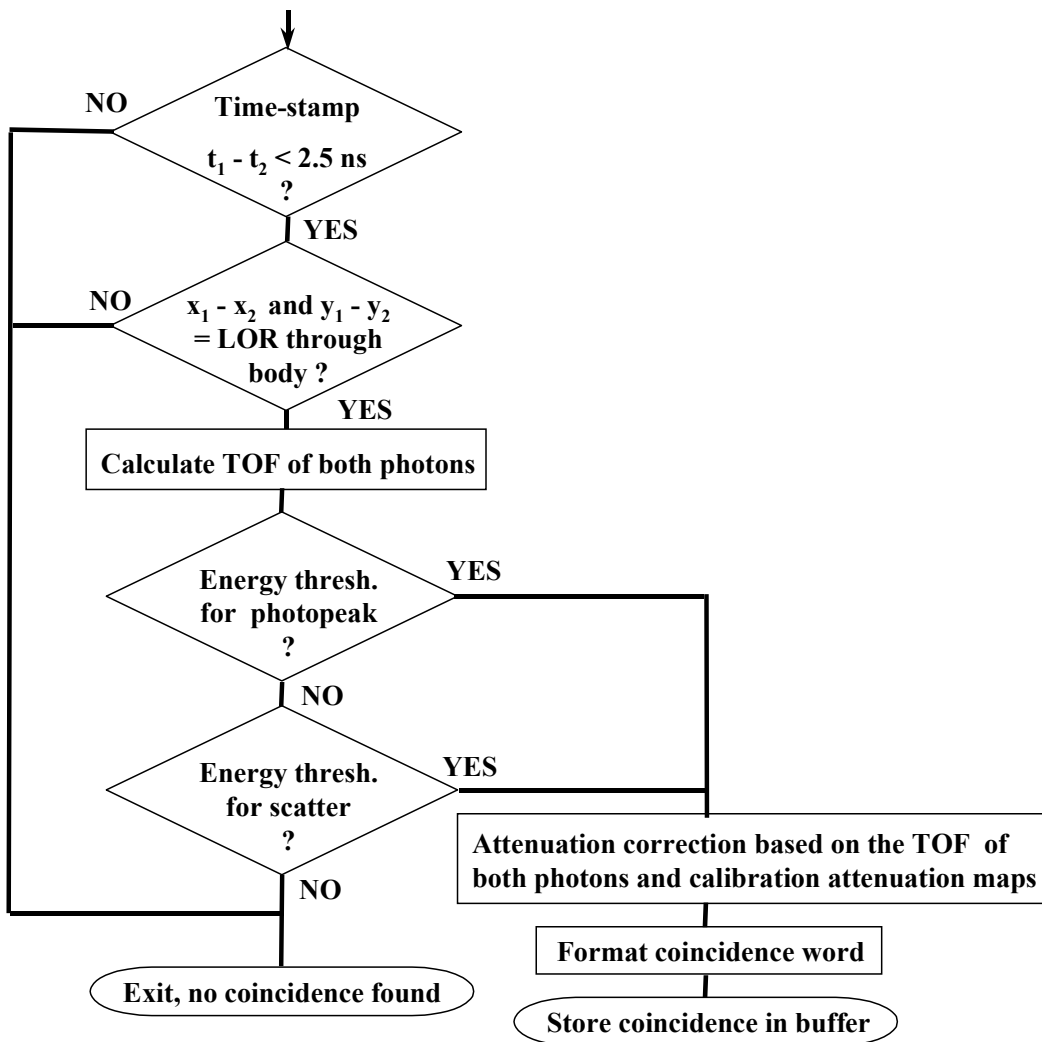


Figure 13-25. List of operations performed in the processors of component 158.

13.4.14.3 General scheme for implementing a system with higher bandwidth and maximum coincidence detection efficiency

The following is a general scheme, based on the requirements of the maximum radiation dose delivered to the patient and the complexity of the coincidence detection algorithm, for implementing the circuits at the output of the 3D-Flow pyramid for sorting the photons (or events) in the original sequence, regaining a fixed latency time with respect to when the event occurred in the detector, and for identifying all coincidences.

The basic idea of the approach is very simple. There is no segmentation of the detector in sectors as was done before. If the radiation delivered to the patient creates 80×10^6 single photons per second, the circuit described above for sorting and realigning the latency needs to run also at 80×10^6 . A single circular buffer is implemented at the speed equal to or higher than the rate of the single photon created.

Each photon detected within the sampling time window of 50 ns is compared with all other photons of the same time window (e.g., 6 comparisons for 4 photons, 10 for 5 photons, 15 for 6 photons, (or $(n \times (n-1))/2$), regardless of whether or not the x, y position of the two photons being compared lie along a line passing through the patient's body.

A 3D-Flow processor can be used for implementing the comparison circuit. A set of 3D-Flow processors working in parallel could perform all comparisons of detecting coincidences within a sampling period. For example, one 3D-Flow chip would be sufficient for a 5 mCi dose to the patient corresponding to about 80×10^6 single photons per second activity of a PET with about 150 cm FOV. The number of comparisons are so limited, compared to the approach used in the current PETs, which instead require more than 1 million comparisons every 250 ns for a FOV of about 150 cm, that it is not a problem to perform all of them.

In the event the real-time algorithm required to execute the comparison program listed in Figure 13-25 is longer than the time interval between two consecutive input data, a stack of 3D-Flow (for one chip in x and y dimensions) similar to the stack implemented in the first stage of photon identification, can also be implemented at this stage, since all operations are synchronous and the latency of the data received are identical and are referred to the same event acquired at a specific time in the detector. The combination of the two circuits, a) the sorting and realigning latency circuit running at the speed higher than the single photons acquired by the detector and b) the real-time coincidence algorithm implemented with the

3D-Flow architecture (which allows the execution of an algorithm longer than the time interval between two consecutive data) will guarantee the identification of all possible coincidences, and will calculate the TOF of the pair of photons and apply to them the attenuation correction.

13.4.14.4 Format of the output word of the “coincidences” from the 3D-Flow pyramid to the buffer memory

The format of the output word of the “coincidences” (pair of photons) from the 3D-Flow pyramid to the buffer memory is the following:

bits 0-19 crystal spatial ID (hit1); bits 20-23 Depth of interaction (hit1); bits 24-29 photon energy (hit1);

bits 30-33 time-of-flight (hit1 and hit2);

bits 34-53 crystal spatial ID (hit2); bits 54-57 Depth of interaction (hit2); bits 58-63 photon energy (hit2);.

Two 20-bit fields for spatial ID of hit1 and hit2 allows for coding up to 1,048,575 crystals. Two-4 bit DOI fields allow for a depth of interaction of both hits with up to 1.56 mm resolution when 25 mm thick crystals are used. The energy of the two photons is coded in 64 intervals from the smallest to the highest energy value. The 4-bit field for the time-of-flight makes it possible to locate within 7.5 cm resolution the point of interaction along the line which connects the two crystals, and to measure up to 75 cm the distance in any direction inside the patient’s body. The maximum measurement could be increased by changing the coincidence time window parameter. For instance, a 3-ns coincidence time window parameter will allow the measurement of any interaction that had travelled up to about 90 cm inside the patient’s body).

13.4.15 Device operation in PET, SPECT, and CT mode

Simultaneous operation in PET/SPECT/CT mode can be performed. The instrument can detect and separate the photons acquired during transmission of 60 keV (CT scan), and during emission of 140 keV (SPECT), and emission of 511 keV (PET) mode (see Section 12.4, Section 13.4.1. The real-time algorithm identifying and separating the three types of photons is described in Section 13.4.11, and the output word carrying the information of the photons identified for the three modalities is described in Section 13.4.12).

If the memory buffer is not installed on the 3D-Flow DAQ-DSP board, all photons from the three modalities are forwarded to the pyramid buffer memory.

Buffer memories of different sizes can be installed up to a maximum of two DIMM memories of 4 GB each, making it possible to accumulate up to 1 billion coincidences. This is equivalent to 50 seconds of scanning at the acquisition rate of 20 million coincidences per second, (or equivalent to 13.8 hours scanning buffering at the rate of the current PET devices of 20,000 coincidences per second).

13.4.16 Reading results from the event buffer memory and packing for transmission in the PETLINK digital interconnect standard

The IBM PC reads the data from the two DIMM buffer memories of the pyramid (or from the buffer memories of the DAQ-DSP boards when installed). The format may be changed by a program in C++ on the IBM PC CPU if it is desired to conform with the PETLINK [165] digital interconnect standard. However, the user might consider using the format described above in Section 13.4.14.4, because it provides information on the energy of the photon and the TOF, which is useful information for improving the signal-to-noise ratio of the image during reconstruction.

14 Comparison of the 3D-Flow approach vs. current approach

The PET with the 3D-Flow system differs from the current PET systems by providing the capability of delivering to the patient a very low radiation dose and of performing the examination in a shorter time, thus at lower cost, making the device suitable for cancer screening instead of being used only with patients with higher risks.

Figure 14-1 summarizes the differences between the two systems. The analysis of the performances have been made based on measurements made on the current PET manufactured by GE as reported in [23] and described also in Section 11.2.2.6.3.2. PET from other companies do not have performance very different from GE Advance (see [24, 19] and Section 3.1), and in several models the performance is even worst.

The efficiency of the current PET instrument was expressed as the ratio of coincidences detected to the radioactivity delivered to the patient, or 0.014%. This was calculated as 200×10^3 coincidences per second found, divided by 1.424×10^9 disintegration per second of the source activity, at half the scanning time period of 60 seconds, which started 20 seconds after injection of 66 mCi of the tracer ^{15}O -water. Based upon this finding, the efficiencies of the other intermediate stages were calculated or estimated with the purpose of discovering which stages are least efficient and most in need of improvement. It is in those stages that we find the greatest opportunity to improve overall efficiency, and that is where the effort involved will provide best results. (See also Section 3.1 for the description of a direct measurement of the efficiency during examination).

The efficiency of the PET of this proposal with the 3D-Flow (see bottom-right of Figure 14-1) is 10% (calculated as 4.75×10^6 coincidences/sec found, divided by 47.4×10^6 disintegration/sec of the source activity, at half the scanning time period of 60 seconds, which started 20 seconds after injection of 2.2 mCi).

The number of coincidences per second found by the PET with the 3D-Flow system (4.5×10^6) is 22.5 times greater than that found by the GE Advance PET (200×10^3). The radiation dose to the patient required by the PET using the 3D-Flow system is on 2.2 mCi. That required by the GE Advance PET is 66 mCi, 30 times greater.

The total difference in efficiency between the two systems for this type of measurement is $22.5 \times 30 = 675$ times, which is well above the factor of 400 claimed in the preface of this book.

The values in the third column from the left in Figure 14-1 report the efficiency for the GE PET (and similar machines) at the different stages. Low efficiencies spotlight stages needing improvement, and at only 8.1%, the electronics stage shows the greatest need.

(The estimate of 8.1% efficiency of the electronics is even optimistic. In reality it might be worse than that, because the particular examination described in [23] was made on the brain, where the radioisotope concentration is higher than many other parts of the body. The computations have been done with the assumption of an average equal distribution of the radiation over the entire body and to account for 8.5% FOV over the entire body. Accounting for a higher concentration of radiation in the brain compared to the feet would give an efficiency for the electronics of even less than 8.1%.).

The next lowest efficiency stage is the field of view (FOV), which provides only 8.5% efficiency and is also dependent, in the current PET, upon the electronics. The detector design used in the current PET presents an absolute limitation on the size of the FOV, a “brick wall,” for the following reasons:

1. The current technical approach to comparing for coincidences every sampling period all possible lines of response between pairs of detectors located where the line connecting them (LOR) passes through the patient's body requires a very large number (e.g., over a million comparisons every 50 ns when 2,304 PMT are used. See Section 14.7.2.3) number of comparisons to be made if the FOV is increased. This approach is not practical, nor is it cost effective.
2. To find a solution to the problems of limitation and cost versus complexity in changes in the hardware is not possible. The circuit and cabling required by the current technical approach of the LOR as well as the poor efficiency in the photon identification circuitry at the front end, preclude achieving enough of an improvement in efficiency to justify building larger PET detectors. This puts a higher return on investment out of reach, because the goal of performing more examinations per day is unattainable

Changing the role of PET to screening for cancer							
Current PET systems				PET of this proposal with 3D-Flow			
Radiation dose	$(^{15}\text{O-water})$ 277 mrem	7/12 of 66 mCi = 38.5 mCi = 1,424 MBq		7/12 of 2.2 mCi = 1.2 mCi = 47.4 MBq	$(^{15}\text{O-water})$ 9.2 mrem		
	MBq	MBq = million Becquerel = million disintegration (or million coincidences) per second				MBq	
Photons not scattered and/or absorbed in the body	214	~15%	(1) 7% to 25% pair of photons in time coincidence leave the body			~15%	7.1
Field-of-view (FOV)	18	~8.5%	(2) FOV 15-25 cm Photons lost FOV Brick wall (B)			~95%	6.7
Solid angle	3.2	~18%	(3) Photons lost			~92%	6.2
Stopping power (SP)	2.5	~80%	(4) Stopping power + photofraction + crystal scatter SP year 1990 (30 mm = 95%) years 1998-2000 (10 mm = 57%) Photons Crystal SP for 25 mm thick = 91% Photon not stopped			~80%	5
(Photon identification)			(5) Bottle neck (C) Module dead-time for 1-2 μs, when hit found 0.5 - 1 MHz Boundary 2x2 block Limited analog proc. Poor timing resolution Poor Signal-to-Noise Brick wall (A) - Poor photon identification - Dead time			~95%	4.7
Electronics	0.2	~8.1%	(6) Bottle neck (C) 0.5 - 1 MHz Bottle neck (D) 4 MHz 1,344 ch. 56 ch. DETECTOR LOR (700) Brick wall (B) Too many LOR				
(Coincidence detection)							
0.014% Efficiency		0.2 million coincidences/sec found		4.7 million coincidences/sec found		10% Efficiency	

Figure 14-1. Comparison of the efficiency between the 3D-Flow PET system and the current systems.

The third area, with a low efficiency of 18% of the solid angle will automatically increase with the extension of the FOV as shown in row (2) of the same figure.

In summary, two “brick walls” and two “bottlenecks” have been identified in the electronics of the current PET systems (they are common also to the other PET such as the ones manufactured by CTI/Siemens) that are the cause of the low efficiency. The removal of them will improve the overall efficiency over 400 times.

Two sets of inventions remove them: group A removes “brick wall A” and “Bottleneck C” (see row (5) of Figure 14-1), while group B removes “brick wall B” and “bottleneck D,” (see row (6) of Figure 14-1. The removal of “brick wall B” with a much simplified hardware electronics allows the increase of the FOV shown in row (2) of the same figure.)

The following subsections of this chapter describe in detail the limits of the current PET electronics and the details of the solution that overcomes each one of them can be found in Section 13.

14.1 Requiring 1/30 the radiation to the patient with the 3D-Flow system.

The top of Figure 14-1 shows the radiation dose delivered to the patient with the current PET systems and with the PET of this proposal using the 3D-Flow architecture. The radiation dose of 66 mCi of ¹⁵O-water delivered to the patient for an examination with the GE Advance PET [23] (corresponding to an effective radiation dose of 227 mrem [11], which is approximately equivalent to what a person in Seattle (WA) [166] receives during one year from all other sources), is 30 times more than the 2.2 mCi radiation dose required to be delivered to the patient with a PET of this proposal incorporating the 3D-Flow design. (2.2 mCi of ¹⁵O-water, corresponds to an effective dose of 9.2 mrem. This is equivalent to radiation received on a one-way flight at high altitude between the United States and Europe or Japan).

14.2 Identifying from 14 to 40 times more photons than the current PET

The PET using the 3D-Flow system finds 22.5 times the number of coincidences found per second by the GE Advance PET (calculated as 4.5×10^6 coincidences/sec found by the PET with the 3D-Flow system, divided by 200×10^3 coincidences/sec found by the GE Advance PET). Similar performance differences occur in the case of CTI/Siemens PET models (SeeSection 3.1).

14.3 Photons scattered and absorbed in the body of the subject

The first reduction in photons from the original activity of the source of radiation (the tracer of imaging agent carrying the isotope) internal to the body of the patient is the Compton scatter and absorption inside the patient's body. The larger the volume of the matter encountered by the photons in their journey, the more chances there are that they will be scattered or absorbed. Thus depending on the weight of the subject, this stage should account for a loss of photons in time coincidence from a 75% to 93%.

(A simulation indicating more precisely the number of photons lost here with respect to a subject of a given weight can be performed with software packages from Stanford Linear Accelerator Center and Los Alamos National Laboratory referenced in [173, 174, 175, 176]. See also the definition of the term "Monte Carlo" in the glossary of this document. The simulation by Tumer reported in [167] shows in Figure 71 that 1.2×10^8 photons/sec leave the phantom out of 2.3×10^8 photons/sec created. This corresponds to an efficiency of 52%. Since PET technique requires two photons in coincidence, the percentage of the photons in time coincidence is the square of the percentage of the single photons, thus 27%. The phantom used by Tumer was a cylinder 20 cm x 20 cm in diameter that could be compared to the head of a human, while the estimate of the photons in time coincidence leaving a whole body is only from 7% to 25% depending on the person's weight. While the previous software simulation package is for more general use, the SimSET [168] software package developed by the University of Washington, Division of Nuclear Medicine, is more specifically for the simulation of PET, SPECT and X-ray events).

At this stage, for either case, assuming only 15% of the photons in coincidence leave the body of the subject, the original $1,424 \times 10^6$ pairs of photons emitted per second by the radiotracer, as shown in row (1) of Figure 14-1 are reduced to 214×10^6 pairs of photons per second. In the case of the PET with the 3D-Flow, which has an activity of 47.4×10^6 pairs of photons per second, this stage reduces them to 7.1×10^6 pairs of photons per second.

14.4 Field-of-view (FOV)

The field of view (FOV) of current PET devices is 15 cm to 25 cm. As mentioned above, the impracticability of the current approach of the

electronics, where all lines of response (LOR) are checked for coincidences, requires an exorbitant number of comparisons. When it is desired to increase the FOV, an impasse, “brick wall B,” (see row (2) of Figure 14-1) is encountered. This reason, together with the low increase in efficiency provided by the PET advances in the last 25 years, has not encouraged investors to manufacture PET devices with larger FOVs. The increase in the number of crystals required in doing so would not repay their cost.

On the other hand, the two- to three-fold increase in cost of the proposed PET device with a greatly enlarged FOV would be capable of performing up to ten times as many examinations per day as current PET because of the reduced duration of an examination. Furthermore it extends the prospective market to include use of the device as a screening implement in addition to its current use as a diagnostic tool for patients at high risk for cancer. Thus, investors can expect a return of their investment in a shorter time and the possibility of realizing greater returns in an extended market.

Row (2) of Figure 14-1 shows that for an increase from 15 cm FOV to 157.4 cm, the efficiency of the detected photons by the PET is increased from about 8.5% to about 95%. Only a minor number of photons are lost in the lower part of the legs and the feet. The “singles” generated from the section adjacent to the detector FOV are also greatly reduced (see also Figure 3-2) because most of the activity is within the FOV of the detector.

The use of an examination protocol as described in [16, 19] and in Section 3 will further capture more photons, leaving less dispersion in the legs, thus increasing the efficiency even if the field of view is shorter than the actual height of the patient. This protocol manipulates the tracer kinetics by occulting blood circulation to the legs with cuffs in order to maintain the difference between activation and baseline signals longer than standard protocols.

The 214×10^6 pairs of photons per second for the examination with GE PET are reduced at this stage to 18×10^6 pairs of photons per second, while for the proposed 3D-Flow PET the 7.1×10^6 pairs of photons per second are reduced to 6.7×10^6 pairs of photons per second.

14.5 Solid angle

Having increased the FOV, the solid angle will also increase as shown in row (3) of Figure 14-1 from about 18% to about 92%. The 18×10^6

pairs of photons per second for the examination with GE Advance PET are reduced at this stage to 3.2×10^6 pairs of photons per second, while for the proposed 3D-Flow PET the 6.7×10^6 pairs of photons per second are reduced to 6.2×10^6 pairs of photons per second.

14.6 Crystal stopping power, photofraction, and crystal scatter

Ideally when a 60 keV, 140 keV, or 511 keV photon interacts with a crystal, all energy would be deposited and converted to light. However, that is not the case for many crystals even if the thickness of the crystal is increased. Semiconductor detectors [169, 170] will have a better stopping power and a much more efficient detection of x and γ rays, however, they require to operate at low temperature ($T = -196^\circ\text{C}$).

Photons in crystal detectors undergo Compton scatter (see Section 13.4.5.4), and some of the secondary photons leave only a portion of the 511 keV of the incident photon in the detector. Part of the energy leaves the crystal in the form of another photon. Different crystals have different characteristics, but if the electronics had the capability to analyze thoroughly the signals created by an incident photon, then the useful information could be extracted from its energy spectrum, and some events with crystal Compton scatter would be captured.

The 3D-Flow design with digital signal processing capabilities at this stage, would be very useful for extracting the energy spectrum [171] by processing the signal from each channel, and these signals can also be integrated with the information from their neighbors. The flexibility of the 3D-Flow allows the designer to choose and combine different detectors, each one aiming to provide the essential information at the lowest possible cost. The processing capability of the 3D-Flow system can process the information from different detectors of a given view angle of the source.

An efficiency for both designs (old and new) of 80% has been assumed at this stage (see row (3) of Figure 14-1).

The estimate acceptance of 80% of the photons in time coincidence at this stage, provides a reduction from 3.2×10^6 pairs of photons per second in time coincidence to 2.5×10^6 pairs of photons per second in time coincidence. The same efficiency was also calculated for the 3D-Flow PET which provides a reduction from 6.2×10^6 pairs of photons per second in time coincidence to 5×10^6 pairs of photons per second in time coincidence.

14.6.1 Crystal stopping power

Crystals with high density (see Table 11-1) provide a good stopping power. The PET built in the years 1990-1996 (see Table 1-3) used mainly 30 mm BGO crystals which are reported in Table 1 of [1] to have 91% efficiency for 511 KeV when 25 mm thickness is used and 100% efficiency for 140 keV photons.

In part due to the cost and in part due to the limitation of the current electronics for PET, during the most recent years the crystal thickness has been reduced from 30 mm to 10-15 mm [110, 38]. (The 3D-Flow architecture of the novel approach presented herein overcomes the electronics limitation.) Most recent PET from 1996 to 2000 and the ones on the drawing board are using crystals with a thickness of 10 mm [12, 110, 111] (see also Section 3.1 for the 57% crystal efficiency claimed for the GSO PENN PET) and 15 mm (see Section 11.2.2.1.1).

The crystals used in the GE Advance PET, the measurements of which are used in Figure 14-1, have BGO crystal thickness of 30 mm, which provides a stopping power efficiency close to 100%, and their proposed new design projects a crystal thickness of 25 mm, which provides about 90% efficiency in stopping power.

14.6.2 Photofraction

The measure of the capability of a scintillation detector to absorb photons is the photofraction. Several factors such as: attenuation coefficient, crystal density, effective Z, and detector size affect the photofraction that can be measured as:

$$\text{Photofraction} = \frac{\text{Number of Photopeak Events}}{\text{Total number of Events}}$$

A photopeak event is that which occurs when most of the photoelectric interaction results in full deposition of the gamma-ray energy in the detector.

The photofraction of a BGO crystal 5.6 mm x 30 mm x 30 mm is about 65%, and less for GSO, and BaF₂.

14.6.3 Crystal scatter vs. scatter in the patient's body

Although one cannot distinguish between the crystal scatter and scatter in the patient's body, the digital signal processing of the 3D-Flow can capture the useful crystal scatter by summing the energy from neighboring detectors and applying DSP filtering algorithm. With the use of graded absorbers, it can also recognize most of the events reaching the detector that were scattered within the patient's body. With a DSP at each channel, the efficiency at this stage should not be calculated as the reduction provided by the stopping power minus the reduction factor of the photofraction, because the digital signal processing can capture some useful crystal scatter.

The body scatter which cannot be rejected by the electronics at this stage will be rejected by the off-line image reconstruction algorithm, while the crystal scatter events recognized by the real-time 3D-Flow DSP processing will contribute to improve the image quality.

14.7 Electronics

The reason for the poor efficiency of the electronics (8.1% or lower in the current PET; see row (5) of Figure 14-1) is to be attributed first to the poor identification of the photons and their characteristics (this operation is common for the three modalities: PET, SPECT, and CT). Because identification of the good photon candidates at the first stage was not optimized, the following stage, the detection of coincidences (see row (6) of Figure 14-1), becomes meaningless. If one of the pair of photons has already been discharged, the device obviously cannot find coincidences.

14.7.1 Identification of photons and extraction of their characteristics

Several factors responsible for poor particle identification are a consequence of the approach taken to the electronics of the current PET. Attempting to improve improving the photon identification by trimming and fine-tuning the electronics in the PETs using the current approach has definite limits, "brick wall A."

No matter how much analog signal processing is put into the current PET design, the problem remains that the complete sources of information and the hardware platform to handle them are missing.

The information to the north, east, west, and south of the signal from the incident photon are missing; thus it is impossible to reconstruct the total energy of the incident photon. The positioning is also difficult to

calculate. As long as there is a fixed segmentation of a 2x2 detector module, there will always be an incident photon that will hit the edges or corners of the block and some information on one side of the hit will be missing (see Section 13.4.8).

Unless a drastic change in the overall approach (in detector block segmentation, analog processing, processing for increased timing, spatial resolution, and signal-to-noise improvement) is made, it will be impossible to effect significant improvement.

In order to tear down this “brick wall A,” the data acquisition system of the PET should acquire data from all channels of the detector, and then the electronics should provide a method to evaluate each channel to determine if it is the head of a cluster of the incident photon (2x2, 3x3, 4x4, 5x5, etc., depending on the energy of the photon and the area covered by one channel). This can only occur if no boundaries are set *a priori*, and if each channel can have on its own processing unit all the information (including signals from its neighbors) necessary to determine if it is the head of a cluster of an incident photon..

The 3D-Flow overcomes this “brick wall” with its architecture. Data from each channel (PMT, or more generally, any sensor within a given view angle) are acquired, converted to energy through a look-up table before summation, exchanged with the neighbors, and processed for photon characteristic extraction. Each individual channel is analyzed at a rate of 20 MHz to determine if it is the head of a cluster of an incident photon with respect to all its neighbors.

Most of the PETs used in hospitals nowadays operate on a time window of about 12 ns over signals with a time resolution of about 2.5 ns when attempting to separate one event from the other. Considering that in 2.5 ns the photon travels a distance of 75 cm, and that in 12 ns it travels 3.6 meters, the timing resolution provided is not of great help in identifying the coincidence event. It is so broad that many events could have occurred during that time; and the resolution is so poor that it does not help to separate the photon of one event from the photon of another event. In other word, more to the point, it cannot tell for sure if two detected photons belong to the same event.

The 3D-Flow system can achieve better timing resolution by acquiring for each signal rising edge the timing information (time-stamp) of the photon absorbed by the detector. The signal is sensed by the CFD which passes the logical output on to a time-to-digital converter (TDC), which

produces a 500 ps resolution time-stamp. The time-stamp is then processed by the FPGA and the 3D-Flow for best timing resolution determination. (The 3D-Flow can also extract timing information by means of the DSP on the acquired PMT signals).

14.7.1.1 Front-end electronics of the 3D-Flow system vs. current PET FE electronics

In Figure 14-2a, at left, is shown the Digital Signal Processing (DSP) of the 3D-Flow system with digital signal integration functionality as opposed to the analog signal processing implemented in the current PET systems in Figure 14-2b.

The specific circuit shown at right in Figure 14-2b is used in several models of PET devices manufactured by CTI/Siemens [172]. Although it has the merit of being able to remotely control 8 parameters to fine-tune each channel (the gain of the 4 preamplifiers, the constant fraction discriminator threshold, the x and y offset, and the time alignment of the system clock), those variables still place a limit on the processing of the analog signal compared to the flexibility of digital signal processing.

In the same circuit used in the current PET, the signals received from 4 photomultipliers (PMTs) are then combined and integrated over a period of the order of 1 μ s to form an energy signal and two position signals (axial and transaxial).

Any attempt at processing of the above signals will encounter a brick wall, because they carry the information of 4 PMTs and cannot be decomposed for further enhancement of energy, spatial resolution, or timing resolution. The attempts made in the current PET, with its mix of look-up tables and analog processing to decompose the signals and decode the position and energy information absorbed by the crystal that was hit, will never be able to achieve good performance, because the neighboring information to the 4 PMTs (2x2 array) is missing.

The gain control of the preamplifier is good; however, if the PMT does not deliver an optimum signal, it does not help to be able to increase the gain of it. A better control would be that of the power supply to the PMT as in the 3D-Flow system.

The sum of 4 analog signals used in current PET may be critical because it adds in the noise as well, while the 3D-Flow converts the ADC counts of each individual channel through the internal look-up tables and subtracts individually the noise of each channel, by means of its DSP functionality, before summing them.

The position and energy lookup tables shown on the right of Figure 14-2b encounters the difficulties and limitations in identifying position and energy of the incident photon as explained in Section 13.4.9.

Using a look-up table immediately after receiving, from each channel and not from each group of four, the ADC counts from the analog-to-digital converter (as is projected in this new proposal) provides the possibility of including all specific corrections for each channel (gain, non-linear response of the channel, pedestal subtraction, etc.).

The 3D-Flow can extract much more information (area, decay time, etc.) from the signal received performing digital signal processing on the last four or five received signals from the direct PMT channel and on the 3, 8, 15, or 24 signals from the neighboring PMTs via the North, East, West and South ports of the 3D-Flow.

The tuning of each channel with a digital look-up table is also convenient, because the calibrating parameters can be generated automatically from calibration measurements.

Digital Signal Processing vs. Analog Signal Processing

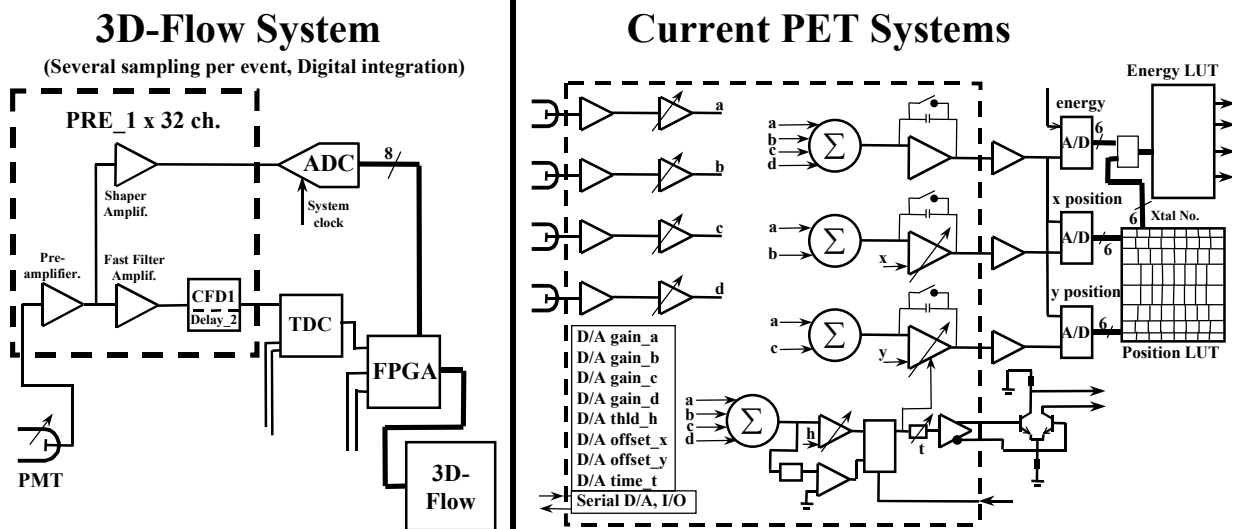


Figure 14-2. Digital Signal Processing vs. Analog Signal Processing Front-End for PET with digital signal integration.

14.7.1.2 Elimination of the detector blocks boundaries

The fixed cabling in current PET of the 2x2 PMTs is another limitation. When a photon hits the detector at the edge of the 2x2 block and the energy is split between the two blocks, both may reject it because they do not see enough energy.

This is solved with the 3D-Flow system where each signal (PMT with a group of crystals associated with it) is checked to see the local maximum of a cluster against its 3, 8, 15, or 24 neighbors without any boundary limitation. Details on how this functionality is achieved in the hardware implementation is shown in Figure 15-7.

With the 3D-Flow approach, the entire PET system is seen as a single large array instead of several 2x2 blocks that, introduce boundaries. There is no difference in efficiency in event identification between the crystals in the center and those on the edge of a 2x2 block because there is no block definition, but each channel is a block that receives the information from all its neighbors.

14.7.1.3 Elimination of the incoming data bottleneck

There is a bottleneck, shown as “Bottleneck C” in Figure 14-1 (See also Section 13.4.2), in the incoming data in the current PET for the following reasons:

- a) The detector in current PET is segmented into 56 modules [23] (or a number not very different for PET from other companies, see Section 11.2.2). Each module covers a large detector area; and when crystals with slow decay time are used, the entire module is unable to acquire data (dead time) for 1 to 2 μ s when a hit is detected. (This corresponds to a capability of receiving photons continuously from the same module only at a maximum rate of 0.5 to 1 MHz.). For an activity of about 100×10^6 single photons per second received from a detector with 56 modules, there is a 44% probability that a photon will hit a module during a sampling time period of 250 ns. This has to be compared with 0.43% probability that one of the 1152 detector elements of the 3D-Flow implementation will be hit by an incident photon every 50 ns when the activity at the input is the same, 100×10^6 single photons per second. (See also Section 16).
- b) The coincidence electronics in the current PET cannot handle the 1,344 acquisition channels, but an arbitrary reduction is made to

56 channels. The reduction is based on a simple check to find out if a signal received from the sum of 4 channels is within a certain energy window. To avoid this bottleneck, a more thorough check of all the characteristics of the incident photon, to see if it conformed to the ones expected, would be required.

The 3D-Flow system overcomes the above “bottleneck C” because it has a sampling rate of 20 MHz for a 64-bit word received individually on each of the 1,344 channels, sustainable continuously on all detectors. A real-time algorithm that checks thoroughly all parameters characterizing a photon is executed on the data of an entire event and each channel is investigated to determine if it could be the head of a cluster. The 3D-Flow feature of extending the processing time in one pipeline stage, allows the execution of real-time algorithms longer than the time interval between two consecutive input data (see Section 12). In the event the rate of 20 MHz cannot be sustained for other reasons not dependent upon the electronics, such as crystal slow decay time, having the 3D-Flow handle each single channel of the 1,344 channels means that only one channel out of 1,344 (and not one out of 56 as is in the current PET) will be dead for the duration of the decay process in the crystal.

14.7.2 Coincidence detection logic

14.7.2.1 The approach of coincidence detection used in the current PET

The approach to detecting coincidences in current PET machines installed in hospitals is similar. I will describe only the General Electric Advance, and I will provide the references to a similar one implemented by CTI/Siemens. Together, the above-mentioned manufacturers have the largest section of the PET market in the world.

Their approach requires the electronics to compare all pairs of signals from crystals which are points on a line passing through the patient's body.

Using this approach, for a system with n channels, all possible comparisons between all channels are: $(n \times (n-1))$ divided by 2. Since in the PET application only the crystals which are a point on a line passing through the patient's body are useful, the number obtained for all possible combinations further divided by 2, will be approximately equal to all LOR of a PET.

Current PET [23, 116] for a 15-cm FOV have about 56 modules and perform about 700 comparisons along all LOR passing through the

patient's body. This implies that ALL comparisons (about 700) are executed every 250 ns at each LOR, even if NO hit occurred at a specific module. The number of 700 comparisons is calculated by applying the above formula as follows: $(56 \times 55)/2 = 1540$ provides all possible combinations, and since not all LOR pass through the patient's body, approximately half are the total LOR which need comparison.

The use of this approach on a PET with an increased field of view runs into "brick wall B." (See Figure 14-1). The number of LOR to be checked and compared will increase enormously, the complexity of the consequent circuitry will also increase, and the time available to execute all the comparisons will not be sufficient. If a larger number of channels are arbitrary dropped as is done now from 1,344 to 56 channels, additional inefficiency will be introduced. Any decision to perform the coincidence detection task using the current approach has a drawback which introduces inefficiency, becomes very costly, or is impossible to execute within a short sampling time period.

On the left of row (6) of Figure 14-1, bottleneck C at the front end is shown. This problem, as described above, also affects the coincidence detection efficiency, because the arbitrary reduction of the number of photons detected by the 1,344 channels to 56 channels lowers the probabilities that a photon will find its companion in time coincidence.

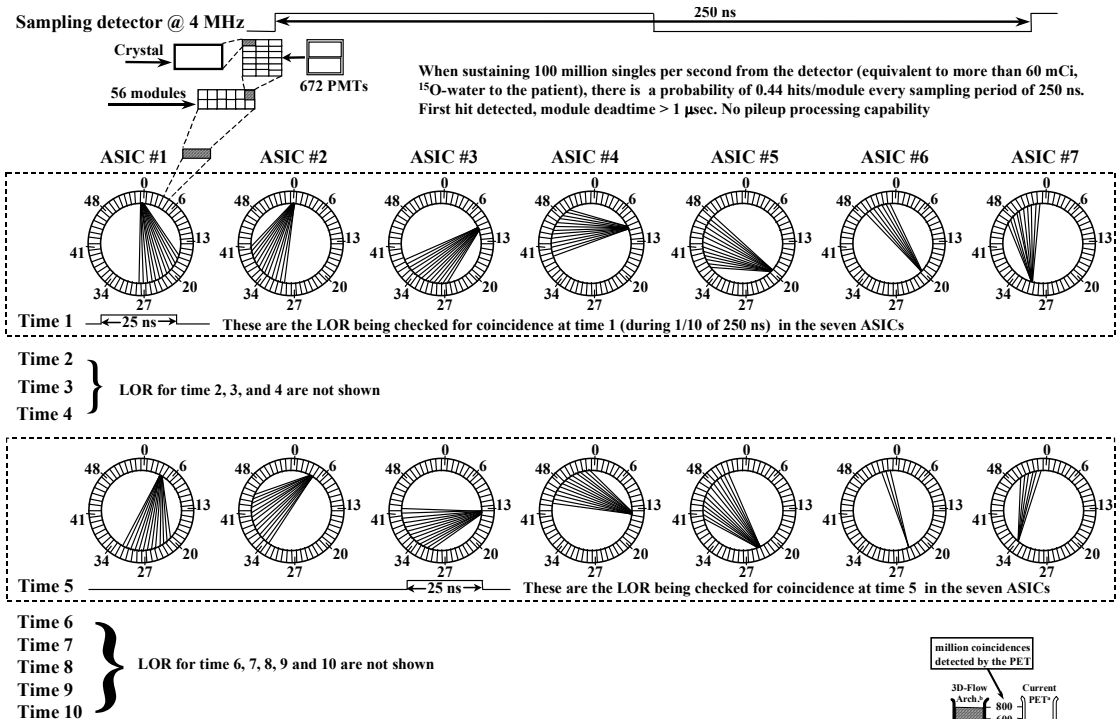
The entire hardware system of the current approach by GE Advance and the coincidence electronics is described in the patent [116] and in references [117]. The 1,344 blocks are reduced in number and grouped into 56 modules with 24 blocks per module, for the reason that the cost of a circuit testing all possible combinations (LOR) of 1,344 blocks would be exorbitant

Every 250 ns, all 56 modules (see Figure 14-4) acquire the information from a set of 24 crystal blocks. The first "single" satisfying the energy requirements received in one of the 24 blocks of a module prevents other "singles" in the same module from becoming coincidence candidates. This arbitrary selection of the first single among all the possible candidates introduces dead time. For an activity at the detector of 100×10^6 photons per second, the probability that a module is hit during the 250-ns sampling time period is 0.44 hits per module. The calculation is: during an activity of 100×10^6 singles per second hitting the detector (which requires an estimated dose of more than 60 mCi of ^{15}O -water to be delivered to the patient for a PET with a FOV of 15 cm.), then each of the

56 modules has the probability of receiving, during every 250 ns, the number of incident hits divided by the number of modules multiplied by the sampling rate $(100 \times 10^6) / (56 \times 4 \times 10^6) = 0.44$.

Figure 14-3 shows the line of response tested by each of the seven ASICs of the GE PET during time slots 1 and 5 of the 10 time slots of 25 ns each within the sampling time of 250 ns. Table 14-1 provides the interconnection between the 56 modules and the seven coincidence ASICs, and Figure 13-23 show the layout of the 56 modules and the 7 coincidence ASICs. The entire circuitry can detect one coincidence during the sampling time of 250 ns, providing a maximum coincidence rate of 4×10^6 per second (see reference [23]). However, measurements performed have shown a rate of 200×10^3 coincidences per second at half the scanning time period of 60 seconds starting 20 second after injection of the patient with 66 mCi of ¹⁵O-water radiotracer [23] (See also Section 11.2.2.6.3.2).

CTI/Siemens uses the same approach which is described in [105], and its ASIC implementation is described in [120]. The coincidence detection circuit is based on the same approach as for the General Electric PET, but the CTI/Siemens device detects coincidences among 16 modules instead of 56 modules (see [121]. Note that the 3D-Flow with its novel approach detects coincidences among 1,344 or more modules requiring only six comparisons). In 1993, a subsequent VLSI implementation [123] of the



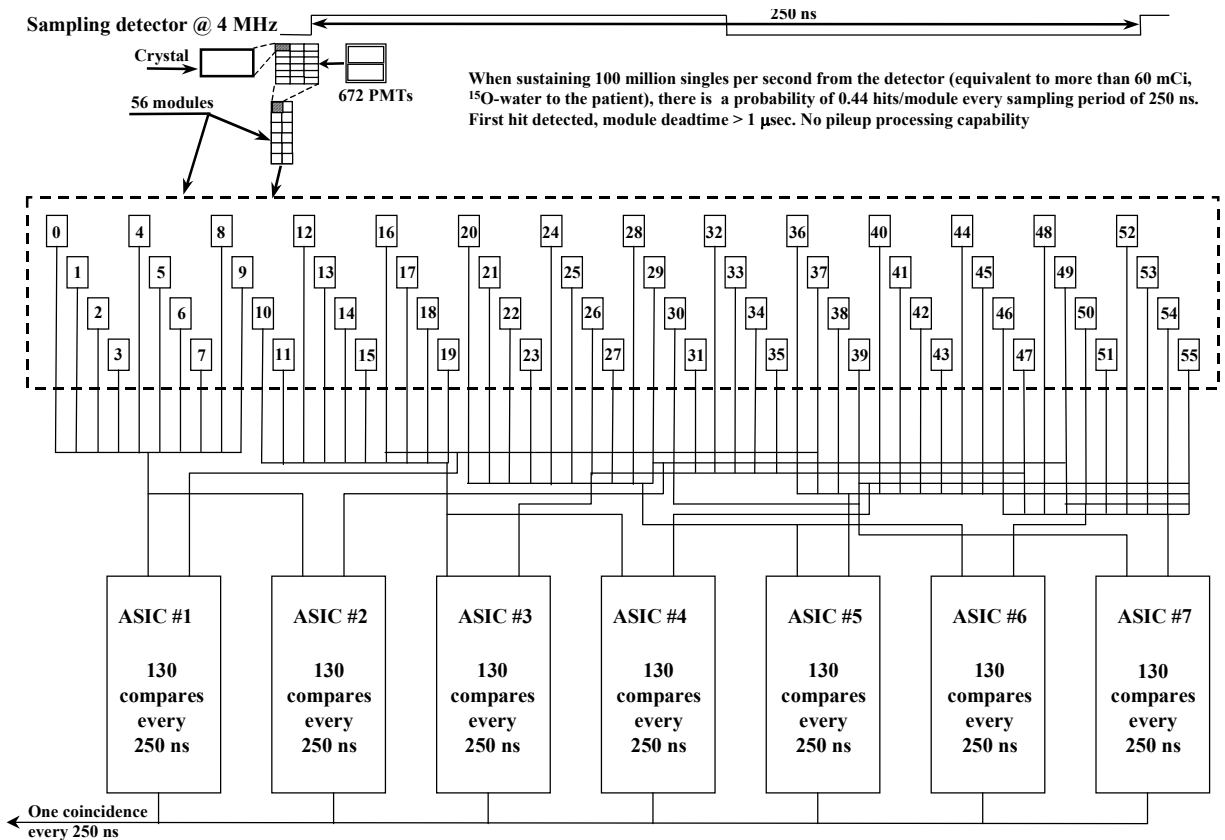
Fix relation (connection) between the detector and the coincidence electronics.
All comparison (about 700) at each LOR are executed even if NO hit occurred at a specific module

coincidence circuit by the same group presents an improvement by optimizing the silicon area.

Figure 14-3. LOR checked for coincidence as implemented on the GE Advance. Data from 56 detector modules are sent to 7 ASICs according to the connection scheme reported in Table 14-1. Each ASIC performs 13 comparisons each time slot of 25 ns. The first row of the figure indicated with “Time 1” shows the detector modules that are compared (e.g. at top left of Time 1, module 0 is compared with module 16, then with 17, and so on). The figure shows only the comparisons along the line of response LOR during Time 1 and Time 5.

Table 14-1. Connection of each of the 7 ASIC detecting coincidences to the 56 detector modules.

ASIC #	Detector module to ASCII column	Detector module to ASCII row
1	0-9	16-37
2	0-9	29-49
3	10-19	26-47
4	10-19	39-55
5	20-29	36-55
6	20-29	49-55
7	30-39	46-55



Fix relation (connection) between the detector and the coincidence electronics.
All comparison (about 700) at each LOR are executed even if NO hit occurred at a specific module

Figure 14-4. Connection scheme of the 56 detector modules to the 7 ASICs for the GE Advance. See also Table 12-1. Each ASIC performs 130 comparisons every 250 ns. One coincidence can be found out of about 700 comparisons with data from modules every 250 ns.

14.7.2.2 Elimination of need to compare an extremely large number of LOR when the FOV increases

The novel approach that tears down “brick wall B,” the comparison of all LOR used in current PET, is based upon the principle that the ONLY photons compared are those whose characteristics show them to be a candidate for coincidence.

Using this approach, the performance requirements of the electronics drop considerably. The number of comparisons to be made are very few and are mostly related to the radiation concentration (or activity) delivered to the patient and not as much to the size of the detector, as is the case in the approach of the current PET.

The 3D-Flow approach to finding coincidences in a PET system is to identify all possible candidates within the sampling time of 50 ns (no more than 4 candidates are expected for a radioactive dose of 5 mCi delivered to the patient, see also Section 13.4.2, and Section 13.4.13) and to look for a coincidence only among those candidates. It is not necessary to test all LOR as is done by the current approach; it is more efficient to move the fewer (less than 4) photon candidates for coincidence to a coincidence circuit through a pyramidal funnelling structure such as the 3D-Flow.

For example, a radiation activity of 5 mCi (radiotracers with short half-life, such as ¹⁵O-water or ⁸²Rb, provide the highest activity) generates about 30×10^6 “singles” per second that create a signal to the electronics for a PET with a FOV of 30 cm. For a PET with a FOV of 157 cm, that same radiation activity generates about 80×10^6 “singles” per second that create a signal to the electronics.

The entire electronics runs at 20 MHz. Thus, every sampling period of 50 ns an average of 4 singles are candidates for coincidences (80×10^6 singles per second that create a signal to the electronics for a FOV of 157 cm, divided by 20 MHz = 4).

In the above case, it will be required to implement a circuit with only 6 comparators, comparing all possible combinations of the four singles. (See Section 13.4.14.2).

Simulation results show that only two photons out of four will turn into a coincidence, thus the maximum expected rate for a 5 mCi radiation dose will be 20×10^6 coincidences per second.

This is to be compared with the approach used in the current PET which performs about 700 comparisons of the timing and characteristics of the “singles” made by 7 ASICs operating at 40 MHz for a 15 cm FOV [116] for the determination of coincidences on LOR among only 56 modules which decode, at most, 12,096 crystals.

14.7.2.3 3D-Flow coincidence detection circuits vs. GE Advance coincidence circuit

In summary, the innovative concept described herein for detecting coincidences requires only 6 comparisons where current PET devices require about 700 and one ASIC instead of seven, and it provides a detection rate of up to 40 million coincidences per second as opposed to only 4 million coincidences per second provided by current PET devices. This coincidence circuit would remain the same, 6 circuits comparing every 50 ns all possible combinations of the 4 singles, as long as the radiation dose does not exceed 5 mCi.

It would be impossible to match this performance in a PET with a 157.4-cm FOV and 2,304 PMTs (as described in Section 17) using the approach of the current PET without an unacceptable reduction in efficiency. With the coincidence detection approach used in the current PET, it would be necessary to execute 1,326,528 comparisons every 50 ns (calculated with the above formula $(n \times (n-1))/4$, that is $(2,304 \times 2,303)/4 = 1,326,528$). It is obvious that building such a circuit performing all those comparisons every 50 ns, besides being prohibitively costly, would be impossible.

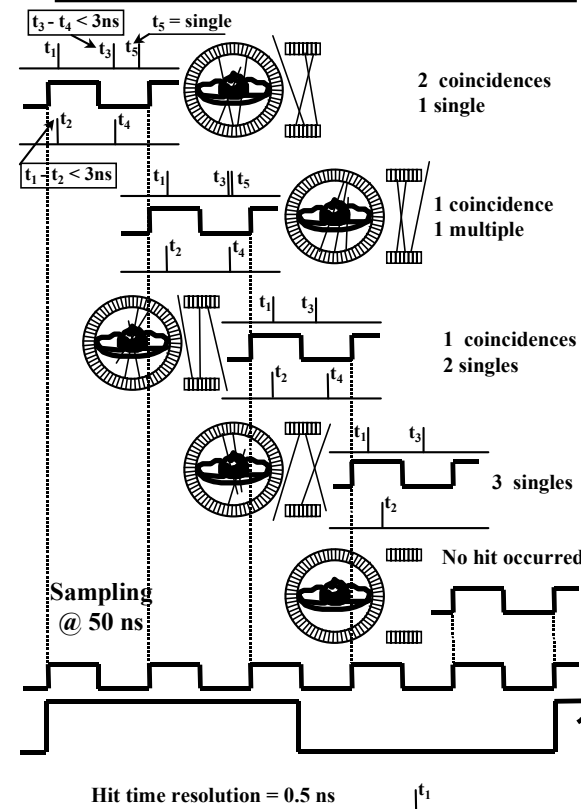
Using the approach which is implemented in the current PET operating in the hospitals, it will be required to execute 1,326,528 comparisons every 50 ns (calculated with the above formula $(n \times (n-1))/4$, that is $(2,304 \times 2,303)/4 = 1,326,528$). It is obvious that building such a circuit performing all those comparisons every 50 ns, besides being costly, would be impossible.

Figure 14-5 shows the 3D-Flow coincidence detection vs. the current approach to finding coincidences in PET. The first thing to notice is that

the approach used in the current PET systems, shown at right, entails many LOR even though the FOV is only 15 cm. On the other hand, in the 3D-Flow approach, presented at left, the lines of response are very few and they are proportional to the activity of the radiation and not to the

3D-Flow System

Hits are recorded from 1152 modules every 50 ns

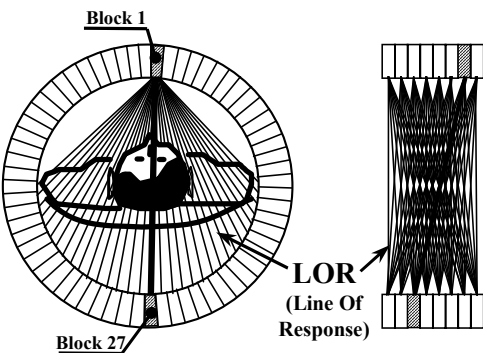


Calculate time interval between two hits (< 2.5 ns)

Compares only hits found within 50 ns (~ 0 to 6)

Current Systems

Hits are recorded from 56 modules every 250 ns



Block 1 - Hit time resolution = 2.5 ns

Block 27 - Hit time resolution = 2.5 ns

Coincidence window width = 12.5 ns

Compares ~ 700 LOR every 250 ns

Figure 14-5. The 3D-Flow PET coincidence detection approach vs. the current approaches to find coincidences in PET.

14.7.2.4 Elimination of the outgoing data bottleneck

The current PET system has a limitation of about 4 MHz on the output throughput, as stated for General Electric Advance in [116] and for CTI/Siemens in [121]. This is referred to in Figure 14-1 as “Bottleneck D.”

In practice, the performance of detecting 4 million coincidences per second is never achieved and measurements on CTI/Siemens model ECAT EXACT HR using phantoms show (in Figure 14-1 of [22]) a saturation in detecting true+scatter of about 400,000 coincidences per second. The GE Advance shows in [23] saturation in detecting true+scatter of about a half million coincidences per second. One reason for such low efficiency is the front-end circuit, Bottleneck D, that has reduced the channels from 1,344 to 56 by checking only the energy value and without performing a thorough check of the characteristics of a photon.

The elimination of outgoing “bottleneck D” with the 3D-Flow design is achieved by increasing the level of saturation of the outgoing detection of coincidences to 40 million coincidences per second. The design parameter of sustaining coincidence detection up to 40 million coincidences per second has been set as described in Section 13.4.14.2. The output of 40 million coincidences per second is provided by having four independent detection of single photons at 20 MHz in the four sectors of the detector. When each sector has found a single photon that is in coincidence with a photon of another sector, then at most two coincidences can be found, providing a maximum throughput of 40 MHz. Section 13.4.13 provides the scheme to choose a specific output bandwidth of the entire system, while Section 13.4.14.3 provides a general scheme for its implementation with maximum efficiency.

15 Modular Hardware Implementation in IBM PC or VME platform for systems of any size

The modularity, flexibility, programmability and scalability of the 3D-Flow system for the electronics of PET/SPECT/CT apply to all phases of the system, from the components to the IBM PC chassis, (or crate(s) for the VME implementation).

The same hardware can be used to replace the electronics of current PET as well as for building new systems of different sizes, making use of different detectors that provide analog and digital signals. The programmability of the 3D-Flow system can acquire, move, correlate, and process the signals to best extract the information of the incident photons and find the coincidences.

Two examples of implementation are described herein.

One, based on the IBM PC platform, has the advantage of providing the latest and most powerful CPUs and peripherals at the lowest price because of the large volume of its market. However, it has the disadvantage that particular care must be taken in the connectors and cables carrying the information between processors located on different boards.

The other, based on VME, has the advantage of a robust and reliable construction with the signals between processors on different boards carried through a secure backplane. However, the market for the latter is smaller, the prices are higher, and the boards with the latest components take more time to get into production.

For each platform, IBM PC, or VME, two systems have been designed. For applications requiring less processing, a system with 4 channels for each 3D-Flow processor is presented. For applications requiring higher computational needs, such as when detectors with economical crystals having slow decay time are used, a system with one channel per processor is presented.

15.1 A single type of DAQ board

Having selected a platform (IBM PC, or VME) and the processing needs (4 channels per processor, or one channel per processor), only one type of DAQ-DSP board is necessary for the entire application. The

following section will describe the boards for the four-channel application: IBM PC 64 channel, IBM PC 256 channels, VME 64 channels, or VME 256 channels.

15.1.1 IBM PC DAQ boards

15.1.1.1 IBM PC board with 64 analog channels and 32 digital I/O

The 64 analog signals from the PET/SPECT detector are converted into digital and formatted to be interfaced to the 3D-Flow system via ADC and FPGA. One additional element, the time-to-digital converter (TDC) chip/function, is described in Section 13.4.10.

Figure 15-1 shows the front and rear views of a mixed-signal IBM PC-compatible board accommodating 64 channels processed by a stack of 5 layers of 3D-Flow processors with a 2-layer filtering and channel funneling in a partial 3D-Flow pyramid (see Section 13.4.12.1, Section 13.4.12.2, Figure 17-1, and reference [163]). Each channel of 3D-Flow processor stack handles one analog input data (see Section 13.4.3.2).

All dimensions of the components and connectors shown in Figure 15-1 are scaled to the real sizes of boards. The analog-to-digital converter from Analog Devices AD9281 has two ADC per chip @ 28 MHz, in a package of 9 x 9 mm, it dissipates only 225 mW, and it has a low cost of \$4.5 per chip. The need of carrying 64 analog channels with some digital channels through the small back panel of an IBM PC compatible board is not a problem because there exists on the market a PCI board with 64 analog inputs (e.g., CYDAS 6400 from 2HR from CyberResearch has 64-channels A/D with 16-bit resolution, 8 digital inputs and 8 digital outputs in a single connector).

The power dissipation estimated in Table 15-1, shows that it requires about 20.47 Watt per 3D-Flow board.

The interconnection between processors residing on different boards is implemented by using connectors and cables on the top of the boards (e.g., AMP MICTOR, Matched Impedance Connector System having characteristics for carrying signals with 250 ps rise time. See Figure 15-7).

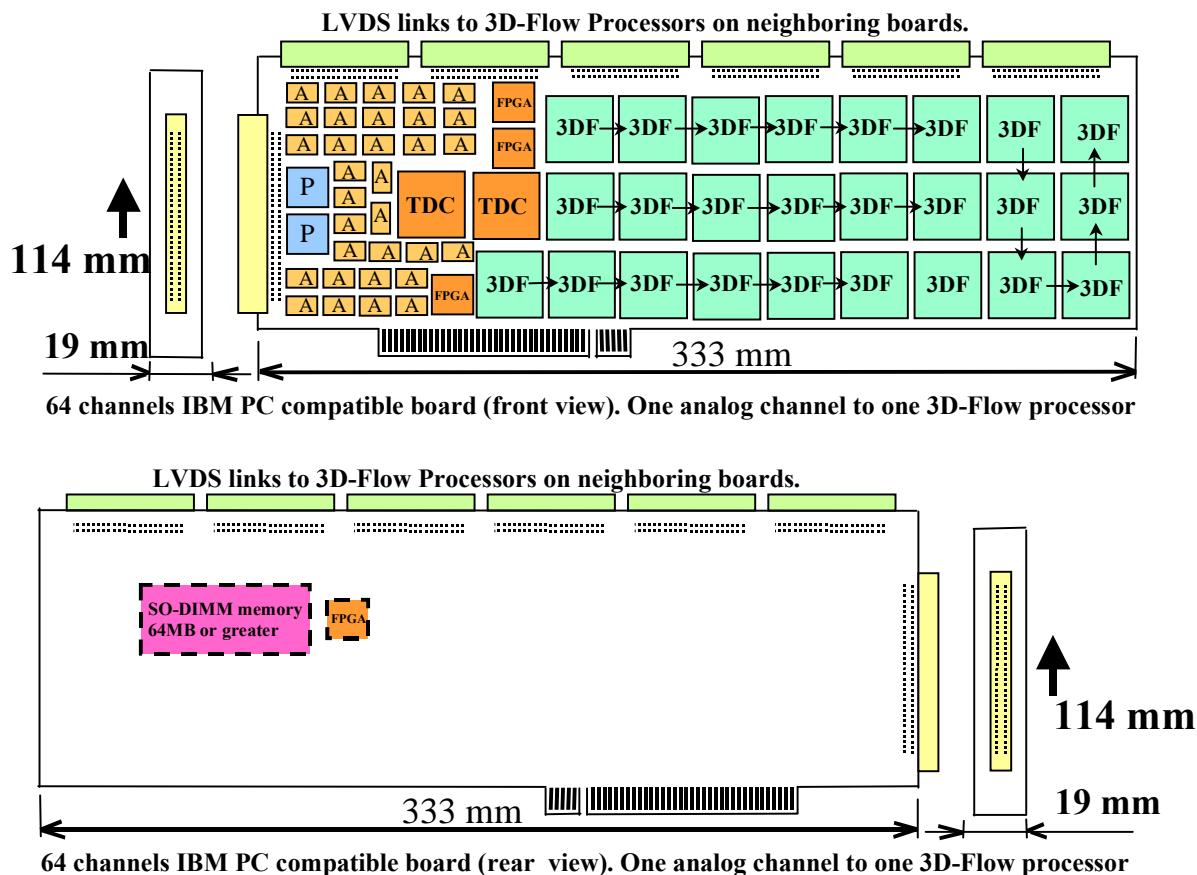


Figure 15-1. 64 channels IBM PC compatible 3D-Flow board. One analog channel to one 3D-Flow processor.

The control of the 3D-Flow processor (program downloading into the 3D-Flow processors, real-time algorithm initialization, processing and system monitoring) is performed via the RS232 ports as described in [163, 164, 156]. Each 3D-Flow DAQ-DSP board implements 16 Serial I/O ports which are directly controlled from the IBM PC CPU via the PCI bus. One additional serial port downloads the circuits into the FPGAs.

The coincidence candidates found among the 64 channels of the board are sent out from chip 154 of Figure 17-1 through two wires carrying LVDS signals to the connector on the back panel of the IBM PC board. (A single connector on the back panel similar to the one assembled on the

CYDAS 6400 board from CyberResearch carries analog and digital signals. Wires are separated as shown in Figure 17-3 and sent to the detector and to the patch panel connected to the pyramid board.) The two wires carrying the LVDS signals are sent to the pyramid board of Figure 15-5 through the patch panel shown in Figure 17-3.

A SO-DIMM buffer memory can be installed on the back of the board to acquire a high rate and a high volume of single photons during SPECT or CT scanning.

Table 15-1 . 3D-Flow IBM PC board component list and power dissipation estimate for 64 channels.

#	Type	Device	Package [mm]	IC power [Watt]	total power [Watt]
32	A	AD9281	28-pin SSOP (10.3 x 7.9)	0.225	7.2
2	P	32-channel preamplifier	256-pin FineLine BGA (17 x 17)	0.5	1
2	TDC	Time-to-Digital Converter	225-pin BGA MO-151 (27x27)	0.5	1
25	3DF	3D-Flow	672 FineLine BGA (27 x 27)	0.35	8.75
4	FPGA	Altera – Xilinx- ORCA	484-pin FineLine BGA (22.8 x 22.8)	0.3	1.2
1	SO-DIMM	Synchronous DRAM (64MB) 3.3 volt @ 400 mA	144-pin module (28 x 67)	1.32	1.32
				Total	20.47

15.1.1.1.1 Timing and synchronization issues of control signals in the 3D-Flow system

The 3D-Flow system is synchronous. This makes it easier to build and to debug. The most important task is to carry the clock, reset, clear, and control signals to each 3D-Flow component pin within the minimum clock skew.

This task can be accomplished without using special expensive connectors, delay lines, or sophisticated, expensive technology because the processor speed required to satisfy the design runs at only 80 MHz. The expected worst clock skew for the distribution of one signal to up to 729 chips (equivalent to a maximum of 11,664 processors) is a maximum of 450 ps (e.g., by using three stages of the PECL component 100E111L that has 50 ps worst case within-device skew for the first stage and 200 ps worst case part-to-part skew for the subsequent two stages. Or using LVDS DS92LV010A. See reference [163]). Control signal distribution can be implemented with several technologies.

15.1.1.2 IBM PC board with 256 analog channels and 32 digital I/O

Figure 15-2 shows the layout of a 3D-Flow IBM PC board handling 256 electronic input channels. Each channel of the 3D-Flow processor stack handles four analog input data (see Section 13.4.3.1). A special assembly consisting of a cable, printed circuit and connector is required to carry the 256 analog signals. Components are assembled on both sides of the board.

The power dissipation estimated in Table 15-2, shows that about 47.35 Watt per 3D-Flow DAQ-DSP board is required. The other sections of the board are similar to the one previously described in Section 15.1.1.1 for the 64 channels.

Table 15-2. 3D-Flow IBM PC board component list and power dissipation estimate for 256 channels

#	Type	Device	Package [mm]	IC power [Watt]	total pow. [Watt]
128	A	AD9281	28-pin SSOP (10.3 x 7.9)	0.225	28.8
8	P	32-channels preamplifier	256-pin FineLine BGA (17 x 17)	0.5	4
8	TDC	Time-to-Digital Converter	225-pin BGA MO-151 (27x27)	0.5	4
25	3DF	3D-Flow	672 FineLine BGA (27 x 27)	0.35	8.75
6	FPGA	Altera – Xilinx- ORCA	484-pin FineLine BGA (22.8 x 22.8)	0.3	1.8
				Total	47.35

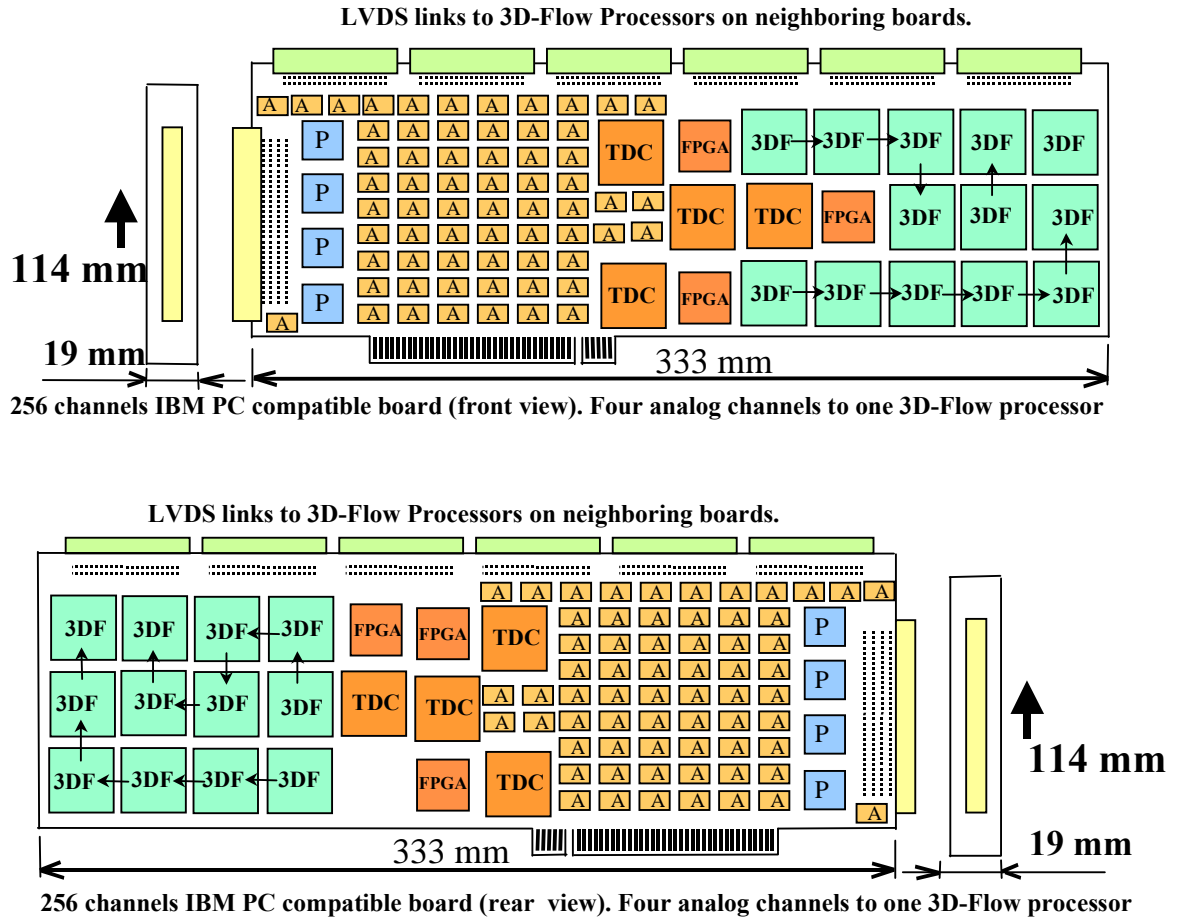


Figure 15-2. 256 channel IBM PC compatible board; four analog channels to one 3D-Flow processor

15.1.2 VME DAQ boards

A system analogous to the 3D-Flow for IBM PC, such as the one described in Section 15.1.1.1, can be implemented with VME boards shown in Figure 15-3, and Figure 15-4. The interconnection between processors residing on different boards is implemented through a VME backplane as shown at the bottom of Figure 15-7.

The control of the 3D-Flow processor (program downloading into the 3D-Flow processors, real-time algorithm initialization, processing, and

system monitoring) is performed via the RS232 ports as described in [163, 164, 156].

The coincidence candidates found among the 64 channels (or 256 channels) are sent out from chip 154 of Figure 17-1 by means of LVDS signals through the connector J1 located on the top part of the front panel of the boards shown on Figure 15-3, and Figure 15-4. Local accepted data on each board are then sent to the pyramid board shown in Figure 15-6 through a patch panel similar to the one shown in Figure 17-3.

15.1.2.1 VME board with 64 analog channels and 32 digital I/O

Figure 15-3 shows the layout of the 64 channels 3D-Flow DAQ-DSP VME board. Components are installed only on one side of the board. It would be possible to install a SO-DIMM buffer memory on the rear of the board (indicated with dashed line) for applications with high-rate, high volume of data during SPECT and CT scanning.

Each channel of the 3D-Flow processor stack handles one analog input data (see Section 13.4.3.2).

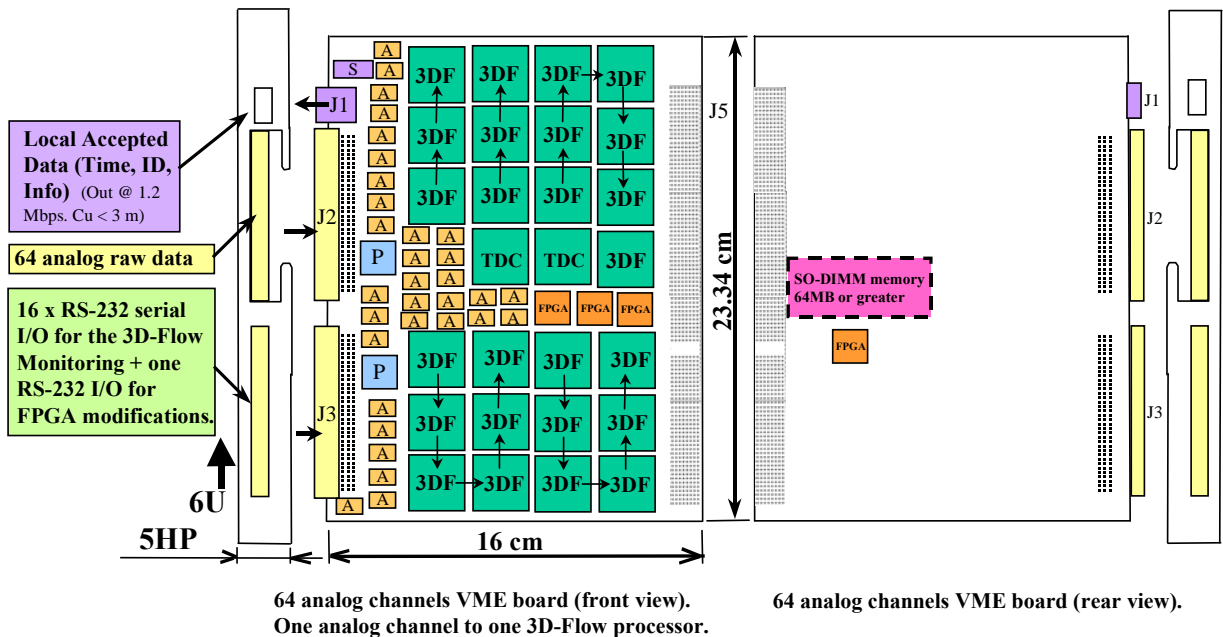


Figure 15-3. 64 channel VME board; one analog channel to one 3D-Flow processor .

15.1.3 VME board with 256 analog channels and 32 I/O

Figure 15-4 shows the layout of the 256-channel 3D-Flow DAQ-DSP VME board. Components are installed on both sides of the board. It is possible to install a SO-DIMM buffer memory (indicated with dashed line) for applications with high-rate, high volume of data during SPECT and CT scanning.

Each channel of the 3D-Flow processor stack handles four analog input data (see Section 13.4.3.1)

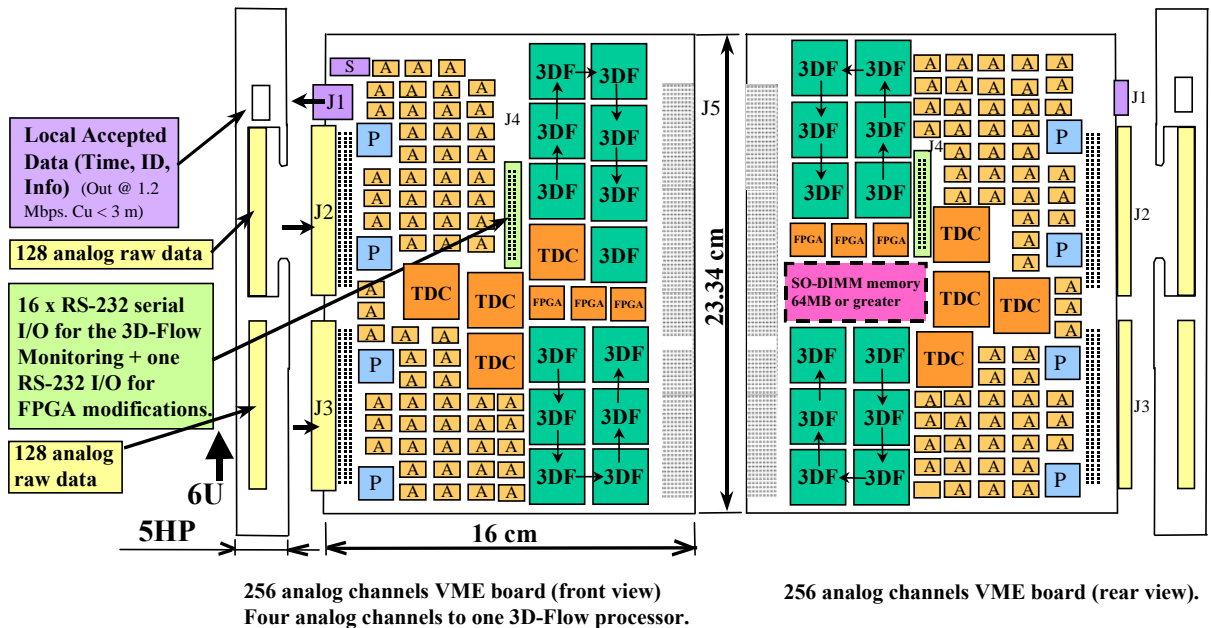


Figure 15-4. 256 channel VME board; four analog channels to one 3D-Flow processor .

15.2 A single type of Pyramidal & buffer board

A single type of pyramidal, coincidence detection and buffer board implements in IBM PC or VME platform the logical circuits described in the right section (indicated with “Pyr. Layer 3” and “Coincidence Stack”) of Figure 16-1, in the three right-most columns of Figure 13-3, and in Figure 13-23.

The pyramidal board receives the data relative to the photons validated by the real-time algorithm executed on the 3D-Flow DAQ-DSP boards through a patch panel shown in Figure 17-3. It then, performs the functionality attenuation correction described in Section 13.4.6, separating the photons found into the three modalities (PET, SPECT, and CT), the channel reduction in Section 13.4.12, and the coincidence identification in Section 13.4.14. The board stores results, the coincidences found (or the single photon validated by the algorithm for SPECT and CT when the buffer memories on the DAQ-DSP boards are not installed), in the two DIMM buffer memories, which can have a capacity up to 4 GB each for a total maximum of 1 billion events accumulated (one event or coincidence is in the 64-bit format described in Section 13.4.14.4), during a single study session.

An additional DIMM module memory of 512 MB stores the coefficients for the attenuation correction acquired during calibration scan as described in Section 13.4.6.

Results are read from the buffer memories by the IBM PC CPU via the PCI bus (or VME CPU via the VME bus) and sent to the graphic workstation via a standard high-speed local area network.

15.2.1 IBM PC Pyramidal and buffer board

Figure 15-5 shows the layout of the IBM PC pyramid, attenuation correction, and coincidence detection board. Components are assembled on only one side of the board, and there are three 168-pin slots for synchronous DIMM memories @ 100 MHz. Two slots are designated as buffer memories storing events (single photons from SPECT and/or CT modality and photons in coincidence for PET modality) and one slot is designated as a memory module storing the attenuation correction coefficients.

Data are received from the connector on the backpanel and are read by the IBM PC CPU via the PCI bus.

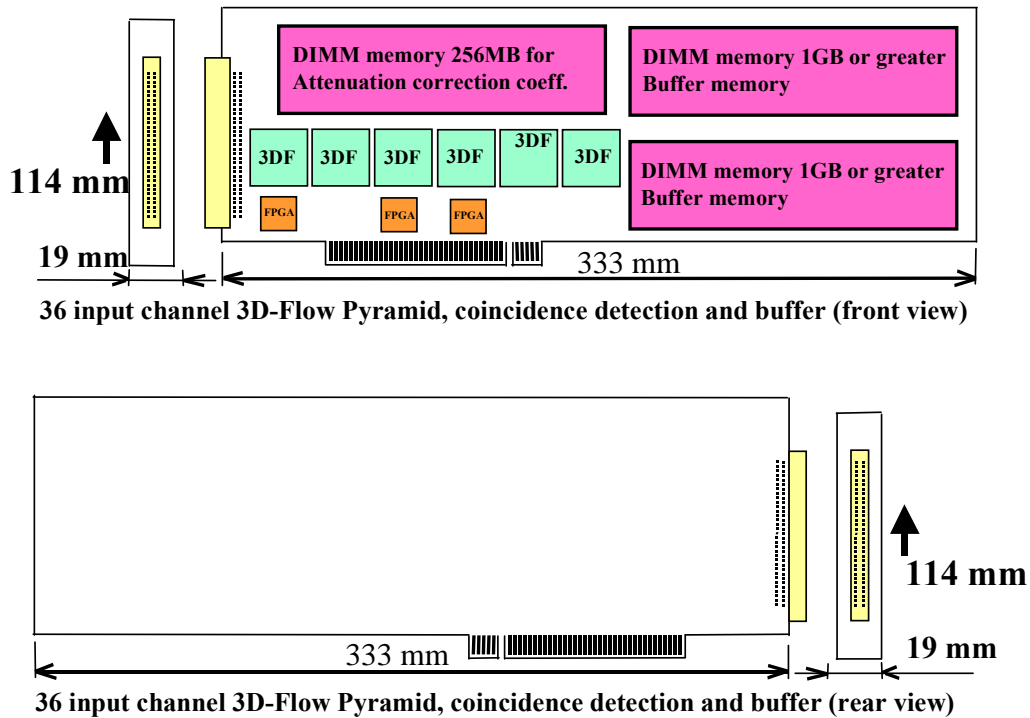


Figure 15-5. IBM PC 3D-Flow Pyramid board for channel reduction, event sorting, and coincidence detection.

15.2.2 VME PC Pyramidal and buffer board

Figure 15-6 shows the layout of the VME pyramid, attenuation correction, and coincidence detection board. Components are assembled on only one side of the board, and there are three 168-pin slots for synchronous DIMM memories @ 100 MHz. Two slots are designated as buffer memories storing events (single photons from SPECT and/or CT modality and photons in coincidences for PET modality) and one slot is designated as a memory module storing the attenuation correction coefficients.

Data are received from the connector on the front-panel and are read by the VME CPU (e.g., VMIVME 7587 from VMIC Co.) via the VME bus.

Table 15-3 shows the power dissipation estimated by the IBM PC, or VME pyramid board.

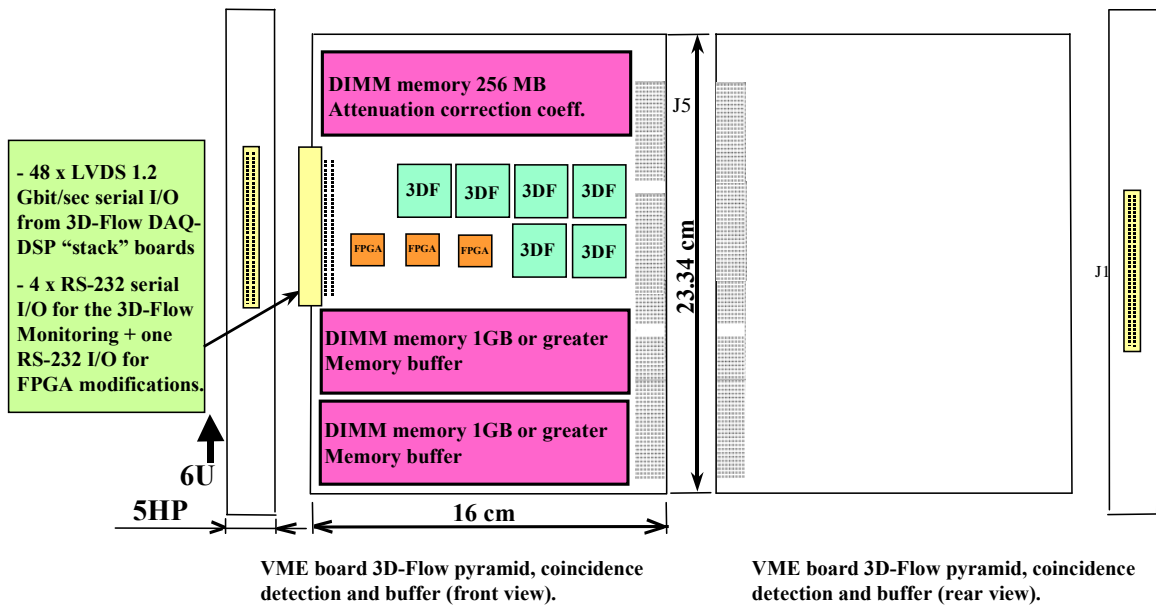


Figure 15-6. VME 3D-Flow Pyramid board for channel reduction, event sorting, and coincidence detection.

Table 15-3 . 3D-Flow IBM PC pyramid board component list and power dissipation estimate.

#	Type	Device	Package [mm]	IC power [Watt]	total power [Watt]
6	3DF	3D-Flow	672 FineLine BGA (27 x 27)	0.35	2.1
3	FPGA	Altera – Xilinx- ORCA	484-pin FineLine BGA (22.8 x 22.8)	0.3	0.9
3	DIMM	Synchronous DRAM (1GB) 3.3 volt @ 650 mA	168-pin module (133.35 x 31.75)	2.145	6.435
				Total	9.435

15.3 3D-Flow neighboring connection on the edge of the IBM PC board, or on the backplane of the VME crate.

The backplane carrying the information to/from the neighboring processors is built, in the IBM PC compatible implementation, with cables/connectors carrying LVDS signals located at the opposite edge of the PCI edge connector of the board. Figure 15-7 shows the assembly of the interconnection between 3D-Flow processors on different boards.

The following details of inter-board communication are very important and show the feasibility of the implementation of the detector without boundaries. All information (including the example of one type of connector with suitable characteristics for this application) is provided.

Each board has 64 channels and 5 layers of 3D-Flow processors. 64 channels is equivalent to: 8 processors per side, multiplied by 2 ports per processor (connections between processors are point-to-point, thus one port for input and one port for output) comes to 16 ports per side per layer. Five layers have a total of 80 ports. Each port transmits/receives in LVDS on two wires, totalling 160 wires per side. Speed up to 1.2 Gbps can be easily achieved with the current LVDS drivers from several vendors (e.g. LSI logic). Matched impedance connectors such as AMP MICTOR can provide good a connection with the ground bar at the center of the connector for a 250 ns signal rise-time characteristic. There is a discrete ground bus every half inch of the connector length, which can be assigned to either power or ground in any combination. The connector with 190 positions is only 76.2 mm x 5.2 mm which makes it feasible to implement the processors interconnecting buses on one side of the board. Each board needs four such connectors at most to provide the communication of the 3D-Flow processors in all four directions North, East, West, and South ports.

The interconnection of the processors assigned to the border between the head and the torso of the detector where the side processors of the torso are connected to the side processors of the head which are half in number, requires only 80 wires: the processor of the torso which does not have a direct connection with the processor of the head, moves its data through the neighboring torso-processor connected to the head).

The mother board (see center left section of Figure 15-7 for the physical implementation of the logical interconnection shown on the center right of the figure) accommodating 18+1 DAQ-DSP 3D-Flow

board, in the version IBM PC compatible, could be accommodated on a standard motherboard PBPW 19P18 from CyberResearch (this motherboard has 18 PCI +1 slot for CPU, or one ISA and 17 PCI) or from Industrial Control. Both companies offer chassis with power supplies up to 800 Watts; Industrial Control also offers chassis series 7100 with up to 1600 Watts.

The 3D-Flow inter-chip communication on the VME 6U platform is implemented on a printed circuit board backplane as shown at the bottom of Figure 15-7. The same number of connections are required as the ones described in the previous case for the IBM PC.

A magnified area of the interconnection between a section of the connectors 361 to 461, to 541 is shown at the bottom right of Figure 15-7. Five layers of printed circuit board (PCB) are required in order to facilitate routing of traces with no crossing. The pattern of the connections on the backplane is regular, thus requiring only short PCB traces as shown at the bottom right of Figure 15-7 (the example of the connection pattern for three layers is shown in the figure). The distance between the connectors is 20.32 mm providing traces length less than 10 cm. The distance between two pins of 2 mm with two traces between pins permits construction of only 5 layers PCB reaching speed of hundreds of MHz with differential LVDS signaling.

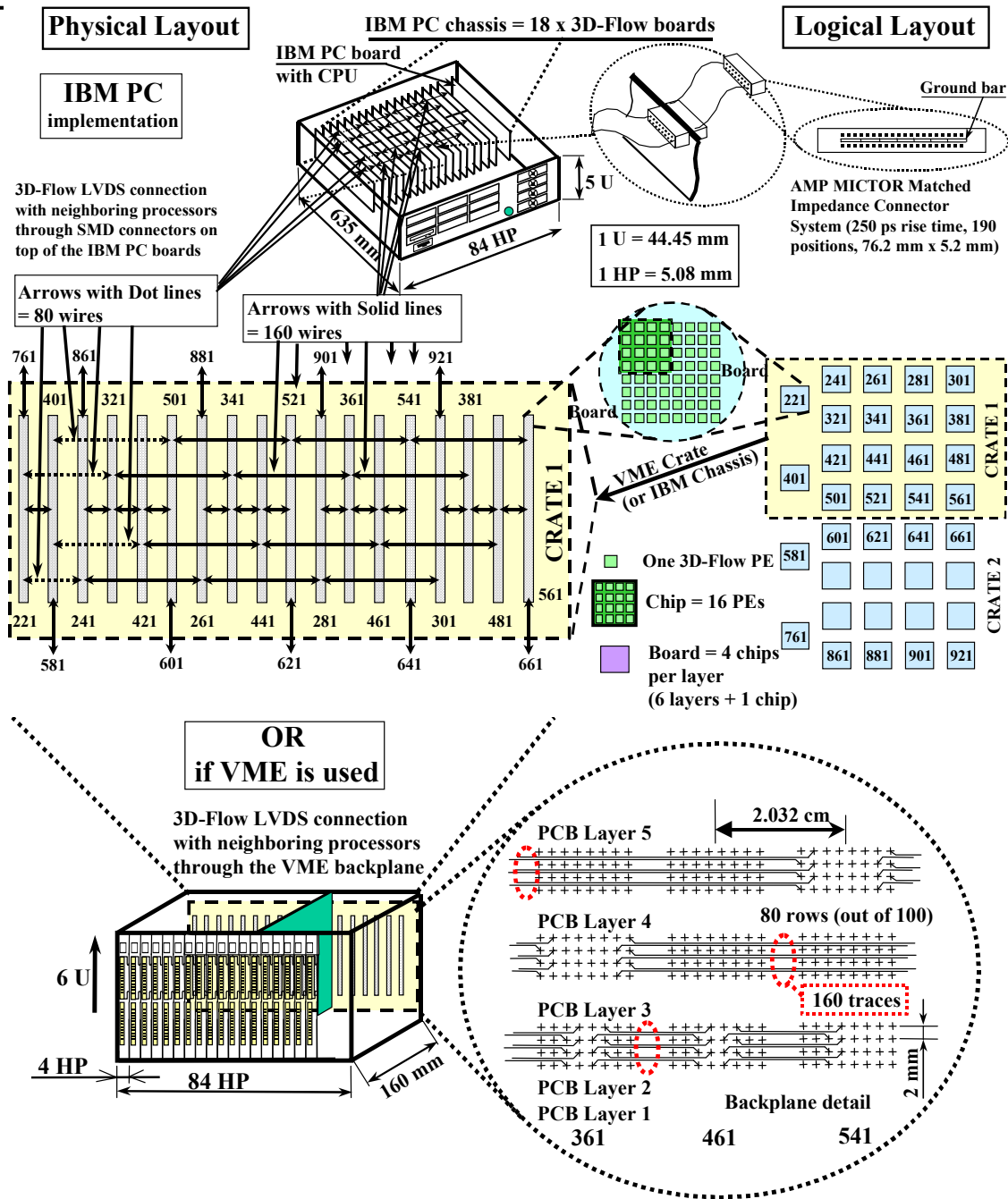


Figure 15-7. Backplane carrying the information to/from the neighboring 3D-Flow processors.

16 Application: Replacing the electronics of the current and past PET for lowering the cost and the radiation to the patient.

16.1 Logical layout for a 3D-Flow system replacing the electronics of the current and past PET for lowering the cost and the radiation to the patient

Following is the scheme of how to build a flexible, higher performance DAQ-DSP system that can be interfaced to different existing PET devices. A specific real-time program for each different PET device can be downloaded into the 3D-Flow system to tune the photon identification and coincidence detection to a specific detector.

Figure 16-1 shows the logical layout for a 3D-Flow system replacing the electronics of the current and past PET.

The interface to the current or older PET devices can be located at the PMT level by taking the analog signals from the photomultipliers of the old or current PET devices and sending them to the 3D-Flow system. The left side of Figure 13-2 shows the physical layout of the use of the 3D-Flow system in a typical whole-body PET currently used in hospitals. Only five 3D-Flow DAQ-DSP boards and one 3D-Flow pyramidal board will be required if, in addition to replacing the current electronics, the small photomultipliers (19 mm in diameter) are also replaced with larger photomultipliers (38 mm in diameter). However, if this change would present a practical problem in disassembling the blocks and in coupling the larger photomultipliers with the crystals, then one could simply multiply the number of input channels of the 3D-Flow system by four and use the current detector hardware. In the latter case eighteen 3D-Flow DAQ-DSP boards should be used in place of five, and the scalability of the 3D-Flow system will allow the processing of the signals from the detector as in the case shown in Figure 13-2.

The occupancy of each detector module every sampling period of 50 ns using the new approach is only 0.017 vs. the 0.44 of the GE Advance implementation. (For the same 100 million “singles” events per second from the detector in a 15 cm FOV PET, the occupancy of each of the 288 modules is $(100 \times 10^6) / (288 \times 20 \times 10^6) = 0.017$. The occupancy of each of the 56 modules every sampling period of 250 ns for the GE Advance is calculated as $(100 \times 10^6) / (56 \times 4 \times 10^6) = 0.44$).

Figure 16-1 shows on the left a detector of a size (18,432 crystals) similar to that of the current whole-body PET operating in hospitals (the

PETs operating today in hospitals have a number of crystals ranging from 12,000 to 27,000. See Section 11.2.2).

In the figure, 64 crystals are coupled to a PMT of 38 mm in diameter, giving a total of 288 PMTs or detector modules, or electronic channels. (It should be pointed out here that, as mentioned above, if problems arise in replacing the existing small PMTs with the larger PMTs, the electronic channels of the 3D-Flow system can be increased.)

For the estimated highest activity of 100×10^6 photons per second that the detector should ever sustain (the highest activity is limited by the maximum radiation dose that can be delivered to the patient), the 288 processors per layer of the 5 five layers of the 3D-Flow stack system execute the programmable photon identification algorithm as described in Section 13.4.11.

The estimated reduction of photons to 80×10^6 is processed by the first layer of the pyramid as described in Section 13.4.12.1. Zero data are suppressed, insertion of the MSB of the ID and time-stamp is done before the data is funneled into the pyramid.

The photons with different time-stamp t_1 , t_2 , t_3 , etc. indicated in Figure 16-1 with γ - t_1 , γ - t_2 , and γ - t_3 travel through the pyramid, which performs the channel reduction function. All these operations are still executed on 3D-Flow chips residing on the 3D-Flow DAQ-DSP board as described and simulated in Section 13.4.12.2.

The fixed time latency of the data with respect to its origin, which was lost through the different paths followed in the pyramid, is regained in the functionality of the next board (see Section 13.4.14.1, and Section 15.2). Photons which occurred at the same time t_1 , with an ID showing that they originated from the patient's body, are identified by the coincidence detection circuit as described in Section 13.4.14.2. Singles are discharged.

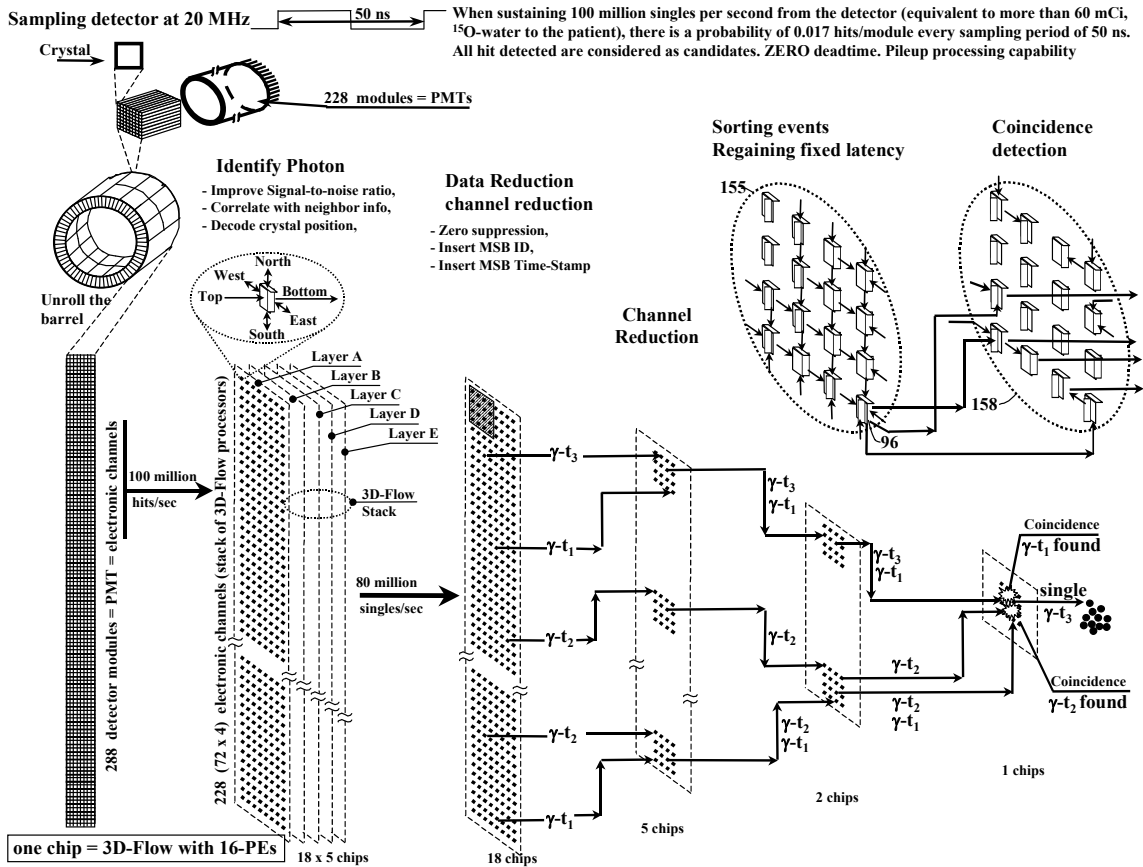


Figure 16-1. Logical layout for a 3D-Flow system replacing the electronics of the current and past PET for lowering the cost and the radiation to the patient.

17 Application: Design for the construction of a PET with 400⁺ fold efficiency improvement

PET detectors with fast crystals with a short decay time offer better time resolution, require electronics with simple real-time algorithm, can detect more photons at a high rate of radiation activity produced by the isotope without incurring pileup effects. However, they are more expensive and are subject to the licence of one manufacturer.

In order to provide more flexibility in the possible implementations of PET/SPECT/CT devices, following are provided examples with both slow and fast crystals.

The ratio of 256 crystals (or a single crystal of equivalent size in a “continuous” detector) coupled to a photomultiplier of 38 mm in diameter has been selected.

In the event the light emitted by a certain type of crystal adopted in a particular PET design is not sufficient, or the S/N ration does not allow decoding of 256 crystals, then the number of PMT and electronic channel can be multiplied by four and the 256 channel 3D-Flow DAQ-DSP board can be used in place of the 64 channel board. (The computation by the 3D-Flow DSP required for decoding 64-channels in place of 256 will be reduced, allowing each 3D-Flow to handle four electronic channels).

17.1 PET/SPECT/CT application using slow crystals

The first crystal with slow decay used in nuclear medicine, single photon and positron, was the NaI(Tl); later, BGO was used. Their cost is relatively low compared to the fast crystal with short decay time such as LSO.

A 3D-Flow system for a PET/SPECT/CT with a field of view of 157.4 cm is described in this section. Given the one-to-one ratio between 3D-Flow processors and detector electronic channels and the high capability of the system of executing complex real-time algorithm on each detector channel (a channel consists of all electrical signals provided by the sensors within a view angle of the detector), this example is more suitable for PET with slow crystals where it is more difficult to extract the photon characteristics information. However, it can also be used for other types of detectors, even if the electronics might seem over dimensioned. The example of the 3D-Flow electronics requiring lower performance, because better, faster crystals are used and four detector channels can be assigned

to one 3D-Flow processor, is shown in Section 17.2. The electronics in that case is reduced and less costly, while the fast crystals cost more.

17.1.1 Logical layout of the electronics for a PET/SPECT/CT system requiring high performance for extracting photon characteristics from slow crystals

Figure 17-1 shows the logical layout of the electronics for a PET/SPECT/CT system with 157.4 cm FOV and 2,304 electronic channels.

The system has a one-to-one coupling between an electronic channel and one 3D-Flow processor stack, providing high performance digital signal processing on each channel for extracting the photon characteristics information from low cost slow crystals with long decay time.

The section on the left of the figure shows the functionality and the arrangement of the 38 DAQ-DSP boards. The DAQ-DSP boards are indicated by the number from 221, 241, 261... through 921.

Each board consist of a 5-layer stack implementing the function of photon identification (see Section 13.4.11) and a 2-layer pyramid. One, layer of the pyramid, indicated by the number 6 in the figure, implements zero suppression (see Section 13.4.12.1); and the second, indicated by the number 7, implements channel reduction (see Section 13.4.12.2). During SPECT and CT modes of operation at high-rate and high-volume of coincidences created by the source, processor 82 of chip 153 collects the data (single photon of SPECT and CT energies) and sends them to the buffer memory installed on the 3D-Flow DAQ-DSP board. Each layer of the stack consists of four 3D-Flow chips having a total of 64 processors. The first layer of 64 processors is interfaced to the 64 detector electronic channels via the FPGAs (see Section 13.4.4.3).

The 36 boards are accommodated in two crates.

On the right section of the figure we have three 3D-Flow chips numbered 155, 156, 157 which receive the photon candidates for coincidence (one pair of LVDS wires per 3D-Flow DAQ-DSP board of the system) and route them to the processor indicated by the number 96 for chips 156 and 157, and to processors 96 and 84 for chip 155.

The 3D-Flow program at processor 84 and 96 (see flowchart in Figure 13-22) sorts the events in the original sequence and regains the fixed time latency with respect to when they were originated.

The four sets of data are realigned in time at this stage to the original event and corresponding to the four sectors of Figure 13-24. They are received from the three processors indicated by the number 96 and from processor 84 and are sent to chip 158, which performs the six comparisons A-B, A-C, A-D, B-C, B-D, C-D as described in Section 13.4.14.2.

Photons in coincidence are sent to coincidence memory buffer 1 and buffer 2. Three comparators are connected to buffer memory 1 and the other three are connected to buffer memory 2. Unmatched photons are discarded at this stage. The list of operations to be performed by the 3D-Flow processors of chip 158, which performs the comparisons, are listed in Figure 13-25.

In the event the operation at this stage needs to be increased beyond the time interval between two consecutive input data, the 3D-Flow architecture implemented at the photon identification stage (see Section 13.4.11, and Section 12) and indicated in the figure as chip 159 and chip 160 can also be implemented at this stage, since the incoming data are synchronous and have a fixed latency time from when they were created.

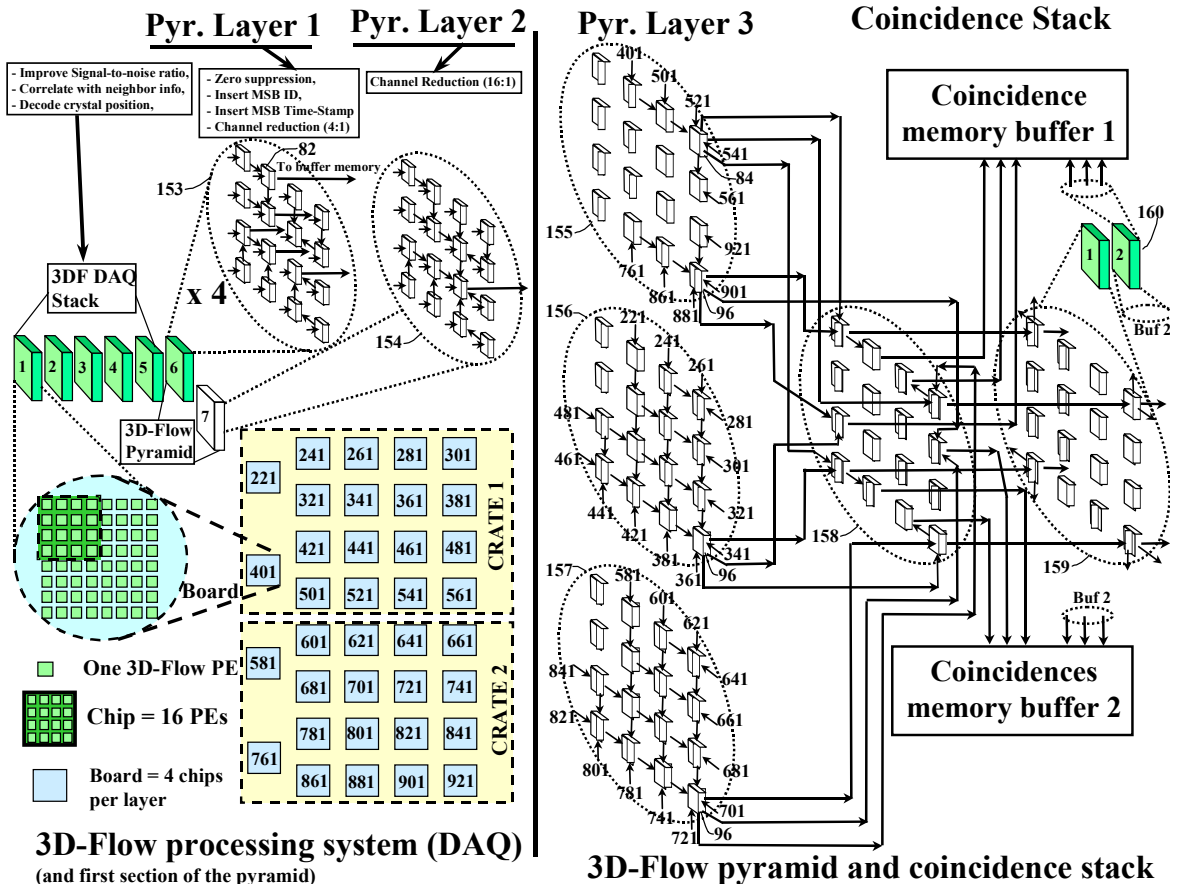


Figure 17-1. Logical layout for a PET/SPECT/CT system requiring high performance for extracting photon characteristics from slow crystals.

17.1.2 Logical and Physical layout for a PET/SPECT/CT requiring high performance for extracting photon characteristics from slow crystals.

Figure 17-2 shows how the logical layout of the electronics for a PET/SPECT/CT system with 157.4 cm FOV and 2,304 electronic channels relates to the detector elements. In the center of the figure are shown the 36 DAQ-DSP boards from 221 to 921 accommodated in two chassis (or crates for VME implementation) indicated by the numbers 237 and 238.

Each board consists of four chips per layer, indicated by the number 140, for 5 layers of stack, one full layer of the pyramid and $\frac{1}{4}$ layer for the next layer of the pyramid (see top right of Figure 17-2).

Each chip consists of 16 processors. The 64 processors of the first layer are connected to the photomultipliers and other sensors that receive data from the detector. (The ratio of 256 crystals to one photomultiplier can be changed to 64 to one and the 3D-Flow DAQ-DSP boards with 256 channels can be used in place of the 64 channels). The segmentation and mapping of the detector to the 3D-Flow system is also described in Section 13.3 and Table 13-1.

The bottom of Figure 17-2 shows the physical layout of the detector consisting of an elliptical gantry of about 100 cm wide and 50 cm tall on the torso section, and 40 cm in diameter at the head section. These dimensions correspond to all other parameters shown at the left, top and right of the array of boards in the center of the figure.

Any parameter can be calculated from the numbers reported in the side of the board array. For instance, the number of PMTs for the head are easily calculated as the 32 PMTs shown at the left of the figure, multiplied by 8 PMT for the head section of the axial view. Similarly, the number of crystals for the head and for the torso can be calculated. The field of view can also be calculated by knowing the crystal dimensions increased by approximately 0.35 mm per side for the material between crystals.

At the joint between the head section and the torso section where four boards (221, 401, 581, and 761) are connected to eight boards from 241 to 861, the connection of the processors on the right side of 221 in the figure are alternately connected one to every other processor on the left side of 241 and 321. The processor that is not connected physically to the processor of the head will move its data to that neighboring processor that has a connection).

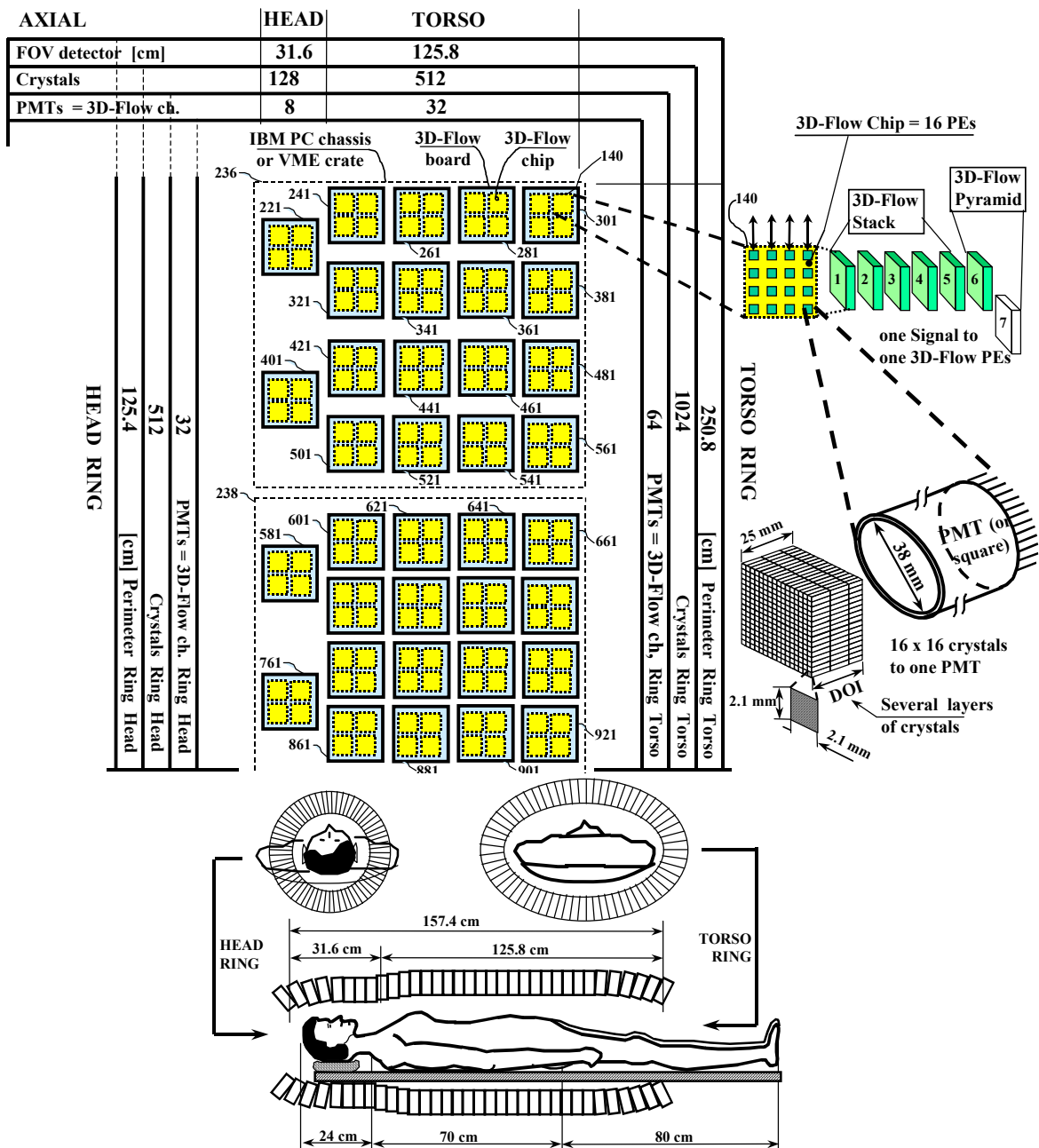


Figure 17-2. Logical and physical layout for a PET/SPECT/CT system requiring high performance for extracting photon characteristics from slow crystals

17.1.3 Physical layout for a PET/SPECT/CT system requiring high performance for extracting photon characteristics from slow crystals.

Figure 17-3 shows the implementation on the IBM PC platform of the electronics for a PET/SPECT/CT system with 157.4 cm FOV and 2,304 channels.

The entire electronics consists of two IBM PC chassis, such as that commercially available from CyberResearch or Industrial Control, accommodating 36 DAQ-DSP boards as described in Section 15.1.1.1 and one 3D-Flow pyramid board of the type described in Section 15.2.1.

The list of the hardware needed and the estimated power dissipation is shown in Table 17-1.

Each of the 36 DAQ-DSP boards has a connector on the back panel carrying the signals from the detector and the results of the coincidence candidates (or single photons for SPECT and PET mode) to the pyramid board through the patch panel shown in the center the figure. (The center left of the figure shows the connector type, which at one end plugs into the back of the IBM PC board and then the wires are split to go to the detector and to the patch panel).

A local area network provides easy communication between the chassis. Each chassis has a Pentium CPU or similar with Unix, Linux or NT Windows operating system which allows supervision and monitoring of the activity of the 3D-Flow system as described in [163, 164, 156] and collection of the results.

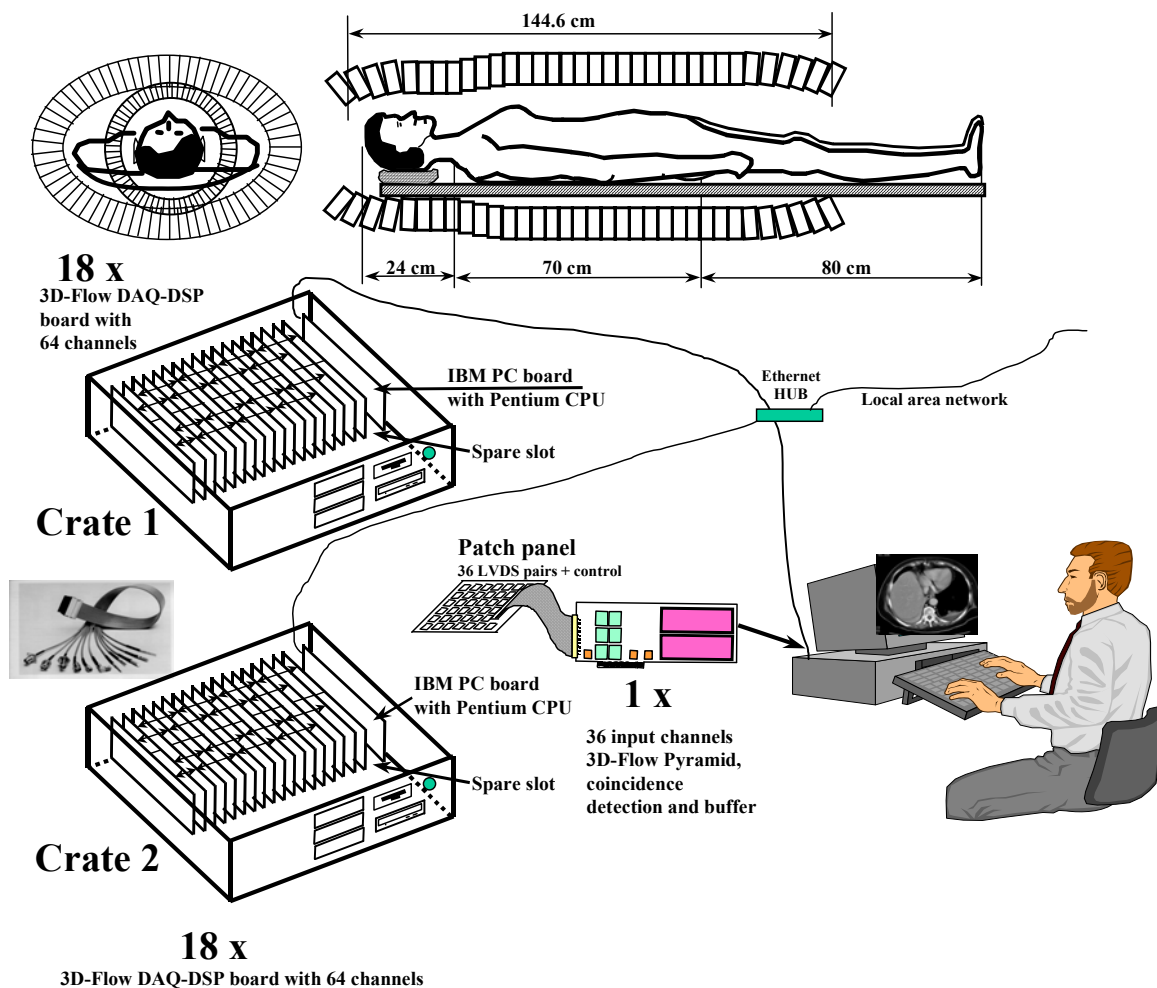


Figure 17-3. Physical layout for a PET/SPECT/CT system using slow crystals

Table 17-1 . 3D-Flow IBM PC base system for a whole-body PET with 157.4 cm FOV and 2,304 channels.

#	Type	Device	Package [mm]	IC power [Watt]	total power [Watt]
36	3D-Flow DAQ-DSP	64 channels. (one analog channel to one 3D-Flow ch)	IBM PC board (333 x 114)	20.47	736.92
2	SBC	e.g. from CyberResearch 2 serial RS232 ports, one USB, 400 MHz CPU, PCI SVGA controller, 768 MB RAM, IDE I/O for floppy and HD, SCSI, Ethernet, mouse, keyboard,	IBM PC board	25	50
1	3D-Flow Pyramid		IBM PC (333 x 114)	7.29	7.29
2	Passive backplane	CyberResearch model PBPW 19P18 (18 PCI + 1 slot for CPU)			
2	IBM PC Rack-Mount	Cyber Research RWFD 19P18-8 (fault-tolerant rack-mount PC with 800W power supply, 9 drive bays, room for 20 full-length PCI-Bus cards)	800 Watt power supplies for each chassis		
				Total	793.29

17.2 Logical and physical layout for a PET/SPECT/CT system using fast crystals

Figure 17-4 shows how the logical layout of the electronics for a PET/SPECT/CT system with 126 cm FOV and 1,792 electronic channels relates to the detector elements.

In the center of the figure are shown the 8 DAQ-DSP boards from 200 to 900 accommodated on one chassis (or crates for VME implementation) indicated with the number 235.

Each board consists of four chips, indicated by the number 140, per layer for 5 layers of stack, one full layer of the pyramid and $\frac{1}{4}$ layer for the next layer of the pyramid (see top right of Figure 17-4).

Each chip consists of 16 processors. The 64 processors of the first layer are connected to the photomultipliers and other sensors that receive

data from the detector. (The ratio of 256 crystals to one photomultiplier can be changed to 64 to one, in which case the number of 3D-Flow DAQ-DSP boards should be multiplied by four).

The bottom of Figure 17-4 shows the physical layout of the detector, consisting of an elliptical gantry for the torso of about 100 cm wide and 50 cm tall at the torso section, and 40 cm in diameter at the head section. These dimensions correspond to all other parameters shown at the left, top, and right of the array of boards in the center of the figure.

Any parameter can be calculated from the numbers reported in the side of the board array. For instance, the number of electronic channels for the head are easily calculated as the 16 shown at the left of the figure, multiplied by 4 for the head section of the axial view. Similarly, the number of crystals for the head and for the torso can be calculated. The field of view can also be calculated by knowing the crystal dimensions increased by approximately 0.35 mm per side for the material between crystals.

The list of hardware needed and the estimated power dissipation is shown in Table 17-2

Table 17-2 . 3D-Flow IBM PC base system for a whole-body PET with 126 cm FOV and 1792 channels.

#	Type	Device	Package [mm]	IC power [Watt]	total power [Watt]
8	3D-Flow DAQ-DSP	256-channels. (one analog channel to one 3D-Flow ch)	IBM PC board (333 x 114)	47.35	378.96
1	SBC	e.g. from CyberResearch 2 serial RS232 ports, one USB, 400 MHz CPU, PCI SVGA controller, 768 MB RAM, IDE I/O for floppy and HD, SCSI, Ethernet, mouse, keyboard,	IBM PC board	25	25
1	3D-Flow Pyramid		IBM PC (333 x 114)	7.29	7.29
2	Passive backplane	CyberResearch model PBPW 19P18 (18 PCI + 1 slot for CPU)			
1	IBM PC Rack-Mount	Cyber Research RWFD 19P12-8 (fault-tolerant rack-mount PC with 800W power supply, 9 drive bays, room for 12 full-length PCI-slots and 6 ISA slots)	800 Watt power supplies		
				Total	411.25

18 Cost for a PET/SPECT/CT system of different sizes and using fast or slow crystals

Table 18-1 shows the cost of the main components of a whole-body PET of recent development such as the CTI/Siemens 966/EXACT3D with slow crystals and 23.4 cm FOV. The cost of the main components is shown to be about half a million dollars.

The volume of the BGO crystals and the number of photomultipliers used are based on the layout of the PET shown in Figure 11-5.

The duration of the examination is over 15 times that of the PET using the new 3D-Flow approach. This is because, in the current PET, in order to cover 157.4 cm of FOV, 7 bed positions are required. The FOV is in effect less than 23.4 cm because each bed-position scanning must include some overlap of the previous one. Furthermore, the lower efficiency of the device in capturing photons, require delivery of a higher radiation

dose to the patient and at least 10 minutes of scanning for each position, while the new 3D-Flow PET accumulates a larger amount of photons in less than 4 minutes scanning.

Table 18-1. Cost of the main components of a current whole-body PET, 23.4 cm FOV, of recent development with slow crystals.

model	crystals volume/cost [cm ³ /\$]	Photomultipliers number/cost [#/\$]	Estimated cost of the electronics	Estimated total cost
Current PET 23.4 cm FOV CTI/Siemens 966/EXACT3D (see Section 11.2.2.6.1)	13,602/~\$136,020 (BGO ~ \$10/cm ³)	1,728/~\$276,480 (3/4" ~ \$160 each)	~\$100,000	~\$512,500

Table 18-2 shows the cost of the main components of a future whole-body PET of future development, based on the current approach such as the CTI/Siemens 966/EXACT3D, but with 157.4 cm FOV and slow crystals.

The cost of the main components is shown to be about three and half a million dollars.

The volume of the BGO crystals and the number of photomultipliers used are based on the layout of the PET shown in Figure 11-5 multiplied by 6.7 which is the multiplication factor of the larger FOV.

The cost of the electronics has also been multiplied by 6.7. However, as discussed in Section 14.7.2.3, the 1.3 million comparisons every 250 ns required by this approach, used in the current PET, form a “brick-wall” difficulty. The cost to overcome this difficulty would be prohibitive, unless an inefficient solution is adopted.

Table 18-2. Estimated cost of the main components of a future whole-body PET, 157.4 cm FOV, with slow crystals based on the approach used in current PET.

model	crystals volume/cost [cm ³ /\$]	Photomultipliers number/cost [#/\$]	Estimated cost of the electronics	Estimated total cost
Future PET 157.4 cm FOV based on the approach used in the PET CTI/Siemens 966/EXACT3D (see Section 11.2.2.6.1)	91,493/~\$914,937 (BGO ~ \$10/cm ³)	11,577/~\$1,852,320 (3/4" ~ \$160 each)	~\$670,000	~\$3,437,257

Table 18-3 shows the cost of the main components of a whole-body PET with slow crystals, 157.4 cm FOV, proposed here for future development, based on the new approach of the 3D-Flow described herein.

The cost of the main components is shown to be about 1.37 million dollars.

The volume of the BGO crystals and the number of photomultipliers used are based on the layout of the PET shown in Figure 17-2.

The ratio between the number of photomultipliers and the detector area to readout has been based on the number of photomultipliers per detector area used in several PET built by Karp and co-workers [37] and on the promising results by the tests performed by Andreaco and Rogers [98] in decoding 256 BGO crystals per block (See also Section 13.3).

The DSP capability at each channel of the detector should facilitate and improve position, energy, and timing resolution. In the event it will be necessary to use a different ratio between PMT and detector area because of low performance of the PMT or the crystals, than the 256 channels 3D-Flow board (see Section 15.1.1.2) should be used, or the number of 3D-Flow boards with 64 channels should be multiplied by four.

The cost of two IBM PC chassis of electronics and one 3D-Flow pyramid board has been generously estimated at \$260,000.

Table 18-3. Estimated cost of the main components of a future whole-body PET , 157.4 cm FOV, with slow crystals based on the new approach of the 3D-Flow described herein.

model	crystals volume/cost [cm ³ /\$]	Photomultipliers number/cost [#/\$]	Estimated cost of the electronics	Estimated total cost
Future PET 157.4 cm FOV based on the new approach of the 3D-Flow (see Section 17.1)	65,028/~\$650,280 (BGO ~ \$10/cm ³)	2,304/~\$460,800 (1 ½" ~ \$200 each)	~\$260,000	~\$1,371,080

The lower cost advantage is provided by the geometric elliptical shape of the new proposed gantry requiring a smaller volume of crystals and the higher performance electronics with no detector boundary, which can extract more photons from 25 mm thickness crystals (compared to the 30 mm crystals), can use fewer photomultipliers (because the DSP

capabilities on each channel improves the S/N ratio), and can improve the energy resolution and the crystal decoding.

The shorter scanning time allows the examination of more patients per day, thus leading to earlier return of the invested capital as well as lowering the cost of examination to the patient or insurance company.

Table 18-4 shows the cost of the main components of a whole-body PET with slow crystals, with a 126 cm FOV, proposed here for future development, based on the new approach of the 3D-Flow described herein.

The cost of the main components is shown to be about 1 million dollars, and this implementation still provides many advantages in lower scanning time, lower radiation, better image quality, and lower examination cost.

Table 18-4. Estimated cost of the main components of a future whole-body PET, 126 cm FOV, with slow crystals based on the new approach of the 3D-Flow described herein.

model	crystals volume/cost [cm ³ /\$]	Photomultipliers number/cost [#/\$]	Estimated cost of the electronics	Estimated total cost
Future PET 126 cm FOV based on the new approach of the 3D-Flow	50,577/~\$505,770 (BGO ~ \$10/cm ³)	1,792/~\$358,400 (1 1/2" ~ \$200 each)	~\$200,000	~\$1,064,170

Table 18-5 shows the cost of the main components of a whole-body PET with fast crystals, 126 cm FOV, proposed here for future development, based on the new approach of the 3D-Flow described herein.

It is difficult to estimate the cost of the LSO crystals because the patent is owned by a single company; however, the cost of all other components is lowered (see Section 17.2), because fewer photomultipliers are required. In addition the real-time computation of the electronics is simpler due to the fact that the faster crystals provide better signals.

Table 18-5. Estimated cost of the main components of a future whole-body PET, 126 cm FOV, with fast crystals based on the new approach of the 3D-Flow described herein.

model	crystals volume/cost [cm ³ /\$]	Photomultipliers number/cost [#/\$]	Estimated cost of the electronics	Estimated total cost
Future PET 126 cm FOV based on the new approach of the 3D-Flow (see Section 17.2)	50,577/\$_??? patent is owned by a single company (LSO ~ \$??/cm ³)	1,792/~\$358,400 (1 1/2" ~ \$200 each	~\$120,000	~\$_?

19 Glossary

2x2 detector block boundary	The 2x2 detector block boundary is provided by the grouping of the 2x2 PMTs which do not have information exchange with adjacent PMTs.
Alpha Particle	A positively charged particle emitted by certain radioactive materials. Alpha particles can be stopped by a sheet of paper.
Alpha Radiation	The least penetrating type of radiation. Consists of two positively charged particles, called protons, and two neutral particles, called neutrons. Alpha radiation can be stopped by the dead layer of skin that covers our bodies or by a thin sheet of paper. Alpha radiation poses a hazard if it is ingested into the body by inhalation or along with food or water.
APD	Avalanche Photodiode.
ASIC	Application Specific Integrated Circuit
Attenuation	Reduction of the energy of the photon due to the absorption by the matter found on its path
Background Radiation	The radioactivity in the environment including cosmic rays from space and radiation that exists everywhere - in the air, in the earth, and in man-made materials that surround us. The average American receives about 360 millirem of background radiation per year.
Beta Particle	A negatively charged particle emitted from an atom during radioactive decay. A beta particle is an electron that has a mass equal to 1/1837 that of a proton. A beta particle can be stopped by an inch of wood or a thin sheet of aluminum.
Beta Radiation	Emitted from nucleus of an atom during fission. It can pass through one or two centimeters of water or human flesh. Beta radiation can be stopped by an inch of wood or a thin sheet of aluminum. There is an inhalation hazard from beta radiation
BGO	Bismuth germanate, or Bi ₄ Ge ₃ O ₁₂
Compton Scatter	Compton scattering is the collision between a photons and a loosely bound outer shell orbital electron of an atom. (See Section 13.4.5.4 for a more in depth explanation).
CsF	Cesium Fluoride
CT	X-ray computed tomograph scanner
Curie	A unit of measure for radioactivity. It measures of the number of radioactive atoms decaying in a given period of time e.g, disintegrations per minute. The curie is equal to 37

	$\times 10^9$ disintegrations per second, which is approximately the rate of decay of 1 gram of radium. A curie is also a quantity of any nuclide having 1 curie of radioactivity.
Dosimeter	A device, such as a film badge, which can be worn and used to measure the radiation dosage a person receives over a period of time.
EEC	European Economic Community Concerted Action of Cellular Regeneration and Degeneration
Electron	A subatomic particle with a negative electric charge and a mass 1/1837 that of a proton. It circles the nucleus of an atom
FPGA	Field Programmable Gate Array
FWHM	Full-width at half-maximum
Gamma Radiation	A form of electromagnetic, high energy radiation emitted from a nucleus. Gamma rays are essentially the same as X-rays and require dense, heavy shielding, such as lead, brick, or concrete, to stop them.
Geiger Counter	An instrument for detecting and measuring beta and gamma radiation.
GSO	Gadolinium orthosilicate
GSO(Ce)	Cerium-doped Gadolinium orthosilicate.
Half-life	The length of time in which any radioactive substance will lose one-half of its radioactivity. The half-life of a substance may vary in length from a fraction of a second to many years
head of a cluster	The sensor absorbing the highest scintillating light of the incident photon compared to its neighbors. See local maxima detection in Section 13.4.11.2
Isotope	Different forms of the same chemical element which are distinguished by having different numbers of neutrons in the nucleus. A single element may have many isotopes. For example, the three isotopes of hydrogen are protium, deuterium, and tritium.
LGSO	90% Lutetium and 10% Gadolinium, has very similar properties to LSO. (made by Hitachi Chemical Co)
LLRW	An acronym for low-level radioactive waste that is ordinary material that has become contaminated with radioactivity. LLRW is classified according to the amount of radioactive materials it contains and the length of time those materials remain radioactive. Gloves, clothing, and trash can be contaminated. Nuclear reactor components, mechanical parts, tools, and equipment become contaminated during routine use. These materials must be disposed of as low-level radioactive waste.
LSO	Lutetium orthosilicate, doped with a small amount of cerium
LVDS	Low Voltage Digital Signaling
millirem	A unit of radiation dosage equal to one-thousandth of a rem. An individual member of the public can receive up to 500 millirems per year according to federal standards. This limit does not include radiation received for medical treatment nor does the limit include the 300 millirems people receive annually from background radiation.
Monte Carlo	Selects a random nuclear process. The term "Monte Carlo" was coined by von Neumann, Ulam and Fermi from work on the atomic bomb during World War II. The term should

	reflect the idea that a conceptual roulette wheel could be employed to select the random nuclear processes. The random number generated by today's computers determines which interaction will occur by comparing probabilities (i.e. cross sections) of each interaction. The process is repeated and a particle is tracked in the target until it deposits all its energy or decays. Examples of Monte Carlo codes are: EGS4 [¹⁷³] originally developed at Stanford Linear Accelerator Center; MCNP [¹⁷⁴] developed at Los Alamos National Laboratory; LAHET [¹⁷⁵] from Los Alamos; MCNPX [¹⁷⁶] currently available only on UNIX platform, combines the theoretical model of LAHET code with the general features of MCNP.
Multiples	More than two photons within the time window of one event (typically 3 ns, corresponding to the diameter of the detector of 90 cm)
NEC	Noise Equivalent Count rate $NEC = T/(1 + S/T + R/T)$. Where T = True, S = Scatter, R = Random
NEMA	National Electrical Manufacturers Association (Committee to standardize performance measurements for the users of PET scanners for purposes of accepted measurements.
Neutron	An uncharged particle with a mass nearly equal to the mass of a proton. Neutrons are the particles that sustain a chain reaction in a nuclear reactor. Neutrons can be shielded by water.
Nucleus	Core or center of an atom containing protons and/or neutrons. Although the nucleus is only about 1/10,000 of the diameter of an atom, it contains nearly all the mass of an atom.
PET	Positron Emission Tomography
Phantom	A cylinder of 20 cm in diameter and the axial length 18.5 cm (it is larger than a brain and smaller than a body. A head is typically 18 x 10 cm
Prompts	Prompts or events that are found within a selected "coincidence window" (typically 10-20 ns). Prompts that are found in coincidence are either True (T), Randoms (R) or Scatter (S). $P = T + R + S$
Proton	A subatomic particle with a positive electric charge and a mass 1,837 times that of an electron.
PSF	point spread function
Radiation	Refers to the process of emitting energy in the form of rays or particles which are thrown off by disintegrating atoms the penetrate matter; may consist of alpha, beta, or gamma radiation.
Radioactivity	A process by which unstable atoms of an element emit or radiate the excess energy of their nuclei and change (or decay) to atoms of a different element or to a lower energy form of the original element. The property possessed by some elements, such as uranium of spontaneously emitting alpha, beta or gamma rays.
Radon	A radioactive gas which occurs in nature which cannot be seen, smelled, or tasted. Current estimates indicate that radon is responsible for the major portion of our exposure to background radioactivity
Random	Simultaneous decays of more than one pair electron-positron within the "coincidence window." Randoms are reduced by reducing the "coincidence window" Δt time. Time-of-flight across tomograph ring requires $\Delta t > 2$ ns. (Typically is 12 ns for current PET)

REM	An acronym for Roentgen Equivalent Man, a measure of radiation exposure that indicates the potential impact on human cells. Since human exposure to radiation usually involves very small doses, smaller units, called millirems are used. A millirem is 1/1000 of a rem. At relatively low levels of radiation - less than 10 rad - the rem and rad (millirem, millrad) are used interchangeably for beta, gamma and X-ray radiation
Scatter	A photon that deviates its path because interact with matter, but still reaches the detector (Compton scatter). The short time interval of the detection of the two hits in the opposite side of the detector validates the event, however the chord drawn between the two points where the detectors were hit, give the wrong information of where the photons originated
Scatter fraction:	Is the ratio of scattered events to total events, which are measured by the scanner at a low enough count rate so that random coincidences are negligible.
Sensitivity	Detection Efficiency. Measure of the counting efficiency of the system with a known amount and distribution of activity. The volume sensitivity is given as cps/given activity concentration ($\mu\text{Ci/ml}$ or MBq/ml)
Septa	The lead walls (which define the holes) of a 1- to 2-inch-thick slab of lead containing a geometric array of holes, are called "septa."
SimSET	SimSET: "Simulation System for Emission Tomography", a simulation package that uses Monte Carlo techniques to model the physical processes and instrumentation used in emission imaging. Developed by the University of Washington, Division of Nuclear Medicine.
Singles	All hits on the detector, until they have not been recognized as true coincidences, scatters, or randoms, are called singles
SNM	Society of Nuclear Medicine
Spatial resolution	Is the characterization of the width of the image point spread function (PSF), which is reported as the full-width at half-maximum (FWHM)
TOF	Time-of-flight. Time interval require by the photon to reach the detector after being generated by the annihilation electron-positron. (An alternative description is: the difference in arrival time of two photons at the two detectors, where the source is localize along the line of flight). $C = 1 \text{ ns/foot}$. 500 ps timing resolution provides 8 cm localization
True	A pair of photons that were directly coming from an annihilation electron-positron, without Compton Scattering
Voxel	Volume Element. The 3-D volume of the tissue called voxel is determined by multiplying the pixel size by the thickness of an image slice.
YSO?	Yttrium oxyorthosilicate, doped with a small amount of cerium

20 Bibliography

- [1] Phelps, M.E., et al., The Changing of Positron Imaging System. *Clinical Positron Imaging*, vol. 1(1):31045, 1998.
- [2] Crosetto, D., A fast cluster finding system for future HEP experiments. *Nuclear instruments and Methods in Physics Research A311* (1992) 49-56.
- [3] Crosetto, D.: A modular parallel processing system for trigger decision and DAQ in HEP experiments. *Nuclear Instruments and Methods in Physics Research, A315*, (1992), 487-490.
- [4] Burns, A. et al.: The BOSC project, European Particle Accelerator Conference, EPAC 90, Nice (12-16 June 1990),
- [5] Crosetto, D.: Fast Digital parallel processing module (FDPP), CERN/DD 89/33 (AC) (1989).
- [6] Buono, S., and Crosetto, D.: Fast Digital Parallel Processing Module Software Development." CERN/ECP 90-22, 21 December 1990.
- [7] Crosetto, D., et al.: Parallel array of digital signal processors as central decision element for upper level triggers in High Energy Physics experiments, *IEEE, Transaction in Nuclear Science*, February 1988.
- [8] Crosetto, D. A fast digital data processor for the FEMC trigger (VME version), User's manual, rev. 1.0, CERN-DELPHI/87-DAS-58 July 1st, 1987.
- [9] GEM Collaboration: GEM Technical design report, Superconducting Super Collider Laboratory, July 31, 1993. (Crosetto's design is included at page 7-11, to 7-14.
- [10] LHCb collaboration Technical Proposal. A large Hadron Collider Beauty Experiment for Precision Measurements of CP Violation and Rare Decay. CERN LHCC 98-4, LHCC/P4. 20 February 1998.
- [11] Stabin, M.G., et al., Radiation Dose Estimates for Radiopharmaceuticals. Oak Ridge Institute for Science and Education, Mail Stop 51, P.O Box 117, Oak Ridge, TN 37831, April, 1996.
- [12] Cherry, S.R., et al.: MicroPET: A High Resolution PET Scanner for Imaging Small Animals. *IEEE. Trans. Nucl. Sci.*, vol. 44(3):1161-1166, June 1997.
- [13] Marriot, C.J., et al.: High-resolution PET imaging and quantitation of pharmaceutical biodistributions in small animal using avalanche photodiode detectors. *J. Nucl. Med.*, vol. 35, pp. 1390-1396, August 1994.
- [14] Rajeswaran, S., et al.: 2D and 3D imaging of small animals and the human radial artery with high resolution detector for PET. *IEEE Trans. Nucl. Sci.*, vol. 11, pp.386-391, April 1992.
- [15] Watanabe, W., et al.: A high resolution PET for animal studies. *IEEE Trans. Nucl. Sci.*, vol. 11, pp. 577-580, April 1992.
- [16] Moreno-Cantu, J.J., et al.: Enhancement of signal-to-noise ratio in H₂ 15O bolus PET activation studies using a combined cold-bolus/switched protocol," in *Quantitative Functional Brain Imaging with Positron Emission Tomography*, R.E. Carson, M.E. Daube-Witherspoon, and P. Herscovitch, Eds. Bethesda, MD: Academic, June 1997.
- [17] Badawi, R.D., et al., The Effect of Camera Geometry on Singles Flux, Scatter Fraction and True and Random Sensitivity for Clinical 3D PET – a Simulation study. *Nuclear Science Symposium and Medical Imaging*, October 24 –30, 1999. M10-81.
- [18] Zubal IG, et al.: Computerized 3-Dimensional Segmented Human Anatomy *Med. Phys.* **21**(2): 299-302, 1994
- [19] Moreno-Cantu', J.J. et al., Evaluation of the ECAT EXACT HR+ 3D PET Scanner in 15O-water Brain Activation Studies. *IEEE Trans. Nucl. Sci.*, Dec. 1998, vol. 17(6):979-985.

- [20] Eriksson, L., et al.: A simple data loss model for positron camera systems. *IEEE Trans. Nucl. Sci.*, vol. 41(4):1566-1570, August 1994.
- [21] Moisan, C., et al.: A Count Rate Model for PET and its Application to an LSO HR PLUS Scanner. *IEEE Trans. Nucl. Sci.*, 1997, pp. 1186, 1190.
- [22] Wienhard, K., et al.: The ECAT EXACT HR: Performance of a New High Resolution Positron Scanner. *Journal of Computer Assisted Tomography*, vol. 18(1):110-118, 1994.
- [23] DeGrado, T.R., et al.: Performance Characteristics of a Whole-Body PET Scanner, *Juournal of Nuclear Medicine*, vol. 35(8):1398-1406, August 1994,
- [24] Cherry, S.R., et al.: Improved Detection of Focal Cerebral Blood Flow Changes Using Three-Dimensional Positron Emission Tomography. *Journal of Cerebral Blood Flow and Metabolism*, vol. 13, No. 4, 1993.
- [25] Duxbury, D.M., et al.: Preliminary results from the new large-area PETRA positron camera. *IEEE Trans. Nucl. Sci.* pp. 1222-1226, 1999.
- [26] Brix, G., et al.: Performance Evaluation of a Whole-Body PET Scanner Using the NEMA Protocol. *The journal of Nuclear Medicine*, vol. 38(10):1614-1623, October 1997.
- [27] Ter-Pogossian, M.M., et al.: The Super PET 3000-E: A PET Scanner Design for High Count Rate Cardiac Applications. *Journal of Computed Assisted Tomography*, vol. 18(4):661-669, July/August 1994.
- [28] Townsend, D.W., et al.: A Rotating PET Scanner Using BGO Block Detectors: Design, Performance and Applications. *The Journal of Nuclear Medicine*, vol. 34(8):1367-1376, August 1993.
- [29] Wienhard, K., et al.: Performance Evaluation of the Positron Scanner ECAT EXACT. *Journal Computer Assisted Tomography*, vol. 16(5):804-813, October 1992.
- [30] Dahlbom, M., et al.: Whole-Body Positron Emission Tomography: Part I. Methods and Performance Characteristics. *The Journal of Nuclear Medicine*, vol. 33(6):1191-1199, June 1992.
- [31] Guerrero, T.M., et al.: Characterization of a whole body imaging technique for PET. *IEEE Trans. Nucl. Sci.*, vol. 37(2):676-679, April 1990.
- [32] Rota Kops, E., et al.: Performance Characteristics of an Eight-Ring Whole Body PET Scanner. *Juornal of Computed Assisted Tomography*, vol 14(3):437-445, June 1990.
- [33] Mullani, N.A., et al.: Design and Performance of Posicam 6.5 BGO Positron Camera. *The Journal of Nuclear Medicine*, vol. 31(5):610-616, May 1990.
- [34] Dahlbom, M., et al.: A study of the possibility of using multi-slice PET systems for 3D imaging. *IEEE Trans. Nucl. Sci.*, vol. 36(1):1066-1070.
- [35] Kearfott, K.J., et al.: Evaluation of the Performance Characteristics of the PC 4600 Positron Emission Tomograph. *Journal of Computed Assisted Tomography*, vol. 8(3):502-513, June, 1984.
- [36] Lewellen, T.K., et al.: Investigation of the Count Rate Performance of General Electric Advance Positron Emission Tomograph. *IEEE Trans. Nucl. Sci.*, vol. 42(4):1051-1057, August, 1995.
- [37] Karp, J.S., et al.: Three-Dimensional Imaging Characteristics of the HEAD PENN-PET Scanner. *The Journal of Nuclear Medicine*, vol. 38(4):636-643, April 1997.
- [38] Schmand, M., et al.: Performance Evaluation of a new LSO High Resolution Research Tomograph –HRRT. *IEEE Nuclear Science Symposium and Medical Imaging Conference*, Seattle (WA), M4-2, October 24 – 30, 1999.
- [39] Rouze, N.C., et al.: A High Resolution, High Sensitivity Dedicated Research Scanner. *IEEE Nuclear Science Symposium and Medical Imaging Conference*, Seattle (WA), , October 24 –30, 1999. M10-36.
- [40] Valk, P.E., et al. Whole-body PET Imaging with [18F] Fluorodeoxyglucose in Management of Recurrent Colorectal Cancer. *Arch. Surg.*, vol. 134, pp. 503-513, May 1999.

-
- [41] Mandelkern, A. Mark, Nuclear techniques for medical imaging: Positron Emission Tomography. *Annu. Rev. Nucl. Part. Sci.* 1995. 45:205-54.
 - [42] Hays, T.M., et al.: A mathematical model for the distribution of the Fluorodeoxyglucose (FDG) in human. *Jurn. Nucl. Med.* vol. 40(8):1358-1366, August 1999.
 - [43] Schelstraete, K. et al.: The kinetics of ¹³N-ammonia incorporated in human tumors. *Nucl. Med. Comm.* vol. 6 pp. 461-470 (1985).
 - [44] Choi, Y., et al.: Quantification of Myocardial blood flow using ¹³N-ammonia and PET: Comparison of tracer models.
 - [45] Iida, H., et al.: Myocardial blood flow: comparison of oxygen-15-water bolus injection, slow infusion and oxygen-15-carbon dioxide slow inhalation. *Journ. Nucl. Med.* vol. 36(1) 78-85, Jan. 1995.
 - [46] Hichwa, R.D., et al.: Construction of a whole body blood flow model for use in positron emission tomography imaging with ¹⁵O-water. *Journ. of pharmacokinetics and biopharmaceutics.* vol. 25, pp 539 (1997)
 - [47] NCRP Report No. 100 May 1, 1989.
 - [48] Radon potential. Map of US. Environmental Protection Agency (EPA).
 - [49] Friedberg, W., et al.: Guidelines and technical information provided by the US Federal Aviation Administration to promote radiation safety for air carrier crew members. *Radiation Protection Dosimetry*, vol. 86, No. 4 pp. 323-327 (1999), Nuclear Technology publishing.
 - [50] ICRP Publication 60, *Annals of the ICRP* 21, pp. 42-46; 1991. ICRP Publication 75, *Annals of the ICRP*, 27, p.25; 1991, NCRP Report 116, P38; 1993.
 - [51] Townsend, D.W., et al.: *Journal of Nuclear Medicine* 28:1554 (1987).
 - [52] Marsden, P.K., et al.: The performance of a multiwire proportional chamber positron camera for clinical use. *Phys. Med. Biol.* 34(8):1043-1062 (1989).
 - [53] Bateman, J.E., et al.: *Nuclear Instruments and methods* 225:209 (1984).
 - [54] Kapusta, M., et al.: Comparison of the scintillation properties of LSO:Ce manufactured by different laboratories and LGSO:Ce. *IEEE Conf. rec., Nucl. Sci. Symp. and Med. Imag.* N20-27. October 24-30, 1999, Seattle (WA).
 - [55] Derenzo, S., Comparison of detector materials for time-of-flight positron tomography. *IEEE workshop on time-of-flight tomography*, May 1982.
 - [56] McIntyre, J.A. Plastic scintillators for time-of-flight tomography. *IEEE, Workshop on time-of-flight tomography*, May 1982.
 - [57] Storm, E., and Israel, H.I.: Photon cross sections from 0.001 to 100 MeV for elements Z = 1 to Z = 100. Los Alamos National Laboratory, (1967, 1979). *Nucl. Data Tables A* 7, 565-681 (1970).
 - [58] Hubbell, J.H., and Seltzer, S.M.: Tables of X-Ray Mass Attenuation Coefficients and Mass Energy-Absorption Coefficients for 1 keV to 20 MeV for Elements Z = 1 to 92 and 48 Additional Substances of Dosimetric Interest. U.S. Secretary of Commerce, NIST, NISTIR-5632, (1989, 1990, 1996)
 - [59] Pauwels, D., et al.: A novel inorganic scintillator: Lu₂Si₂O₇:Ce³⁺ (LPS). *conf. record. Nucl. Sci. Sym. and Med. Imag.* October 24-30, 1999, Seattle (WA), N7-3.
 - [60] Derenzo, S.E., et al.: Measurements of the Intrinsic Rise Times of Common Inorganic Scintillators. *conf. record. Nucl. Sci. Sym. and Med. Imag.* October 24-30, 1999, Seattle (WA), N10-2.
 - [61] Chepel, V.Y.: *Nucl. Trks. Rad. Meas.* 21 (1993) 47.
 - [62] Iwanczyk, J., et al. *IEEE Trans. Nucl. Sci.* NS-39 (1992) 1275.
 - [63] Glasser, F. et al.: *Nucl. Instr. And Meth. A* 322 (1992) 619.

- [64] Anderson, D.F.: Physics Letter B 118:230 (1982).
- [65] Fiorini, C., et al.: Position and Energy resolution of a new gamma-ray detector based on a single CsI(Tl) scintillator coupled to a silicon drift chamber array. IEEE, conf. rec. Nucl. Sci. Symp. and Med. Imag. pp. 796-801, 1998.
- [66] www.burle.com
- [67] www.hamamatsu.com
- [68] www.photonis.com
- [69] Shao, Y., et al.: Evaluation of Multi-Channel PMT's for Readout of Scintillator Array. Conference record of the Nuclear Science Symposium and Medical Imaging, pp. 1055-1059. 1995.
- [70] Boutot, J.P. et al.: Multianode photomultiplier for detection and localization of low light levels. IEEE Trans. Nucl. Sci., vol NS-34, pp 449-452, 1987.
- [71] Comby, G. et al.: Test of a new 64 channel PMT for imaging. Nucl. Inst. Meth. Vol. A269, pp. 246-260, 1988.
- [72] Engels, R., et al.: A new 64-channel area detector for neutrons and gamma rays. IEEE, conf. rec. Nucl. Sci. Symp. and Med. Imag. pp. 776-779, 1998.
- [73] Cherry, S.R., et al.: A comparison of PET detector modules employing rectangular and round photomultiplier tubes. IEEE Trans. Nucl. Sci., vol. 42(4):1064-1068 (Aug. 1995).
- [74] Mmoszynski, M. et al.: Large area avalanche photodiodes in X-Rays and light detection. IEEE, Nucl. Sci. Symp., and Med. Imag. N4-2, October 24-30, 1999 Seattle (WA).
- [75] Allier, C. et al.: Scintillation light read-out by low-gain thin avalanche photodiodes in silicon wells. IEEE, Nucl. Sci. Symp., and Med. Imag. N4-3, October 24-30, 1999 Seattle (WA).
- [76] Shah, K.S., et al.: Planar Processed APDs and APD arrays for Scintillation Detection. . IEEE, Nucl. Sci. Symp., and Med. Imag. N4-5, October 24-30, 1999 Seattle (WA).
- [77] Lecompte, R., et al.: High resolution positron emission tomography with a prototype camera based on solid state scintillation detectors. IEEE Trans. Nucl. Sci., NS-37, pp. 805-811, 1990.
- [78] Paulus, M.J., et al.: Comparison of the Beveled-Edge and Reach-Through APD structures for PET applications. Conf. rec., Nucl. Sci. Symp. and Med. Imag., vol. 4, pp. 1864-1868, 1994.
- [79] Casey, M.E., et al.: A multycrystal two dimensional BGO detector system for positron emission tomography. IEEE Trans. Nucl. Sci., NS-33, pp. 460-363, 1986.
- [80] Paulus, M.J., et al.: A low-noise, wide-band CMOS charge-sensitive preamplifier for use with APD/LSO PET detectors. IEEE Trans. Nucl. Sci. vol. 43(3):1666-1671, June 1996.
- [81] Lecomte, R., et al.: An APD-based quad scintillator detector module with pulse shape discrimination coding for PET. IEEE, conf. rec. Nucl. Sci. Symp. and Med. Imag. pp. 1445-1447, 1998.
- [82] Saudi, A., et al.: Investigation of Depth of interaction by pulse shape discrimination in multicrystal detectors read out by avalanche photodiodes. IEEE, conf. rec. Nucl. Sci. Symp. and Med. Imag. pp. 1078-1082, 1998.
- [83] McIntyre, R.J., et al.: A short-wavelength selective reach-through avalanche photodiode. IEEE Trans. Nucl. Sci., vol. 43, pp. 1341-1346, 1996.
- [84] Lecompte, R., et al.: Investigation of GSO, LSO and YSO scintillators using reverse avalanche photodiodes. IEEE, conf. rec. Nucl. Sci. Symp. and Med. Imag., vol. 1, pp. 212-216, 1997.
- [85] Huber, J., et al.: Development of a 64-channel PET detector module with depth of interaction measurement. IEEE presentation at the Nucl. Sci. Symp. and Med. Imag., M4-6, Seattle, October 24-30, 1999.

-
- [86] Huber, M.H., et al.: Characterization of a 64 channel PET detector using photodiodes for crystal identification. *IEEE. Trans. Nucl. Sci.*, vol 44(3):1197-1201, June 1997.
 - [87] Moses, W.W., et al.: Performance of a PET detector module utilizing an array of silicon photodiodes to identify the crystal of interaction. *IEEE, Trans. Nucl. Sci.*, vol. 40(4):1036-1040., August 1993.
 - [88] Gruber, G.J., et al.: A discrete scintillation camera module using silicon photodiode readout of CsI(Tl) crystals for breast cancer imaging. *IEEE Trans. Nucl. Sci.*, vol. 45(3):1063-1068, June 1998.
 - [89] Moses, W.W., et al.: A "winner-take-all" IC for determining the crystal of interaction in PET detectors. *IEEE Trans. Nucl. Sci.*, NS-43, pp. 1615-1718, 1996.
 - [90] Yu, H., et al.: A high-speed and high-precision Winner-Select-Output (WSO) ASIC. *IEEE, conf. rec. Nucl. Sci. Symp. and Med. Imag.*, pp. 656-660, 1997.
 - [91] Derenzo, S.E., et al.: Initial characterization of a position-sensitive photodiode/BGO detector for PET. *IEEE Trans. Nucl. Sci.*, vol. 36(1):1084-1089, February 1989.
 - [92] Townsend, D., et al., The high-density avalanche chamber (HIDAC) positron camera. *J. Nucl. Med.* 28, pp. 1554-1562, 1987.
 - [93] Bateman, J.E., et al.: The Rutherford Appleton Laboratory's Mark 1 multiwire proportional counter positron camera. *Nucl. Instrum. Methods A* 225 209-2031.
 - [94] Flower, M.A. et al.: Clinical trials of the prototype Rutherford Appleton Laboratory MWPC positron camera at the Royal Marsden Hospital. *Nucl. Instrum. Methods A* 269 pp. 350-353, 1988.
 - [95] Gys, T.: An overview of Current developments in Position-Sensitive Hybrid Photon detectors and photo-multiplier tubes. *IEEE Conf. rec. of the Nucl. Sci. Symp. and Med. Imag.* N4-1, Seattle, October 24-30, 1999.
 - [96] Kwait, P., et al. *Phys. rev. A* 48 (1993) R867.
 - [97] Pedroff, M.D., et al.: *Appl. Phys. Lett.* 51:406 (1987).
 - [98] Rogers, J.G., et al.: Testing 144- and 256-crystal BGO block detectors. *IEEE. Conf. Rec. Nuclear Sci. Symp. and Med. Imag.*, vol. 3, pp. 1837-1841, 1993.
 - [99] Surti, S., et al.: Optimizing the Performance of a PET Detector using Discrete GSO Crystals on a Contiguous Lightguide. *Conf. Rec. Nucl. Sci. Symp. and Med. Imag.* N3-58, Seattle, October 24-30, 1999.
 - [100] Phelps, M., et al.: Application of annihilation coincidence detection to transaxial reconstruction tomography. *J. Nucl. Med.* 16:210-224; 1975.
 - [101] Siegel, S., et al.: Development of Continuous Detector for High Resolution Animal PET System. *Conf. Rec. Nucl. Sci. Symp. and Med. Imag.*, pp. 1662-1666, 1994.
 - [102] Schmand, M., et al.: Performance results of a new DOI detector block for High Resolution PET-LSO Research Tomograph HRRT. *IEEE Trans. Nucl. Sci.*, vol. 45(6):3000-3006, December 1998.
 - [103] Young, J.W., et al.: FPGA based front-end electronics for a high resolution PET scanner. *Conf. rec. of the Nucl. Sci. Symp. and Med. Imag.* M3-22, Seattle, October 24-30, 1999
 - [104] Cherry, S.R., et al.: Optical Fiber readout of scintillator array using a Multi-Channel PMT. *IEEE Conf. Rec. Nucl. Sci. Symp. and Med. Imag.*, pp. 1766-1770, 1995.
 - [105] Cutler, P.D., et al.: Use of digital front-end electronics for optimization of a modular PET detector. *IEEE Trans. Nucl. Sci.*, vol. 13, pp. 408-418, 1994.
 - [106] Siegel, S., et al.: Simple Charge Division Readouts for Imaging Scintillator. *IEEE conf. rec.* pp. 13-17, 1995.

- [107] Melcher, C.L., et al.: Scintillation Properties of LSO:Ce Boules. IEEE, conf. rec., Nucl. Sci. Symp. and Med. Imag., pp.154-157, 1998.
- [108] Meng, L.J., et al.: Performance results of a prototype depth-encoding PET detector. IEEE Nuclear Science Symposium and Medical Imaging Conference, Seattle (WA), M3-49, October 24 –30, 1999.
- [109] Moisan, C., et al.: Simulating the performances of an LSO based position encoding detector for PET. IEEE, conf. rec. Nucl. Sci. Symp. and Med. Imag., pp. 1211-1215, 1996.
- [110] Karp, J.S., et al.: A high-resolution GSO-based brain PET camera. IEEE, Nucl. Sci. Symp., and Med. Imag. M4-8, October 24-30, 1999 Seattle (WA).
- [111] Surti, S., et al.: Optimazing the performance of a PET detector using discrete GSO crystals on a continuous lightguide. IEEE, Nucl. Sci. Symp., and Med. Imag. M3-58, October 24-30, 1999 Seattle (WA).
- [112] Karp, J.S., et al.: A position-sensitive detector for use in positron emission tomography. Nucl. Instrum. Methods A273:891-897, 1988.
- [113] Ficke, D.C., et al.: A GSO(Ce) block type detector for high count rate PET application. IEEE, conf. rec. 1994, pp. 1859-1863.
- [114] Spinks, T.J., et al.: Performance of a new 3D-only PET scanner – the EXACT3D. IEEE Conf. Rec. Nucl. Sci. Symp. and Med. Imag., pp. 1275-1279, 1996.
- [115] Adam, L.E., et al.: Performance evaluation of the whole-body PET scanner ECAT EXACT HR+ following IEC standard. IEEE Trans. Nuc. Sci., vol. 44:1172-1179, 1997.
- [116] Mertens, J.D., et al.: US Patent No. 5,241,181. “Coincidence detector for a PET scanner.” Assignee: General Electric Company, August 31, 1993.
- [117] Mertens, J.D. and Bhend, W.L.: Digital Coincidence detection: a scanning VLSI implementation. IEEE Trans. Nucl. Sci., vol. 40(6):2037-2039, 1993.
- [118] Lewelen, T.K., et al.: Investigation of the performance of the General Electric ADVANCE positron emission tomograph in 3D mode.
- [119] Karp, J.S., et al.: Performance Standards in Positron Emission Tomography. J Nucl Med 1991; 12: 2342-2350.
- [120] Newport, D.F., and Young, J.W.: An ASIC implementation of digital front-end electronics for a high resolution PET scanner. IEEE Trans. Nucl. Sci., vol. 40(4), August 1993.
- [121] Dent, H.M., et al.: A real time digital coincidence processor for positron emission tomography. IEEE Trans. Nucl. Sci., vol. 33(1):556-559, 1986.
- [122] Newport, D.F., et al.: Coincidence Detection and selection in Positron Emission Tomography using VLSI. IEEE Trans. Nuc. Sci., vol. 36(1):1052-1055, February 1989.
- [123] Young, J.W., et al.: Optimum Bandwidth Usage in Digital Coincidence Detection for PET. IEEE conf. rec., Nucl. Sci. Symp. and Med. Imag., pp. 1205-1208, 1993.
- [124] Bruckbauer, T., et al.: Evaluation of the ECAT EXACT HR with ASCII for Clinical Routine 3D Measurements. IEEE Trans, Nucl. Sci. 1378-1382, 1996.
- [125] Hartz, R.K, et al.: US Patent No. 5,210,420. Positron emission tomography scanner. Assignee: Positron Corporation (Houston, TX), May 11, 1993.
- [126] Mullani, N.A.: US Patent No. 4,864,138. Positron emission tomography camera. Assignee: Clayton Foundation for Research (Houston, TX), September 5, 1989.
- [127] Mullani, N.A.: US Patent No. 4,642,464. Positron emission tomography camera. Assignee: Clayton Foundation for Research (Houston, TX), February 10, 1987.

-
- [128] Mullani, N.A.: US Patent No. 4,563,582. Positron emission tomography camera. Assignee: Clayton Foundation for Research (Houston, TX), May 24, 1984.
 - [129] Dahlbom, M., et al.: A YSO/LSO Phoswich array detector for single and coincidence photon imaging. Conf. rec. Nucl. Sci. Symp. and Med. Imag., pp. 1165-1169, 1997.
 - [130] Dahlbom, M., et al.: Performance of a YSO/LSO Phoswich detector for use in PET/SPECT systems. IEEE Trans. Nucl. Sci., vol. 44(3):1114-1119, June 1997.
 - [131] Saoudi, A., and Lecomte, R.: A Novel APD-based detector module for multi-modality PET/SPECT/CT scanners. IEEE Conf. Rec. Nucl. Sci. Symp. and Med. Imag., pp. 1089-1093, 1998.
 - [132] Allemand, R., et al.: Potential advantages of a Cesium Fluoride scintillator for a time-of-flight positron camera. J. Nucl. Med., vol. 21, pp. 153-155, 1980.
 - [133] Mullani, N.A., et al.: System design of fast PET scanner utilizing time-of-flight. IEEE Trans. Nucl. Sci., vol. NS-28, pp. 104-107, 1981.
 - [134] Moses, W.W., and Derenzo, S.E.: Prospects for Time-of-Flight PET using LSO scintillator. IEEE Trans. Nucl. Sci., vol. 46(3):474-478, June 1999.
 - [135] Yamamoto, S., et al.: A GSO depth of interaction detector for PET. IEEE Trans. Nucl. Sci., vol. 45(3):1078-1082, 1998.
 - [136] Karp, J.S., et al.: Depth of interaction determination in Na(Tl) and BGO scintillation crystals using a temperature gradient. Nuclear Instr. and Methods, A, vol. 260, pp509-517, October 1987.
 - [137] Shimizu, K. et al.: Development of a 3-D detector system for positron CT. IEEE Trans. Nucl. Sci. vol. 35(1):717-729, February 1988.
 - [138] Rogers, J.: A method for correcting the depth of interaction blurring in PET cameras. IEEE Trans. Nucl. Sci. vol. 14(1):146-150, March 1995.
 - [139] Miyaoka, R.S., et al.: Effect of Detector Scatter on Decoding Accuracy of a DOI Detector. IEEE Conf. rec. of the Nucl. Sci. Symp. and Med. Imag. M3-34, Seattle, October 24-30, 1999.
 - [140] Tornai, M.P., et al.: Positioning and Energy Response of PET Block Detectors with Different Light sharing schemes. IEEE Trans. Nucl. Sci., vol. 41(4):1458-1463, August 1994.
 - [141] Miyaoka, R.S., et al.: Design of a Depth of interaction (DOI) PET Detector Module. IEEE Trans. Nucl. Sci., vol. 45(3):1069-1073, June 1998.
 - [142] Shao, Y., et al.: A study of inter-crystal scatter in small scintillator arrays designed for high resolution PET imaging. IEEE Trans. Nuc. Sci., NS-43(3):1938-1944, 1996.
 - [143] Comanor, K., et al.: Algorithms to identify detector Compton scatter in PET imaging. IEEE Trans. Nucl. Sci. NS-43(4):2213-2218, 1996.
 - [144] Schmand, M., et al.: Advantages using pulse shape discrimination to assign the depth of interaction information (DOI) from a multi layer phoswich detector. IEEE, Trans. Nucl. Sci., vol. 46(4), August 1999.
 - [145] Moisan, C., et al.: Segmented LSO Crystals for Depth of interaction Encoding in PET. IEEE, Conf. Rec. Nucl. Sci. Symp. and Med. Imag., vol. 2 pp. 1112-1116, 1997.
 - [146] Murayama, H. et al.: Design of a Depth of interaction Detector with a PS-PMT for PET. IEEE Conf. rec. of the Nucl. Sci. Symp. and Med. Imag. M4-1, Seattle, October 24-30, 1999.
 - [147] Moses, W.W., et al.: A room temperature LSO/PIN photodiode PET detector module that measures depth of interaction. IEEE Trans. Nucl. Sci., vol. 42(4):1085-1089, August 1995
 - [148] Huber, J.S., et al.: Calibration of a PET detector module that measures depth of interaction. IEEE Trans. Nucl. Sci., vol. 45(3):1268-1272, June 1998.

-
- [149] Shao, Y., et al.: A Study of depth of interaction measurement using bent optical fibers. IEEE Conf. Rec. Nucl. Sci. Symp. and Med. Imag., pp. 1440-1444, 1998.
 - [150] Correia, J.A., et al.: Performance of Small Animal PET Instrument with 1 mm Resolution. IEEE Conf. rec. of the Nucl. Sci. Symp. and Med. Imag. M7-32, Seattle, October 24-30, 1999.
 - [151] McIntyre, J.A., et al.: A positron emission tomograph design for 3/4 mm resolution. IEEE, conf. rec. Nucl. Sci. Symp. and Med. Imag. pp. 1357-1361, 1994.
 - [152] Karp, J.S., et al.: Evaluation of volume imaging with the HEAD PENN-PET scanner. IEEE Conf. rec. Nucl. Sci. Symp. and Med. Imag., pp. 1877-1881, 1994.
 - [153] Freifelder, R., et al.: Design and performance of the HEAD PENN-PET scanner. IEEE Trans. Nucl. Sci., vol. 41(4):1436-1440, August 1994.
 - [154] Karo, J.S., et al.: Event localization in a continuous scintillation detector using digital processing. IEEE Trans. Nucl. Sci., vol. 33:550-555, 1986.
 - [155] Mankoff, D.A., et al.: A local coincidence triggering system for PET tomographs composed of large-area position-sensitive detectors. IEEE Trans. Nucl. Sci., vol. 37:730-736, 1990.
 - [156] Crosetto, D., "System Design and Verification Process for LHC Programmable Trigger Electronics" IEEE NSS-MIC Seattle (WA) Oct. 24-30, 1999. <http://www.3d-computing.com/pb/nss99.pdf>
 - [157] Crosetto, D., "Massively Parallel-Processing System with 3D-Flow Processors." IEEE Computer Society. 0-81816-6322-7194, pp.355-369.
 - [158] Crosetto, D. "High-Speed, Parallel, Pipelined, Processor Architecture for front-end Electronics, and Method of Use Thereof." LHCb 96-2, TRIG 96-1
 - [159] Paans, A.M.J., et al.: The imaging of positron emitters in single photon and coincidence mode: evaluation of SPECT and PET systems. 18th annual International Conference of IEEE Engineering in Medicine and Biology Society, Amsterdam 1996, pp. 846-847.
 - [160] Karp, J.S., et al.: Event localization in a continuous scintillation detector using digital processing. IEEE Trans. Nucl. Sci., vol. 33(1):550-555, February 1986,
 - [161] Crosetto, D.: Detailed design of the digital electronics interfacing detectors... LHCb 99-006, 5 May, 1999 CERN – Geneva.
 - [162] Anger R.T.: The Anger scintillation camera, Rao D.V., Ed.: Physics of Nuclear Medicine, Recent Advances, New York, American Institute of Physics, 1984.
 - [163] Crosetto, D.: LHCb base-line level-0 trigger 3D-Flow implementation." Nuclear Instruments and methods in physics research, Section A 436 (1999) 341-385.
 - [164] Crosetto, D.: Real-time system design environment for multi-channel high-speed data acquisition system and pattern recognition. 11th IEEE Real time conference, Santa Fe, New Mexico, USA, 14-18 June 1999. pp. 329-336.
 - [165] Jones, F.Williams, PETLINK, CTI System, Inc. 810 Innovation Dr. Knoxville, TN 37932-2571. www.cti-pet.com/bjones.nsf.
 - [166] Huges, G.: Special report: Radon in Washington. June 1994, Division of Radiation Protection Airdustrial Center, Building 5 P.O. Box 47827 Olympia, Washington 94504-7827.
 - [167] Tumer, O. Tumay, U.S. Patent No. 5,821,541. Method and apparatus for radiation detection.
 - [168] http://depts.washington.edu/~simset/html/simset_main.html (SimSET: "Simulation System for Emission Tomography", a simulation package that uses Monte Carlo techniques to model the physical processes and instrumentation used in emission imaging.

-
- [169] Armantrout G.A.: Principles of semiconductor detector operation, in *Semiconductor Detectors in Future of Nuclear Medicine*. New York, The Society of Nuclear Medicine, 1971.
 - [170] TerPogossian MM, Phelps ME: Semiconductor detector system. *Semin. Nucl., Med.*, 3:343-365, 1973.
 - [¹⁷¹] Birks, J.B.: The theory and practice of scintillation counting. New York, MacMillan Co., 1964.
 - [172] Binkley, D.M., et al.: A Custom CMOS Integrated Circuit for PET Tomograph Front-End Applications. *IEEE, conf. rec.* pp. 867 871, 1993.
 - [173] Nelson, W.R., et al.: The EGS4 code system, SLAC-256-UC-32. Stanford Linear Accelerator Center. 1985.
 - [174] Hendricks, J.S., MCNP4B, LANL Memorandum. Los Alamos National Laboratory, 1997.
 - [175] Prael, R.E. et al.: User Guide to LCS: The LAHET code system," LA-UR-893014, Los Alamos National Laboratory; 1989.
 - [176] Hughes, H.G., et al.: MCPNPX-The LAHET/MCNP Code Merger. XTM-RN(U) 97-012, Los Alamos National Laboratory; 1997.